

https://dspace.org/

Measurement of residual stresses in thick-walled composite pipes

Carpenter, Henry William

2016
http://hdl.handle.net/10539/20036

Downloaded from a DSpace repository. https://dspace.org/

Measurement of Residual Stresses in Thick-Walled Composite Pipes

Henry William Carpenter

A thesis submitted to the Faculty of Engineering and the Built Environment, University of the Witwatersrand, Johannesburg, in fulfilment of the requirements for the degree of Doctor of Philosophy.

Johannesburg, August 2015

Declaration

I declare that this thesis is my own, unaided work, except where otherwise acknowledged. It is being submitted for the degree of Doctor of Philosophy in the University of the Witwatersrand, Johannesburg. It has not been submitted before for any degree or examination at any other university.

Signed this __ day of _____ 20__

_____

Henry William Carpenter.

Acknowledgements

The support of the DST/NRF Centre of Excellence in Strong Materials (CoE-SM) towards this research is hereby acknowledged. Opinions expressed and conclusions arrived at, are those of the author and are not necessarily to be attributed to the CoE-SM.

Additionally, I would like to thank the following people:

Professor Robert Reid for his supervision, support, and encouragement during the course of this research project. I would also like to thank Robert for his extensive efforts with regard to the journal publications related to this work.

The lab staff at the NWE Barloworld laboratories for the manufacture of the test fixtures, as well as the supervision and guidance they provided with regards to operation of the different equipment and machinery required to perform the experimental testing.

Professor Ratnam Paskaramoorthy, for his efforts with regards to the journal publications related to this research.

My partner, Nicci, and my parents, Sheila and Kenneth, as well as my siblings and close friends, for their support and encouragement.

Abstract

The Sachs method of residual stress measurement allows for the determination of the residual stresses that exist through the thickness of a pipe or disk. Compared to other methods of residual stress measurement, this method is advantageous since the full state of stress can be determined in a single experiment. Additionally, these residual stresses can be determined analytically, with no need for time-consuming finite element (FE) modelling. Although the Sachs method has seen extension to pipes of cylindrical orthotropy, no solution exists for application of this technique to layered anisotropic pipes.

This work presents an extension of the Sachs method to layered anisotropic pipes, of any wall thickness. Under the assumption of linear elasticity, the response of a pipe to removal of material from the outer surface is utilised to determine the released residual loads. These loads are used to evaluate the state of stress that existed prior to any material removal. It is demonstrated that not only is this method accurate for layered anisotropic pipes, but also superior to previous extensions of Sachs' method when thick-walled orthotropic pipes are considered.

Using the current method, the residual stress state within three thick-walled filament wound glass fibre reinforced plastic (GFRP) pipes is experimentally measured. The first of these pipes is wound entirely at the industry-standard winding angle of $\pm 55^{\circ}$. The remaining two pipes each comprise layers of two separate winding angles. The first of these is wound at $\pm 65^{\circ}$ within the inner layer, and $\pm 47^{\circ}$ within the outer layer. The second layered pipe is wound at $\pm 75^{\circ}$ and $\pm 36^{\circ}$, respectively. Layers of approximately 0.3 mm thickness were incrementally ground from the outer surface of the pipes, and the corresponding strain responses measured using strain gauges bonded to the inner surfaces. The resulting residual axial, hoop and in-plane shear stress distributions all satisfy the requirement of self-equilibrium, and the radial stress distributions all vanish to zero at the inner and outer surfaces.

Using the measured data of each pipe configuration, the effect of removal of thicker layers is investigated. It is shown that for relatively simple stress states, little or no loss in the resolution of the residual stress distributions occurs. It is also demonstrated that error

analysis, based upon the standard linearised differential relationships, is highly dependant on the removed layer thickness, and thus not suited for this method of residual stress measurement. An improved method of error analysis is consequently presented, based upon a sensitivity analysis of the residual stress distributions to the level of experimental scatter in the measured strain responses. This method is used to determine the true bounds in error of the measured stress distributions of each pipe configuration.

Published Work

Aspects of this thesis have been published in the following references:

- H.W. Carpenter, R.G. Reid, and R. Paskaramoorthy. Extension of the layer removal technique for the measurement of residual stresses in layered anisotropic cylinders. *International Journal of Mechanics and Materials in Design*, 10(3): 269–280, 2014.
- H.W. Carpenter, R.G. Reid, and R. Paskaramoorthy. Measurement of the Distribution of Residual Stresses in Layered Thick-Walled GFRP Pipes. *Experimental Mechanics*, 54(9): 1627-1638, 2014.
- H.W. Carpenter, R.G. Reid, and R. Paskaramoorthy. The effect of residual stresses and wind configuration on the allowable pressure of thick-walled GFRP pipes with closed ends. *International Journal of Mechanics and Materials in Design*, DOI: 10.1007/s10999-014-9280-z, 2014.

In addition to these publications, the following paper has been submitted for review to the journal *Journal of Engineering Materials and Technology*:

- H.W. Carpenter, R.G. Reid, and R. Paskaramoorthy. Sensitivity Analysis of the Crack Compliance and Layer Removal Methods for Residual Stress Measurement in GFRP Pipes. *Submitted for review to Journal of Engineering Materials and Technology*, MATS-15-1133, June 2015.

Contents

Declaration i

Acknowledgements ii

Abstract iii

Published Work v

Contents vi

List of Figures xiii

List of Tables xxi

List of Abbreviations xxii

List of Symbols xxiii

1 Introduction 1

2 Literature review 5

2.1 X-ray diffraction 5

2.2 Neutron diffraction 6

2.3 Hole-drilling methods 6

2.4 Sectioning methods 10

2.5 Radial cutting method 12

2.6 Contour method 14

2.7 Crack compliance method 15

2.8 Sachs' method 19

3 Objectives **23**

4 Theory **24**

4.1 Constitutive equations 25

4.2 Ply displacements 26

4.3 Ply strains 27

4.4 Ply stresses 27

4.5 Boundary conditions 28

4.6 Loading 29

5 Proposed method **31**

5.1 Finding the induced stress 33

5.2 Finding the applied loading 36

5.3 Finding the residual stress distributions 38

5.4 Error analysis 41

5.5 Special case: Filament-wound pipes 42

6 Validation of current method **45**

6.1 Problem 1: Thick-walled isotropic pipe 46

6.2 Problem 2: Thin-walled orthotropic pipe 50

6.3 Problem 3: Thick-walled orthotropic pipe 52

6.4 Problem 4: Thick-walled anisotropic pipe 55

7 Materials and Experimental technique **58**

7.1 Experimental equipment 58

7.1.1 Strain gauges 58

7.1.2 Temperature sensor 59

7.1.3 Data acquisition system 59

7.1.4 Computer 61

7.1.5 Cylindrical grinding machine 61

7.1.6 Micrometer 61

7.1.7 Fans and heaters 61

7.2 Materials and Specimen preparation 62

7.2.1 Filament-wound GFRP specimens 62

7.2.2 Material properties 62

7.2.3 Specimen length 64

7.2.4 Strain gauge placement 64

7.3 Experimental Procedure 65

7.3.1 Temperature compensation 65

7.3.2 Method 67

7.3.3 Precautions 68

7.3.4 Estimation of measurement error 69

8 Results and Discussion **71**

8.1 ±55° Filament-wound pipe 71

8.1.1 Measured strain response 71

8.1.2 Residual stress distributions 75

8.2 ±65°/±47° Filament-wound pipe 82

8.2.1 Measured strain response 82

8.2.2 Residual stress distributions 86

8.3 ±75°/±36° Filament-wound pipe 93

8.3.1 Measured strain response 93

8.3.2 Residual stress distributions 97

9 Further investigation: Increasing the thickness of the removed layers 105

9.1 ±55° Filament-wound pipe 106

9.2 ±65°/±47° Filament-wound pipe 111

9.3 ±75°/±36° Filament-wound pipe 116

10 Further investigation: Error analysis **122**

10.1 Basis of error analysis 122

10.2 ±55° Filament-wound pipe 124

10.2.1 Full data set 125

10.2.2 Reduced data set 132

10.2.3 Error bar estimation 139

10.3 ±65°/±47° Filament-wound pipe 144

10.3.1 Full data set 144

10.3.2 Reduced data set . . . 147

10.3.3 Error bar estimation . . . 149

10.4 ±75°/±36° Filament-wound pipe . . . 153

10.4.1 Full data set . . . 154

10.4.2 Reduced data set . . . 156

10.4.3 Error bar estimation . . . 157

11 Conclusions **162**

12 Recommendations **164**

REFERENCES **165**

A Determination of material and transformed stiffness matrices **185**

B Theoretical derivation **189**

C Issues with the current extensions of Sachs' method for determining residual stresses in cylindrically orthotropic pipes **193**

D Derivation of matrix-form equations for determination of the pipe constants **201**

D.1 Finding pipe constants of remaining pipe after the removal of m layers . . . 201

D.2 Finding constants of the layer m . . . 205

D.2.1 Finding the constants when layer m comprises material of ply k . . . 205

D.2.2 Finding the constants when layer m comprises material of two plies 208

E Self-correcting mechanism of current method **212**

F Material properties **216**

F.1 E-Glass fibre 216

F.2 Epoxy resin 216

F.3 Lamina properties 218

G FE models for determining residual stresses **219**

G.1 Determining the residual loads of layer m 219

G.2 Determining the residual stresses in layer m 222

H Calibration of the LM35D temperature sensor **223**

I Determination of required specimen length **225**

I.1 Determining the coefficients of thermal expansion 225

I.2 Thermal FE model 226

J Temperature compensation of the measured strain data **232**

K Measuring the temperature due to grinding **235**

L Determining SD variations in measurement scatter **238**

L.1 ±55° Filament-wound pipe 239

L.2 ±65°/±47° Filament-wound pipe 241

L.3 ±75°/±36° Filament-wound pipe 244

M Sensitivity analysis for the ±65°/±47° and ±75°/±36° filament-wound pipes **247**

M.1 ±65°/±47° Filament-wound pipe 247

M.1.1 Full data set 247

M.1.2 Reduced data set 255

M.2 ±75°/±36° Filament-wound pipe 263

M.2.1 Full data set 263

M.2.2 Reduced data set 271

List of Figures

4.1 Laminated composite pipe 24

5.1 Residual stress measurement technique 33

6.1 Assumed linear strain variations 47

6.2 Axial stress distributions of the thick-walled isotropic pipe $(t/d_i) = 1.875$. 48

6.3 Hoop stress distributions of the thick-walled isotropic pipe $(t/d_i) = 1.875$. 49

6.4 Radial and shear stress distributions of the thick-walled isotropic pipe $(t/d_i) = 1.875$ 49

6.5 Axial and hoop stress distributions of the thin-walled orthotropic pipe $(t/d_i) = 0.01875$ 51

6.6 Radial and shear stress distributions of the thin-walled orthotropic pipe $(t/d_i) = 0.01875$ 51

6.7 Axial stress distributions of the thick-walled orthotropic pipe $(t/d_i) = 1.875$ 53

6.8 Hoop stress distributions of the thick-walled orthotropic pipe $(t/d_i) = 1.875$ 54

6.9 Radial and shear stress distributions of the thick-walled orthotropic pipe $(t/d_i) = 1.875$ 55

6.10 Axial and hoop stress distributions of the thick-walled anisotropic pipe $(t/d_i) = 0.1875$ 56

6.11 Radial and shear stress distributions of the thick-walled anisotropic pipe $(t/d_i) = 0.1875$ 57

7.1 Kyowa KFG-5-120-D17-23 strain gauge rosette [234] 59

7.2 Three-wire connection of strain gauges to DAQ 60

7.3 Test specimen geometry and strain gauge positioning 65

8.1 Measured axial strain response of the ±55° specimen 73

8.2 Measured circumferential strain response of the ±55° specimen 74

8.3 Measured 45° strain response of the ±55° specimen 75

8.4 Axial stress distributions of the ±55° pipe 77

8.5 Hoop stress distributions of the ±55° pipe 79

8.6 Radial stress distributions of the ±55° pipe 79

8.7 Shear stress distributions of the ±55° pipe 81

8.8 Bounds of meso-scale shear stresses of the ±55° pipe 82

8.9 Measured axial strain response of the ±65°/±47° specimen 84

8.10 Measured circumferential strain response of the ±65°/±47° specimen 85

8.11 Measured 45° strain response of the ±65°/±47° specimen 86

8.12 Axial stress distributions of the ±65°/±47° pipe 87

8.13 Hoop stress distributions of the ±65°/±47° pipe 89

8.14 Radial stress distributions of the ±65°/±47° pipe 90

8.15 Shear stress distributions of the ±65°/±47° pipe 91

8.16 Bounds of meso-scale shear stresses of the ±65°/±47° pipe 92

8.17 Measured axial strain response of the ±75°/±36° specimen 94

8.18 Measured circumferential strain response of the ±75°/±36° specimen 96

8.19 Measured 45° strain response of the ±75°/±36° specimen 97

8.20 Axial stress distributions of the ±75°/±36° pipe 98

8.21 Hoop stress distributions of the ±75°/±36° pipe 100

8.22 Radial stress distributions of the ±75°/±36° pipe 101

8.23 Shear stress distributions of the ±75°/±36° pipe 102

8.24 Bounds of meso-scale shear stresses of the ±75°/±36° pipe 104

9.1 Strain responses of the ±55° specimen for the reduced data set 106

9.2 Comparison of the axial stress distributions of the ±55° pipe 107

9.3 Comparison of the hoop stress distributions of the ±55° pipe 108

9.4 Comparison of the radial stress distributions of the ±55° pipe 109

9.5 Comparison of the shear stress distributions of the ±55° pipe 110

9.6 Axial strain distribution ±55° pipe 111

9.7 Strain responses of the ±65°/±47° specimen for the reduced data set 112

9.8 Comparison of the axial stress distributions of the ±65°/±47° pipe 113

9.9 Comparison of the hoop stress distributions of the ±65°/±47° pipe 114

9.10 Comparison of the radial stress distributions of the ±65°/±47° pipe 114

9.11 Comparison of the shear stress distributions of the ±65°/±47° pipe 115

9.12 Strain responses of the ±75°/±36° specimen for the reduced data set 117

9.13 Comparison of the axial stress distributions of the ±75°/±36° pipe 117

9.14 Comparison of the hoop stress distributions of the ±75°/±36° pipe 118

9.15 Comparison of the shear stress distributions of the ±75°/±36° pipe 119

9.16 Comparison of the radial stress distributions of the ±75°/±36° pipe 120

9.17 Comparison of the radial stress distributions of the ±75°/±36° pipe, based upon numerically decreased layer thickness 121

10.1 Simulated axial strain variations and polynomial fits for the full data set of the ±55° pipe 126

10.2 Simulated circumferential strain variations and polynomial fits for the full data set of the ±55° pipe 127

10.3 Simulated 45° strain variations and polynomial fits for the full data set of the ±55° pipe 128

10.4 Axial stress variations for the full data set of the ±55° pipe 129

10.5 Hoop stress variations for the full data set of the ±55° pipe 130

10.6 Radial stress variations for the full data set of the ±55° pipe 131

10.7 Shear stress variations for the full data set of the ±55° pipe 131

10.8 Simulated axial strain variations and polynomial fits for the reduced data set of the ±55° pipe 133

10.9 Simulated circumferential strain variations and polynomial fits for the reduced data set of the ±55° pipe 134

10.10 Simulated 45° strain variations and polynomial fits for the reduced data set of the ±55° pipe 135

10.11 Axial stress variations for the reduced data set of the ±55° pipe 136

10.12 Hoop stress variations for the reduced data set of the ±55° pipe 137

10.13 Radial stress variations for the reduced data set of the ±55° pipe 138

10.14 Shear stress variations for the reduced data set of the ±55° pipe 139

10.15 Improved error bars of the axial stress distributions for both data sets of the ±55° pipe 141

10.16 Improved error bars of the hoop stress distributions for both data sets of the ±55° pipe 142

10.17 Improved error bars of the radial stress distributions for both data sets of the ±55° pipe 142

10.18 Improved error bars of the shear stress distributions for both data sets of the ±55° pipe 143

10.19 Simulated axial strain variations and polynomial fits for the full data set of the ±65°/±47° pipe 145

10.20 Axial stress variations for the full data set of the ±65°/±47° pipe 146

10.21 Simulated axial strain variations and polynomial fits for the reduced data set of the ±65°/±47° pipe 148

10.22 Axial stress variations for the reduced data set of the ±65°/±47° pipe . . . 149

10.23 Improved error bars of the axial stress distributions for both data sets of the ±65°/±47° pipe 150

10.24 Improved error bars of the hoop stress distributions for both data sets of the ±65°/±47° pipe 151

10.25 Improved error bars of the radial stress distributions for both data sets of the ±65°/±47° pipe 152

10.26 Improved error bars of the shear stress distributions for both data sets of the ±65°/±47° pipe 153

10.27 Axial stress variations for the full data set of the ±75°/±36° pipe 155

10.28 Improved error bars of the axial stress distributions for both data sets of the ±75°/±36° pipe 158

10.29 Improved error bars of the hoop stress distributions for both data sets of the ±75°/±36° pipe 159

10.30 Improved error bars of the radial stress distributions for both data sets of the ±75°/±36° pipe 159

10.31 Improved error bars of the shear stress distributions for both data sets of the ±75°/±36° pipe 160

C.1 Comparison of the axial and hoop stress distributions for thin and thick-walled orthotropic pipes under internally and externally applied pressures . 194

C.2 Comparison of the axial and hoop stress distributions for thin and thick-walled orthotropic pipes under applied axial load 196

C.3 Comparison of the axial and hoop stress distributions for a thick-walled isotropic pipe $(t/d_i) = 0.375$ 200

E.1 Simulated strain variations 213

E.2 Axial and hoop stress distributions 214

E.3 Radial and shear stress distributions 215

G.1 CTETRA mesh used in FE models 220

H.1 LM35 calibration 224

I.1 Axisymmetric model 227

I.2 CTRIAX6 mesh used in thermal FE models 228

I.3 Axial stress at inner surface, with increased specimen length 229

I.4 Hoop stress at inner surface, with increased specimen length 229

I.5 Axial stress distribution for 120 mm long and infinite length pipes 230

I.6 Hoop stress distribution for 120 mm long and infinite length pipes 231

I.7 Radial stress distribution for 120 mm long and infinite length pipes 231

J.1 Axial CTE distribution for $\pm 75^\circ/\pm 36^\circ$ pipe 233

J.2 Measured and thermally compensated axial strain variation of "Gauge set C" of the $\pm 75^\circ/\pm 36^\circ$ pipe 234

K.1 Thermal camera calibration 236

K.2 Thermal image of grinding procedure 236

K.3 Temperature profile of region Ar1 237

L.1 Axial SD variation of the ±55° specimen 240

L.2 Circumferential SD variation of the ±55° specimen 240

L.3 45° SD variation of the ±55° specimen 241

L.4 Axial SD variation of the ±65°/±47° specimen 242

L.5 Circumferential SD variation of the ±65°/±47° specimen 243

L.6 45° SD variation of the ±65°/±47° specimen 243

L.7 Axial SD variation of the ±75°/±36° specimen 244

L.8 Circumferential SD variation of the ±75°/±36° specimen 245

L.9 45° SD variation of the ±75°/±36° specimen 246

M.1 Simulated axial strain variations and polynomial fits for the full data set of the ±65°/±47° pipe 248

M.2 Simulated circumferential strain variations and polynomial fits for the full data set of the ±65°/±47° pipe 249

M.3 Simulated 45° strain variations and polynomial fits for the full data set of the ±65°/±47° pipe 250

M.4 Axial stress variations for the full data set of the ±65°/±47° pipe 252

M.5 Hoop stress variations for the full data set of the ±65°/±47° pipe 253

M.6 Radial stress variations for the full data set of the ±65°/±47° pipe 253

M.7 Shear stress variations for the full data set of the ±65°/±47° pipe 255

M.8 Simulated axial strain variations and polynomial fits for the reduced data set of the ±65°/±47° pipe 256

M.9 Simulated circumferential strain variations and polynomial fits for the reduced data set of the ±65°/±47° pipe 257

M.10 Simulated 45° strain variations and polynomial fits for the reduced data set of the ±65°/±47° pipe 258

M.11 Axial stress variations for the reduced data set of the ±65°/±47° pipe . . . 260

M.12 Hoop stress variations for the reduced data set of the ±65°/±47° pipe . . . 261

M.13 Radial stress variations for the reduced data set of the ±65°/±47° pipe . . . 262

M.14 Shear stress variations for the reduced data set of the ±65°/±47° pipe . . . 263

M.15 Simulated axial strain variations and polynomial fits for the full data set of the ±75°/±36° pipe . . . 264

M.16 Simulated circumferential strain variations and polynomial fits for the full data set of the ±75°/±36° pipe . . . 265

M.17 Simulated 45° strain variations and polynomial fits for the full data set of the ±75°/±36° pipe . . . 266

M.18 Axial stress variations for the full data set of the ±75°/±36° pipe . . . 268

M.19 Hoop stress variations for the full data set of the ±75°/±36° pipe . . . 269

M.20 Radial stress variations for the full data set of the ±75°/±36° pipe . . . 270

M.21 Shear stress variations for the full data set of the ±75°/±36° pipe . . . 271

M.22 Simulated axial strain variations and polynomial fits for the reduced data set of the ±75°/±36° pipe . . . 272

M.23 Simulated circumferential strain variations and polynomial fits for the reduced data set of the ±75°/±36° pipe . . . 273

M.24 Simulated 45° strain variations and polynomial fits for the reduced data set of the ±75°/±36° pipe . . . 274

M.25 Axial stress variations for the reduced data set of the ±75°/±36° pipe . . . 275

M.26 Hoop stress variations for the reduced data set of the ±75°/±36° pipe . . . 276

M.27 Radial stress variations for the reduced data set of the ±75°/±36° pipe . . . 278

M.28 Shear stress variations for the reduced data set of the ±75°/±36° pipe . . . 278

List of Tables

7.1 Lamina material properties 63

F.1 E-Glass material properties 216

F.2 Epoxy material properties 217

F.3 Lamina material properties 218

List of Abbreviations

$\mu\epsilon$	Micro-strain (Strain$\times 10^6$)
AC	Alternating Current
CTE	Coefficient of Thermal Expansion
DAQ	Data acquisition
DC	Direct Current
DHD	Deep Hole Drilling
DIC	Digital Image Correlation
EAC	Environmentally Assisted Cracking
EDM	Electric Discharge Machining
FE	Finite Element
FRP	Fibre Reinforced Plastic
GFRP	Glass Fibre Reinforced Plastic
MPC	Multi-Point Constraint
PEEK	Polyether ether ketone
RBE	Rigid Body Element
RH	Relative Humidity
SD	Standard Deviation
UPS	Uninterruptable Power Supply

List of Symbols

α	Coefficient of thermal expansion (CTE)
α_f	CTE of fibre
α_m	CTE of matrix
α_1	CTE in fibre direction
α_2	In-plane CTE transverse to fibre direction
α_3	Out-of-plane CTE transverse to fibre direction
α_x	CTE in axial direction
α_θ	CTE in circumferential direction
α_r	CTE in radial direction
$\alpha_{x\theta}$	In-plane shear CTE in cylindrical coordinate system
β^k	Constant, dependant on material properties of ply k
γ^0	Angle of twist per unit length
γ_{12}	In-plane shear strain in material coordinate system
γ_{23}	Shear strain in $2-3$ plane, referenced to the material coordinate system
γ_{31}	Shear strain in $1-3$ plane, referenced to the material coordinate system
γ_{xr}	Shear strain in $x-r$ plane, referenced cylindrical coordinate system
γ_{xr}^k	Shear strain in $x-r$ plane within ply k, referenced cylindrical coordinate system

$\gamma_{\theta r}$	Shear strain in $\theta - r$ plane, referenced cylindrical coordinate system
$\gamma_{\theta r}^{k}$	Shear strain in $\theta - r$ plane within ply k, referenced cylindrical coordinate system
$\gamma_{x\theta}$	In-plane shear strain in cylindrical coordinate system
$\gamma_{x\theta}^{k}$	In-plane shear strain within ply k in cylindrical coordinate system
$\gamma_{x\theta}^{m}$	Measured in-plane shear strain response for removal of m layers
Γ^{k}	Constant, dependant on material properties of ply k
δ^{k}	Constant, dependant on material properties of ply k
$\Delta\epsilon$	Change in strain
ΔT	Change in temperature
ζ^{k}	Constant, dependant on material properties of ply k
η^{k}	Constant, dependant on material properties of ply k
θ	Circumferential position or direction
θ_i	Circumferential strain term for removal of layer i, taking Poisson's effect into account
ϑ^{k}	Constant, dependant on material properties of ply k
ι_i^{k}	Constant, dependant on material properties of ply k
κ_i^{k}	Constant, dependant on material properties of ply k
λ_i^{k}	Constant, dependant on material properties of ply k
ξ_i^{k}	Constant, dependant on material properties of ply k
ϱ^{k}	Constant, dependant on material properties of ply k
ϵ	Strain
ϵ_1	Strain in fibre direction
ϵ_2	In-plane strain transverse to fibre direction

ϵ_3	Out-of-plane strain transverse to fibre direction
ϵ_x	Axial strain
ϵ_x^0	Constant through-thickness axial strain
$\epsilon_x^k(r)$	Axial strain within ply k, evaluated at radial position r
ϵ_x^m	Measured axial strain response for removal of m layers
ϵ_θ	Circumferential strain
$\epsilon_\theta^k(r)$	Circumferential strain within ply k, evaluated at radial position r
ϵ_θ^m	Measured circumferential strain response for removal of m layers
ϵ_r	Radial strain
$\epsilon_r^k(r)$	Radial strain within ply k evaluated at radial position r
ϵ_{45}^m	Strain measured at an orientation of 45° relative to the axial direction, for the removal of m layers
$\epsilon_{T_1}^m$	Measured strain at temperature T_1 for removal of m layers
$\epsilon_{T_2}^m$	Measured strain at temperature T_2 for removal of m layers
ϵ_{20}^m	Strain for removal of m layers, referenced to 20°C
ϵ_{20}^0	Strain before removal of any layers, referenced to 20°C
ν	Poisson's ratio
ν_f	Poisson's ratio of isotropic fibre
ν_m	Poisson's ratio of matrix
ν_{12}	Poisson's ratio of unidirectional lamina. Primary strain in direction 1, Poisson's strain in direction 2 of material coordinate system
ν_{13}	Poisson's ratio of unidirectional lamina. Primary strain in direction 1, Poisson's strain in direction 3 of material coordinate system
ν_{23}	Poisson's ratio of unidirectional lamina. Primary strain in direction 2, Poisson's strain in direction 3 of material coordinate system

$\nu_{x\theta}$	Poisson's ratio in cylindrical coordinate system
$\nu_{\theta x}$	Poisson's ratio in cylindrical coordinate system
ρ_f	Density of fibres
ρ_m	Density of matrix
σ_1	Stress in fibre direction
σ_2	In-plane stress transverse to fibre direction
σ_3	Out-of-plane stress transverse to fibre direction
σ_i^m	Stress i in layer m. May be axial, hoop, radial, or in-plane shear stress
σ_x	Axial stress
$\sigma_x^k(r)$	Axial stress within ply k, evaluated at radial position r
σ_θ	Hoop stress
$\sigma_\theta^k(r)$	Hoop stress within ply k, evaluated at radial position r
σ_r	Radial stress
$\sigma_r^k(r)$	Radial stress within ply k, evaluated at radial position r
$\sigma_r^k(r_k)$	Radial stress within ply k, evaluated at radial position r_k, which is the location of the interface between plies k and $k+1$
τ_{12}	In-plane shear stress in material coordinate system
τ_{23}	Out-of-plane shear stress in material coordinate system
τ_{31}	Out-of-plane shear stress in material coordinate system
$\tau_{x\theta}$	In-plane shear stress in cylindrical coordinate system
$\tau_{x\theta}^k(r)$	In-plane shear stress within ply k in cylindrical coordinate system, evaluated at radial position r
$\tau_{\theta r}$	Out-of-plane shear stress in cylindrical coordinate system

$\tau_{\theta r}^{k}(r)$	Out-of-plane shear stress within ply k in cylindrical coordinate system, evaluated at radial position r
τ_{xr}	Out-of-plane shear stress in cylindrical coordinate system
$\tau_{xr}^{k}(r)$	Out-of-plane shear stress within ply k in cylindrical coordinate system, evaluated at radial position r
ϕ	Fibre orientation, measured from the axial direction of the pipe
ϕ_i	Axial strain term for removal of layer i, taking Poisson's effect into account
χ^k	Constant, dependant on material properties of ply k
ψ^k	Constant, dependant on material properties of ply k
ω^k	Constant, dependant on material properties of ply k
Ω^k	Constant, dependant on material properties of ply k
Ω	Measure of resistance in Ohms
A_1^k	Constant of ply k, dependant on pipe geometry and loading conditions
A_2^k	Constant of ply k, dependant on pipe geometry and loading conditions
$\boldsymbol{C}$	Material stiffness matrix
$\bar{\boldsymbol{C}}$	Transformed material stiffness matrix
C_{ij}	Term corresponding to the ith row and j^{th} column of the material stiffness matrix
$\bar{C}_{ij}$	Term corresponding to the ith row and j^{th} column of the transformed material stiffness matrix
$\bar{C}_{ij}^{k}$	Term corresponding to the ith row and j^{th} column of the transformed material stiffness matrix of ply k
$e_{\gamma_{x\theta}}^{m}$	Error in in-plane shear strain in circumferential coordinate system, for removal of m layers
$e_{\epsilon_\theta}^{m}$	Error in circumferential strain, for removal of m layers
$e_{\epsilon_x}^{m}$	Error in axial strain, for removal of m layers

$e^m_{\sigma_i}$	Error in stress i within layer m
$e^m_{F_x}$	Error in axial force, for removal of m layers
$\hat{e}^m_{F_x}$	Error in axial force, within layer m
$e^m_{L_i}$	Error in load i, for removal of m layers
$e^m_{T_x}$	Error in torque, for removal of m layers
$\hat{e}^m_{T_x}$	Error in torque, within layer m
$e^m_{P_I}$	Error in pressure applied to inner surface of layer m
$e^m_{P_O}$	Error in pressure applied to outer surface of layer m
E	Young's modulus
E_f	Young's modulus of fibre
E_m	Young's modulus of matrix
E_1	Young's modulus of lamina in fibre direction
E_2	Young's modulus of lamina transverse to fibre direction
E_3	Young's modulus of lamina transverse to fibre direction
E_x	Young's modulus in axial direction
E'_x	Equivalent Young's modulus in axial direction
E_θ	Young's modulus in circumferential direction
E'_θ	Equivalent Young's modulus in circumferential direction
E_r	Young's modulus in radial direction
F_x	Axial force
F^m_x	Residual axial force release by removal of m layers
$F^{\overline{m}}_x$	Residual axial force release by removal of layer m

G	Shear modulus
G_f	Shear modulus of fibre
G_m	Shear modulus of matrix
G_{12}	In-plane shear modulus of lamina
G_{13}	In-plane shear modulus of lamina
G_{23}	Out-of-plane shear modulus of lamina
$G_{x\theta}$	In-plane shear modulus in cylindrical coordinate system
$L_i^{\overline{m}}$	Error in load i applied to layer m. Load may be axial force, torque, or pressure
M_f	Mass of fibres within a lamina
M_m	Mass of matrix within a lamina
P_O	External pressure
P_I	Internal pressure
P_m	Residual pressure released by removal of m layers or residual radial stress at inner surface of layer m
P_{m-1}	Residual pressure released by removal of $m-1$ layers or residual radial stress at outer surface of layer m
r	Radius, radial position, or radial direction
r_0	Inner radius = R_I
r_k	Outer radius of ply k
r_m	Inner radius of layer m
r_{m-1}	Outer radius of layer m
R	Resistance
$\mathrm{R_Q}$	Resistance of quarter-bridge completion resistor

$\mathrm{R}_{\mathrm{gauge}}$	Resistance of strain gauge
R_I	Inner radius
R_O	Outer radius
$\boldsymbol{S}$	Material compliance matrix
$\bar{\boldsymbol{S}}$	Transformed material compliance matrix
S_{ij}	Term corresponding to the ith row and j^{th} column of the material compliance matrix
$\bar{S}_{ij}$	Term corresponding to the ith row and j^{th} column of the transformed material compliance matrix
$\bar{S}_{ij}^{k}$	Term corresponding to the ith row and j^{th} column of the transformed material compliance matrix of ply k
T_1	An arbitrary room temperature
$\boldsymbol{T}_1$	Transformation matrix
T_2	An arbitrary elevated temperature
$\boldsymbol{T}_2$	Transformation matrix
T_m	Temperature at which data was recorded for the removal of layer m
T_x	Torque
T_x^m	Residual torque release by removal of m layers
$T_x^{\overline{m}}$	Residual torque release by removal of layer m
$u^k(x,r)$	Axial displacement within ply k, evaluated at axial position x and radial position r
$v^k(x,r)$	Circumferential displacement within ply k, evaluated at axial position x and radial position r
V	Voltage
V_f	Volume fraction of the fibres within a lamina
V_m	Volume fraction of the matrix within a lamina

$w^k(r)$	Radial displacement within ply k, evaluated at radial position r
$w^k(r_k)$	Radial displacement within ply k, evaluated at the radial position r_k, which is the location of the interface between plies k and $k+1$
x	Axial position or direction

1 Introduction

In recent years, the fibre reinforced plastics (FRP) industry has grown rapidly. These materials are increasingly utilised because of the excellent strength-to-weight ratio and good corrosion resistance properties that they exhibit. One of the most important structures that are manufactured using FRP are tubes or pipes. These are utilised in many industries. For example, in the automotive industry, carbon fibre tubes are used as drive shafts to transfer torque loads between different components. In the marine sector, high performance yachts make use of carbon fibre stern tubes and masts. In the aerospace and military industries, FRP's are utilised to manufacture launch tubes, radomes, missiles, and tubular components for satellites. By far the most common use for FRP pipes is for the transportation of corrosive liquids and gases. The good corrosion resistance of these materials stems from the properties of the resin systems [1–3]. Epoxy resins have the best corrosion resistance properties, but these are significantly more expensive than vinyl-ester and polyester resins [4]. Vinyl-ester resins are considered a good compromise between epoxy and polyester resins and are consequently widely used in corrosion resistant structures [5]. Glass fibre is the most common choice of reinforcement, since it is far cheaper than carbon fibre and yet still has excellent strength characteristics.

Despite the corrosion resistance of the resin systems, most of these GFRP structures are susceptible to failure by environmentally assisted cracking (EAC). This type of failure is characterised by the propagation of cracks through the reinforcing fibres or fibre bundles, normal to the fibre direction [2,3]. Cracks in the resin form a direct path for the corrosive media to come into contact with the reinforcing fibres [3]. The corrosive media can also reach the fibres by diffusion through the resin [3]. To counter this, resin-rich or thermoplastic liners [6–8] are utilised. Liners, however, do not completely eliminate this process, and merely increase the time taken for the chemically aggressive media to reach the reinforcing fibres [9]. Once the fibres are reached, chemical attack commences. This mechanism comprises surface leaching, as well as the exchange of metallic ions from the fibres (generally calcium and aluminium) with the hydrogen ions present in the solution [3,10]. To combat chemical attack, ECR-glass fibres have been developed, which have improved chemical resistance. The use of these types of fibres have significantly prolonged the time-to-failure

of GFRP structures to EAC [2,11], but this failure mechanism still remains a serious issue. Apart from the material properties of the fibres and resin, EAC is highly dependant on the applied loading on the structure. The rate of crack propagation is directly associated with the crack tip intensity [3], and therefore this type of failure always occurs in regions of tensile stress [11–13]. Accordingly, the level of tensile stress and consequent strains arising from the applied loading are minimised by employing large safety factors [6, 8] in the design of GFRP pipes, which leads to relatively thick-walled structures [14]. Thick-walled geometry, however, promotes the formation of residual stresses [15].

Residual stresses in FRP components arise from a number of factors including the cure shrinkage of the resin, differences in the coefficients of thermal expansion of the fibre and resin, and differences in the mechanical properties arising from variations in fibre orientation across plies [16]. The residual stresses that develop in GFRP pipes are generally tensile at the inner surface [15], which tends to negate the corrosion resistance of the material. Additionally, the magnitude of these stresses is often comparable to the stresses arising from the mechanical loading of these pipes, and ignoring them misrepresents the overall state of stress [17], increasing the risk of failures associated with EAC. The residual stresses that develop in FRP pipes may also introduce fibre waviness or micro-buckling [18], which reduce the overall strength and quality of these structures [16]. Additionally, transverse cracks develop in regions where the residual stresses exceed the yield strength of the resin [16], and these propagate through the resin and regions of the resin/fibre interface. Not only do these cracks promote EAC by providing a means for the corrosive media to reach the reinforcing fibres, they often also lead to delamination of the plies within the structural laminate [16].

The adverse effects of residual stresses within FRP pipes have led to a considerable number of studies focussed on the reduction of these stresses during the manufacturing process. Tarnopolskii et al. [19] investigated the effect of layer-by-layer wind and cure of filament-wound components. In this work they demonstrated that, under certain process conditions, the residual radial stresses that develop within these components can not only be minimised, but also change sense from tensile to compressive, reducing the risk of the development of circumferential cracks. Beil' et al. [20] proposed a method of altering the through-thickness winding angle to reduce the residual stresses that develop in filament-wound rings. Lu et al. [21] investigated the effect of the tape tension during the filament-winding of both glass fibre, and carbon fibre reinforced thermoplastic pipes. They demonstrated that the through-thickness residual stresses of these components can be controlled and reduced by varying the winding tension during the manufacturing process. White and Hahn [22] investigated the effect of the cure cycle of composite laminates on the resulting residual stresses. These authors demonstrated that the residual stresses

could be minimised by reducing the cure and post-cure temperature, and increasing the cooling time. Although not focussed specifically on FRP pipes this work is of some interest, and similar results might be achieved if applied to these structures. Lee et al. [23] proposed a method of "smart" curing thick filament-wound FRP's. This method consists of controlling the temperature at both the inner and outer surface of the component during cure, allowing for a more uniform cure temperature through the wall-thickness to be achieved, thereby reducing the resulting residual stresses. The effect of the material properties of the mandrel on the residual stresses in filament-wound composite pipes has been investigated by White and Zhang [24]. These authors demonstrated that the residual stresses within these structures are significantly affected by both the stiffness and coefficient of thermal expansion of the mandrel material. Consequently, they concluded that these stresses can be minimised by proper selection of a mandrel material, but this depends on both the lay-up and geometry of the pipe. Binienda and Wang [25] proposed an expandable mandrel be used in the manufacture of FRP pipes. The purpose of a mandrel of this type is to apply a large tensile pre-stress to hoop-wound reinforcing fibres during the curing procedure. Once cured, release of this load causes the fibres to relax, subsequently loading the surrounding resin in compression. Residual compressive stresses within the resin are desirable, as these can inhibit the growth of cracks [16].

Although manufacturing processes can reduce the residual stresses within FRP pipes to some extent, these stresses still need to be taken into account when determining the overall stress state of these components. A number of models have been developed to predict the residual stress state within FRP pipes [15, 26–30]. These models, however, require knowledge of certain parameters that govern the formation of the residual stresses; parameters which are dependant on the properties of the materials. For instance, the cure shrinkage of the resin is required, and this is dependant on the quantity of catalyst and accelerator, as well as ambient temperature conditions during initial cure [15]. In addition to this, certain models require cure kinetics parameters [27, 29, 30], which are determined by measuring the cure rate and state of cure simultaneously [31]. Even if these parameters are exactly known, a certain level of inaccuracy in the residual stresses can be expected, because of the current inability to precisely model non-linear effects [16] such as the visco-elasticity of the resin.

The most effective procedure for determining the residual stress state within FRP pipes is to measure them directly. Measurement of the residual stresses is important for two reasons [16]: Firstly, to allow the overall stress state to be determined, and thus to enable the design of safer and more efficient FRP pipes, and secondly, to validate and promote the development of improved models for the prediction of residual stresses within these structures. This work extends an existing method of residual stress measurement, to allow

the residual stress state within any layered FRP pipe to be determined. Previously, this method was only capable of measuring residual stresses in relatively thin-walled pipes of orthotropic lay-up.

2 Literature review

There are many different techniques of residual stress measurement. Although a number of these techniques could be utilised to measure the residual stresses within FRP pipes, they vary in degree of complexity and some may be difficult to implement. This section reviews some of the most prominent non-destructive and destructive methods of residual stress measurement, and assesses the suitability of each method to measurement of residual stresses in FRP pipes.

2.1 X-ray diffraction

X-ray diffraction is one of the primary non-destructive methods of residual stress measurement. This technique measures the strains in polycrystalline materials through the variations of the interplanar spacing in the crystal lattice. Soft X-rays are most commonly used, which have a penetration depth of only about 50 μm [32]. X-rays from synchrotron sources, however, do have greater penetration [33]. The small penetration depths of X-rays make the measurement of residual stresses within thick-walled structures problematic. Although it can be achieved by removal of successive layers [34], this negates the non-destructive nature of this residual stress measurement technique.

X-ray diffraction has been applied to metal matrix composites [32, 35–38]. Since this method requires that the material be crystalline [39], its application to FRP components is limited. Researches have, however, addressed this issue by adding small metallic particles [40–43], roughly the same size as a fibre diameter, into the resin during the manufacture of FRP components. The residual stresses within these particles are measured using X-ray diffraction, and these stresses used to determined the stresses in the surrounding resin through a "stress transmission tensor" [44]. Although the residual stresses within FRP pipes could potentially be measured using the same technique, there are difficulties associated with measuring stresses on curved surfaces, since the path length of the scattered beam is increased [39], introducing errors in the measured strain. Additionally,

adding metallic particles to the resin is not practical, particularly when the manufacture of the components is out-sourced. This method of residual stress measurement is consequently deemed unsuitable for the measurement of residual stresses in FRP pipes.

2.2 Neutron diffraction

Neutron radiation has far greater penetration depths than X-rays [45], and can be used to measure residual stresses up to depths of about 50 mm [39]. Unfortunately, the resolution of these measurements is limited, and variations in stress over distances of less than 1 mm cannot be measured using neutron diffraction [39].

Neutron diffraction has been applied to measure the residual stresses within metal matrix composites [32], but like the X-ray diffraction technique, it cannot be applied to non-crystalline materials [39] like GFRP. Measurement of residual stresses within non-crystalline FRP's would require the addition of metallic fillers to the resin during manufacture of the laminate which, as discussed, makes it impractical to apply this method to measurement of residual stresses in FRP pipes.

2.3 Hole-drilling methods

The hole-drilling method was originally proposed and used by Mathar [46] on isotropic materials. This method of residual stress measurement has become a widely utilised technique, and even has an ASTM Standard Test Procedure [47]. This method involves drilling a hole normal to the surface of a component that contains residual stresses. The release of the residual stresses by drilling induces a resultant strain field in the vicinity around the hole [48]. The strain response is usually measured using strain gauges [49]. The positioning of the strain gauges relative to the hole is of crucial importance [50], as they are sensitive to hole-eccentricity errors [49, 51]. Consequently, special strain gauge rosettes are specified in the ASTM Standard Test Procedure [47] that improve the accuracy of gauge alignment. Optical techniques such as Moiré interferometry [52–55], Holographic Interferometry [56–59] and Electronic Speckle Pattern Interferometry [60–64], as well as Digital Image Correlation (DIC) [65, 66] have also been used to measure the strain response to hole drilling in isotropic materials. The hole-drilling method can be used to measure uniform through-thickness residual stresses, as well as stresses that vary through the specimen thickness, by through-hole drilling and incremental-hole drilling techniques, respectively [49].

The first extension of the through-hole drilling technique for the measurement of residual stresses in orthotropic materials was presented by Bert and Thompson [67]. These authors proposed an approximate calculation procedure for the determination of the residual stresses. Thereafter, Lake et al. [68] investigated the application of the hole-drilling method to thin GFRP laminates. These authors experimentally measured what Bert and Thompson [67] referred to as "proportionality constants", and demonstrated that for thin laminates, through-hole drilling produces the desired strain responses, with no need for drilling the hole to an optimum depth. The approximate analysis of Bert and Thompson has also been extended [50, 69] for measurement of through-thickness residual stresses by the incremental-hole drilling method. In these works, Sicot et al. [69] measured the residual stresses in $[0_2/90_2]_s$ and $[0_8]$ carbon/epoxy laminates, and investigated [50] the effects of different experimental parameters on the residual stresses measured in $[0_2/90_2]_s$ and $[0_4/90_4]_s$ carbon/epoxy laminates. An exact formulation for the measurement of uniform through-thickness residual stresses by the through-hole technique, in a limited class of orthotropic materials, was presented by Schajer and Yang [70]. These authors utilised this method to determine the residual stresses within a graphite/epoxy laminate. Recently, Pagliaro and Zuccarello [71] presented an exact formulation, also for the measurement of residual stresses by the through-hole drilling method, but extended the application to any orthotropic laminate. These authors used this approach to measure the residual stresses within unidirectional, cross-ply, and angle-ply GFRP laminates.

For most hole-drilling experiments, calibration factors (which are utilised to relate the measured strain response to the released residual stresses) must be found. These depend on the material properties, strain gauge rosette geometry, as well as the hole diameter and depth [70]. These factors can be determined experimentally [68, 72], numerically using FE simulation [50, 69, 73–76], or analytically [77, 78]. Factors determined using FE simulation, however, are generally more consistent than those determined experimentally [49]. Additionally, use of FE analysis to determine the calibration factors allows a greater flexibility in the specimen shape, material properties, and experimental procedure than if only analytically calculated or experimentally measured factors are used [73]. In addition to the complexities surrounding the determination of the calibration factors, there are experimental factors which limit the application of the through-hole or incremental hole drilling methods. Generally, the strain gauge rosette is between two to four times the hole diameter, making the region covered by the rosette too large in comparison to the released strain field [51], inevitably limiting the sensitivity of the method. In cases where strain gauges are inadequate, use of optical methods such as Moiré interferometry [79] may prove invaluable, but determining the residual stresses using these methods is usually computationally intensive [49]. The measured data also depends on the drilling and translational speeds [51], and these need to be optimised for each experiment. Despite

these limitations, it is feasible that the hole-drilling method can be applied to measure the residual stresses within FRP pipes, although it appears that no such work has been done. Since, the sensitivity of the strain response diminishes once the depth of the hole surpasses about half the diameter [49], and the hole is usually stopped at a depth slightly greater than the diameter [80], this method can only be used to measure the through-thickness residual stresses in very thin-walled FRP pipes. Alternatively, it could be used to measure the near surface stresses in thick-walled FRP pipes. The entire through-thickness residual stress state within these pipes is desired, however, and this method alone is not suitable for measurement of this sort.

The deep hole-drilling (DHD) method is a variation of the hole-drilling method proposed by Mathar, and can be used to measure the residual stresses within thick components. Initial development of this technique was carried out by Zhandanov and Gonchar [81], Beaney [82] and Jesensky and Vargova [83]. It requires a small diameter hole to be drilled through the component, which is then accurately measured as a function of depth and angular position. A core of material of larger diameter is then trepanned out around the hole, releasing the residual stresses. The dimension change of the reference hole as a result of the trepanning is measured, and utilised to determine the magnitude of the in-plane residual stresses. Through-thickness residual stresses can also be estimated by measuring the change in core length during the trepanning process [84]. It is assumed that introduction of the reference hole does not significantly affect the residual stress state, and that the residual stresses around the hole are relaxed completely by the trepanning of the surrounding core [85]. Another assumption of this method is that the component can be modelled as a stack of plates, and that the release of residual stresses within a single plate does not affect the deformation of the reference hole within the surrounding plates [86].

Leggatt et al. [86] investigated the accuracy of the DHD method using a 100 mm wide metal bar, which was plastically deformed by 4-point bending. The DHD method was applied to the bar, employing a 6 mm diameter gun-drilled reference hole. Electric discharge machining (EDM) was used to trepan a core of roughly 22 mm diameter around the hole. The diameter of the reference hole was measured before and after trepanning using an air probe. These authors reported good agreement, for the middle 80 mm region of the bar, between the results of DHD and the residual stress distribution measured using strain gauges. Poor agreement for the remaining 10 mm wide regions near both surfaces were attributed to "bell-mouthing" [86] of the reference hole due to the drilling process, as well as possible plastic yielding of the reference hole in these regions. DHD has been used to frequently measure the residual stresses within welds [85,87–92], but has also seen application to railway track [93], a steel mill roll [94], and autofrettaged tube [95]. In most cases, the reference holes were measured using air probes, and EDM machining was

utilised for the trepanning process.

The DHD method has been extended to measure the residual stresses within thick, composite laminates [96], however, there appears to be only a single published work of this sort. In this work, Bateman et al. [96] initially extended to orthotropic materials, the isotropic solution of hole distortions for applied far-field stresses, using the approximations derived by Lekhnitskii [97]. They demonstrated that the use of these analytical relationships not only introduces errors, but does not allow for the determination of in-plane shear stresses which may exist [96]. Consequently, they utilised FE simulation to determine the relationships between hole distortions and residual stresses released by the trepanning process. These authors then applied the DHD method to a 22 mm thick carbon/epoxy composite laminate. Measurements were performed in two regions of the composite, with 3.2 mm and 3.25 mm diameter reference holes, respectively. EDM cannot be applied to non-conducting materials [39], and as a result, the trepanning procedure was done using a diamond encrusted hole saw. Although the measured stress distributions presented by Bateman et al. [96] were not compared to any theoretical predictions, or the results of any other method of residual stress measurement, the distributions obtained for both reference hole diameters agreed well.

The DHD method is not restricted to plate geometries, and has been utilised to measure the residual stresses within isotropic pipes [89, 90, 95]. It is therefore possible that the residual stresses within thick-walled FRP pipes can also be measured using this method. There are some limitations, however, which may restrict the accuracy of the measured distributions. George and Smith [95] compared the DHD method to the Sachs method for measurement of residual stresses within an autofrettaged tube. These authors saw discrepancies between the measured distributions of the two methods, and consequently noted that the assumptions surrounding the modelling of a component as an independent stack of plates restricts the DHD method from measuring steep gradients in residual stress. Steep gradients in stress may arise within certain FRP pipes, and therefore the same limitation applies to these structures. George and Smith [95] also noted that the diameter of the trepanned core needs to be quite small to completely release the residual stresses around the reference hole. Since FRP composites are non-conductive, a mechanical machining process is required for the trepanning process. Mechanical machining processes are likely to induce cutting stresses [39]. If the required trepanned core diameter is similar to the reference hole diameter, additional stresses induced during the trepanning process would likely affect the change in the reference hole geometry, introducing errors in the measured residual stresses. Another limitation is the accuracy by which the reference hole can be measured: Air probes have a resolution of roughly 0.5 μm [98], which may introduce significant errors in the residual stress distributions measured in FRP pipes.

Additionally, near-surface residual stresses determined using the DHD method may be erroneous [92], because a significant level of stress relaxation occurs in these regions with introduction of the reference hole. For this reason an integration of the drilling methods has been proposed [92] in which the erroneous surface stresses, determined using the DHD method, are replaced by those measured using the incremental hole-drilling method. The requirement to apply two different hole-drilling techniques to measure the residual stresses within FRP pipes is impractical. Considering the limitations surrounding the method, DHD is likely not the most suitable technique that can be used to measure the residual stresses within FRP pipes.

2.4 Sectioning methods

The sectioning method, involves removing sections from a component containing residual stresses. These are removed in such a way that the residual stress state can be assumed zero after the sectioning procedure. Under these circumstances, the strain change in the sections can be attributed to the complete relaxation of the residual stresses that were previously present, and can be used to determine these stresses. The strain relaxation is usually measured using strain gauges, and it is commonly assumed that the component is in a state of plane-stress before sectioning, making the computation of the residual stresses relatively simple [99]. Out-of-plane stresses near the surface where measurements are made may also have an influence on the measured data, but these are usually ignored [99]. This method has been applied to measure the residual stresses within a number of metallic components such as a welded H-section [100], cold-bent steel plate [101] and in welded seams [102]. Rybicki and his colleagues improved the back-computation analysis for the splitting [103] and parting out [104] procedures for the measurement of residual stresses within girth-welded pipes. Thereafter, Rybicki and Shadley [105] demonstrated the accuracy of these improvements, by simulating the sectioning procedure in a girth-welded pipe using FE analysis. The sectioning method has also been applied to measure the residual stresses within filament-wound E-glass, R-glass, and T-700 carbon fibre pipes [106]. In this work, Casari and his co-workers parted-out sections located along the mid-length of each of the pipes. Each section had strain gauges bonded to both the inner and outer surfaces. They utilised the measured strains to estimate the residual stresses released by the sectioning procedure. Since no through-thickness measurements were taken, only the residual stresses associated with the released residual axial and circumferential bending moments [106] could be computed. By applying the sectioning method in this manner, the components of the residual stresses that are self-equilibrating in bending cannot be resolved. Although these stresses may be negligible in many cases, there are a number situations where they cannot be neglected. An example of this is the case of a layered

FRP pipe, that has discontinuous residual strain profiles across the layers. A pipe of this nature would result from the layer-by-layer wind and curing technique investigated by Tarnopolskii et al. [19]. Since the individual layers are not separated during sectioning, the discontinuous residual strains that exist between these are not relieved, and consequently the residual stresses associated with these strains are not released.

These additional stresses could be measured by bonding strain gauges across the specimen thickness, either on the free edge before sectioning, or on newly exposed surfaces after cutting. Further cuts can then be made, to divide the specimen into sub-sections, each with its own gauge. This is otherwise known as the "slice and dice" method. Ueda et al. [107] proposed an inherent strain, or eigenstrain analysis to determine the tri-axial stress state from strains measured utilising this method. Hill and Nelson [108, 109] investigated the analysis procedure of Ueda et al. [107], and simulated the measurement of the tri-axial residual stresses within a welded plate. The eigenstrain analysis procedure requires extensive amounts of FE simulation to determine the inherent strains associated with the presence of the residual stresses. Consequently, Hill [99] simplified this technique, reducing the amount of FE simulation required to determine the residual stresses. Hill [99] then applied this method to measure the tri-axial residual stress state within a swage-autofrettaged tube, and validated its application by comparing the measured stresses with those determined from FE simulation of the autofrettaging process. Although it has not been applied to FRP pipes, the slice and dice method could potentially be used to measure the residual stresses within these structures, but substantial use of FE simulation can be expected.

Another variation of the sectioning method is ply sectioning. This technique involves the partial, or complete separation of the plies of a laminated composite. In the case of complete separation, this method can be considered a layer removal method. Separation of a ply from a laminate releases the constraints imposed by the adjacent layers [16], resulting in deformation of both the removed ply, and remaining laminate. These deformations are utilised to estimate the residual stresses released by the sectioning procedure. Manson and Seferis [110] placed separation films between different plies of a composite laminate during manufacture. A strain gauge was used to measure the strains released by ply separation, and these measurements were utilised to determine the residual stresses that existed prior to ply separation. Chapman et al. [111] applied a similar approach to measure the residual stresses within unidirectional graphite/PEEK laminates. Joh et al. [112] partially separated the plies of a graphite/epoxy $[0_2/90_4]_{13s}$ cross-ply laminate using a low-speed diamond cutter, and measured the strain response using Moiré interferometry. Gascoigne [113] also utilised Moiré interferometry, to measure the residual strains released by separation of the plies of a cross-ply laminate. Separation of the plies was performed

using a diamond-wafering saw, and measurements were taken on the upper surface, as well as on the edge of the laminate. Additionally, Gascoigne [113] measured the residual strains at the end of a thick-walled cross-ply graphite/epoxy cylinder by parting-out a thin section. Once again, measurements were taken using Moiré interferometry. Although this measurement was applied to an FRP pipe, it is of no particular interest for the current scheme of work. The reason for this is that the residual stresses that develop in the regions of the ends of a pipe are different to the stresses that develop over the majority of the pipe length. Through-thickness shear stresses develop at the free ends, a consequence of the absence of axial stresses in these regions. The current scheme of work is not concerned with measurement of the residual stresses that occur close to the edges of FRP pipes, but is rather focussed on the regions free from edge effects. Complete separation of the plies of an FRP pipe can be considered the same as the Sachs method of residual stress measurement, which is discussed later in this section. Additionally, the ply-sectioning technique could potentially be utilised in conjunction with the parting-out method employed by Casari et al. [106], so that the additional residual stresses that are self-equilibrating in bending can be measured. Separating plies from a curved section of material in this sense, however, may be difficult to achieve.

2.5 Radial cutting method

The radial cutting method is a variation of the sectioning method, and is commonly utilised to measure the residual hoop and radial stress distributions within cylindrical components. This method involves slitting a component axially through the wall thickness, thereby releasing the inherent circumferential bending moment. The resulting deformations allow an estimate of this moment to be determined, and the associated residual hoop and radial stresses to be calculated. Experimental testing using this technique is simple, and can be performed relatively quickly. The residual stresses can be determined analytically, which is favourable, and consequently this method has seen considerable application to FRP pipes [114–120] and discs [121–125].

Andersen and Lystrup [114] applied the radial cutting method to filament-wound carbon fibre/PEEK pipes. These authors measured the diameter change due to axial splitting, and used this data to estimate the residual hoop stresses that existed in the pipes prior to cutting. Cohen [115] used the relationships derived by Lekhnitskii [97] to determine the residual hoop and radial stresses in filament-wound pipes which were manufactured under different process conditions. Kim and Lee [117] utilised the radial cutting method to measure the residual hoop and radial stresses in thick-walled carbon fibre pipes. Additionally, these authors extended this technique to allow for the determination of the

residual stresses within components of radially varying material properties. Of all of the radial cutting experiments, Kaddour et al. [118] were the only researchers to measure the axial strain response, in addition to the circumferential strain response, to the splitting procedure. In this work, thin-walled E-glass/epoxy, kevlar/epoxy and carbon/epoxy filament-wound pipes were considered. These authors utilised the measured data to determine the residual hoop stresses at the outer and inner surfaces the pipes. They reported that considering the axial strain response provides a better estimate of the hoop stresses released by the splitting procedure [118]. Additionally, these authors attempted to estimate the axial residual stresses on the pipe surfaces. The axial stresses that they calculated were very small in relation to the hoop stresses, and relatively close to zero. These results, however, are a not true indication of the axial stresses associated with the residual barrelling moments that develop in these pipes. Since the pipes were split only axially, only the residual circumferential bending moments were released. The axial strains that Kaddour et al. [118] measured were, therefore, purely the Poisson's response to the release of these moments. Ideally the axial stresses that they calculated should have been exactly zero, since no residual axial loads were released, but every experiment is subject to measurement error, and this is likely why these stresses were not zero.

The radial cutting method relies on the elastic response of the cylindrical laminate as a whole. The residual axial stress is assumed zero, and the laminate is assumed balanced and symmetric. Consequently, the material is assumed orthotropic, and the residual shear stresses are assumed to be zero. Kaddour et al. [118] demonstrated that this assumption is not always entirely correct. A number of the specimens that they considered exhibited axial displacement across the cut, which implies the existence of residual shear stresses [118]. These authors, however, demonstrated that for a filament-wound lay-up, the relative axial displacement rapidly reduces with increased wall thickness, validating the assumed orthotropy of thicker specimens.

The radial cutting method is an effective technique for measuring the residual stresses within FRP pipes of orthotropic lay-up, but cannot be used to analytically resolve residual stresses within FRP pipes of anisotropic lay-up. Use of FE analysis, however, could address this limitation. However, there are a number of factors which limit the application of the radial cutting method to only certain FRP pipes. Since only the residual circumferential bending moment is released by splitting, only the residual stresses associated with this moment can be found. This method, therefore, cannot resolve the components of the residual hoop stresses that are self-equilibrating in bending. The radial cutting method also cannot be utilised to measure the residual axial and shear stresses that develop in FRP pipes.

2.6 Contour method

Initially introduced by Prime [126], the contour method is a powerful method that can be used to measure the residual stresses that vary in two dimensions. A planar cut is made through a component that contains residual stresses, and the release of the residual stresses normal to the cut plane causes the newly exposed surfaces to deform out of plane. The displacement contour of the surface is measured, and the opposite of this contour is numerically applied as a displacement boundary to the cut part [126]. By superposition, the stresses obtained numerically must be equal to the residual stresses that existed prior to cutting. This method has been used to study the residual stresses that arise from various manufacturing processes such as laser peening [127–131], friction welding [132–137] and fusion welding [138–143].

FE analysis is almost always used to resolved the residual stresses from the measured displacement contours, but in recent publication, Kartal [144] developed analytical solutions to determined the stresses in semi-infinite strips and a finite rectangle, and used these solutions to determine the residual stresses within a plasma-arc welded plate. He reported favourable agreement between the stresses measured using the contour method, and those measured using neutron diffraction. The contour method has seen application to a variety of geometries including pipes [130, 134, 139, 143], and the residual stresses within a number of components have been found using multiple cuts [134, 145, 146]. This method has also been used in conjunction with other methods of residual stress measurement. Pagliaro et al. [147] determined the residual stresses within a plastically deformed 2024-T351 aluminium alloy disc by combining the stresses measured using the contour method with those measured using X-ray diffraction and hole-drilling. They observed good agreement between the stresses determined from the superposition of the results of the different methods, with those measured using neutron diffraction. Brown et al. [148] combined the radial cutting method with the contour method to determine the residual hoop stresses within an electron-beam welded pipe. These researchers initially slit the pipe axially through the wall thickness, and measured the deformation caused by the release of the residual circumferential bending moment. The stresses associated with this moment were determined using FE analysis. The remaining pipe was then cut axially, to expose a new face for measurement of the remaining hoop stresses using the contour method. The results of both methods were then combined to determine the overall residual hoop stresses that existed in the pipe prior to cutting.

The contour method requires precision planar cuts to be made. It is assumed that the cutting procedure does not introduce any additional residual stresses, and therefore does not affect the measured displacement contours arising from the release of the residual

stresses [126]. Wire EDM is a non-contact cutting process which removes material by spark erosion. This machining method allows the required precision cuts to be made and is used in most contour method experiments. Under certain circumstances, EDM can introduce significant residual stresses into a thin layer near the cut surface [149], but optimisation of the cutting parameters allows cutting induced stresses to be minimised such that they can be ignored [126], aligning with the assumptions of the contour method. Although this method of measurement would be ideal for determining the variation of residual stresses within FRP pipes, the application of this technique to FRP composites is limited by the cutting methods that can be applied [17]. Since these materials are poor conductors, wire EDM cannot be used to make the precision cuts required, and only mechanical methods of cutting can be applied. Mechanical methods, however, not only induce additional stresses at the cut surface, but also remove excessive amounts of material, thereby trimming down the out-of-plane deformations [17] required to determined the released residual stresses. This method, therefore, cannot be applied to measure the residual stresses within FRP pipes.

2.7 Crack compliance method

The crack compliance method [150] is also known as the compliance method, successive cracking method, fracture mechanics approach, slotting method, or incremental slitting method [39]. This method was originally introduced by Vaidyanathan and Finnie [151], and requires a slot to be incrementally deepened through the thickness of a component containing residual stresses. As the depth of the slot increases, so the residual stresses normal to the cut plane are released. The release of these stresses alters the state of stress within the remaining component, which must always satisfy force equilibrium. This change in stress manifests in the form of deformation of the component. These deformations are measured, and can be used to determine the residual stresses released by each increment in depth of the slot, allowing the through-thickness residual stress distribution to be estimated.

Strain gauges are most commonly used to measure the deformation of the component caused by the incremental slitting, although optical techniques like Moiré interferometry [152, 153] and DIC [154–156] have been used. Additionally, measurement of the crack mouth opening has been performed [157, 158]. For through-thickness measurement, strain gauges are bonded on the "back face", directly below the cut, and these are usually aligned normal to the cut plane. Sometimes a second strain gauge is bonded on the "top face", in close proximity to the cut. This gauge allows for increased resolution of the surface residual stresses [39], but its response saturates relatively quickly, thereby preventing its

sole use to determine the through-thickness residual stresses. Wire EDM is the preferred method of cutting [39], since, as discussed, it is a non-contact method and, using optimised operating parameters, does not introduce significant cutting stresses. Unfortunately this cutting method is limited to conducting materials. Mechanical machining of the slot, such as sawing [153, 159, 160] and use of milling cutters [161, 162] have also been utilised, and these are not limited by the conductivity of the material. Mechanical methods, however, introduce significant cutting stresses, and can affect the strain response of the top face gauges, thereby producing erroneous near-surface stresses [39]. Fortunately, the strain gauges bonded to the back face are not significantly affected by additional cutting stresses, and accurate results can be obtained, provided that thermal effects associated with the cutting process are eliminated [39]. A focussed ion beam has also been used to create the slot in thin films [154] and tiny components [155]. A slot extended to between 90% and 95% through the thickness of a component can produce accurate results. Beyond these depths, however, difficulties arise with regard to supporting the mass of the free ends of the component, and the strain response is greatly affected by this [163]. Additionally, the finite length of the strain gauges also influences the measured strain response as the depth of cut approaches the specimen thickness [163].

The analysis of the residual stresses using the crack compliance method comprises two separate steps, namely the forward and inverse solutions [39]. In the forward solution, the deformation response of the structure as a function of slot depth, or the "compliances", are determined for known stress fields. This can be done using a fracture mechanics approach or FE analysis [39, 150]. The fracture mechanics approach can only be applied to certain geometries, and assumes the presence of an infinitesimally thin crack. Cheng and Finnie [164], and Prime and Finnie [165] did, however, present solutions for a finite-width slot in a semi-infinite plate. In cases where fracture mechanics solutions do not exist, or for near surface measurements, where the width and shape of the slot become important, the compliances are found utilising FE analysis [39]. In many cases, the stress fields utilised to determine the compliances comprise unit pulses, which are uniform stresses assumed to be released with each increment in cut depth [39]. Series expansion is another alternative, and it is assumed that the residual stresses can be described by a series expansion of functions [150]. Compliances for a number of different types of functions have been found. Legendre polynomials are the most common, since they automatically satisfy the self-equilibrium requirement [150,162,166,167] for orders greater than 1. Power series expansions [168,169] have also been employed, as well as Fourier series [170]. In some cases, polynomial functions cannot accurately describe the residual stress distribution [39]. To address this, Gremaud et al. [171] proposed a spline-based method that they referred to as "overlapping piecewise functions". Prime and Hellwig [172] adopted similar functions to determine the residual stresses within an aluminium-alloy plate, laser-cladded with a

copper alloy.

The inverse solution makes use of the compliances, obtained with the forward solution, to determine the residual stresses that best match the measured strain response. When series expansion is used, the inverse solution often employs a least-squares approach, where a best fit of the compliances to the measured data allows the coefficients of each series order to be determined [39, 150]. Since the strain fit is not constrained to pass through all the experimentally measured data, this method is fairly tolerant to small measurement errors [17]. Applying this approach in the case of unit pulses, however, produces a strain fit that exactly matches the measured data, since the number of unknown coefficients is exactly equal to the number of slit depths [173], causing it to be quite sensitive to measurement errors. An example of this sensitivity can be found in the work presented by Sharma and Bakis [174]. These authors used pulse functions to estimate the residual hoop and radial stresses within C-shaped filament-wound rings, and the stress distributions that they obtained varied significantly through the wall thickness. Tikhonov regularisation [173] is often utilised to address the issue associated with the use of pulse functions. Regularisation somewhat smooths the resulting residual stress distribution, by allowing a mismatch between the strain fit and the measured strain data, and often requires an iterative process to determine the degree of smoothing that should be applied [163]. Regularisation, however, is not limited to the use of pulse functions. Schajer and Prime [175] utilised regularisation with Legendre polynomials and pulse functions, to extrapolate the residual stress distributions of a heat-treated and quenched 7050-T7452 aluminium forging beyond the measurable limit, through the remainder of the specimen thickness. In addition to regularisation, strain fits can be altered by applying a weighting to the measured data [150]. The crack compliance method has been used to measure the residual stresses within layered components [165, 172, 176, 177] and even a metal matrix composite [178], but has seen little application to FRP composites [160, 174, 179–183].

The residual hoop stresses within cylindrical components can be measured by employing an axial slit [39]. This approach was first proposed by Cheng and Finnie [184]. These authors measured the residual hoop stresses in a water-quenched 7050 aluminium cylinder, and a ring cut from the cylinder. The residual stresses in the cylinder were determined under a plane-strain assumption, while the stresses in the ring were determined under a plane-stress assumption. The axial slit was introduced from the outer surface of the components, and incrementally deepened using a milling cutter. The strain response was measured on the outer surface, at varying distances from the slit. The compliances were found using a fracture mechanics approach, based upon the relationships they derived in a previous paper [185], and the stresses described using Legendre polynomials of up to 4th order. These authors later extended [186] this analysis to measure the residual hoop

stresses within a thick-walled, water-quenched, steel cylinder. This technique of hoop stress measurement has been applied to autofrettaged cylinders [187, 188], solid isotropic cylinders [169,189] and rings [190,191], and even a rail-road wheel [192]. Akbari et al. [181] used this approach to measure the hoop stress distribution in a $[90/\pm45/90]$ carbon/epoxy filament-wound ring. An axial slit was incrementally deepened from the outer surface of the ring, and the resulting circumferential strain response was measured directly below the cut. These authors utilised FE analysis to determine the compliances of unit pulse stresses. Consequently, they used Thikhonov regularisation for the strain fit, and demonstrated its effectiveness in stabilising the residual stress distribution obtained using the pulse method. Ganley et al [160] used the crack compliance method, in conjunction with the radial cutting method, to determine the residual hoop stress within a filament-wound carbon/epoxy cylinder. The wall of the cylinder was initially cut through in the axial direction to release the circumferential bending moment. Axial slitting commenced in the remaining section from the inner surface of the cylinder. The circumferential strain response was measured on the outer surface, directly below the cut. FE analysis was used to determine the compliances associated with the pulse functions. The stress distribution obtained using the crack compliance method was then combined with the bending-moment stress distribution obtained using the radial cutting method to give the overall residual hoop stress distribution.

Axial residual stresses in cylindrical components can be measured by making use of a circumferentially orientated slit [39], and either the axial or circumferential strain response can be utilised to determine the residual stresses [39]. Cheng and Finnie [162] measured the residual axial stress distribution within a thin-walled single-pass, circumferentially welded stainless steel cylinder. A circumferential slit was cut from the inner surface of the cylinder, and the circumferential strain response measured on the outer surface. They utilised a fracture mechanics approach, based upon a previous publication [193] of theirs, and used Legendre polynomials and power series functions to describe the residual stress distribution. They noted that under these circumstances, the Legendre polynomials gave better results. Thereafter, Cheng and Finnie [194] extended this work, and measured the residual axial stresses within multi-pass, circumferentially welded stainless steel pipe. Ritchie and Leggatt [161] combined the crack compliance method and the sectioning method to determine the residual axial stresses within a large-diameter butt-welded pipe. They initially cut out sections in the region of the weld, and measured the axial and circumferential strain response, allowing the stresses released by the sectioning to be determined. They then proceeded to measure the remaining residual stresses in each section by incrementally increasing the depth of a circumferentially orientated slit. FE simulations were used to determine the compliances, and the residual stresses were estimated by applying a least squares fit of the compliances to the measured data. Finally, the overall axial stresses were

determined by combining the results of the sectioning approach, with those of the crack compliance method. Interestingly, the residual axial stresses within cylindrical components also can be measured by employing an axial slit [150]. This approach was proposed by Cheng et al. [195], and requires the hoop stresses to within a cylinder to be measured under both plane-strain and plane stress conditions. For measurement under plane-stress conditions, a thin disc is removed from the original cylinder, and the axial slitting method performed. Axial slitting is applied directly to the long cylinder for the plane-strain condition. The difference between the hoop stress distributions measured under these conditions allows the original axial residual stresses within the cylinder to be estimated. This method was later extended by Cheng and Finnie [196], and subsequently improved by Cheng [197].

The crack compliance method is clearly suited to measuring the residual stresses within FRP pipes. The residual hoop stresses can be measured by employing an axial slit, and the radial stresses can be estimated directly from these results [39]. The axial stresses within these pipes can be measured by using a circumferential slit, or the method of Cheng et al. [195] could be extended so that these stresses can be found by employing an axial slit. Due to the complex material properties of these pipes, the compliances would certainly need to be determined with FE simulation. Additionally, these FE models may need to be three dimensional in the case of pipes manufactured with an anisotropic lay-up. Although it has been investigated for orthotropic laminates [183], it is unclear whether or not the residual shear stresses within layered FRP pipes can be accurately measured using the crack compliance method.

2.8 Sachs' method

In 1927 G. Sachs [198] proposed a method for the determination of axisymmetric residual stresses in cylindrical components. The Sachs method of residual stress measurement can be considered a layer removal technique, as it requires the boring-out of material from the centre, or the turning-down of layers of material from the outer surface of a cylindrical body. The axial and circumferential strain response to material removal is used to analytically determine the released residual stresses. The strain responses are typically measured using strain gauges. Sachs' method was originally developed for the measurement of axial, hoop and radial stresses within isotropic cylinders, and has seen much application in this context. Kovač et al. [199] measured the residual stresses within a quenched stainless steel pipe. These authors considered both variants of the method, that is, boring-out from the inner surface, as well as material removal from the outer surface. Material removal was performed on a lathe, using tungsten carbide cutting tools. The axial and circumferential strain response to boring-out was measured on the outer surface of the

pipe using bi-axial strain gauges, and similarly measured on the inner surface of the pipe for turning-down from the outer surface. Botros [200] utilised the Sachs method to measure the residual stresses within cold-worked tubes. They too considered material removal from both the inner and the outer surface of the specimens. Material removal was performed using a chemical etching process, the strain response of the specimens was determined from the diametral and length changes, measured using a calibrated micrometer and a comparator, respectively. Stacey and Webster [201] measured the residual hoop stress distribution within rings cut from a thick-walled autofrettaged steel pipe, and applied both the boring-out and turning down techniques. Venter et al. [188] measured the residual hoop and radial stresses within rings cut from an autofrettaged steel pipe. These authors only considered the boring-out variation of the Sachs method, and compared the results to those measured using the crack compliance and neutron diffraction methods. In addition to these works, Sachs' method has, among others, seen application to autofrettaged pipes [202,203], cold-drawn steel bar [204], turbine-rotor forgings [205], case hardened steel rod [206], and cold expanded holes [207–209].

Sachs' method has seen a considerable number of adaptations. Buhler [210] modified the Sachs equations using a finite-difference approach, to allow for a simple calculation procedure. Druez and Bazergui [211] utilised these simplified equations, and measured the residual stresses within I-800 heat-exchanger tubing. They considered both the boring-out and turning-down techniques, and applied an etching technique to remove material. Strain responses were measured using strain gauges. Ignat'kov [212] presented a solution for determination of the residual stresses within multi-layered isotropic cylinders. Thereafter, Ignat'kov [213] extended this approach to allow for the residual stresses within isotropic cylinders of radially varying material properties to be determined. Nishimura [214] modified the Sachs equations to allow the residual stresses in cylindrical bars and tubes to be determined, using only the change in length of a specimen in response to the removal of material from the outer surface. Sharman et al. [215] developed an FE algorithm, allowing the residual stresses within pressure vessels of geometries more complex than cylinders to be measured. Garcia-Granada et al. [216] extended Sachs' technique to allow for the measurement of non-axisymmetric residual stresses in isotropic cylinders. This procedure makes use of a Fourier series to describe the residual stresses within the components. Terasaki et al. [217] presented an inherent strain technique for the determination of residual stresses in layered isotropic cylinders, using the Sachs technique of material removal. Chen et al. [218] later pointed out that the inherent strain technique of Terasaki et al. [217] can only be applied in cases where the inherent radial strains are negligible, and introduced the concept of an equivalent circumferential inherent strain, which takes account of the inherent radial strains. They then applied this technique to measure the residual stresses within a layered bronze/aluminium pipe.

The first extension of Sachs' method to measurement of residual stresses in cylindrically orthotropic bars and tubes was presented by Olson and Bert [219]. In this work, these authors developed the equations allowing the residual stresses within orthotropic cylinders to be determined from the strain response to the boring-out of material. Voyaidjis et al. [220] presented a similar extension of Sachs' method, but considered both the boring-out and turning-down techniques. Additionally, considering the shear strain response to material removal, these authors developed a solution by which the residual in-plane shear stresses within these components can be determined. This method was utilised by Hung [221] to measure the residual axial, hoop, and radial stresses within cold-drawn Cu 1.8 wt% Be rods. Rasty et al. [222] presented a different derivation to that of Voyaidjis et al. [220] for the determination of the residual hoop and radial stresses, and measured the residual stresses within Zircaloy-4(R) tubes by removing material from the outer surfaces using an electro-chemical etching method. They made use of strain gauges to measure the strain response on the inner surface of the pipes. Voyaidjis and Hartley [223] extended the work of Voyaidjis et al. [220] to allow the residual stresses within layered cylindrically orthotropic rods and tubes to be measured. These authors then applied this method, together with an electro-chemical boring-out technique, to measure the residual axial, hoop, and radial stresses within copper-clad aluminium rods.

The current extensions of Sachs' technique to cylindrically orthotropic components can be used to measure the residual stresses within FRP pipes, although no such work of this sort has been published. There are, however, a number of factors which limit the range of FRP pipes that these methods can be applied to. Since the works of Olson and Bert [219], Voyiadjis et al. [220, 223], and Rasty et al. [222] only consider cylindrically orthotropic materials, they cannot be utilised to measure the residual stresses within FRP pipes of anisotropic lay-up. Additionally, these works [219, 220, 222, 223] make assumptions which further limit their application to relatively thin-walled structures. The first assumption is that the residual hoop and radial stresses can be determined independent of the residual axial stresses, under plane-stress conditions. The second assumption is that the residual axial stresses released by removal of material are uniformly distributed over the thickness of the remaining component. The inaccuracies associated with these assumptions are discussed later in this thesis.

Despite the current limitations, the Sachs method is arguably the best suited, and most practical method for the measurement of residual stresses within FRP pipes. Although it requires the removal of significantly more material than the other destructive techniques of residual stress measurement considered in this section, the Sachs method has the advantage that the entire residual stress state within an FRP pipe can be determined by a single experiment. Additionally, this is the only method that can be used to analytically resolve

the residual stresses within these structures. It is therefore desirable to extend the Sachs method so that the residual stresses within any FRP pipe can be measured. This is the primary focus of the current thesis. In this work, an analytical solution extending the capabilities of the Sachs method to the measurement of residual stresses within layered anisotropic pipes, of any wall thickness, is presented. This is a capability which, to the author's knowledge, has not previously been achieved.

3 Objectives

In light of the limitations of the existing extensions of the Sachs method for measurement of residual stresses within FRP pipes, the main objective of this work is to develop an analytical technique that extends the capabilities of the Sachs method to the measurement of the residual stresses within any FRP pipe. This method must therefore:

- Be capable of measuring the entire residual stress state within layered, cylindrically anisotropic FRP pipes of any wall thickness. Achieving this objective will not only allow the residual stresses within any anisotropic pipe to be measured, but will also address the issues surrounding the current extensions of Sachs' method to orthotropic pipes.

Sachs' method has not previously been applied to FRP pipes. A secondary objective of this work is therefore:

- To utilise the method of residual stress measurement developed in this work to experimentally measure the residual stresses within FRP pipes.
- To investigate factors that may influence the accuracy of the results obtained using the method developed in this thesis.

4 Theory

Sachs' [198] technique of residual stress measurement requires material to either be bored-out from the inner surface, or removed from the outer surface of cylindrical components. The residual stress state is determined by using the measured elastic response of the remaining component to the removal of material. Extending this technique for application to FRP composite pipes or cylinders requires use of the exact elastic solution of these components to applied loading. For this purpose, the solution presented in the excellent textbook of Herakovich [224] is utilised. This solution is based upon the works of Lekhnitskii [225], Scherrer [226], Reissner [227], Pagano [228], Reissner and Tsia [229] and Wilson and Orgill [230]. This section presents the aspects of this solution which are required for the formulation of the method. The laminated FRP pipe under consideration is illustrated in Fig. 4.1.

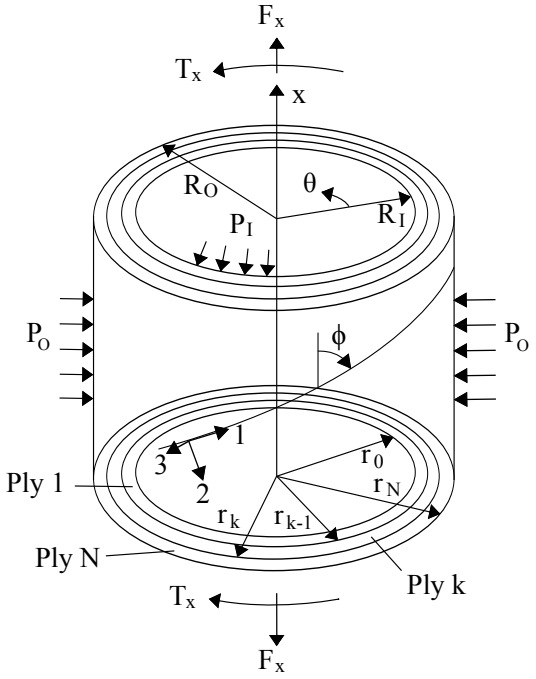

Figure 4.1: Laminated composite pipe

The elastic solution is based upon the condition of an axisymmetric infinitely long pipe, uniformly loaded along its length. As illustrated in Fig. 4.1, the loads considered are that of internal and external pressure, P_I and P_O, as well as axial and torque loads, F_x and T_x, which are related to the integral of axial stress and integral of the moment of shear stress over the pipe wall thickness, respectively. Under these conditions, the stresses that arise are independent of both axial and circumferential position, x and θ, and thus dependant only on radial position, r, through the wall thickness of the pipe.

4.1 Constitutive equations

For an orthotropic ply k within the laminated pipe, the elastic constitutive equations in the material coordinate system $(1, 2, 3)$ [224] are

$$\begin{bmatrix} \sigma_1 \\ \sigma_2 \\ \sigma_3 \\ \tau_{23} \\ \tau_{31} \\ \tau_{12} \end{bmatrix} = \begin{bmatrix} C_{11} & C_{12} & C_{13} & 0 & 0 & 0 \\ C_{12} & C_{22} & C_{23} & 0 & 0 & 0 \\ C_{13} & C_{23} & C_{33} & 0 & 0 & 0 \\ 0 & 0 & 0 & C_{44} & 0 & 0 \\ 0 & 0 & 0 & 0 & C_{55} & 0 \\ 0 & 0 & 0 & 0 & 0 & C_{66} \end{bmatrix} \begin{bmatrix} \epsilon_1 \\ \epsilon_2 \\ \epsilon_3 \\ \gamma_{23} \\ \gamma_{31} \\ \gamma_{12} \end{bmatrix} \tag{4.1}$$

Rotation of this ply by an angle ϕ, as illustrated in Fig. 4.1, measured between the the axial orientation of the pipe and the fibre direction (1) of the material, the elastic constitutive equations of Eq. (4.1) can be transformed into those of a monoclinic material in the cylindrical coordinate system (r, θ, x) [224]:

$$\begin{bmatrix} \sigma_x \\ \sigma_\theta \\ \sigma_r \\ \tau_{\theta r} \\ \tau_{xr} \\ \tau_{x\theta} \end{bmatrix} = \begin{bmatrix} \bar{C}_{11} & \bar{C}_{12} & \bar{C}_{13} & 0 & 0 & \bar{C}_{16} \\ \bar{C}_{12} & \bar{C}_{22} & \bar{C}_{23} & 0 & 0 & \bar{C}_{26} \\ \bar{C}_{13} & \bar{C}_{23} & \bar{C}_{33} & 0 & 0 & \bar{C}_{36} \\ 0 & 0 & 0 & \bar{C}_{44} & \bar{C}_{45} & 0 \\ 0 & 0 & 0 & \bar{C}_{45} & \bar{C}_{55} & 0 \\ \bar{C}_{16} & \bar{C}_{26} & \bar{C}_{36} & 0 & 0 & \bar{C}_{66} \end{bmatrix} \begin{bmatrix} \epsilon_x \\ \epsilon_\theta \\ \epsilon_r \\ \gamma_{\theta r} \\ \gamma_{xr} \\ \gamma_{x\theta} \end{bmatrix} \tag{4.2}$$

The definition of the material stiffness matrix, $\boldsymbol{C}$, and the transformed stiffness matrix, $\bar{\boldsymbol{C}}$, are presented in Appendix A.

Satisfying the equilibrium conditions [224], governed by the cylindrical nature of the pipe, the through-thickness shear stresses $\tau_{\theta r}^k$ and τ_{xr}^k for a particular ply k can be written as

$$\tau_{\theta r}^{k}(r) = \frac{H^k}{r^2} \tag{4.3}$$

$$\tau_{xr}^{k}(r) = \frac{I^k}{r} \tag{4.4}$$

where H^k and I^k are constants of integration [224] in ply k. Assuming perfect bonding between all plies, traction continuity in these regions requires the through-thickness shear stresses $\tau_{\theta r}^{k}$ and τ_{xr}^{k} to be continuous from ply to ply. The consequence of this is that the ply constants, H^k and I^k, are zero [224]. This result can be obtained by starting at either the inner surface of the pipe, at ply $k = 1$ or at the outer surface of the pipe, at ply $k = N$, where the shear stresses $\tau_{\theta r}^{k}$ and τ_{xr}^{k} are zero (since no shear loads in these sense are applied). To satisfy these conditions the constants H^1 and I^1, and H^N and I^N acting on the inner and outer plies must be zero. Since the stresses $\tau_{\theta r}$ and τ_{xr} must be continuous from ply to ply, the constants H^k and I^k for plies within the laminate must also be zero. This is an interesting result, and indicates that in regions free from edge effects, and under the prescribed loading, the through-thickness shear stresses within a laminated composite pipe are zero [224]. Eq. (4.2) consequently reduces to Eq. (4.5). The absence of through-thickness shear stresses, in addition to traction continuity between plies, requires that the axial strain, and twist per unit length be constant across all plies. These are defined as ϵ_x^0 and γ^0, respectively. For the purposes of clarity, the full derivation and explanation of this is provided in Appendix B.

$$\begin{bmatrix} \sigma_x \\ \sigma_\theta \\ \sigma_r \\ \tau_{x\theta} \end{bmatrix} = \begin{bmatrix} \bar{C}_{11} & \bar{C}_{12} & \bar{C}_{13} & \bar{C}_{16} \\ \bar{C}_{12} & \bar{C}_{22} & \bar{C}_{23} & \bar{C}_{26} \\ \bar{C}_{13} & \bar{C}_{23} & \bar{C}_{33} & \bar{C}_{36} \\ \bar{C}_{16} & \bar{C}_{26} & \bar{C}_{36} & \bar{C}_{66} \end{bmatrix} \begin{bmatrix} \epsilon_x \\ \epsilon_\theta \\ \epsilon_r \\ \gamma_{x\theta} \end{bmatrix} \tag{4.5}$$

4.2 Ply displacements

At positions remote from edge effects, the displacements in the axial (u), tangential (v) and radial (w) directions, at the radial position r and axial position x for ply k of a laminated composite pipe can be written [224] as

$$u^k(x, r) = \epsilon_x^0 x \tag{4.6}$$

$$v^k(x, r) = \gamma^0 x r \tag{4.7}$$

$$w^k(r) = A_1^k r^{\lambda^k} + A_2^k r^{-\lambda^k} + \Gamma^k \epsilon_x^0 r + \Omega^k \gamma^0 r^2 \tag{4.8}$$

where ϵ_x^0, γ^0, A_1^k and A_2^k are constants determined by the specified boundary and loading conditions. The terms λ^k, Γ^k, and Ω^k are constants, dependent on the material properties of ply k [224], and can be found using Eqs. (4.9) to (4.11).

$$\lambda^k = \sqrt{\frac{\bar{C}_{22}^k}{\bar{C}_{33}^k}} \tag{4.9}$$

$$\Gamma^k = \frac{\bar{C}_{12}^k - \bar{C}_{13}^k}{\bar{C}_{33}^k - \bar{C}_{22}^k} \tag{4.10}$$

$$\Omega^k = \frac{\bar{C}_{26}^k - 2\bar{C}_{36}^k}{4\bar{C}_{33}^k - \bar{C}_{22}^k} \tag{4.11}$$

4.3 Ply strains

Individual strains within ply k, at the radial position r, are determined using the strain-displacement relations for the regions free from edge effects, and can be written [224] as

$$\epsilon_x^k(r) = \frac{\partial u}{\partial x} = \epsilon_x^0 \tag{4.12}$$

$$\epsilon_\theta^k(r) = \frac{\partial v}{\partial \theta} + \frac{w}{r} = A_1^k r^{(\lambda^k - 1)} + A_2^k r^{(-\lambda^k - 1)} + \Gamma^k \epsilon_x^0 + \Omega^k \gamma^0 r \tag{4.13}$$

$$\epsilon_r^k(r) = \frac{\partial w}{\partial r} = \lambda^k A_1^k r^{(\lambda^k - 1)} - \lambda^k A_2^k r^{(-\lambda^k - 1)} + \Gamma^k \epsilon_x^0 + 2\Omega^k \gamma^0 r \tag{4.14}$$

$$\gamma_{x\theta}^k(r) = \frac{\partial v}{\partial x} + \frac{1}{r}\frac{\partial u}{\partial \theta} = \gamma^0 r \tag{4.15}$$

4.4 Ply stresses

The stresses within ply k, at the radial position r, are determined by combining the constitutive equations of Eq. (4.5) together with Eqs. (4.12) to (4.15). The resulting stresses

are presented in Eqs. (4.16) to (4.19) [224]:

$$\begin{aligned}\sigma_x^k(r) = &\left[\bar{C}_{11}^k + \left(\bar{C}_{13}^k + \bar{C}_{12}^k\right)\Gamma^k\right]\epsilon_x^0 + \left[\left(\bar{C}_{12}^k + 2\bar{C}_{13}^k\right)\Omega^k + \bar{C}_{16}^k\right]\gamma^0 r \\ &+ \left[\bar{C}_{12}^k + \lambda^k\bar{C}_{13}^k\right]A_1^k r^{(\lambda^k-1)} + \left[\bar{C}_{12}^k - \lambda^k\bar{C}_{13}^k\right]A_2^k r^{(-\lambda^k-1)}\end{aligned} \tag{4.16}$$

$$\begin{aligned}\sigma_\theta^k(r) = &\left[\bar{C}_{12}^k + \left(\bar{C}_{22}^k + \bar{C}_{23}^k\right)\Gamma^k\right]\epsilon_x^0 + \left[\left(\bar{C}_{22}^k + 2\bar{C}_{23}^k\right)\Omega^k + \bar{C}_{26}^k\right]\gamma^0 r \\ &+ \left[\bar{C}_{22}^k + \lambda^k\bar{C}_{23}^k\right]A_1^k r^{(\lambda^k-1)} + \left[\bar{C}_{22}^k - \lambda^k\bar{C}_{23}^k\right]A_2^k r^{(-\lambda^k-1)}\end{aligned} \tag{4.17}$$

$$\begin{aligned}\sigma_r^k(r) = &\left[\bar{C}_{13}^k + \left(\bar{C}_{23}^k + \bar{C}_{33}^k\right)\Gamma^k\right]\epsilon_x^0 + \left[\left(\bar{C}_{23}^k + 2\bar{C}_{33}^k\right)\Omega^k + \bar{C}_{36}^k\right]\gamma^0 r \\ &+ \left[\bar{C}_{23}^k + \lambda^k\bar{C}_{33}^k\right]A_1^k r^{(\lambda^k-1)} + \left[\bar{C}_{23}^k - \lambda^k\bar{C}_{33}^k\right]A_2^k r^{(-\lambda^k-1)}\end{aligned} \tag{4.18}$$

$$\begin{aligned}\tau_{x\theta}^k(r) = &\left[\bar{C}_{16}^k + \left(\bar{C}_{26}^k + \bar{C}_{36}^k\right)\Gamma^k\right]\epsilon_x^0 + \left[\bar{C}_{66}^k + \left(\bar{C}_{26}^k + 2\bar{C}_{36}^k\right)\Omega^k\right]\gamma^0 r \\ &+ \left[\bar{C}_{26}^k + \lambda^k\bar{C}_{36}^k\right]A_1^k r^{(\lambda^k-1)} + \left[\bar{C}_{26}^k - \lambda^k\bar{C}_{36}^k\right]A_2^k r^{(-\lambda^k-1)}\end{aligned} \tag{4.19}$$

4.5 Boundary conditions

For perfectly bonded plies, all displacements must be continuous from ply to ply. As already discussed, due to the absence of through-thickness shear stresses, the boundary conditions that follow from this requirement are that of constant axial strain, ϵ_x^0, and angle of twist per unit length, γ^0, across all plies. In addition to these requirements, displacement continuity requires that the radial displacement, w, be continuous across each ply interface. This boundary condition is represented by Eq. (4.20) [224]. Additional boundary conditions associated with the equilibrium requirements also exist. A consequence of the traction continuity requirements, is that the radial stresses, σ_r, must be continuous across each ply interface. This is represented by Eq. (4.21) [224]. Additionally, the radial stresses that exist at the inner and outer surfaces of the pipe must be exactly equal and opposite to the pressure loads, P_I and P_O, applied to these surfaces, respectively. These boundary conditions are represented in Eqs. (4.22) and (4.23) [224].

$$w^k(r_k) = w^{k+1}(r_k) \qquad \text{(Interface at } r_k \quad k = 1, \dots, N-1) \tag{4.20}$$

$$\sigma_r^k(r_k) = \sigma_r^{k+1}(r_k) \qquad \text{(Interface at } r_k \quad k = 1, \dots, N-1) \tag{4.21}$$

$$\sigma_r\left(R_I\right) = -P_I \tag{4.22}$$

$$\sigma_r\left(R_O\right) = -P_O \tag{4.23}$$

4.6 Loading

The axisymmetric loading conditions considered are internal, P_I, and external, P_O, pressures, as well as axial, F_x, and torque, T_x, loads. The boundary conditions associated with applied pressure loads have already been discussed, and are presented in Eqs. (4.22) and (4.23). The axial force and torque that exist at the ends of the laminated pipe are determined by integrating the axial stresses, σ_x, and the moment of the in-plane shear stresses, $\tau_{x\theta}$, across the wall thickness of the pipe. The axial and torque loads are formulated in Eqs. (4.24) and (4.25) for a pipe of N plies, respectively.

$$\begin{aligned}
F_x =& \int_{r_0}^{r_N} 2\pi\sigma_x(r) r \; dr \\
=& 2\pi \sum_{k=1}^{N} \int_{r_{k-1}}^{r_k} \sigma_x^k(r) r \; dr \\
=& 2\pi \sum_{k=1}^{N} \Bigg[\left(\bar{C}_{11}^k + \left\{ \bar{C}_{13}^k + \bar{C}_{12}^k \right\} \Gamma^k \right) \epsilon_x^0 \left(\frac{r_k^2 - r_{k-1}^2}{2} \right) \\
&+ \left(\bar{C}_{16}^k + \left\{ \bar{C}_{12}^k + 2\bar{C}_{13}^k \right\} \Omega^k \right) \gamma^0 \left(\frac{r_k^3 - r_{k-1}^3}{3} \right) \\
&+ \frac{\left(\bar{C}_{12}^k + \lambda^k \bar{C}_{13}^k \right)}{\lambda^k + 1} A_1^k \left(r_k^{(\lambda^k+1)} - r_{k-1}^{(\lambda^k+1)} \right) \\
&+ \frac{\left(\bar{C}_{12}^k - \lambda^k \bar{C}_{13}^k \right)}{-\lambda^k + 1} A_2^k \left(r_k^{(-\lambda^k+1)} - r_{k-1}^{(-\lambda^k+1)} \right) \Bigg]
\end{aligned} \tag{4.24}$$

$$
\begin{aligned}
T_x =& \int_{r_0}^{r_N} 2\pi\tau_{x\theta}(r)r^2\ dr \\
=& 2\pi \sum_{k=1}^{N} \int_{r_{k-1}}^{r_k} \tau_{x\theta}^k(r)r^2\ dr \\
=& 2\pi \sum_{k=1}^{N} \Bigg[\left(\bar{C}_{16}^k + \left\{ \bar{C}_{26}^k + \bar{C}_{36}^k \right\} \Gamma^k \right) \epsilon_x^0 \left(\frac{r_k^3 - r_{k-1}^3}{3} \right) \\
&+ \left(\bar{C}_{66}^k + \left\{ \bar{C}_{26}^k + 2\bar{C}_{36}^k \right\} \Omega^k \right) \gamma^0 \left(\frac{r_k^4 - r_{k-1}^4}{4} \right) \\
&+ \frac{\left(\bar{C}_{26}^k + \lambda^k \bar{C}_{36}^k \right)}{\lambda^k + 2} A_1^k \left(r_k^{(\lambda^k+2)} - r_{k-1}^{(\lambda^k+2)} \right) \\
&+ \frac{\left(\bar{C}_{26}^k - \lambda^k \bar{C}_{36}^k \right)}{-\lambda^k + 2} A_2^k \left(r_k^{(-\lambda^k+2)} - r_{k-1}^{(-\lambda^k+2)} \right) \Bigg]
\end{aligned}
\tag{4.25}
$$

5 Proposed method

The Sachs [198] method of residual stress measurement has seen extension to both single, and multi-layered pipes of cylindrical orthotropy [219, 220, 223]. These existing methods cannot, however, be used for laminated anisotropic pipes. Additionally, these works assume a state of plane-stress for the determination of the the hoop and radial stresses (making use of the solution of Lekhnitskii [97]), and also assume that the release of axial stresses with material removal results in a uniform axial stress change over the remaining pipe thickness [220]. Although acceptable for thin-walled pipes, these assumptions introduce inaccuracies in the resulting stress distributions when very thick-walled pipes are considered. Further explanation of these inaccuracies is presented in Appendix C. To the author's knowledge, no solution presently exists for extension of the Sachs' method to laminated, anisotropic pipes. The work presented in this section therefore aims to:

- Provide a solution for the determination of the through-thickness distributions of the residual stresses in layered anisotropic pipes of any wall thickness.
- This will also provide an alternative solution for the determination of though-thickness residual stresses in orthotropic pipes when inaccuracies of the methods that already exist are not acceptable (in the case of thick-walled pipes).

The proposed method follows the same technique of measurement as that of Sachs [198]. For the purposes of this work, only the solution for removal of material from the outer surface of a pipe, while measuring strain change at the inner surface, is presented. This method can, however, easily be extended in the same manner to the case of material removal from the inner surface of the pipe. Throughout this text, the term "ply" is reserved for a single lamina within the pipe laminate, whereas the term "layer" is reserved for material that is removed from the laminate during the experimental process. Measurement of the residual stresses within a ply typically requires progressive removal of several layers.

The residual stresses that potentially exist through the thickness of any composite pipe take the form of axial, σ_x, hoop, σ_θ, radial, σ_r, and in-plane shear, $\tau_{x\theta}$, stresses. No

residual through-thickness shear stresses, τ_{xr} and $\tau_{\theta r}$, can exist in regions far from edge effects, due to the structural symmetry constraints [231]. Under these conditions, the elastic solution presented in Section 4 is valid, provided that the length of pipe is long enough, so that the regions where the response of the pipe to layer removal is measured are free from edge effects. Removal of a layer from the outer surface of a pipe releases the residual stresses that were present within that layer. This release in stress causes the remaining pipe section to deform, since the stress distribution within the remaining pipe alters to always be self-equilibrating. The difference between the original residual stress distribution prior to any material removal, and the stress distribution that exists in the remaining pipe after the removal of some layers is what can be referred to as the induced stress. This method assumes that the induced stress arises as a purely linearly elastic mechanical response. Thus, for a particular induced stress, there exists a unique combination of external loads that have been "applied" to the remaining pipe after the material removal. These loads take the form of axial force, torque, and external pressure, and are the residual loads which must have existed within the removed layers. These loads are defined as F_x^m, T_x^m, and P_m for the removal of m layers. This is as illustrated in Fig. 5.1, for a pipe with N remaining plies. No internal residual pressure load ever exists since the inner surface of the pipe remains unchanged. The following section outlines the proposed method of residual stress calculation. This process involves initially determining the induced stress distribution, through the measured strain response at the inner surface of the pipe, to material removal. The residual loads, F_x^m, T_x^m, and P_m, associated with the removal of m layers, are then found from the induced stress state. Using the same technique, the residual loads released by the removal of the preceding $m-1$ layers can also be found. The residual axial and torque loads that existed only within layer m must be exactly the difference between the residual loads released by the removal of all $m-1$ and m layers, respectively. These, as illustrated in Fig. 5.1, are denoted as $F_x^{\overline{m}}$ and $T_x^{\overline{m}}$, and are evaluated by subtracting the residual axial and torque loads determined for the removal of $m-1$ layers, from those calculated for the removal of all m layers. The residual pressure load released by the removal of $m-1$ layers is equal to the residual radial stress that existed at the outer surface of layer m. Similarly, the residual radial stress at the inner surface of layer m is equal to the residual pressure load determined for the removal of all m layers. The negative of these pressure loads, P_{m-1} and P_m, are applied to the outer and inner surfaces of layer m, and the residual axial and torque loads released by this layer, $F_x^{\overline{m}}$ and $T_x^{\overline{m}}$, also applied to the layer to estimate the residual stress state that existed within this layer prior to any material removal.

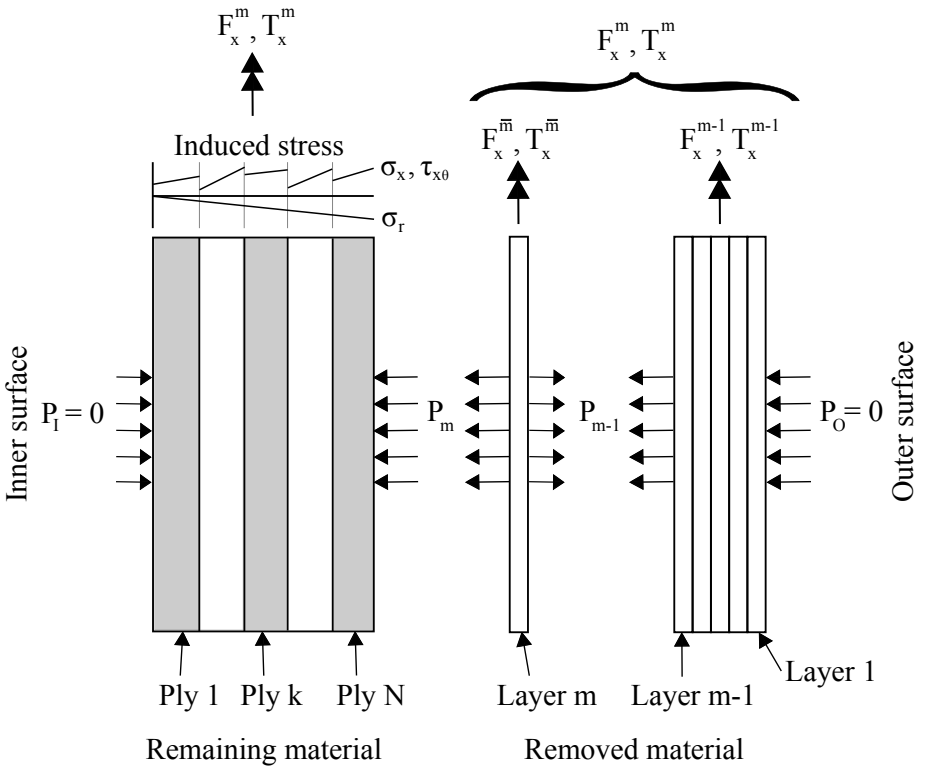

Figure 5.1: Residual stress measurement technique

5.1 Finding the induced stress

As previously mentioned, the removal of material from the inner or outer surface of a pipe induces a change in stress over the remaining wall thickness. This induced stress distribution can be found by considering the deformation of the pipe to the material removal. For material removal from the outer surface, the strain response is ideally measured on the inner surface of the pipe. For this reason all of the equations presented in this section assume measurement of the strain response at the inner surface. To resolve the entire residual stress state released by removal of a layer, the axial, circumferential and shear strain response is required. Assuming that the remaining pipe thickness comprises N plies after the removal of m layers (as illustrated in Fig. 5.1), these strain responses are denoted by the variables ϵ_x^m, ϵ_θ^m, and $\gamma_{x\theta}^m$, respectively. There are many methods of strain measurement. Probably the most common of these methods is to measure the strain response using strain gauges. To resolve the three strain responses, three strain gauges would be required. These would preferably be aligned in the axial, x, circumferential, θ, and 45° (measured from the axial orientation) directions, respectively. From the signal recorded from these gauges, the shear strain response at the inner surface can be found directly from the relationship of Eq. (5.1) [232].

$$\gamma_{x\theta}^{m} = 2\epsilon_{45}^{m} - (\epsilon_{x}^{m} + \epsilon_{\theta}^{m}) \tag{5.1}$$

Measurement of the axial, ϵ_x^m, and shear, $\gamma_{x\theta}^m$, strain response allows for direct determination of the constants ϵ_x^0 and γ^0 associated with the induced stress state within the remaining pipe. Since these constants are invariant through the pipe thickness, $\epsilon_x^0 = \epsilon_x^m$ and $\gamma^0 = \gamma_{x\theta}^m / R_I$ from Eqs. (4.12) and (4.15), respectively. Referring to the elastic solution of Section 4, for a pipe of N remaining plies, there exists $N(A_1^k)$ constants and $N(A_2^k)$ constants that need to be found, so that the induced stress state within the remaining pipe can be obtained. The $2N$ constants are found by utilising Eq. (4.18) where the radial stress at the pipe inner surface is always zero, and Eq. (4.13), where the measured circumferential strain, ϵ_θ^m, is expressed in relation to the required constants. Additionally, the $2(N-1)$ equilibrium conditions are simultaneously applied in the form of Eqs. (4.20) and (4.21) at each ply interface. These are the boundary conditions of continuous radial displacement and stress, and requires the use of Eqs. (4.8) and (4.18) within these regions. The equations resulting from this approach can be written in matrix form, as presented in Eq. (5.2).

$$\boldsymbol{D}\boldsymbol{A} = \boldsymbol{M} \tag{5.2}$$

In Eq. (5.2), the square matrix $\boldsymbol{D}$ contains the terms that are dependant upon the known geometry and material properties of the remaining pipe, and vector $\boldsymbol{A}$ comprises the unknown $N(A_1^k)$ and $N(A_2^k)$ terms. The terms of matrix $\boldsymbol{M}$ are those associated with the measured strains ϵ_x^0, ϵ_θ^m, and γ^0. Appendix D provides the derivation of the generalised equations presented for the terms of each of these matrices. As with the equations presented in Section 4, the variable k refers to the ply k, and these are numbered from the inner surface of the pipe, outward. The non-zero terms of the square matrix $\boldsymbol{D}$ are defined as

$$\left.\begin{aligned} D_{1,1} &= \beta^1 r_0^{(\lambda^1-1)} \\ D_{1,2} &= \delta^1 r_0^{(-\lambda^1-1)} \\ D_{2,1} &= r_0^{(\lambda^1-1)} \\ D_{2,2} &= r_0^{(-\lambda^1-1)} \end{aligned}\right\} \text{ For } k = 1 \tag{5.3}$$

$$\left.\begin{array}{rcl} D_{2k+1,2k-1} &=& \beta^k r_k^{(\lambda^k-1)} \\ D_{2k+1,2k} &=& \delta^k r_k^{(-\lambda^k-1)} \\ D_{2k+1,2k+1} &=& -\beta^{k+1} r_k^{(\lambda^{k+1}-1)} \\ D_{2k+1,2k+2} &=& -\delta^{k+1} r_k^{(-\lambda^{k+1}-1)} \\ D_{2k+2,2k-1} &=& r_k^{\lambda^k} \\ D_{2k+2,2k} &=& r_k^{-\lambda^k} \\ D_{2k+2,2k+1} &=& -r_k^{\lambda^{k+1}} \\ D_{2k+2,2k+2} &=& -r_k^{-\lambda^{k+1}} \end{array}\right\} \text{ For } 1 \leq k \leq N-1 \tag{5.4}$$

where

$$\beta^k = \bar{C}_{23}^k + \lambda^k \bar{C}_{33}^k \tag{5.5}$$

and

$$\delta^k = \bar{C}_{23}^k - \lambda^k \bar{C}_{33}^k \tag{5.6}$$

Eq. (5.3) relates to the boundary conditions on the inner surface, where the radial stress is always zero, and the circumferential strain is equal to that measured experimentally. Eq. (5.4), however, relates to the boundary conditions of continuous radial stress and radial displacement at each ply interface. Equation (5.4) is thus only applicable when the number of plies remaining in the pipe is greater than one. The terms of vector $\boldsymbol{A}$ in Eq. (5.2) are

$$\left.\begin{array}{rcl} A_{2k-1} &=& A_1^k \\ A_{2k} &=& A_2^k \end{array}\right\} \text{ For } 1 \leq k \leq N \tag{5.7}$$

The vector $\boldsymbol{M}$ in Eq. (5.2) is expressed in terms of the measured circumferential strain, ϵ_θ^m, and constant strain terms ϵ_x^0 and γ^0 determined directly from the measured axial, ϵ_x^m, and shear strain response, $\gamma_{x\theta}^m$.

$$\left.\begin{array}{rcl} M_1 &=& -\eta^1 \epsilon_x^0 - \kappa^1 \gamma^0 r_0 \\ M_2 &=& \epsilon_\theta^m - \Gamma^1 \epsilon_x^0 - \Omega^1 \gamma^0 r_0 \end{array}\right\} \text{ For } k = 1 \tag{5.8}$$

$$\left.\begin{array}{rcl} M_{2k+1} &=& -\eta^k \epsilon_x^0 - \kappa^k \gamma^0 r_k \\ & & +\eta^{k+1} \epsilon_x^0 + \kappa^{k+1} \gamma^0 r_k \\ M_{2k+2} &=& -\Gamma^k \epsilon_x^0 r_k - \Omega^k \gamma^0 r_k^2 \\ & & +\Gamma^{k+1} \epsilon_x^0 r_k + \Omega^{k+1} \gamma^0 r_k^2 \end{array}\right\} \text{ For } 1 \leq k \leq N-1 \tag{5.9}$$

where

$$\eta^k = \bar{C}^k_{13} + \left[\bar{C}^k_{23} + \bar{C}^k_{33}\right] \Gamma^k \tag{5.10}$$

and

$$\kappa^k = \left[\bar{C}^k_{23} + 2\bar{C}^k_{33}\right] \Omega^k + \bar{C}^k_{36} \tag{5.11}$$

As with Eq. (5.4), Eq. (5.9) is only applicable when the remaining number of plies in the pipe is greater than one.

Solving Eq. (5.2) allows for the A^k_1 and A^k_2 constants of each of the N plies of the remaining pipe section to be found. These, together with the measured ϵ^0_x and γ^0 values are utilised to determine the induced stress state within the remaining pipe. Finding the induced axial, hoop, radial and in-plane shear stress distributions requires the use of Eqs. (4.16) to (4.19). The induced stress state changes with the removal of each layer, and thus this process is repeated for each layer removal.

5.2 Finding the applied loading

To calculate the residual stresses that existed within layer m, the residual loads released by removal of this layer need to be found. The residual axial, F^m_x, and torque, T^m_x, loads associated with the removal of all m layers can be found by integration of the induced axial, σ_x, and the moment of the shear, $\tau_{x\theta}$, stress distributions across the remaining pipe thickness. The equations resulting from the integration of these stress distributions take the form of Eqs. (4.24) and (4.25), respectively. Once these loads have have been determined, the residual loads associated only with the removal of the layer m, $F^{\overline{m}}_x$ and $T^{\overline{m}}_x$, can be found. This is done by subtracting the residual loads found for the removal of the previous $m-1$ layers from those determined for the removal of all m layers:

$$F^{\overline{m}}_x = \begin{cases} F^m_x & (\text{for} \quad m = 1) \\ F^m_x - F^{m-1}_x & (\text{for} \quad m > 1) \end{cases} \tag{5.12}$$

$$T^{\overline{m}}_x = \begin{cases} T^m_x & (\text{for} \quad m = 1) \\ T^m_x - T^{m-1}_x & (\text{for} \quad m > 1) \end{cases} \tag{5.13}$$

The residual pressure applied to the outer surface of the remaining pipe, P_m, can be obtained by considering the induced radial stress that exists at the newly exposed outer

surface, consequent of the layer removal. This is found using Eq. (4.18) with r set to the radius of the newly exposed surface. By invoking the boundary condition of Eq. (4.23), the residual pressure load, P_m, is exactly equal and opposite to this value. Another way of looking at the situation is that, after the removal of the m layers, the resultant radial stress at the newly exposed surface is the sum of the residual radial stress that existed at this radial position prior to the removal of the any material, and the induced radial stress that arises due to the layer removal. Since this resultant stress must vanish to zero (as no physical external pressure is applied to the outer surface of the remaining pipe), the residual radial stress that existed at this position is exactly the negative of the induced radial stress determined for the material removal. The residual pressure, P_m, is therefore exactly equal to the residual radial stress that existed at the inner surface of the removed layer m. Similarly, the residual radial stress that existed at the outer surface of this layer is exactly the pressure load, P_{m-1}, determined for the removal of $m-1$ layers.

Due to the cylindrical nature of the problem the residual axial and hoop stresses require only a zero force resultant through the thickness of the wall. Additionally, the residual in-plane shear stresses must adhere to the zero-torque requirement about the axis of the pipe. Since there exists a zero-force, zero-torque condition for these stresses, the calculated loads, F_x^m and T_x^m, will tend toward zero as the wall thickness of the remaining pipe tends to zero. Another explanation of this can be related to the measured strains at the inner surface of the pipe, which will approach the negative of the residual strains that existed at this surface, as the wall thickness of the remaining pipe tends to zero. Since these strain responses will not tend toward infinity, the residual loads distributed over the remaining pipe of infinitesimally thin wall thickness must tend to zero. By Eqs. (5.12) and (5.13), the loads in each removed layer depend on the calculated loads for all of the preceding removed layers, and therefore the residual loads calculated for the removal of all of the wall thickness must be equal to the summation of the residual loads determined for each individual removed layer. Since the residual loads must tend to zero as the wall thickness of the pipe tends to zero, the calculated axial, hoop and shear stress distributions will always satisfy the self-equilibrium requirement. Additionally, since the loads $F_x^{\overline{m}}$ and $T_x^{\overline{m}}$ depend only on the values of F_x^m, F_x^{m-1}, T_x^m and T_x^{m-1} respectively, errors do not propagate through the thickness of the pipe. An error in F_x^m will cause an error in the residual axial force determined for layer m. Should the load calculated for the $m+1$ layer, F_x^{m+1}, be accurate, an error in the calculated $F_x^{\overline{m+1}}$ value will oppose the error of the $F_x^{\overline{m}}$ value. The error associated with the calculated F_x^m value will therefore not propagate through to the $m+2$ removed layer. The same can be said for T_x^m. Therefore there exists a built in system of self-correction, where overly tensile stresses are compensated for by overly compressive stresses in the region of error, and visa versa. Further explanation of this mechanism is presented in Appendix E.

5.3 Finding the residual stress distributions

Knowledge of the residual loads released by layer m allow for the average residual stress within this layer to be found. The elastic solution of Section 4 is utilised for this purpose. Determining the stresses using Eqs. (4.16) to (4.19) requires the constants ϵ_x^0, γ^0, A_1^k and A_2^k of this layer to be determined. These are found by simultaneously solving Eqs. (4.24) and (4.25), associated with the residual axial force, $F_x^{\overline{m}}$, and torque, $T_x^{\overline{m}}$, released by the removal of this layer, together with Eq. (4.18), applied to both the inner and outer surfaces of this layer, where the residual radial stress is exactly P_m and P_{m-1}, respectively. These equations can be solved in matrix the form of Eq. (5.14). Appendix D provides the derivations of each of the terms of these matrices, based upon the equations presented in Section 4.

$$\boldsymbol{Y}\boldsymbol{X} = \boldsymbol{Z} \tag{5.14}$$

The terms of the matrix $\boldsymbol{Y}$ are presented in Eq. (5.15). In this case it is assumed that layer m comprises only material from ply k, and that the outer and inner radius of this layer are r_{m-1} and r_m, respectively.

$$\begin{array}{lcllcl}
Y_{11} &=& \beta^k r_m^{(\lambda^k-1)} & Y_{31} &=& \zeta^k \left(r_{m-1}^{(\lambda^k+1)} - r_m^{(\lambda^k+1)} \right) \\
Y_{12} &=& \delta^k r_m^{(-\lambda^k-1)} & Y_{32} &=& \xi^k \left(r_{m-1}^{(-\lambda^k+1)} - r_m^{(-\lambda^k+1)} \right) \\
Y_{13} &=& \eta^k & Y_{33} &=& \psi^k \left(\frac{r_{m-1}^2 - r_m^2}{2} \right) \\
Y_{14} &=& \kappa^k r_m & Y_{34} &=& \chi^k \left(\frac{r_{m-1}^3 - r_m^3}{3} \right) \\
Y_{21} &=& \beta^k r_{m-1}^{(\lambda^k-1)} & Y_{41} &=& \iota^k \left(r_{m-1}^{(\lambda^k+2)} - r_m^{(\lambda^k+2)} \right) \\
Y_{22} &=& \delta^k r_{m-1}^{(-\lambda^k-1)} & Y_{42} &=& \omega^k \left(r_{m-1}^{(-\lambda^k+2)} - r_m^{(-\lambda^k+2)} \right) \\
Y_{23} &=& \eta^k & Y_{43} &=& \varrho^k \left(\frac{r_{m-1}^3 - r_m^3}{3} \right) \\
Y_{24} &=& \kappa^k r_{m-1} & Y_{44} &=& \vartheta^k \left(\frac{r_{m-1}^4 - r_m^4}{4} \right)
\end{array} \tag{5.15}$$

where the terms ζ^k, ϑ^k, ι^k, ξ^k, ϱ^k, χ^k, ψ^k, and ω^k are defined in Eqs. (5.16) to (5.23), and the terms β^k, δ^k, η^k and κ^k are as defined in Eqs. (5.5), (5.6), (5.10) and (5.11), respectively.

$$\zeta^k = \frac{\bar{C}_{12}^k + \lambda^k \bar{C}_{13}^k}{\lambda^k + 1} \tag{5.16}$$

$$\vartheta^k = \bar{C}_{66}^k + \left[\bar{C}_{26}^k + 2\bar{C}_{36}^k\right] \Omega^k \tag{5.17}$$

$$\iota^k = \frac{\bar{C}_{26}^k + \lambda^k \bar{C}_{36}^k}{\lambda^k + 2} \tag{5.18}$$

$$\xi^k = \frac{\bar{C}_{12}^k - \lambda^k \bar{C}_{13}^k}{-\lambda^k + 1} \tag{5.19}$$

$$\varrho^k = \bar{C}_{16}^k + \left[\bar{C}_{26}^k + \bar{C}_{36}^k\right] \Gamma^k \tag{5.20}$$

$$\chi^k = \bar{C}_{16}^k + \left[\bar{C}_{12}^k + 2\bar{C}_{13}^k\right] \Omega^k \tag{5.21}$$

$$\psi^k = \bar{C}_{11}^k + \left[\bar{C}_{13}^k + \bar{C}_{12}^k\right] \Gamma^k \tag{5.22}$$

$$\omega^k = \frac{\bar{C}_{26}^k - \lambda^k \bar{C}_{36}^k}{-\lambda^k + 2} \tag{5.23}$$

The terms of the vector $\boldsymbol{X}$ are the required pipe constants, ϵ_x^0, γ^0, A_1^k and A_2^k, and the order in which they are arranged is presented in Eq. (5.24).

$$\begin{aligned} X_1 &= A_1^k \\ X_2 &= A_2^k \\ X_3 &= \epsilon_x^0 \\ X_4 &= \gamma^0 \end{aligned} \tag{5.24}$$

The terms of the vector, $\boldsymbol{Z}$, contain the residual axial and torque loads obtained for layer m, as well as the residual radial stresses that existed at the inner and outer surfaces of this layer, in terms of the residual pressure loads determined for the removal of m and $m-1$ layers, respectively. These terms are presented in Eq. (5.25).

$$\begin{aligned} Z_1 &= P_m \\ Z_2 &= P_{m-1} \\ Z_3 &= \frac{F_x^{\overline{m}}}{2\pi} \\ Z_4 &= \frac{T_x^{\overline{m}}}{2\pi} \end{aligned} \tag{5.25}$$

Solving Eq. (5.14) allows the constants ϵ_x^0, γ^0, A_1^k and A_2^k to be found. These are substituted into Eqs. (4.16) to (4.19) to determine the average residual stresses that existed within layer m.

It should be noted that enforcing the elastic solution of Section 4 to find the residual stress state that existed within each layer does have some limitations. These are associated with the values of ϵ_x^0 and γ^0, which are assumed constant within a layer. Although this holds true for the mechanical response of the pipe to material removal, it cannot be said to be true for the residual stress state within the pipe itself. Since the process of the formation of residual stresses is dependant on, among others, the cure shrinkage of the resin system, rate of cure, and non-linear visco-elastic behaviour of the resin during cure, it is very likely that the resulting residual ϵ_x and $\gamma_{x\theta}/r$ distributions (or mechanical residual strains) that exist through the pipe thickness are not constant. These residual strain values can, however, be considered constant through the thickness of a removed layer, provided the layer is thin enough. The stresses evaluated at the mid-radius of the layer m, will therefore be very similar to the residual stresses that existed within this region, prior to any material removal. Thus the residual stress distribution through the entire pipe thickness can be described by considering the stresses evaluated at the mid-radius of every removed layer. Since only the average residual stress is obtainable in each layer, the number of layers removed must be sufficiently high to accurately represent the residual stress distributions, especially if these vary significantly through the wall thickness.

Should layer m comprise material of two different plies, two additional A_1^k and A_2^k constants, need to be determined. These are found by invoking the boundary conditions that exist at the interface of the plies in the form of Eqs. (4.20) and (4.21), making use of Eqs. (4.8) and (4.18). The matrix form equations for this case are derived and presented in Appendix D. These equations are only applicable, however, when no residual strain discontinuity exists between the plies. Since the method only allows the average ϵ_x^0 and γ^0 values to be found, the presence of a residual strain discontinuity across the plies will result in inaccurate ϵ_x^0 and γ^0 values determined at the mid-radius of this layer. This, therefore, results in erroneous residual stresses calculated for this region. Under these circumstances, the residual stresses obtained for layer m should be ignored, and the residual stress profile in the region of the ply interface described through extrapolation of the residual stresses obtained for the surrounding layers.

Consecutive removal of layers will produce a continuous variation in measured strain response. The presence of stress discontinuities within a laminated pipe will not produce discontinuities in measured data, but rather results in discontinuous slopes in the measured strain distribution. To represent a continuous strain distribution, it is advisable to fit

polynomials to the measured data, especially in the presence of experimental scatter. The number of polynomials fitted should correspond directly with the number of plies present in the original pipe. This ensures that the discontinuities in the slope of the measured strain distribution, which will occur with the removal of material at each ply interface, are accurately represented. Fitting polynomials to the measured strain data will also ensure that smooth residual stress distributions are obtained.

5.4 Error analysis

The error in the axial, hoop, radial, and shear stress of the removed layer m can be expressed in terms of the errors associated with the measured strain data [233] as

$$e_{\sigma_i}^m = \sqrt{\left(\frac{\partial \sigma_i^m}{\partial \epsilon_x^m} e_{\epsilon_x}^m\right)^2 + \left(\frac{\partial \sigma_i^m}{\partial \epsilon_\theta^m} e_{\epsilon_\theta}^m\right)^2 + \left(\frac{\partial \sigma_i^m}{\partial \gamma_{x\theta}^m} e_{\gamma_{x\theta}}^m\right)^2} \tag{5.26}$$

where σ_i represents each of the stress components in layer m and $e_{\epsilon_i}^m$ is the corresponding measurement error. The error in strain is taken to be either the difference between the value of the polynomial fitted to the measured strain data and the actual measured strain value, or the actual strain measurement uncertainty, whichever is the greater. This approach is the same as described by Prime and Hill [173] and used for obtaining errors in residual stress distributions when using the slitting method.

Since the stresses are not calculated directly from the measured strains, the partial derivative terms of Eq. (5.26) cannot be found directly. Instead, the errors are estimated by considering the response of the stress components to the loads applied to each layer. In this case, the error in each stress component in layer m can be described as

$$e_{\sigma_i}^m = \sqrt{\left(\frac{\partial \sigma_i^m}{\partial F_x^{\overline{m}}} e_{F_x}^m\right)^2 + \left(\frac{\partial \sigma_i^m}{\partial T_x^{\overline{m}}} e_{T_x}^m\right)^2 + \left(\frac{\partial \sigma_i^m}{\partial P_m} e_{P_m}^m\right)^2 + \left(\frac{\partial \sigma_i^m}{\partial P_{m-1}} e_{P_{m-1}}^m\right)^2} \tag{5.27}$$

where $e_{F_x}^m$, $e_{T_x}^m$, $e_{P_m}^m$ and $e_{P_{m-1}}^m$ represent the errors in each of the loads applied to layer m. The error associated with each of the applied loads of Eq. (5.27) can be expressed as

$$e_{L_i}^m = \sqrt{\left(\frac{\partial L_i^{\overline{m}}}{\partial \epsilon_x^m} e_{\epsilon_x}^m\right)^2 + \left(\frac{\partial L_i^{\overline{m}}}{\partial \epsilon_\theta^m} e_{\epsilon_\theta}^m\right)^2 + \left(\frac{\partial L_i^{\overline{m}}}{\partial \gamma_{x\theta}^m} e_{\gamma_{x\theta}}^m\right)^2} \tag{5.28}$$

where $L_i^{\overline{m}}$ represents each of the loads applied to layer m, and $e_{\epsilon_x}^m$, $e_{\epsilon_\theta}^m$ and $e_{\gamma_{x\theta}}^m$ represent the error in each of the measured strain components. The partial derivative terms of Eq. (5.28) are estimated by finding each term separately. This is done numerically by

varying the term in question, while holding the other measurement terms constant. It should be recognised that as a consequence of Eqs. (5.12) and (5.13), the error terms $e^m_{F_x}$ and $e^m_{T_x}$ depend on the errors associated with the residual loads, F_x and T_x, determined for the removal of m and $m-1$ layers, and so

$$e^m_{F_x} = \sqrt{\left(\hat{e}^m_{F_x}\right)^2 + \left(\hat{e}^{m-1}_{F_x}\right)^2} \tag{5.29}$$

$$e^m_{T_x} = \sqrt{\left(\hat{e}^m_{T_x}\right)^2 + \left(\hat{e}^{m-1}_{T_x}\right)^2} \tag{5.30}$$

where $\hat{e}^m_{F_x}$, $\hat{e}^m_{T_x}$, $\hat{e}^{m-1}_{F_x}$ and $\hat{e}^{m-1}_{T_x}$ are the errors associated with the applied axial and torque loads after the removal of m and $m-1$ layers, respectively.

Once the errors in the loads applied to layer m are estimated, the error in each stress component of Eq. (5.27) is found. This is done by using an approach similar to that used to find the errors in load. Each partial differential term of Eq. (5.27) is determined numerically by varying each term in turn while keeping the other load terms fixed.

5.5 Special case: Filament-wound pipes

Filament-wound pipes are manufactured by a continuous winding process, producing a complex weave. This weave results in an anisotropic laminae stacking sequence alternating between the $+\phi$ and $-\phi$ winding angles. This stacking sequence changes with both axial and circumferential position. As the frequency of the alternating stacking sequence increases, the individual lamina thickness relative to the ply thickness decreases, and so the pipe will behave more like an orthotropic pipe. For example, one would expect little or no twisting of a relatively thick-walled filament-wound pipe under applied axial or pressure loads, because the fibres orientated at $+\phi$, which cause the pipe to twist in one direction, are countered by fibres orientated at $-\phi$, which would cause rotation in the opposite direction. In this sense, the bulk-scale behaviour of the pipe demonstrates no coupling between the normal stresses, and shear strains, which is orthotropic behaviour.

Based on the method presented in this section, the bulk-scale residual axial, hoop, radial, and in-plane shear stress distributions that exist over the wall-thickness of the filament-wound pipe can be measured. Since a pipe of this nature can be considered orthotropic at the bulk-scale, a residual in-plane shear stress distribution of zero can generally be expected. The reason for this is that the effects of any fibres orientated in $+\phi$ are countered by those wound at $-\phi$ during cure. A residual in-plane shear stress distribution could

develop, however, under special circumstances. Such a case would arise where a pipe is subject to a torque preload during cure.

To maintain the compatibility requirements of the orthotropic elastic behaviour, additional residual in-plane shear stresses, $\tau_{x\theta}$, must exist at the meso-scale, between laminae of alternating fibre orientation. Over the wall thickness, these must still adhere to the zero-torque requirement, and comply with the strains governed by the bulk-scale orthotropic behaviour. The magnitude of these stresses can be estimated by applying Eq. (4.5), reproduced in Eq. (5.31), using the residual strains obtained from the orthotropic solution.

$$\begin{bmatrix} \sigma_x \\ \sigma_\theta \\ \sigma_r \\ \tau_{x\theta} \end{bmatrix} = \begin{bmatrix} \bar{C}_{11} & \bar{C}_{12} & \bar{C}_{13} & \bar{C}_{16} \\ \bar{C}_{12} & \bar{C}_{22} & \bar{C}_{23} & \bar{C}_{26} \\ \bar{C}_{13} & \bar{C}_{23} & \bar{C}_{33} & \bar{C}_{36} \\ \bar{C}_{16} & \bar{C}_{26} & \bar{C}_{36} & \bar{C}_{66} \end{bmatrix} \begin{bmatrix} \epsilon_x \\ \epsilon_\theta \\ \epsilon_r \\ \gamma_{x\theta} \end{bmatrix} \tag{5.31}$$

Since the stacking sequence changes with both axial and circumferential position, and is not known for any particular position within the pipe, the exact meso-scale shear stress distribution cannot be determined. The shear stress at any particular radial distance, for an assumed fibre orientation can, however, be calculated. In this sense, bounds of the meso-scale shear stresses can be found by calculating the stresses associated with both the $+\phi$ and $-\phi$ wind angles, over the entire thickness of the pipe.

It is also worth mentioning that should residual in-plane shear strains, $\gamma_{x\theta}$, exist over the wall thickness, the bounds of the meso-scale shear stresses will be altered to include the in-plane shear stresses associated with these strains. Also, the presence of these shear strains will alter the averaged residual axial, hoop, and radial stress distributions, because these are coupled with the shear strains at the meso-scale. The change in these distributions, however, would generally be small, since only a single shear-coupling term of the stiffness matrix, $\bar{\boldsymbol{C}}$, would affect each stress component. It is feasible, however, that the effect on these stresses will be significant, if a very large residual in-plane shear strain exists. This would cause the axial and hoop stresses to be discontinuous at the interface of each angle ply, but on average still follow the stresses determined using orthotropic material properties. Unfortunately the residual radial stresses would also be found to be discontinuous across each ply interface, which violates the equilibrium requirements of these stresses. The extent of this discontinuity is negligible, however, irrespective of the magnitude of the in-plane shear strain, since the shear coupling term $\bar{C_{36}}$ is always very small. For the material properties presented in Appendix F, the $\bar{C_{36}}$ term reaches the maximum value of 56.5 MPa, at a wind angle of $+45°$. The magnitude of this term is minute in comparison to the apparent radial stiffness, $\bar{C_{33}}$, of 9653.4 MPa, and the magnitude of the other shear coupling terms, $\bar{C_{16}}$ and $\bar{C_{26}}$, which are both 8413.2 MPa.

In this sense, the discontinuities in radial stress will be so small in comparison to the magnitude of the averaged radial stress distribution, that they will always be negligible and therefore the equilibrium requirements can always be considered satisfied.

6 Validation of current method

The current method of residual stress measurement extends the capabilities of the Sachs method, allowing the residual stresses within layered anisotropic pipes to be measured. This is a capability which to date, has not been achieved, and therefore this method must be validated. The following section deals with this issue. Since the current method is based upon the exact elastic solution, it can also be applied to pipes of isotropic and orthotropic nature. Application of this method to a thick-walled isotropic pipe is investigated, and the results obtained for simulated strain variations compared with those determined using the Sachs method [198]. The problem of a thin-walled orthotropic pipe is then considered, and the application of the current method to a pipe of this nature validated, by comparing the residual stresses obtained, again for simulated strain variations, with those determined using the method of Voyiadjis et al. [220]. A thick-walled orthotropic pipe is then considered, and the accuracy of the current method demonstrated. This is done by comparing the residual stresses obtained using this method, for the simulated strain variations, with those determined using FE analysis. The method of Voyiadjis et al. [220] is also considered for this problem, and the inaccuracies of this method in application to thick-walled orthotropic pipes demonstrated. Finally, the capabilities of the current method for the measurement of residual stresses within a relatively thick-walled, layered anisotropic pipe are demonstrated. Residual stresses associated with simulated strain variations are calculated, and validated by comparing them to those found using FE analysis. For all problems considered, 150 layers were simulated to be removed, and the residual stresses evaluated at the mid-radius of each layer. The resulting stress distributions presented in this section comprise splines fitted to these results.

6.1 Problem 1: Thick-walled isotropic pipe

For application of the current method to an isotropic pipe, the constant terms of Eqs. (4.9) to (4.11) are

$$\lambda = 1 \tag{6.1}$$

$$\Gamma = 1 \tag{6.2}$$

$$\Omega = 0 \tag{6.3}$$

Under these conditions, Eq. (4.24) becomes

$$\begin{aligned} F_x =& 2\pi \sum_{k=1}^{N} \Bigg[\left(\bar{C}_{11}^k + \bar{C}_{13}^k + \bar{C}_{12}^k \right) \epsilon_x^0 \left(\frac{r_k^2 - r_{k-1}^2}{2} \right) \\ &+ \bar{C}_{16}^k \gamma^0 \left(\frac{r_k^3 - r_{k-1}^3}{3} \right) + \frac{\left(\bar{C}_{12}^k + \bar{C}_{13}^k \right)}{2} A_1^k \left(r_k^2 - r_{k-1}^2 \right) \\ &+ \left(\bar{C}_{12}^k - \bar{C}_{13}^k \right) A_2^k \left\{ \ln(r_k) - \ln(r_{k-1}) \right\} \Bigg] \end{aligned} \tag{6.4}$$

All other equations presented for the exact elastic solution in Section 4 do not fundamentally change. The change of Eq. (6.4) does not affect the terms of the matrices of Eq. (5.2), which are used to find the A_1^k and A_2^k constants of the remaining pipe after layer removal. The Y_{32} term of Eq. (5.15) does change, however, and the new expression for this term is presented in Eq. (6.5).

$$Y_{32} = \left(\bar{C}_{12}^k - \bar{C}_{13}^k \right) \left\{ \ln(r_k) - \ln(r_{k-1}) \right\} \tag{6.5}$$

Applying these changes to the current method allows the residual stress distributions within an isotropic pipe to be found. The thick-walled pipe under consideration is assumed to have an internal diameter of 80 mm and wall thickness of 150 mm. This corresponds to a thickness-to-inner-diameter ratio $(t/d_i) = 1.875$. The material properties are assumed those of steel, with the Young's modulus, $E = 200$ GPa, and Poisson's ratio, $\nu = 0.3$. The strain responses on the inner surface, measured in the axial, circumferential and 45° directions, are assumed to vary linearly with the removal of layers from the outer surface of the pipe. These strain variations are illustrated in Fig. 6.1, and are plotted against the percentage (%) thickness removed.

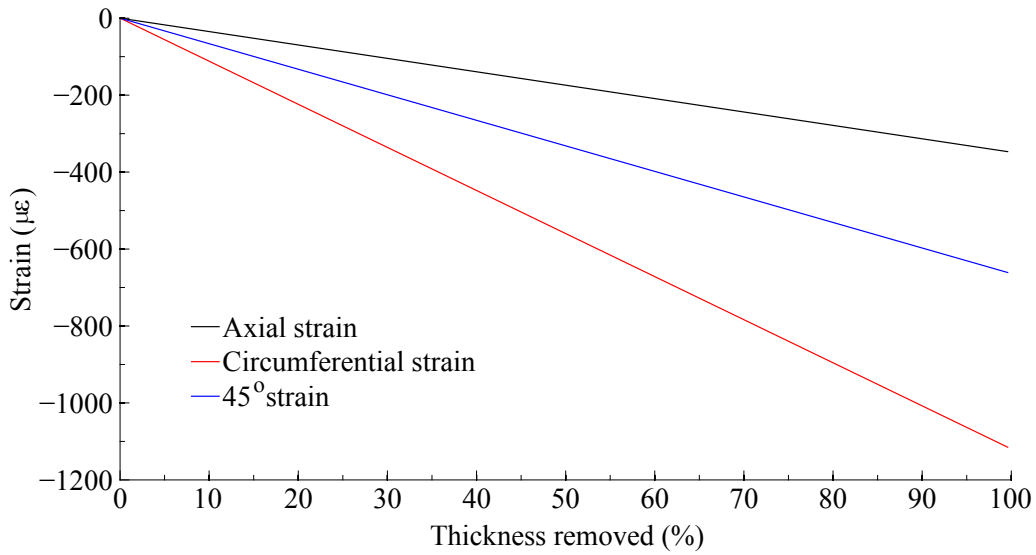

Figure 6.1: Assumed linear strain variations

The corresponding axial stress distribution, obtained using the current method, is presented in Fig. 6.2. Included in this figure are the stress variations determined using the method of Sachs [198], Voyiadjis et al. [220], and Rasty et al. [222]. The method of Rasty et al. [222] is also considered, because these authors presented equations for the calculation of hoop stresses within orthotropic pipes, that differ significantly from those presented by Voyiadjis et al. [220]. The stress distributions are plotted against the normalised through-thickness radial position, where the inner and outer surfaces correspond with -1 and 1, respectively. From this figure, it is clear that the stresses determined using method of Sachs [198], Voyiadjis et al. [220] and Rasty et al. [222] are identical to one another. This is an expected result, since the equations used by each of these methods, for calculating the axial stresses, are equivalent under isotropic conditions. This is demonstrated in Appendix C. More importantly, however, the axial stress variation obtained using the current method is indistinguishable from the stress distribution determined using the method of Sachs [198]. This distribution was integrated over the wall thickness of the pipe, and found to satisfy the zero-force requirement.

The corresponding hoop stress distribution, obtained using the current method, is illustrated in Fig 6.3. This is plotted together with the hoop stress distributions calculated using the equations of Sachs [198], the corrected equations of Voyiadjis et al. [220], which are presented in Appendix C, and those of Rasty et al. [222]. The stress distributions determined using the method of Sachs [198] and the corrected method of Voyiadjis et al. [220] are, as with the axial stress results, identical to one another. Once again, this is an expected result, since the equations of these two methods are equivalent for isotropic pipes.

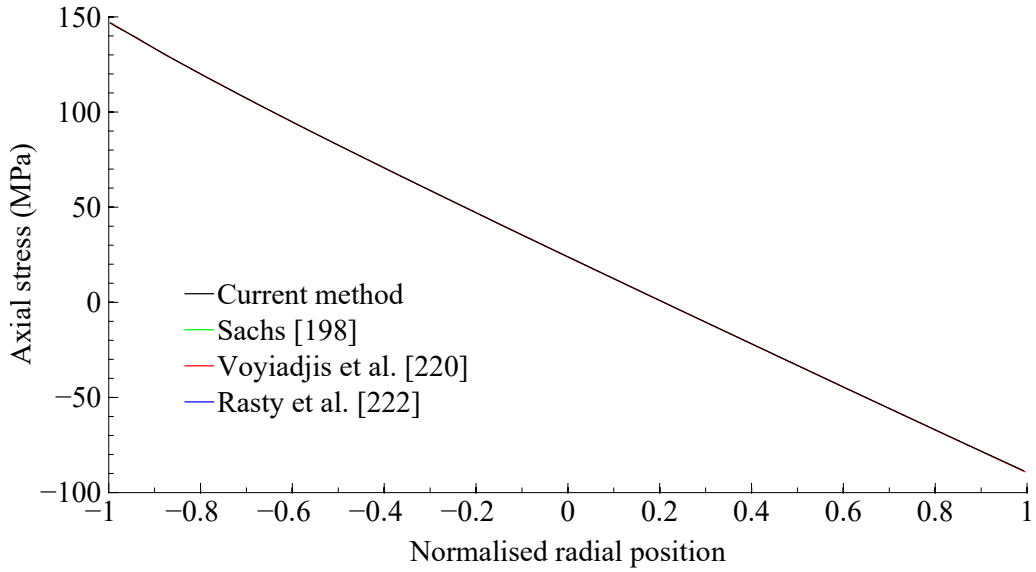

Figure 6.2: Axial stress distributions of the thick-walled isotropic pipe $(t/d_i) = 1.875$

This is demonstrated in Appendix C. The equation presented by Rasty et al. [222] for evaluating this stress, however, is not equivalent to that of Sachs [198] for isotropic materials, and it is for this reason that there is deviation in the hoop stress distribution obtained using this method. Considering the self-equilibrium requirement, which must be satisfied for any measured strain distribution, the method of Rasty et al. [222] is clearly erroneous. The stress distribution obtained using this method is evidently overly compressive, and does not adhere to the zero-force requirement. For this reason, the method of Rasty et al. [222] will not be considered beyond the problem of the thick-walled isotropic pipe. The residual hoop stress distribution determined using the current method is indistinguishable from those obtained using the methods of Sachs [198] and Voyiadjis et al. [220], and produces a zero-force resultant, when integrated over the wall thickness.

The radial stress distributions of the isotropic pipe are presented in Fig. 6.4. As demonstrated in Appendix C, the corrected equations of Voyiadjis et al. [220] and those of Sachs [198] used to calculate the radial residual stresses are equivalent when isotropic material properties are considered. Additionally, the equation presented by Rasty et al. [222] for obtaining these stresses is exactly the corrected equation of Voyiadjis et al. [220]. It is for these reasons that the distributions found by each of these methods are identical. More importantly, the radial residual stress distribution obtained using the current method is indistinguishable from these. This stress distribution is continuous through the wall thickness, and tends to zero at the inner and outer surfaces of the pipe, as required by equilibrium conditions. The residual in-plane shear stress distributions for the isotropic pipe are also presented in Fig. 6.4, and were obtained using the current method, that

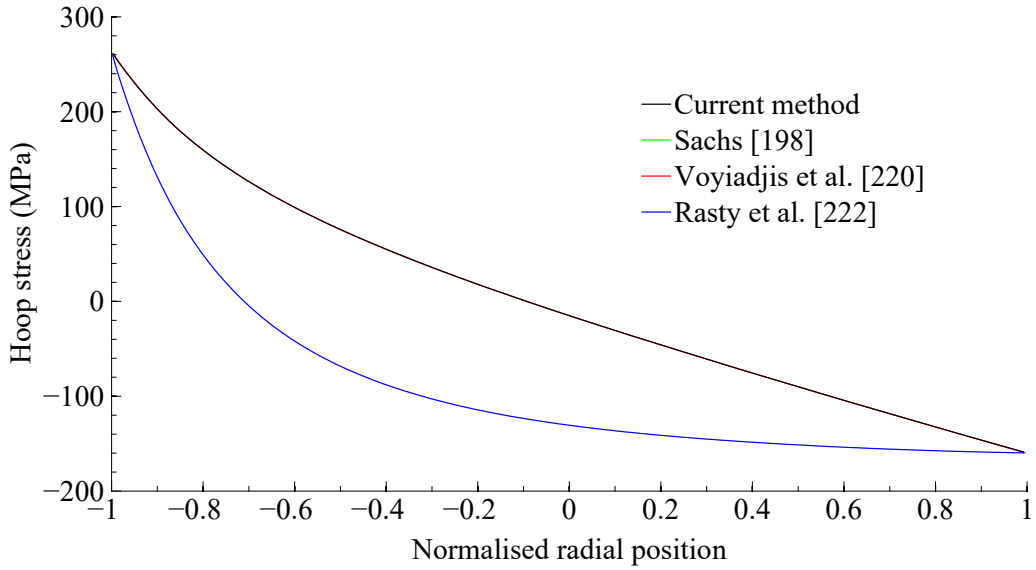

Figure 6.3: Hoop stress distributions of the thick-walled isotropic pipe $(t/d_i) = 1.875$

of Voyiadjis et al. [220], and that of Rasty et al. [222]. Since the equations of Voyiadjis et al. [220] and Rasty et al. [222] are identical, they produce the same residual shear stresses. The distribution produced by the current method is indistinguishable from these, and its moment about the centreline of the pipe, integrated through the wall thickness, produces a zero-torque resultant, thus satisfying the self-equilibrium requirement of this stress component.

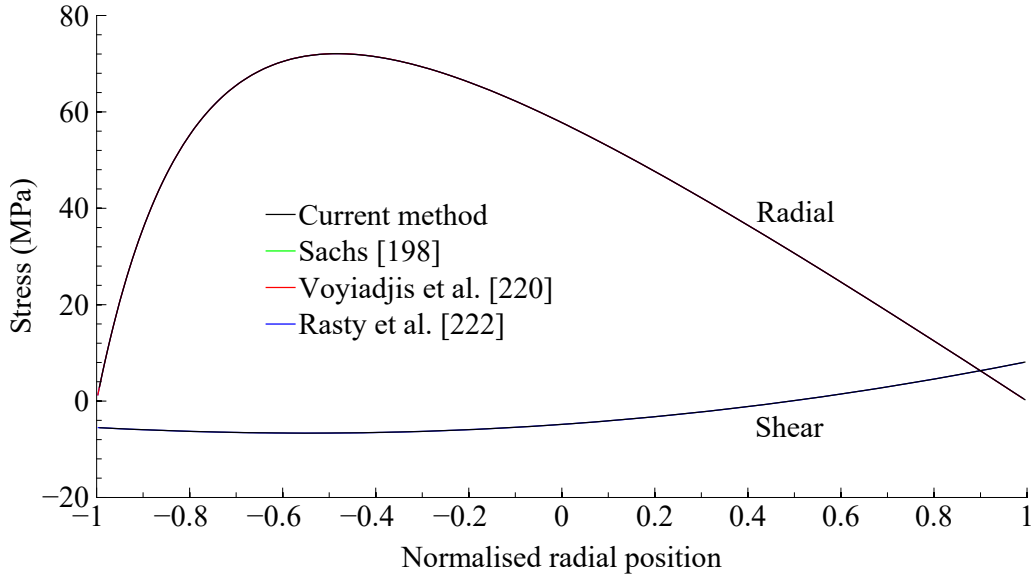

Figure 6.4: Radial and shear stress distributions of the thick-walled isotropic pipe $(t/d_i) = 1.875$

It is clear that the current method of residual stress measurement produces residual axial, hoop, and radial stresses that are identical to those determined using the method of Sachs [198]. This can most certainly be considered validation of the current method in application to isotropic pipes. Unfortunately, no solution to the in-plane shear stress distribution for the original Sachs method could be found, presumably because under normal circumstances, no such residual stresses would develop within pipes of this nature. The results of the current method for this stress component, however, are identical to those obtained using the method of Voyiadjis et al. [220]. This can be considered validation of the current method for measurement of these stresses within isotropic pipes.

6.2 Problem 2: Thin-walled orthotropic pipe

The thin-walled orthoropic pipe under consideration is assumed to have an internal diameter of 80 mm and wall thickness of 1.5 mm, corresponding to $(t/d_i) = 0.01875$. This (t/d_i) ratio is sufficiently small that the method of Voyiadjis et al. [220] can be considered valid. This issue is discussed in Appendix C. The strain variations utilised for this analysis are the linear variations used in the case of the thick-walled isotropic pipe, illustrated in Fig. 6.1. The material properties correspond with those of a $\pm 55^\circ$ filament-wound pipe, where the transformed stiffness matrix, $\bar{\boldsymbol{C}}$, is the average of those obtained for $+55^\circ$ and -55° wind angles. The result is an orthotropic stiffness matrix, with no shear coupling terms. The lamina material properties were estimated using micromechanics, as presented in Appendix A, with the matrix and fibre properties presented in Appendix F. The method of Voyiadjis et al [220] requires the equivalent Young's modulus and Poisson's ratios in the cylindrical coordinate system (r, θ, x). These were extracted from the transformed stiffness matrix of the material, using Eq. (A.2) of Appendix A. The resulting axial and hoop stress distributions, found using the current method and the corrected method of Voyiadjis [220], are illustrated in Fig. 6.5. These are plotted against the normalised radial position. It is clear from the figure that both the axial and hoop stress distributions obtained using the current method are virtually identical to those determined using the corrected method of Voyiadjis et al. [220]. Both stress distributions produce a zero-force resultant when integrated over the pipe wall thickness, and thus adhere to the requirement of self-equilibrium.

The resulting radial and in-plane shear stress distributions determined for the thin-walled orthotropic pipe are illustrated in Fig. 6.6. Both of these stress distributions, obtained using the current method, are indistinguishable from those calculated using the corrected method of Voyiadjis et al. [220]. The radial stress distributions, as required, are continuous through the pipe wall thickness, and tend to zero at the inner and outer surfaces. Also,

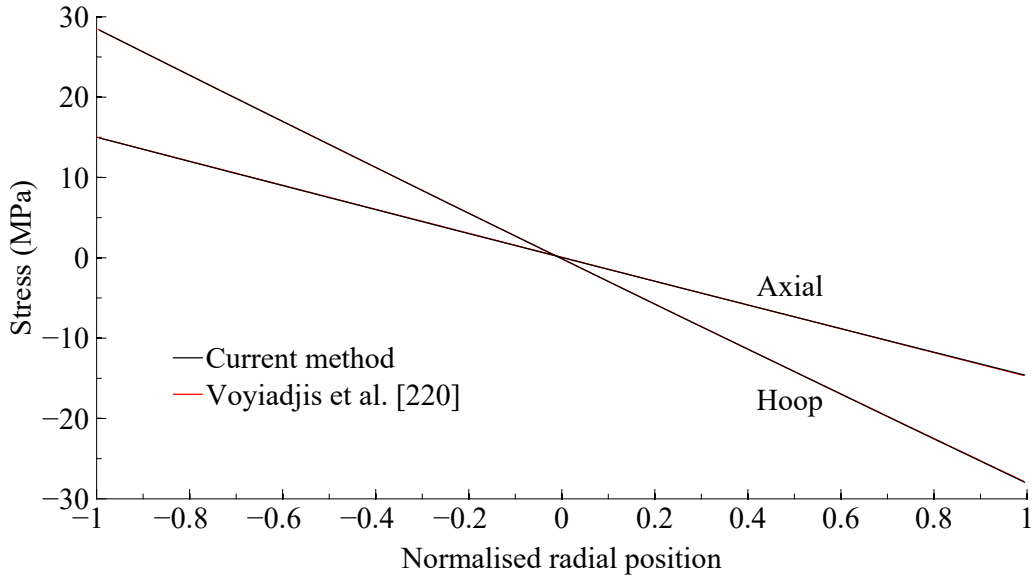

Figure 6.5: Axial and hoop stress distributions of the thin-walled orthotropic pipe $(t/d_i) = 0.01875$

the resulting shear stress distributions, integrated over the wall thickness, adhere to the zero-torque requirement.

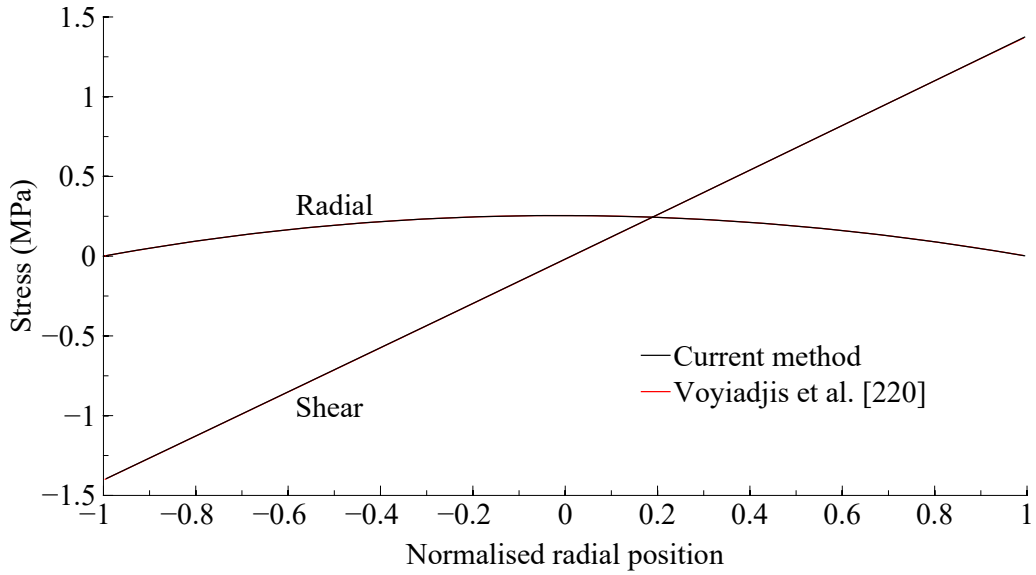

Figure 6.6: Radial and shear stress distributions of the thin-walled orthotropic pipe $(t/d_i) = 0.01875$

The virtually identical residual stress distributions of Figs. 6.5 and 6.6, obtained using both the current method and that of Voyiadjis et al. [220], validates the application of the current method to measurement of residual stresses in orthotropic pipes.

6.3 Problem 3: Thick-walled orthotropic pipe

The thick-walled orthotropic pipe under consideration is assumed to have the same geometric properties as that of the thick-walled isotropic pipe considered in Section 6.1. These are an internal diameter of 80 mm, and wall thickness of 150 mm. The orthotropic material properties are the same as those utilised for the thin-walled orthotropic pipe in the previous problem. The assumed variations in measured strain are, once again, those presented in Fig. 6.1. Due to the assumptions made by Voyiadjis et al. [220], their method will produce inaccurate stress distributions when applied to thick-walled pipes. This is discussed in detail in Appendix C. The resulting axial stress distributions determined using the current method and that of Voyiadjis et al. [220] are illustrated in Fig. 6.7. As expected, the axial stress distributions obtained using these methods are different to one another. Interestingly, the stress distribution determined using the method of Voyiadjis et al. [220] satisfies the self-equilibrium requirement, despite its anticipated inaccurate nature. The distribution determined using the current method also produces a zero-force resultant. It is worth noting that the solution of Voyiadjis et al. [220] approaches the solution of the current method toward the inner surface of the pipe. Since the simulated strains are equal to the negative of the residual strains at the inner surface, both solutions must tend toward the same residual stresses at this location. To demonstrate the accuracy of the solution of the current method, FE analysis was performed, simulating the layer removal process. This was done for six different radial locations through the thickness of the pipe. To find each datum point, three separate FE models were required. The first two were used to determine the residual load released by the removal of a particular layer m, which was simulated to be 1% of the wall thickness. The first FE model simulated the remaining pipe before the removal of layer m, and thus had the same outer diameter of this layer, and an internal diameter of 80 mm. Three separate load cases were generated, each corresponding to the application of unit axial, torque, and external pressure loads. The residual load released by the removal of all $m-1$ layers was found using the combination of results obtained from this model, and the simulated strain variations of Fig. 6.1. The second FE model simulated the remaining pipe after the removal of layer m, again with application of unit axial, torque and external pressure loads. The residual loads applied to the remaining pipe in this configuration, governed by the simulated strain distributions, were then found. The difference between the residual loads found for the second and first FE models is exactly the residual load released by layer m. These were calculated and applied to this layer in the form of a third FE model. The residual stresses obtained from this model, at the region of the mid-radius of layer m, are those included in Fig. 6.7. Further details of the FE models are presented in Appendix G. It is clear from Fig. 6.7 that the FE results are indistinguishable from the results obtained using the current method thus validating the solution of this method.

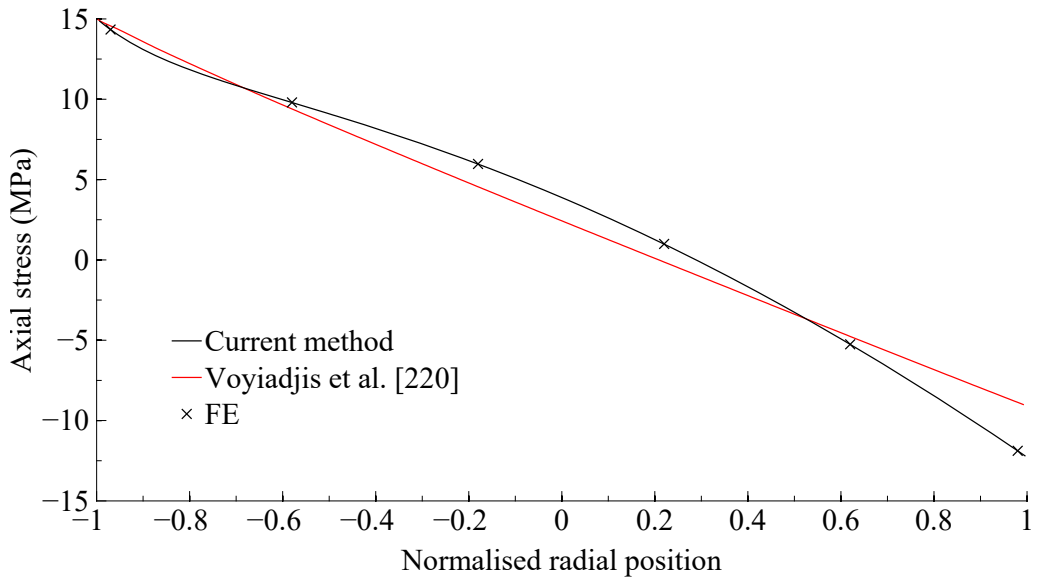

Figure 6.7: Axial stress distributions of the thick-walled orthotropic pipe $(t/d_i) = 1.875$

One might argue that the FE results would be the same as those of the current method, because the FE solution simulates the same calculation procedure for determining the residual stresses, and is therefore not a validation of the current method, but rather a validation of the equations of the exact elastic solution. This is somewhat true. However, comparison of the results of the current method against those of Sachs [198] for a thick-walled isotropic pipe, and against those obtained using the method of Voyiadjis et al. [220] for a thin-walled orthotropic pipe, validates the assumptions of the current method for determining the residual stresses in any removed layer m. Thus applying this approach to the FE simulations is also valid. The only question that remains, is the validity of the application of the exact elastic solution to thick-walled geometry. Since the solutions obtained using FE and the current method are the same, the use of the equations presented for the current method is valid.

The corresponding hoop stress distributions obtained using the current method and the corrected method of Voyiadjis et al. [220], together with those obtained by FE simulation, are presented in Fig. 6.8. As with the axial stress distributions of Fig. 6.7, the FE results are identical to the solution of the current method, validating these results. The stress distributions obtained using both the current method and the corrected method of Voyiadjis et al. [220] adhere to the self-equilibrium requirement. The solution of Voyiadjis et al. [220] is different to that of the current method, but these do approach one another toward the inner surface of the pipe, since both solutions must tend toward the negative of the measured stress at this location.

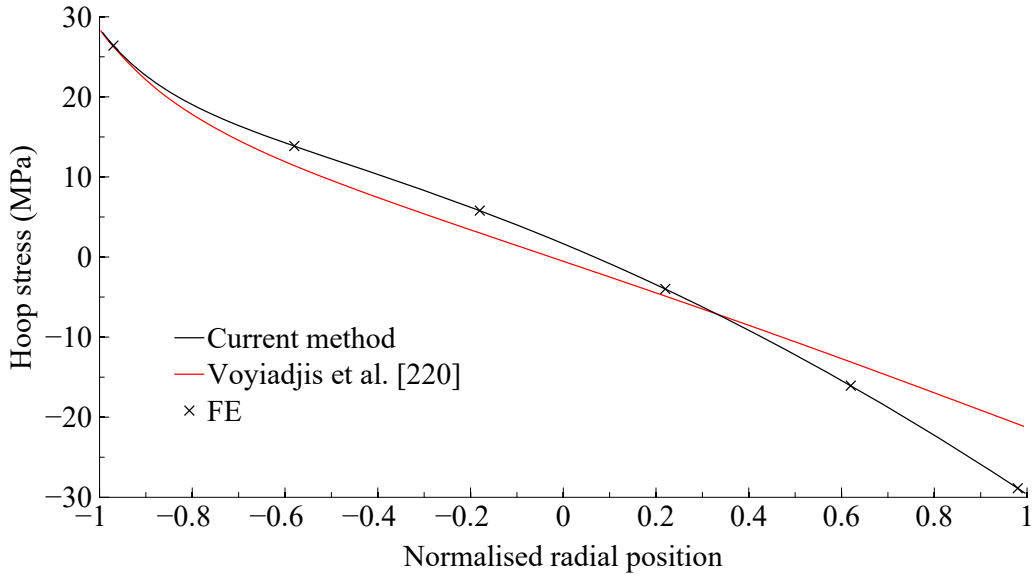

Figure 6.8: Hoop stress distributions of the thick-walled orthotropic pipe $(t/d_i) = 1.875$

The same behaviour is obtained for the radial stress distributions of the thick-walled orthotropic pipe. These distributions are presented in Fig. 6.9. The difference between the results of the current method and that of Voyiadjis et al [220] is expected, because the radial and hoop stresses are coupled via the relationship [220]: $\sigma_\theta = \frac{\partial}{\partial r}(r\sigma_r)$. The radial stresses determined using the corrected method of Voyiadjis et al [220] are therefore subject to the same assumptions that introduce the inaccuracies in the hoop stress distribution. Both methods, however, produce radial stress distributions that, as required, tend to zero at the inner and outer surfaces of the pipe, and are continuous over the wall thickness. Once again, the FE results are identical to those obtained using the current method, validating the application of the current method to measuring radial stresses within thick-walled orthotropic pipes. The shear stress results obtained using both the current method and the method of Voyiadjis et al [220], as well as those obtained from FE simulation, are indistinguishable from one another. These are also included in Fig. 6.9. The solution of Voyiadjis et al. [220] is therefore not erroneous, as with all the other stress distributions found using this method. This is an interesting result. The reason for this is that the assumptions made by these authors, with regard to the the response of a pipe to an applied torque load, aligns itself with the requirements of the exact elastic solution, that being a constant twist per unit length over the entire wall thickness [220, 224]. The erroneous results of the normal stress components, namely the axial, hoop, and radial stresses, do not affect the in-plane shear stress distribution, since the material is orthotropic and these stresses are therefore uncoupled from any shear stress components.

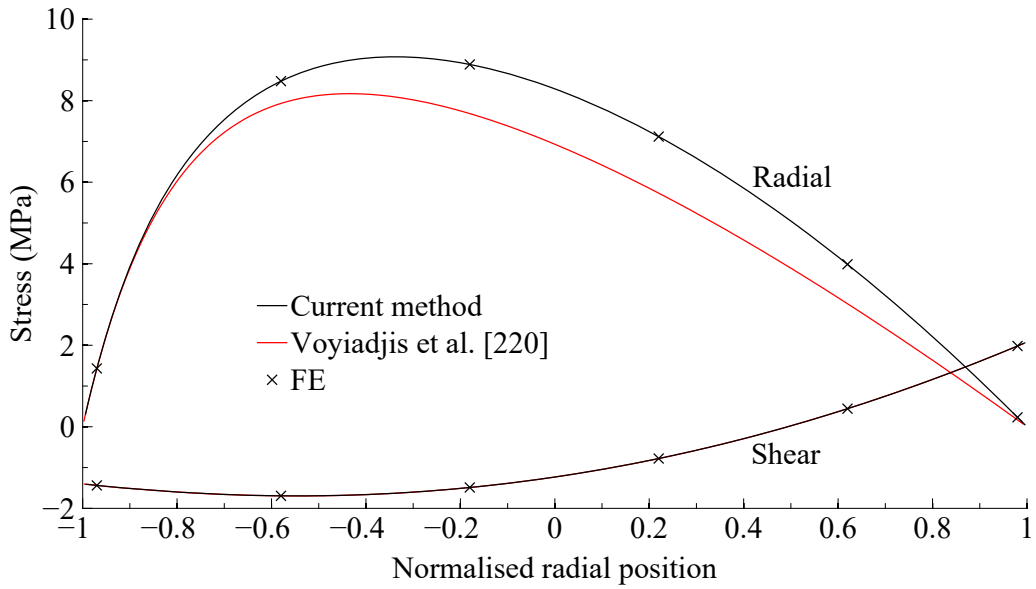

Figure 6.9: Radial and shear stress distributions of the thick-walled orthotropic pipe $(t/d_i) = 1.875$

6.4 Problem 4: Thick-walled anisotropic pipe

The purpose of this problem is to demonstrate the capability of the current method in application to layered, thick-walled anisotropic pipes, for which no solution has previously been presented. The pipe under consideration is moderately thick-walled, with an internal diameter of 80 mm and wall thickness of 15 mm, corresponding to $(t/d_i) = 0.1875$. The pipe was assumed to comprise two plies, each having a thickness of 7.5 mm. The fibre orientation was simulated to be $-45°$ and $+45°$ within the inner and outer plies, respectively. The material properties were taken to be identical to those presented in Appendix F. The simulated strain measurements, once again, are the linear variations presented in Fig. 6.1. The resulting axial and hoop stress distributions obtained using the current method, together with the results determined using FE simulation, are illustrated in Fig. 6.10. The FE simulations followed the same procedure as described for those of the previous problem, where three FE models were required to determine each datum point. The only difference between the models was the simulated geometry, and material properties. The results of the FE simulations are identical to those obtained using the current method. As previously discussed, the FE results do not validate the technique of determining the stress distributions through the wall thickness, since this is identical for both methods, but rather demonstrates that the current method implements exact elastic solution correctly when determining these stresses. Referring to Fig. 6.10, it is interesting to note that there exists a discontinuity in both the axial and hoop stress distributions in the region of the ply interface. Since the inner and outer plies both have the same

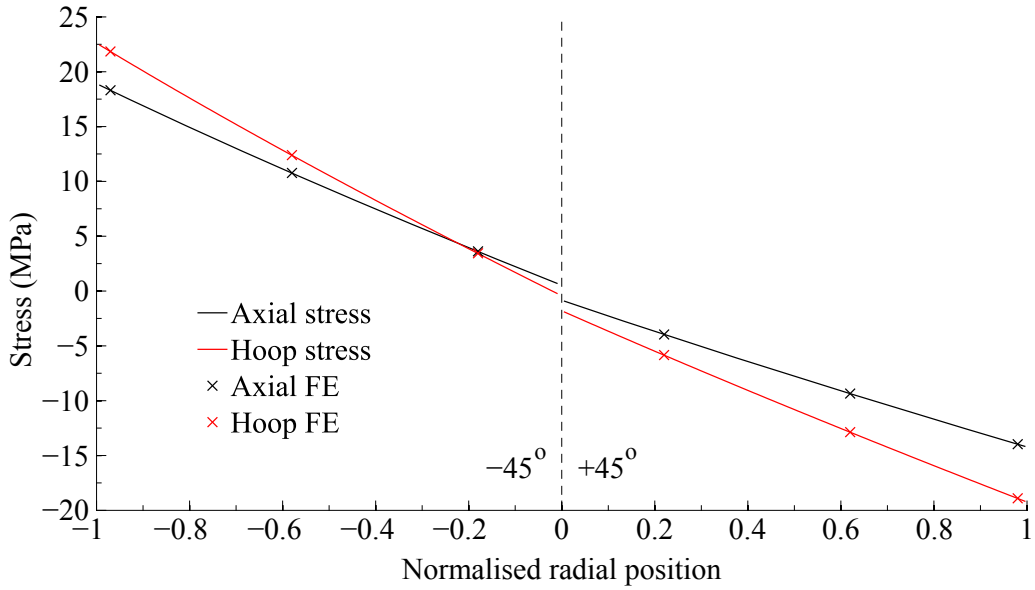

Figure 6.10: Axial and hoop stress distributions of the thick-walled anisotropic pipe $(t/d_i) = 0.1875$

apparent axial, circumferential, and radial stiffness, and the strain variations do not have discontinuous slopes in the region corresponding to material removal at the ply interface, this is a somewhat unexpected result. The reason for these discontinuities lies in the shear coupling terms of the transformed stiffness matrix, $\bar{\boldsymbol{C}}$, of each ply, which are equal and opposite to one another. These produce an opposing effect due to the presence of shear strain in the region of the ply interface, resulting in discontinuities in these stresses for this region. Should the shear strain response have been zero, no discontinuities in these stresses would exist. As expected, the resulting axial and hoop stress distributions produce a zero-force resultant when integrated over the wall thickness, thus adhering to the self-equilibrating requirement of residual stresses.

The corresponding radial and in-plane shear stress distributions obtained for the layered anisotropic pipe are illustrated in Fig. 6.11. As with the variations of Fig. 6.10, the radial and shear stress solutions of the current method are identical to those obtained by FE simulation. As is required, the radial stress distribution is continuous through the thickness, and tends to zero at the inner and outer surfaces of the pipe. The resulting shear stress distribution is much larger in magnitude as compared to any of the previous shear stress distributions, seen in Figs. 6.4, 6.6 and 6.9, which were obtained for the same strain variations. Also, the shear stress distribution of Fig. 6.11, is discontinuous at the region of the ply interface. As with the axial and hoop stress solutions of Fig. 6.10, this result is somewhat unexpected, since the apparent shear moduli of both plies are identical, and no discontinuous slope in strain response is simulated. The reason for these

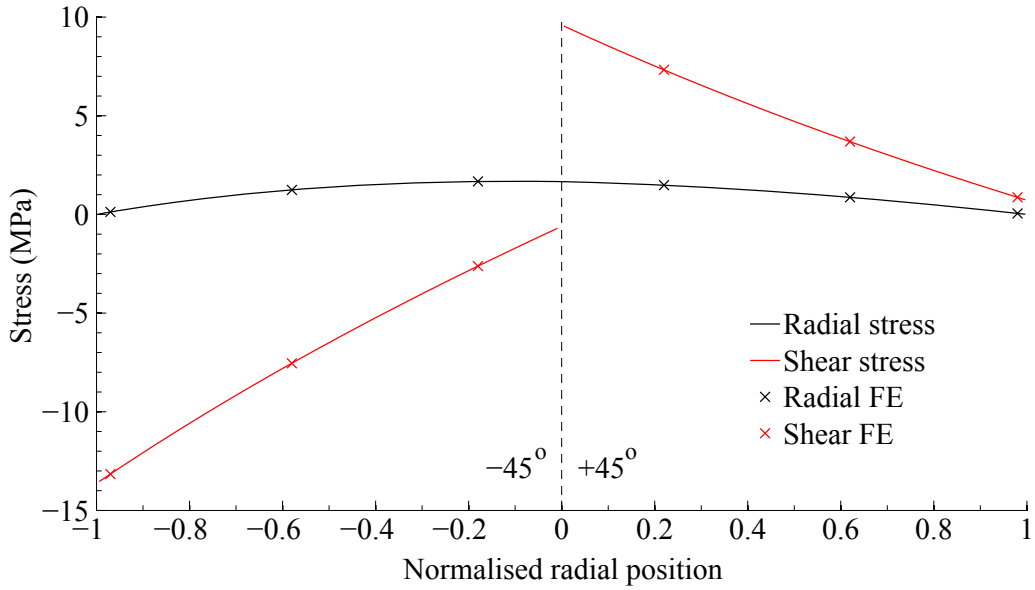

Figure 6.11: Radial and shear stress distributions of the thick-walled anisotropic pipe $(t/d_i) = 0.1875$

results lies, once again, with the shear coupling terms of the transformed material stiffness matrix, $\bar{\boldsymbol{C}}$, of both plies. As has been discussed, these coupling terms are the cause of the discontinuities that arise in the stress distributions of Fig. 6.10, associated with the simulated shear strain response. In the same manner, these opposing shear coupling terms account for the effect of the axial and circumferential strain responses, thereby increasing the magnitude of the shear stress distribution, as well as causing it to be discontinuous at the region of the ply interface. Additionally, this discontinuity is not symmetrically located relative to the line of zero shear stress, and this is associated with the presence of a non-zero shear strain response. However, the shear stress distribution still adheres to the self-equilibrium requirement, producing a zero-torque resultant when its moment about the centreline of the pipe is integrated over the wall thickness.

It is clear from this example that the current method can be used to accurately measure the residual stresses within layered anisotropic pipes. Although demonstrated only for two plies of exact opposing fibre orientation, the basis of the current method on the exact elastic solution allows for layered anisotropic pipes of any wall thickness, number of plies, and fibre orientation, to be measured. This is a capability which no previous extension to the Sachs method of residual stress measurement has demonstrated.

7 Materials and Experimental technique

For the experimental component of this work, the current method was utilised to measure the residual axial, σ_x, hoop, σ_θ, radial, σ_r, and in-plane shear stress, $\tau_{x\theta}$, distributions in three different filament-wound GFRP pipes. Layers were ground from the outer surface of each pipe and the in-plane strain responses measured on the inner surfaces. The strain data were then utilised to determine the through-thickness residual stress distributions that existed within each pipe, using the procedure outlined in Section 5. This section lists the material properties of the GFRP specimens considered for this work, the equipment required to perform the experiment, and also describes the experimental procedure and data recording processes followed.

7.1 Experimental equipment

7.1.1 Strain gauges

Measurement of the axial, ϵ_x, circumferential, ϵ_θ, and shear strain, $\gamma_{x\theta}$, responses at the inner surface of each specimen was required as material was removed from the outer surface. Triaxial Kyowa foil strain gauge rosettes of type KFG-5-120-D17-23 were utilised for this purpose. Fig. 7.1 illustrates a typical Kyowa KFG-5-120-D17-23 strain gauge rosette. As can be seen in this figure, the rosettes each contained three strain gauges, orientated at 0°, 45°, and 90°. Details of the gauges are listed below:

Nominal gauge length : 5 mm
Nominal resistance : 120 Ω
Gauge factor : 2.16 ± 1% (24°C, 50% RH)
Adoptable thermal expansion : 23.4 PPM/°C
Temperature coefficient of gauge factor : 0.008 %/°C

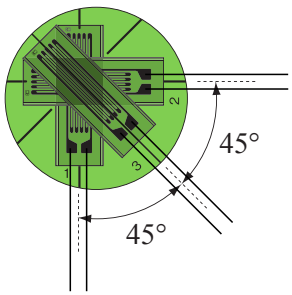

Figure 7.1: Kyowa KFG-5-120-D17-23 strain gauge rosette [234]

7.1.2 Temperature sensor

The strain readings for each layer removal were recorded in a somewhat temperature-stable room. For the purposes of thermal compensation of the strain readings, the room temperature over the course of the experiment needed to be measured. This was done by means of a LM35D temperature sensor. The sensor requires a DC power supply of between 4 V to 30 V, and the output signal is directly proportional to temperature, 10 mV/°C with a typical accuracy of ±0.5°C [235].

Calibration of the specific LM35D sensor utilised in the experiment was performed for improved accuracy of the measured values to ±0.1°C. Details of the calibration procedure of this sensor are provided in Appendix H. The resulting calibration equation obtained from this procedure is

$$T = 100.911 \times U - 0.580 \tag{7.1}$$

where T is the temperature in degrees Celsius, and U is the output reading of the sensor in volts. The excitation voltage supplied to the LM35D sensor was 10.0 V.

7.1.3 Data acquisition system

A National Instruments data acquisition (DAQ) system was used for both strain and temperature measurement during the course of the experiment. This was equipped with SCXI-1520 and SCXI-1521/B strain gauge cards. Both cards have built in Wheatstone bridge completion resistors, and supply an excitation voltage to the bridge. The DAQ system was powered through an uninterruptable power supply (UPS) to ensure any fluctuation in the 220 V AC power supply did not affect the measurements in any way.

The SCXI-1520 is a versatile card that has 8 channels, and allows connection of active

strain gauges forming either a quarter-bridge, half-bridge, or full-bridge configuration. The SCXI-1314 terminal block forms the interface connection between the strain gauges and the SCXI-1520, and this module houses the quarter-bridge completion resistors. The strain gauges were connected in the three-wire configuration. This set up is illustrated in Fig. 7.2. In this figure, the quarter-bridge completion resistor of the Wheatstone bridge is assigned the resistance value R_Q, which is the same as the nominal resistance of the active strain gauge, denoted by R_{gauge}, 120 Ω. The half-bridge completion resistors, denoted by the variable R, are located in the SCXI-1520 strain gauge card. These both have a nominal resistance of 5 kΩ. For the purposes of this work, the excitation voltage supplied to the Wheatstone bridge was set to 2.5 V. The SCXI-1520 strain gauge module can also be used to supply an excitation voltage, and measure the response of many other sensors. Consequently, this card was used to supply a 10.0 V excitation to the LM35D sensor, as well as measure the output voltage of this sensor.

The SCXI-1521/B strain gauge card is a 24 channel module, but only makes prevision for 120 Ω, quarter-bridge strain gauges to be connected. The SCXI-1317 terminal block forms the interface connection between the active strain gauges and the SCXI-1521/B strain gauge card. Unlike the SCXI-1314 module, the SCXI-1317 does not contain any bridge completion resistors. All of these are housed within the SCXI-1521/B strain gauge card, and these all have a nominal resistance of 120 Ω. The strain gauges measuring the pipe strain response were connected to the strain gauge card using the three-wire configuration. An illustration of this set-up is included in Fig. 7.2. As with the SCXI-1520/SCXI-1314 configuration, the excitation voltage across each Wheatstone bridge was set to 2.5 V. The SCXI-1520 and SCXI-1521/B strain gauge modules of the DAQ system also allow for onboard shunt calibration of each Wheatstone bridge, with internal shunt resistors of 100 kΩ. Gain factors are determined automatically during the calibration process. These factors are then used within the software on the computer attached to the DAQ system to determine the measured strain.

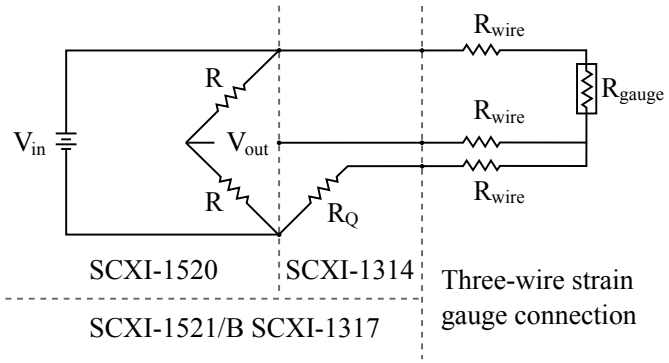

Figure 7.2: Three-wire connection of strain gauges to DAQ

7.1.4 Computer

A computer running National Instruments Labview 8.1 through Microsft XP was used to control the DAQ system, and store the measured data.

7.1.5 Cylindrical grinding machine

A Jones-Shipman 1305 EIT cylindrical grinding machine was used to grind off layers from the outer surface of each test specimen. Two steel end caps were manufactured to secure each specimen in the machine. The first of these was held in position with a four-jaw grip, attached to the drive of the grinder. The second end cap was supported in position using a tail-stock secured to the bed of the grinding machine.

7.1.6 Micrometer

A micrometer was used to measure the diameter of each test specimen before and after each layer removal. The micrometer allowed for measurements to a resolution of 0.01 mm to be made.

7.1.7 Fans and heaters

The strain responses were recorded in a fairly temperature-stable room. Fans were used to circulate the air within the room. Since the experiment took a number of weeks to complete, the stable room temperature in the room drifted over time. Temperature changes affect the output of any strain gauge, due to thermal expansion of the specimens, gauge factor shift, and changes in resistance of the strain gauges. Thermal compensation of the recorded strain data was thus required. To do this, the room needed to be heated and cooled a number of times during course of the experiment. Heater fans were used for this purpose. The procedure followed for the thermal compensation of the measured strain data is discussed in detail later within this work.

7.2 Materials and Specimen preparation

7.2.1 Filament-wound GFRP specimens

Three thick-walled filament-wound GFRP pipes were subject to experimental measurement. These were manufactured by GRP Tubing (Pty) Ltd of Somerset West, South Africa. The glass fibre used in the manufacture these pipes was E-glass, and the epoxy resin system was Epikote L 1100 with Epikure 294 curing agent. All pipes had an internal diameter of 80 mm, and wall thickness of 15 mm. The first of the pipes was wound entirely with the industry standard wind angle of $\pm 55^{\circ}$. The cure cycle consisted of curing the pipe at room temperature for a period of 12 hours, followed by 2 hours at 60°C. Postcure was then done at 80°C for a period of 8 hours. Once cured, the pipe was ground by the manufacturer to the desired wall thickness of 15 mm, and removed from the mandrel. The remaining two pipes comprised two plies, wound at different winding angles. The inner ply of each of the laminated pipes was 5 mm thick, and the outer ply 10 mm thick. The first of these pipes was wound at $\pm 65^{\circ}$ in the inner ply, and $\pm 47^{\circ}$ in the outer ply. The second of these pipes was wound at $\pm 75^{\circ}$ and $\pm 36^{\circ}$ in the inner and outer plies, respectively. These pipes were manufactured in two stages. The first stage consisted of winding the inner ply, then curing it in the same fashion as the $\pm 55^{\circ}$ pipe. Once cured the inner ply was ground to the desired thickness of 5 mm, followed by winding of the outer ply. The cure procedure was then repeated, and the overall wall thickness ground to 15 mm. Once this was completed, the pipe was removed from the mandrel.

Although the filament-wound pipes comprise laminae that form a lay-up that is anisotropic at the meso-scale, the stacking sequence arising from the winding process alternates with both circumferential and axial position, resulting in a pipe that can be considered orthotropic at the bulk scale. The measurement of the residual stresses within these pipes, therefore, does not call on the full capabilities of the current method, which is desired for demonstration purposes. Unfortunately, manufacture of a high quality, fully anisotropic thick-walled pipe is challenging, since it would need to comprise separate plies, each wound entirely with fibres orientated in a single particular direction. Due to these complexities, no such pipe could be sourced.

7.2.2 Material properties

The fibre volume fraction of the specimens was specified by the manufacturer to be within the range of 0.529 and 0.567. Due to the nature of the manufacturing method, the fibre volume fraction may vary through the thickness of filament-wound pipes. The degree of

this variation is highly dependant on the winding tension utilised during the manufacturing process. A variation in volume fraction will give rise to material properties that vary through the thickness of a pipe. Should the through-thickness variation in volume fraction be known, the elastic behaviour arising from the varying material properties can be simulated by discretising the pipe into many "plies", and reducing the thickness of the removed layers such that the volume fraction within each of these can be assumed constant. For the purposes of this work, however, the fibre volume fraction was assumed constant through the wall thickness of all of the specimens, and this was taken as 0.548, the mean value within the range specified by the manufacturer. Material properties of each of the specimens were estimated using the micromechanics procedure, presented in Appendix A. The properties of E-glass were taken directly from the ASM engineering materials handbook [236]. The property data sheet of the Epikote L 1100/Epikure 294 resin system [237] does not list the Poisson's ratio of the material, which is required to estimate the lamina material properties. For this reason the material properties of the resin were experimentally measured. This was done in accordance with the ASTM D 638 [238] standard test. The material properties of the E-glass, experimentally measured properties of the epoxy resin, and those obtained using micromechanics for a unidirectional lamina are listed in Appendix F. For the purposes of clarity, the material properties estimated for unidirectional GFRP are reproduced in this section, and are listed in Table 7.1. The transformed stiffness matrix, $\bar{\boldsymbol{C}}$, of a lamina rotated through any wind angle, ϕ, can be estimated from these properties, using the equations presented in Appendix A. As discussed in Section 5, due to the complex weave produced by the filament winding procedure, where the stacking sequence between $+\phi$ and $-\phi$ changes with both axial and circumferential position, for any specific radial position, the material properties of a ply within a filament-wound pipe can be considered orthotropic at the bulk scale. Under these conditions, the transformed stiffness matrix calculated for each $\pm\phi$ wind angle is the average of those determined for $+\phi$ and $-\phi$, and is thus does not contain any shear-coupling terms.

Table 7.1: Lamina material properties

Longitudinal modulus, E_1 (MPa)	40887
Transverse modulus, $E_2 = E_3$ (MPa)	7905
Shear modulus, $G_{12} = G_{13}$ (MPa)	2437
Shear modulus, G_{23} (MPa)	2855
Poissons ratio, $\nu_{12} = \nu_{13}$	0.298
Poissons ratio, ν_{23}	0.384

7.2.3 Specimen length

The required length of the test specimens used in the experiment was the subject of some investigation. In order for meaningful results to be obtained using the current method, the strain response of the mid-section of each specimen, where the strain responses were measured, needed to be free from edge effects. This has already been discussed in Section 5. To achieve this condition, the specimens needed to be fairly long. To determine the required pipe length, FE analysis was performed in the form of axisymmetric thermal models. Appendix I provides the details of these models. The FE simulations established that a pipe length of 220 mm was required such that the mid-section had reached far-field conditions, free of edge effects. This specimen length, however, is too long to be practical. Such a length would make it very difficult to access the mid-section on the inner surface of the specimen, to accurately align and bond the strain gauge rosettes. Additionally, this specimen length would make it quite difficult to solder the lead wires of the strain gauges. To address these issues, the length of pipe considered in the experiments needed to be reduced. A pipe length of 120 mm was found to allow for accurate strain gauge placement and alignment. It was also found that the mid-length of a specimen of this length would experience stresses within 5% of the desired far-field conditions of an infinitely long pipe. This accuracy was considered acceptable for the purposes of this investigation, and specimen lengths of 120 mm were consequently used. Specimens were cut from the filament-wound GFRP pipes using a band saw, and then faced using a lathe.

7.2.4 Strain gauge placement

After the test specimens were cut from the filament-wound GFRP pipes, each was carefully examined. None of the specimens contained any cracks and irregularities, and thus the analytical approach of the exact elastic solution of Section 4, is valid. The inner surface of each test specimen was lightly sanded with 300 grit sand-paper and cleaned with acetone. Three sets of strain gauge rosettes were bonded to the inner surface at the mid-length of each test specimen, located circumferentially at 120° to one another. This positioning is illustrated in Fig. 7.3. The three strain gauges within each rosette were orientated at 0°, 45°, and 90°, measured relative to the axial orientation. These were aligned in this sense so that the axial, circumferential, and in-plane shear strain responses could be measured directly. Lead wires were soldered to each gauge using Kyowa T-F3 gauge terminals, which were then bonded to the inner surface of the specimens.

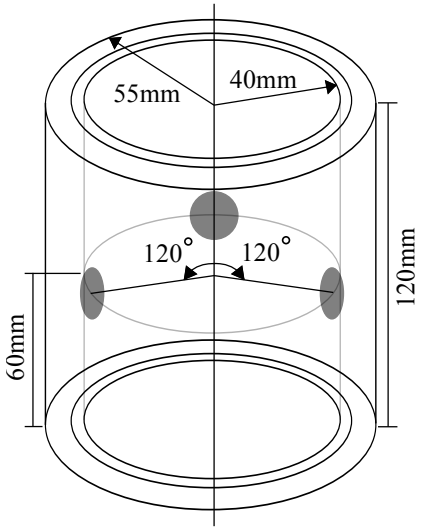

Figure 7.3: Test specimen geometry and strain gauge positioning

7.3 Experimental Procedure

A total of three specimens were considered for this investigation, one for each of the three pipe configurations. As has been mentioned, the experiment took a number of weeks to perform. Over this period, the stable temperature of the room, in which the strain readings were recorded, drifted due to changes in ambient conditions. This required that the strain data be temperature compensated so that only the mechanical strain response of the specimens to material removal could be determined. The following section describes the method of temperature compensation, and outlines the experimental procedure followed, as well as the precautions taken during the experimental process.

7.3.1 Temperature compensation

Although a three-wire quarter-bridge connection of the strain gauges to the DAQ system was utilised, changes in the stable room temperature affected the strain data recorded over the duration of the experiment. Since the quarter-bridge completion resistors of the Wheatstone bridges, to which each strain gauge was connected, took the form of onboard resistors housed within the SCXI strain gauge modules, instead of dummy strain gauges bonded to a GFRP substrate, the three-wire connection only compensated for changes in the lead resistances with temperature. The effect of temperature change on the recorded strain data is associated with factors such as thermal expansion of the test specimens, gauge factor shift of the strain gauges, as well as minor changes in strain gauge resistance,

since this would most certainly not be the same as the change in resistance of the quarter-bridge completion resistors with temperature. Even if dummy strain gauges were used to compensate for these effects, temperature compensation of the strain data would still be required. Although the coefficient of thermal expansion of the GFRP material on which the active and dummy strain gauges would be bonded to would be the same, the geometry change of a specimen with the removal of material alters the elastic response of the specimen to temperature variations. This change in thermo-mechanical behaviour is associated with the cylindrical nature of the pipes, and would be most prominent in the layered specimens since, with the removal of material, the thickness of the outer and inner plies, relative to one another, would change drastically, thereby significantly altering the average through-thickness material properties of the specimens. One might argue that the temperature response measured by the dummy gauge can match that of the active strain gauge simply by matching the geometries of the GFRP to which the these gauges are bonded. This would, however, require removal of material from the inactive GFRP, thereby releasing residual stresses, inducing a mechanical strain response at the dummy gauge. Assuming that the the residual stresses released for both the test specimen, and inactive GFRP are the same, the strain induced at the dummy gauge would completely cancel out the strain response measured by the active strain gauge bonded to the test specimen. Replacing the dummy gauge after the removal of material is also not an option, since the resistance of any individual gauge will be slightly different from the next, and the bonding process of the new dummy gauge will also slightly alter the resistance of this gauge, affecting the output of the Wheatstone bridge. Unless strain readings are recorded in an accurately temperature controlled environment, it is clear that the requirement for temperature compensation of the measurement data cannot be avoided.

The process of temperature compensation employed in this work is relatively simple, and required the strain response of each gauge, with changes in temperature, to be measured. This was done by heating the room by means of fan heaters, recording the strain change between the elevated and normal room temperatures. To account for the change in thermo-mechanical behaviour of the specimens with material removal, the procedure of measurement of the strain response with temperature was performed weekly, over the course of the experiment. From these results "fictitious" coefficients of thermal expansion (CTE) were determined. These are referred to as "fictitious" since they not only include the thermo-mechanical response of the pipes, but also account for the minor changes in gauge factor, as well as resistance changes of the strain gauges and bridge-completion resistors with temperature. These fictitious CTEs were plotted against the amount of material removed to which they correspond, and least squares polynomials fitted over the full range of material removal. These polynomials allowed estimation of the fictitious CTEs for removal of any number of layers. From these, all of the measured strain data of each strain

gauge were referenced to the same temperature. A temperature of 20°C was chosen as a reference temperature. The final step in the thermal compensation procedure was to zero the compensated strain response with respect to the strain corresponding to no material removed. Appendix J provides an example of how the thermal compensation was done.

7.3.2 Method

The experimental method outlined in this section is described for a single specimen. This procedure was followed for each pipe configuration, and the experiment was performed concurrently on all three specimens. Before the experiment commenced, the strain gauges of the specimen were soldered to the DAQ system, and shunt calibration performed once strain readings stabilised with room temperature.

The outputs from the strain gauges and temperature sensor were recorded at room temperature for a period of 5 min, at 1 s intervals. The recorded values for each gauge were averaged over this period.

The fan heaters were then switched on, and left to heat the room. After a period of at least 14 hours, output strains of each gauge were recorded together with the temperature readings. The change in strain measurements resulting from the heating of the room allowed for temperature compensation to be implemented at a later stage.

The heaters were turned off, and the temperature of the room allowed to stabilise for at least 24 hours.

The specimen was unsoldered from the DAQ system.

The outer diameter of the specimen was measured using the micrometer. Three measurements were taken, and the average value assigned as the actual specimen diameter.

The strain gauge lead wires were tucked into the inner cavity of the specimen and it was then secured into the cylindrical grinding machine, by means of the steel end caps.

Roughly 0.3 mm of the wall thickness of the specimen was ground off, in increments of 0.025 mm. The specimen was then removed from the cylindrical grinding machine.

After removing the steel end caps from the ends of the specimen, the strain gauge lead wires were soldered to the DAQ system, with each strain gauge connected to the same channel as before.

The specimen was left in the room for a period of 6 hours, to ensure that the output strains had stabilised with the room temperature.

The measured strain values and temperature were recorded and the experimental procedure repeated.

Each day, an average of two layers were removed. The procedure of heating the room and measuring the strain change with temperature was done each weekend. In this sense, the change of strain with temperature every 10 removed layers was recorded.

The experimental procedure was stopped once the wall thickness of the specimen reached roughly 0.6 mm, and it became increasingly fragile.

After measuring the final specimen diameter, strain measurements for the final grind were taken at both room, and elevated temperatures.

The sections of material upon which each strain gauge rosette was bonded was then removed from the remaining pipe. This was done by cutting through the rest of the wall thickness, parting-out the strain gauges. A diamond coated disk on a Bridgeport vertical milling machine was used for this purpose. This procedure released the remainder of the residual stresses within the specimen.

The final strains were recorded, at both room and elevated temperatures.

7.3.3 Precautions

It must be ensured that the strain data has stabilised with the room temperature. For this reason, strain data was recorded every minute over the entire time from soldering the gauges to the DAQ system, to the point at which the experimental data was recorded. This allowed the stabilising time to be determined. This was checked for each removed layer. Only once the readings were stable, was the experimental data recorded. The time for the output readings to stabilise was found to be around 6 hours after gauges were soldered to the DAQ system after layer removal, 12 hours to stabilise when heating the room with the fan heaters, and 24 hours to stabilise after turning the heater fans off for the room to cool.

Generally, the DAQ system would need to be left on for a reasonable period of time, to ensure it is fully warmed up for recording the experimental data. Since it was continuously on, recording data from the point of soldering to the point of recording the actual experimental data, this was not an issue.

Ensure that each strain gauge is connected to the same channel of the DAQ system after each layer removal. The shunt calibration performed for each strain gauge was unique to each channel. Also, the quarter-bridge completion resistors in the SCXI strain gauge cards have a slightly different resistance for each channel. Swapping the strain gauges connected to a specific channel would result in completely inaccurate measurements.

Grinding forces should be kept to a minimum, to ensure the specimen does not reach a temperature where significant machining stresses are induced. Grinding increments of 0.025 mm from the specimen wall thickness was chosen to minimise the grinding forces applied to the specimen, as well as minimise the heat generated by the grinding process. The maximum temperature seen by the specimen during grinding was in the region of about 42°C, well below the maximum cure temperature of 80°C. Under these conditions machine-induced stresses can be considered negligible. Grinding temperatures were measured using a FLIR T640 thermal imaging camera. Appendix K provides a description of the procedure followed to obtain this result.

7.3.4 Estimation of measurement error

Initially, the errors in the measured data were estimated by considering the measured fictitious CTEs and the temperature at which each measurement was recorded. For any particular strain gauge, the maximum difference between the polynomial fitted to the measured CTE distribution and an actual measurement was determined. The maximum error for each datum point was then found by multiplying this maximum difference in CTE by the difference in temperature at which each datum point was measured, and the temperature of 20°C to which all of the strain data was referenced during the process of temperature compensation. Throughout the remainder of this text, the temperature compensated strain data is referred to as the "measured" strain data. The initial estimated measurement errors, were smaller than 5 $\mu\epsilon$ for all specimens.

Unfortunately the scatter in strain measurement about the polynomial fits was significantly larger than this value for all of the strain distributions. A major source of this scatter is directly associated with the manner in which the experiment was performed. To allow the layers to be removed from the specimen, the strain gauges were disconnected from the DAQ system, and reconnected after each layer removal. Since the gauges were connected as quarter-bridge active gauges, the connections between the each gauge and the DAQ system fell within the Wheatstone bridge. Although the these were always soldered, there were clearly still resistance changes associated with each removal and connection. These resistance changes registered as strains, amplified by the Wheatstone bridge, resulting in scatter. It is very difficult to quantify the error associated with each connection, since the

resistance change would be different for each connection. In this sense, true measurement errors could not be determined. These errors, however, are a significant component of the scatter in the measured data, and are therefore taken into account in the uncertainty analysis by considering the differences between the measured data and the corresponding polynomial fits. A far better way of measurement, which unfortunately was not followed, is to connect the strain gauges as full-bridge connections to the DAQ system, thereby limiting the impact of the resistance change with each connection. This could be implemented by still having a single active gauge, with the three remaining dummy gauges making up the remainder of the Wheatstone bridge, taking the form of precision resistors, located within the cavity of the specimens.

8 Results and Discussion

The measured strain response of each of the three strain gauge rosettes on each of the three specimens is presented in this section. The least-squares polynomials fitted to each data set are also presented on the same axes. The resulting residual stress distributions determined using the current method are also presented in this section. These comprise splines fitted to the stresses evaluated at the mid-radius of each removed layer, using the polynomials fitted to the measured strain variations. The stresses were obtained using MATLAB software. The stress distributions all include error bars, based upon the difference between the polynomial strain fits, and the measured data of each removed layer. Also included in this section are figures illustrating the bounds of additional residual shear stress that must exist, a consequence of the meso-scale anisotropy associated with the filament-wound nature of the pipes. Unfortunately only the bounds can be determined, since the stacking sequence at any particular location is not known.

8.1 $\pm 55^{\circ}$ Filament-wound pipe

8.1.1 Measured strain response

The measured axial, circumferential, and 45° strain responses of the $\pm 55^{\circ}$ filament-wound specimen are presented in Figs. 8.1 to 8.3. Three sets of measurements are presented in each figure, corresponding to the three strain gauge rosettes bonded to the inner surface of the specimen. For clarity these are defined as "Gauge set A", "Gauge set B" and "Gauge set C". All measured strains are plotted against percentage (%) wall thickness removed. The final data points of each gauge set, assigned to 100% material removal, are the strains measured after the parting-out of the strain gauge rosettes, once the layer removal process was terminated. Although the material thickness was roughly 0.6 mm at this point, it is assumed that the parting-out of the gauges released the remaining residual stresses within the specimen. Under these circumstances, the measured strains as a result of the parting-out are exactly the negative of the residual strains that existed

at the inner surface of the specimen, thus equating to the removal of 100% of the wall thickness. Included in these figures are the least-squares polynomials fitted to each data set, which where used to determine the residual stress distributions. The order of these polynomials were chosen to be as low as possible, but high enough that the trends in measured strain data were sufficiently described. This was done to ensure as little waviness in the resulting stress distributions as possible; waviness which develops as a consequence of the measurement scatter. For all strain responses, the scatter of the measured data about the polynomial fits increases with the amount of removed material.

The polynomials fitted to the axial strain data of all of the strain gauge rosettes of Fig. 8.1 were all limited to 3rd order, and these were forced to pass through the value of zero strain at 0% of the thickness removed. It is clear from the figure that the polynomial fits of "Gauge set A" and "Gauge set C" are in excellent agreement with one another. The polynomial fit of "Gauge set B", however, is significantly different from these in two distinctive regions. These regions correspond with between roughly 5% to 35% and between 80% to 100% thickness removed, and indicate a level of discrepancy between the measured results of this gauge set to the other two gauge sets. For the region of 80% to 100% thickness removed, it is clear that the divergence of the trend in the strain response of "Gauge set B" from those of the other gauge sets cannot be attributed to measurement error alone. This behaviour is quite strange, and would not be expected to occur in a completely orthotropic pipe. Such a pipe would most certainly contain residual stresses that are axisymmetric, and thus the strain response of each gauge set would share identical trends. In reality the pipe is not geometrically axisymmetric at the meso-scale, owing to the filament-wound construction and non-homogeneous nature of the material from which the pipe is made. Thus the residual stresses that develop, although self-equilibrating, are not truly axisymmetric. Release of these somewhat non-axisymmetric residual stresses affect the measured strain response of each gauge set slightly differently, resulting in different trends in strain response. This behaviour is also somewhat amplified through the decrease in what can be referred to as the level of orthotropy of the pipe, as the wall thickness of the pipe decreases with removal of material. Consider the construction of a filament-wound pipe; the wall thickness is made up of a complex weave of laminae oriented at $+55^{\circ}$ and -55°, in a stacking sequence that alternates with axial and circumferential position. As the wall thickness is reduced, the number of laminae above any particular gauge set reduces, and the relative thickness of a single lamina to the overall wall thickness increases. In this sense, the effect that a single lamina, oriented at either $+55^{\circ}$ of -55°, becomes more significant as the wall thickness of the pipe decreases. It can be said that the level of orthotropy local to any strain gauge position decreases, and affects each strain gauge rosette differently, since the lamina stacking sequence above each rosette is different. This mechanism is also most likely the cause of the increase in measurement scatter as

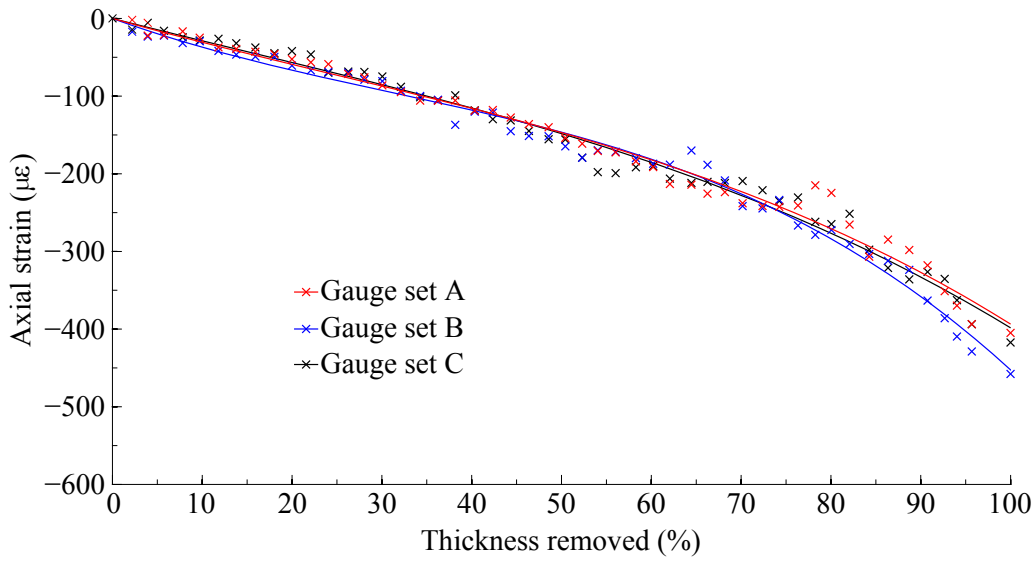

Figure 8.1: Measured axial strain response of the ±55° specimen

the number of layers removed from the pipe increases. Owing to this effect, the maximum difference in magnitude between any of the measured results occurs at 100% material removed, with a value of just less than 60 $\mu\epsilon$ between "Gauge set A" and "Gauge set B".

Polynomials of 3rd order were fitted to the circumferential strain data measured for "Gauge set A" and "Gauge set B" of the ±55° specimen, illustrated in Fig. 8.2. It was found that a 2nd order polynomial sufficiently described the measured circumferential data of "Gauge set C". The polynomials were all forced through zero strain for 0% thickness removed. When compared to the axial strain measurements of Fig. 8.1, it appears that the scatter in the measured circumferential data is smaller. This is, however, purely due to the difference in magnitude of the measured data of the two directions. The scatter also increases with the amount of material removal, as a consequence of the local anisotropic effects which result due to the lowered level of orthotropy. In general the trends in measured strain data of all of the gauge sets are the same, and it appears that these are relatively insensitive to the release of the non-axisymmetric residual stresses associated with the non-homogeneous nature of the material from which the pipe is made. The reason for this may lie in the circumferential stiffness of the pipe which, on average, is about twice that of the axial stiffness for the ±55° wind angle. Therefore small variations in the residual stress distribution around the circumference of the pipe, when released, are likely not large enough to significantly alter the trends in measured circumferential strain about the inner surface of the pipe. The polynomial fits of "Gauge set A" and "Gauge set B" are in excellent agreement for the first 50% of the thickness removed. Between 0% and 30% thickness removed, however, the polynomial fit of "Gauge set C" is slightly different to these, likely owing to the difference in the order of the polynomial fits. From removal

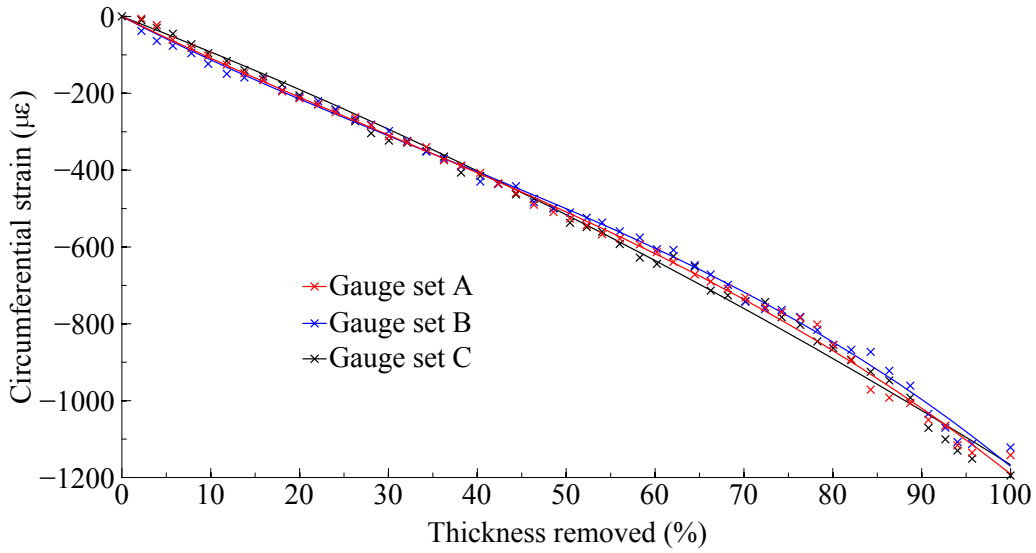

Figure 8.2: Measured circumferential strain response of the ±55° specimen

of roughly 50% to 100% of the thickness, the polynomials fitted to the measured data of "Gauge set A" and "Gauge set B" follow the same trends, but are slightly offset from one another. The trend of "Gauge set C" is slightly different from these, but approaches a very similar value in strain for 100% material removed.

The measured 45° strain responses of "Gauge set A" and "Gauge set B" required 3rd order polynomials to be fitted. "Gauge set C", however, required a polynomial of 4th order to adequately fit the measured strain data. These are illustrated in Fig. 8.3. As with the polynomial fits of the axial and circumferential variations of Figs. 8.1 and 8.2, these polynomials were forced to pass through zero strain for 0% of the wall thickness removed. There is a clear difference in the trends in the response measured by each gauge set, more so than the differences in trends encountered in the strain variations of Fig. 8.1. Additionally, there is increased divergence between the trends of each gauge set with increased removal of material. The largest difference between the polynomial fits occurs in the region of roughly 85% thickness removed. The magnitude of this difference is about 150 $\mu\epsilon$, and occurs between the polynomial fits of "Gauge set A" and "Gauge set C". The likely cause of the differences in the measured trends is, as previously discussed, associated with the non-homogeneous nature of the material from which the pipe is made, resulting in residual stresses that are not truly axisymmetric. In addition to scatter in the measured data, there appears to be a distinct waviness in the measured 45° strains about each of the polynomial fits, which are not as noticeable in the measured axial and circumferential strain distributions. For each gauge set, the amplitude of the waviness also increases with the amount of material removed, and is most noticeable in the measured strain distribution of "Gauge set C". It is believed that this waviness results due to the

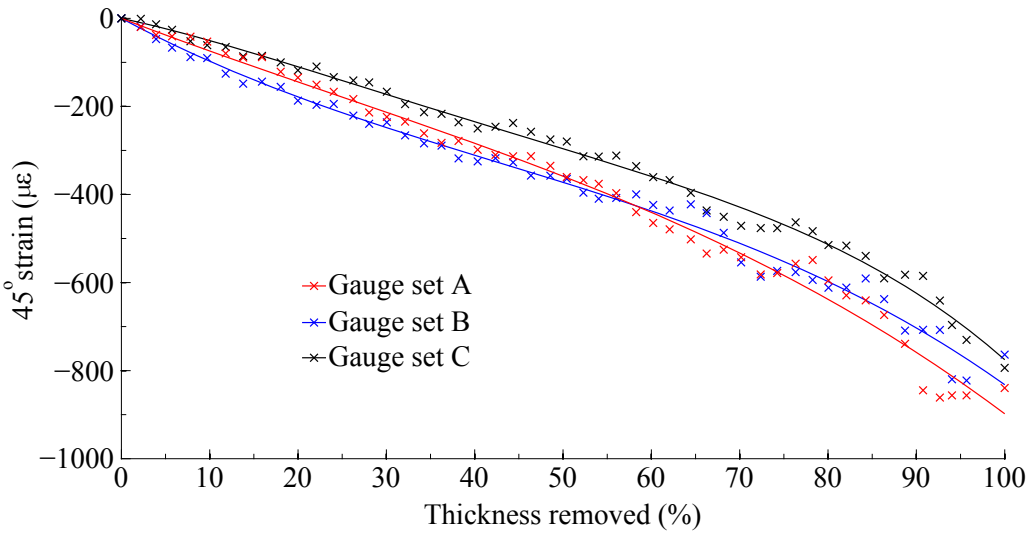

Figure 8.3: Measured 45° strain response of the ±55° specimen

release of the additional meso-scale residual shear stresses, which exist as a consequence of the material anisotropy. For the removal of each layer, almost certainly more material oriented at either +55° or −55° is removed at any particular location. This is a consequence of the spatial aliasing arising from the thickness of each removed layer versus the distance over which the weave pattern repeats. In this sense, the equilibrating meso-scale shear stresses are not released as fully-equilibrating stresses, and thus a residual torque load is applied to the remaining pipe section. This torque load would alternate, as the stacking sequence of the plies alternates, generating a waviness in the strain response. This effect is amplified by the ever decreasing level of orthotropy above each gauge set with increased material removal.

8.1.2 Residual stress distributions

The axial stress distributions of the ±55° pipe, evaluated using the polynomial fits of Figs. 8.1 to 8.3, are illustrated in Fig. 8.4. The error bars estimated using the method described in Section 5 are included in this figure. The stress distributions are plotted against the normalised radial position and comprise splines fitted to the axial stresses evaluated at the mid-radius of each removed layer. The final stresses at the inner surface of the pipe were calculated assuming a state of plane-stress after the parting-out of the strain gauge rosettes. The constitutive equations of an orthotropic material under this condition are [224]:

$$\begin{bmatrix} \sigma_x \\ \sigma_\theta \\ \tau_{x\theta} \end{bmatrix} = \begin{bmatrix} \bar{Q}_{11} & \bar{Q}_{12} & 0 \\ \bar{Q}_{21} & \bar{Q}_{22} & 0 \\ 0 & 0 & \bar{Q}_{66} \end{bmatrix} \begin{bmatrix} \epsilon_x \\ \epsilon_\theta \\ \gamma_{x\theta} \end{bmatrix} \tag{8.1}$$

where

$$\bar{Q}_{ij} = \bar{C}_{ij} - \frac{\bar{C}_{i3}\bar{C}_{3j}}{\bar{C}_{33}} \tag{8.2}$$

and ϵ_x, ϵ_θ, and $\gamma_{x\theta}$ are the residual axial, circumferential and in-plane shear strains of the inner surface, and thus the negative of those measured after the parting-out procedure.

As can be expected for a pipe of this nature, the axial stress distributions are all largely linear over the wall thickness. The maximum tensile stress occurs at the inner surface, with a value of roughly 16.5 MPa. Toward the outer surface, the stress becomes increasingly compressive, until it reaches a final minimum value of about -12 MPa. Each distribution satisfies the requirement of self-equilibrium when integrated over the wall thickness, which is an expected result, as discussed in Appendix E. The stress distributions obtained for each gauge set are in excellent agreement with one another. The largest difference between these results occurs at the outer surface, between the solutions of "Gauge set B" and "Gauge set C". The magnitude of this difference is less than 3.5 MPa. Interestingly, despite the difference in the trends in the axial strain response of "Gauge set B" from the other two gauge sets, seen in Fig. 8.1, the resulting stress distributions of Fig. 8.4 lie very close to one another, especially in the region approaching the inner surface of the pipe. This is a positive result, and an indication that the deviation of the axial stress distribution from the axisymmetric stress condition, a direct consequence of the non-homogeneous nature of the material of the pipe, is very small. These results support the assumption of an axisymmetric state of residual stresses inherent in the elastic solution of Section 4, and thus also assumed by the current method of residual stress measurement. From the three axial stress distributions, it would appear that the solution of "Gauge set C" is most convincing. This is due to the fact that it is the least wavy of the distributions within this figure. When compared to this stress distribution, the self-correcting nature of the current method, discussed in Appendix E, is evident in the stress distributions of the other gauge sets. Both of these are seemingly over compressive at the normalised radial positions between 0.7 to 1, and -0.9 to -0.3. This is countered by an overly tensile stress in the normalised radial region between -0.3 to 0.7 which ensures requirement of self-equilibrium is maintained. The magnitude of the error bars correlates directly with the quality of the measured data, since they are based on the differences between the polynomial strain fits and the measured data. The error bars generally decrease in magnitude from the outer to the inner surface of the pipe. This behaviour is directly associated with the mechanical response of the pipe

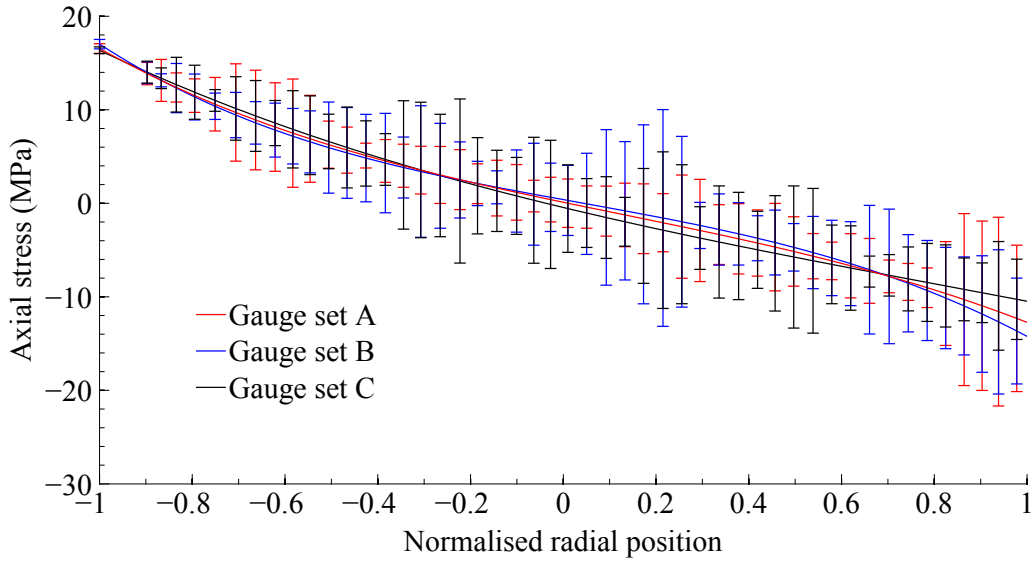

Figure 8.4: Axial stress distributions of the ±55° pipe

to the released residual loads as the wall thickness decreases. As the thickness decreases, so the magnitude of the measured strain responses increase, with the increased sensitivity to the released residual loading. Although the scatter in the measured strain variations of Figs. 8.1 to 8.3 increases with the amount of material removed, the severity of the scatter decreases relative to the magnitude of the measured response. Thus, the magnitude of the error estimated for the released residual loads decreases with increased material removal, resulting in a decrease in the magnitude of the error bounds. Despite this, the magnitude of the error bars in each stress distribution is very large over the majority of the wall thickness. This is somewhat unexpected, because of the excellent agreement between the solutions of each gauge set. Also, considering the measured strain distributions of Figs. 8.1 and 8.2, there are regions where the differences between the polynomials fitted to the strain data of each gauge set are larger than the differences between the polynomials and the respective measurement data to which they correspond. It would be expected that the differences between the stress distributions for these regions, would extend beyond the error bounds, but this not the case and the error bars are much larger than the differences in the resulting stress distributions. The error bars obtained for the inner surface of the pipe, however, are much smaller than the error bars throughout the wall thickness. These, unlike the other error bars, do not depend on the propagation of error from the layers removed before the parting procedure, but only depend on the difference between the polynomial fits and the corresponding measured strain data for 100% material removal. These differences were applied directly to Eq. (8.1) to obtain the error bounds for this region.

The hoop stress distributions of the ±55° pipe, evaluated using the polynomial strain fits

of each gauge set, are illustrated in Fig. 8.5. These comprise splines fitted to the values in stresses evaluated at the mid-radius of each removed layer, and stress determined at the inner surface of the pipe, utilising the plane-stress assumption of Eq. (8.1). The stress distributions are plotted with the error bars found for each removed layer. The stress distributions are largely linear, as can be expected within a filament-wound pipe of only one ply, and all adhere to the zero-force requirement of self-equilibrium. The maximum tensile stress of about 31 MPa occurs at the inner surface of the pipe, becoming increasingly compressive until it reaches an average value of roughly -23 MPa at the outer surface. These magnitudes are about twice as large as the axial residual stresses obtained at the inner and outer surfaces of the pipe, seen in Fig. 8.4. The hoop stress distributions of each gauge set are in excellent agreement with one another, and the largest difference of roughly 7 MPa occurs at the outer surface of the pipe, between the solutions of "Gauge set B" and "Gauge set C". As with the axial stress distributions of Fig. 8.4, the results of "Gauge set C" seem most accurate, since the solution of this gauge set is the least wavy of the results. The self-correcting nature of the current method is evident when the other two stress distributions are compared to this. Both results of "Gauge set B" and "Gauge set A" appear to be overly compressive between the normalised radial positions of 0.7 and 1, and between those of -0.9 and -0.3. These compressive regions are countered by overly tensile stresses between the normalised radial positions of -0.3 and 0.7, ensuring the requirement of self-equilibrium is achieved. The magnitude of the error bars generally decrease in magnitude toward the inner surface of the pipe. As discussed, this is associated with the increased sensitivity of the specimen to the release of residual loads as the wall thickness decreases. Very large error bars occur for each stress distribution, at random positions through the wall thickness. Additionally, in light of the excellent agreement between the results of the three gauge sets, the magnitude of the majority of the error bars over the entire wall thickness of the pipe are significantly larger than expected.

The radial stress solutions of each gauge set of the $\pm 55^{\circ}$ pipe are illustrated in Fig. 8.6. Included in this figure are the error bars determined for each removed layer. As required by equilibrium conditions, each of the residual radial stress distributions vanishes to zero at both the outer and inner surfaces of the pipe. The maximum radial stress is an order of magnitude smaller than the maximum axial stress obtained for this pipe, seen in Fig. 8.4. This maximum occurs close to the mid-radius of the pipe, at a normalised radial position of about -0.18, with an average value of about 1.9 MPa. The results of each gauge set are in excellent agreement with each other, with a maximum difference of roughly 0.14 MPa between the solutions of "Gauge set B" and "Gauge set C". This deviation occurs close to the normalised radial position of 0.7. In relation to the magnitude in residual stresses, the magnitude of the error bars are far less severe than those obtained for the axial and hoop stress distributions of Figs. 8.4 and 8.5. The radial stress evaluated at the mid-radius of

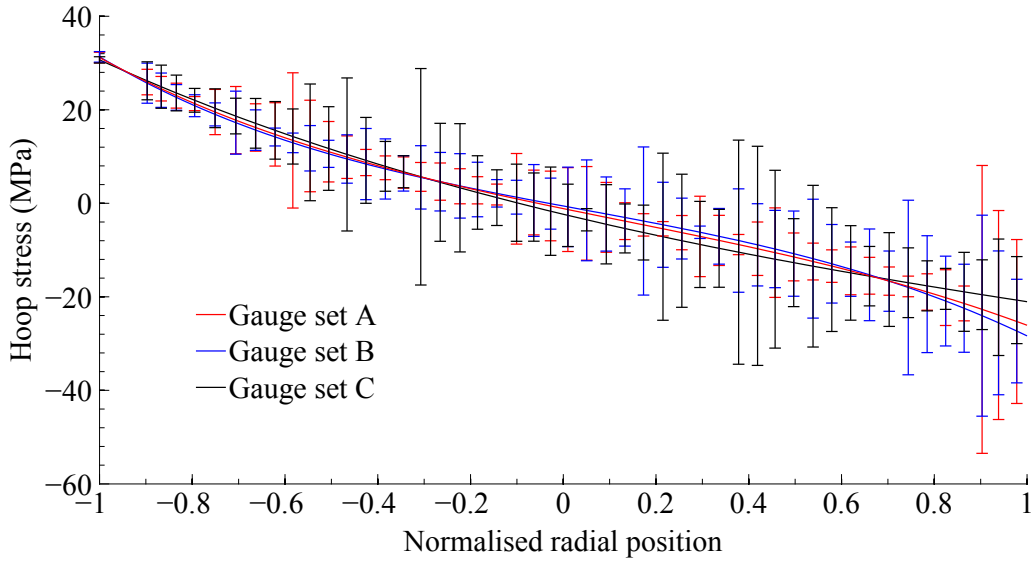

Figure 8.5: Hoop stress distributions of the ±55° pipe

a specific layer will fall between the residual pressure loads applied to the inner and outer surfaces of this layer. Thus, the error in radial stress will be very similar to the error in residual pressure loads determined for both the outer and inner surfaces of this layer. It is for this reason that the the error bounds are quite reasonable. No error bars were found for the final datum point, at the inner surface of the pipe, since these stresses were evaluated under the plane-stress assumption. This assumption enforces the radial stress at the inner surface to always be zero, and thus no error in this sense occurs.

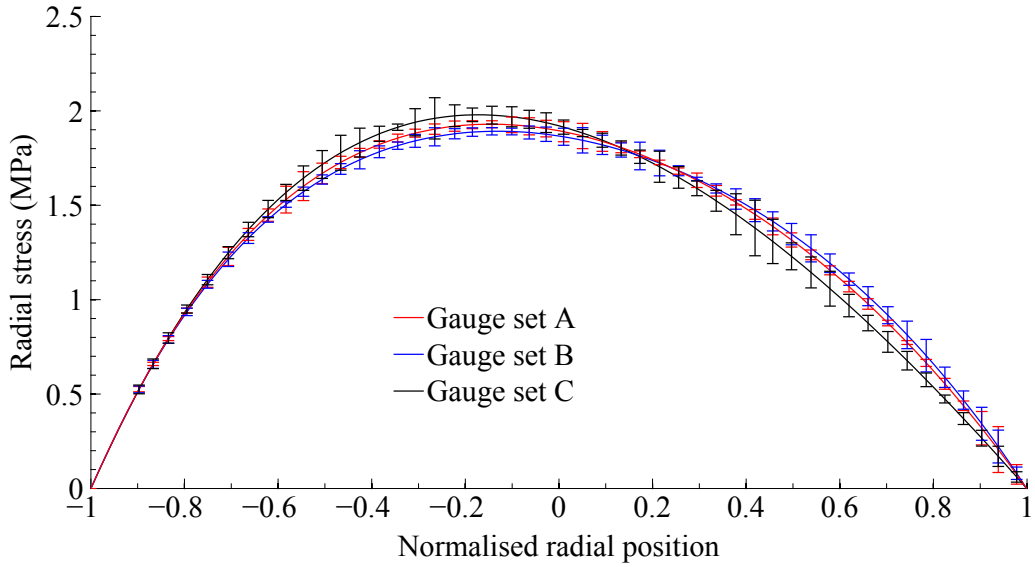

Figure 8.6: Radial stress distributions of the ±55° pipe

The in-plane shear stress distributions obtained for each gauge set of the ±55° pipe are illustrated in Fig. 8.7. Included in this figure are the error bars estimated at the mid-radius of each removed layer. Since the material is assumed orthotropic, these stresses depend only on the residual torque loads determined from the shear strain response of the specimen to the removal of material. The shear strain response is dependant on the measured axial, circumferential and 45° strain responses, and calculated using Eq. (5.1). Considering the 45° strain responses of Fig. 8.3, significant deviation in the shear stress results of each gauge set would be expected because of the different trends in the measured strain response of each of the gauge sets. This does occur in relation to the magnitude of the stresses obtained, but the these magnitudes are small in comparison to those of the residual axial and hoop stress distributions of Figs. 8.4 and 8.5. Additionally, all the shear stress distributions oscillate about the zero-stress state, which is expected to exist through the thickness of a filament-wound pipe that has been manufactured under normal curing conditions. In this sense, the assumption of orthotropic behaviour is somewhat validated, and these stresses can be considered negligible. The error bars obtained for these solutions are very large, and thus very sensitive to scatter in the measured strain distributions. As discussed for Fig. 8.3, there exists a distinctive waviness in the measured strain variation of the 45° strain gauge. It is believed this waviness is attributed to the local anisotropic effects associated with the spatial aliasing arising from the thickness of the removed layers versus the distance over which the the weave above each gauge repeats. More material orientated in a particular direction is therefore removed with each layer. In this sense, the residual shear stresses that exist as a consequence of meso-scale material anisotropy are not released as self-equilibrated stresses, resulting in a residual torque for the removal of each layer. This load would be expected to alternate with the removal of material, as the stacking sequence of the GFRP laminates alternates, producing the waviness in the measured strain distribution. This waviness does not only add to the magnitude of the error bounds, but also affects the resulting shear stress distributions, by altering the polynomials fitted to the measured strain data.

Section 5 describes a method in which the meso-scale in-plane shear stresses can be estimated. These stresses exist to maintain the bulk-scale orthotropic elastic behaviour of the pipe. Since the stacking sequence along any radial line through the thickness of the pipe changes with both axial and circumferential position, and the exact stacking sequence above any of the gauge sets is unknown, only the bounds in which these shear stresses exist can be estimated. For the purposes of this investigation, the bulk-scale shear stresses were taken to be exactly zero. This is a valid assumption since at the orthotropic scale, as discussed in Section 5, no in-plane residual shear stresses would exist in a filament-wound GFRP pipe manufactured under normal curing conditions. This is validated by the shear stress results of Fig. 8.7, where the distributions are of negligible magnitude,

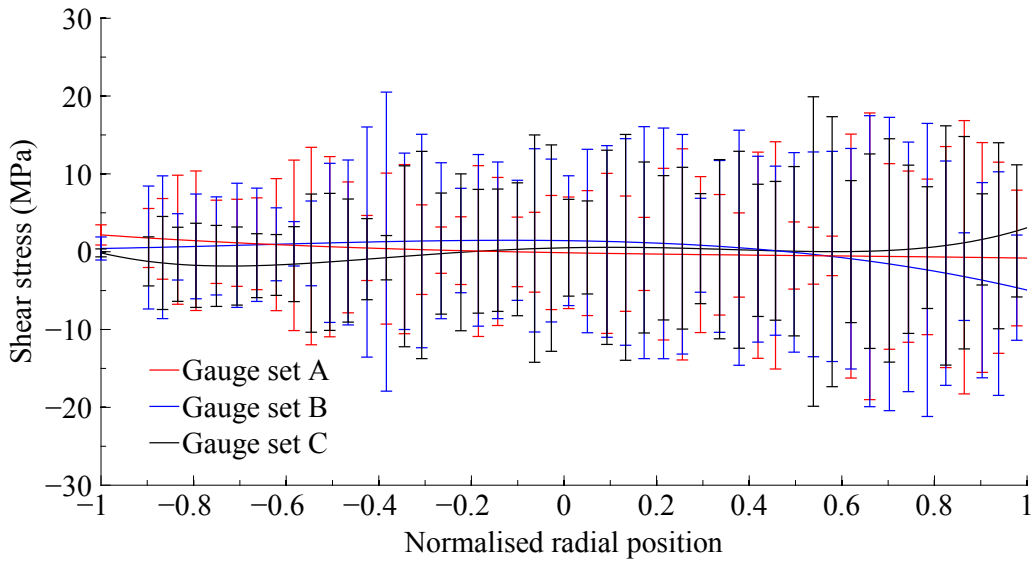

Figure 8.7: Shear stress distributions of the ±55° pipe

and all oscillate about the zero-stress state. In this sense, the shear stresses that must exist at the meso-scale scale are a consequence only of the shear-coupling with the normal axial, ϵ_x, circumferential, ϵ_θ, and radial residual strains, ϵ_r, which are governed by the orthotropic behaviour of the pipe. These residual strain distributions were found by utilising Eq. (5.31), considering the orthotropic material properties and the residual stress distributions of Figs. 8.4 to 8.6. The resulting strains were then substituted back into Eq. (5.31) for each removed layer, this time using the monoclinic material stiffness matrix, $\bar{\boldsymbol{C}}$, of both $+55°$ and $-55°$ wind angles, separately. The resulting bounds of meso-scale residual shear stresses are illustrated in Fig. 8.8. The magnitude of these stresses are close to those of the axial residual stresses of Fig. 8.4. The maximum magnitude also occurs at the inner surface of the pipe, with a value of roughly 15 MPa. The results of each gauge set are in good agreement, with a maximum deviation of about 4 MPa between "Gauge set B" and "Gauge set C" at the outer surface of the pipe. The bounds of these stresses are symmetrical about the zero-stress line for the opposing wind angles. From these bounds, the residual shear stresses that exist for any particular lamina stacking sequence can be estimated. An example of this is included in Fig. 8.8 for two arbitrary lay-ups, "Lay-up 1" and "Lay-up 2". These lay-ups illustrate how the shear stress through the wall thickness must alternate with the alternating stacking sequence of individual laminae. The alternating stresses associated with any stacking sequence must still, however, adhere to the requirement of self-equilibrium.

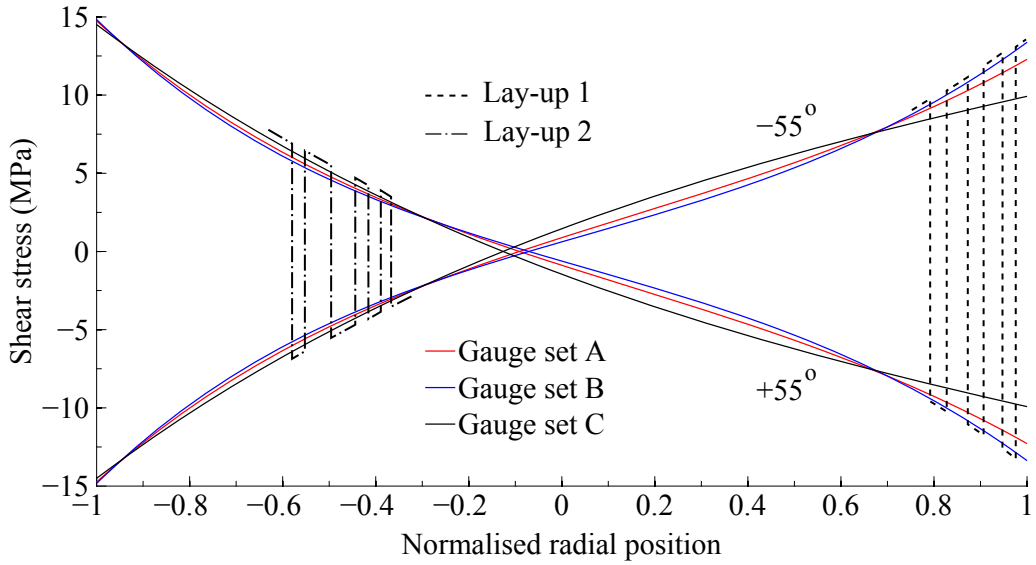

Figure 8.8: Bounds of meso-scale shear stresses of the ±55° pipe

8.2 ±65°/±47° Filament-wound pipe

8.2.1 Measured strain response

The measured axial, circumferential, and 45° strain responses of the ±65°/±47° pipe are illustrated in Figs. 8.9 to 8.11. Included in these figures are the least-squares polynomials fitted to the measured data of each gauge set, denoted "Gauge set A" to "Gauge set C". These strain variations are somewhat different to those of the ±55° pipe, seen in Figs. 8.1 to 8.3. A distinctive change in slope in the strain data occurs at the region corresponding to removal of material at the ply interface. This is directly associated with the release of discontinuous residual stresses, a consequence of the laminated nature of the pipe. This required two separate polynomials be fitted to the measured data. The first of the polynomials was fitted to the data corresponding to removal of the material comprising the outer ±47° ply, and the second to the data corresponding to the removal of material from the inner ±65° ply. Since only a discontinuity in the slope of the measured strain data exists, the polynomials were required to pass through the same value in strain for the region corresponding to removal of material at the ply interface. Enforcing this condition was a relatively simple task. First, the least-squares polynomial was fitted to the data corresponding to removal of material from the outer ply, maintaining the order at low as possible to avoid waviness within the residual stress solutions, but high enough to adequately describe the trend in the measured strain. This polynomial, like those of the ±55° pipe, was forced to pass through zero strain for 0% material removed. The second polynomial was then fitted to the data corresponding to removal of material from the inner

ply. Both polynomials were evaluated at the region corresponding to the ply interface, and the upper and lower values of these set as the upper and lower bounds of possible strain values for this region. The orders of the polynomials were maintained, and each polynomial then forced to pass through values of possible strain between the upper and lower bounds, in increments of 0.5 $\mu\epsilon$. The pair of polynomial fits that maintained the least error relative to the measured strain data, over the entire wall thickness, was then selected for evaluation of the residual stress distributions of the pipe.

The polynomial pairs fitted to the axial strain data of all three gauge sets of Fig. 8.9, were limited to 4th and 2nd order for the regions corresponding to the removal of material from the outer and inner plies, respectively. Over the full range of material removal, the trends in the strain responses of the gauge sets are somewhat different to one another. As has already been discussed, these differences are associated with the non-homogeneous nature of the pipe which, at the meso-scale, is not truly axisymmetric. The consequence of this is that the residual stresses that develop within the pipe are not entirely axisymmetric, resulting in variations in the measured strain responses of the inner surface. Compared to the measured axial strain variations of the $\pm 55^\circ$ pipe, illustrated in Fig. 8.1, the differences between the measured variations the gauge sets of the $\pm 65^\circ/\pm 47^\circ$ pipe are quite severe. The increase in the discrepancy between the variations measured by each gauge set is likely associated with the differences in material properties of the two pipes: Unlike the $\pm 55^\circ$ pipe, the apparent axial stiffness of the $\pm 65^\circ/\pm 47^\circ$ pipe decreases with the removal of material from the outer $\pm 47^\circ$ ply. The decrease in the apparent axial stiffness of this pipe results in axial strain responses that are not only of significantly larger magnitude than those of the $\pm 55^\circ$ pipe, but are also more sensitive to the release of residual stresses that are not truly axisymmetric. This effect is amplified by the decreased level of orthotropy of the remaining pipe with the removal of each layer. For the region corresponding to removal of material from the outer $\pm 47^\circ$ ply, the distributions measured by each gauge set move increasingly further apart toward the region corresponding to the ply interface. The maximum difference for this region occurs between the variations of "Gauge set A" and "Gauge set B", with a magnitude of just more than 100 $\mu\epsilon$. Over the region corresponding to layer removal from the inner ply, the difference between the strain variations of these gauge sets gradually increases to a final magnitude of roughly 140 $\mu\epsilon$. Unlike the trends of "Gauge set A" and "Gauge set B", the strains measured by "Gauge set C" increase over the range of material removal from the inner ply. The largest difference in the measured strain variations occurs at 100% material removed, between the variations of "Gauge set A" and "Gauge set C". The magnitude of this difference is roughly 260 $\mu\epsilon$.

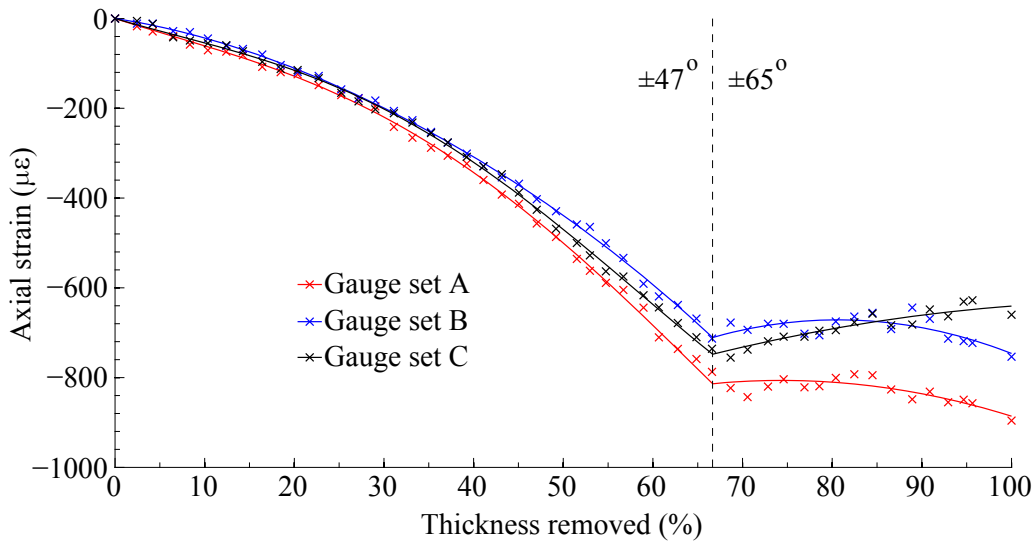

Figure 8.9: Measured axial strain response of the ±65°/±47° specimen

As for Fig. 8.9 the measured circumferential variations of Fig. 8.10 required only 4th and 2nd order polynomials to be fitted over the regions corresponding to removal of material from the ±47° and ±65° plies, respectively. Much like the circumferential strain responses measured for the ±55° pipe, seen in Fig. 8.2, those measured for the ±65°/±47° do not deviate significantly from one another. This behaviour is associated with the high apparent circumferential stiffness of the pipe, which increases with the removal of material from the ply wound at ±47°. The high circumferential stiffness inhibits the sensitivity of the strain responses to the release of residual stresses that are not completely axisymmetric. Although the trends in strain are not significantly affected, the scatter in measured data about the polynomial fits increases with the increased amount of removed material. This increase in scatter can be attributed to local anisotropic effects above each strain gauge, associated with the decrease in the level of orthotropy of the pipe as more material is removed. For the first 40% of thickness removed, the polynomial fits of each gauge set are almost indistinguishable from one another. Thereafter, there is some deviation between the fits. The largest difference for the removal of material from the outer ply occurs in the region of 55% thickness removed, between the polynomial fits of "Gauge set A" and "Gauge set C". The magnitude of the difference for this region is roughly 30 $\mu\epsilon$. For material removal at the ply interface, the largest difference occurs between the polynomial fits of "Gauge set B" and "Gauge set C", with a magnitude of just less than 25 $\mu\epsilon$. In this region, the strain variations demonstrate significant changes in slope. For the removal of material from the inner ±65° ply, the difference between the polynomial fits of "Gauge set A" and "Gauge set C" increases slightly until it reaches a value of roughly 30 $\mu\epsilon$ at 100% material removal. The maximum difference for this region occurs between the polynomial fits of "Gauge set A" and "Gauge set B", with a value of about 38 $\mu\epsilon$.

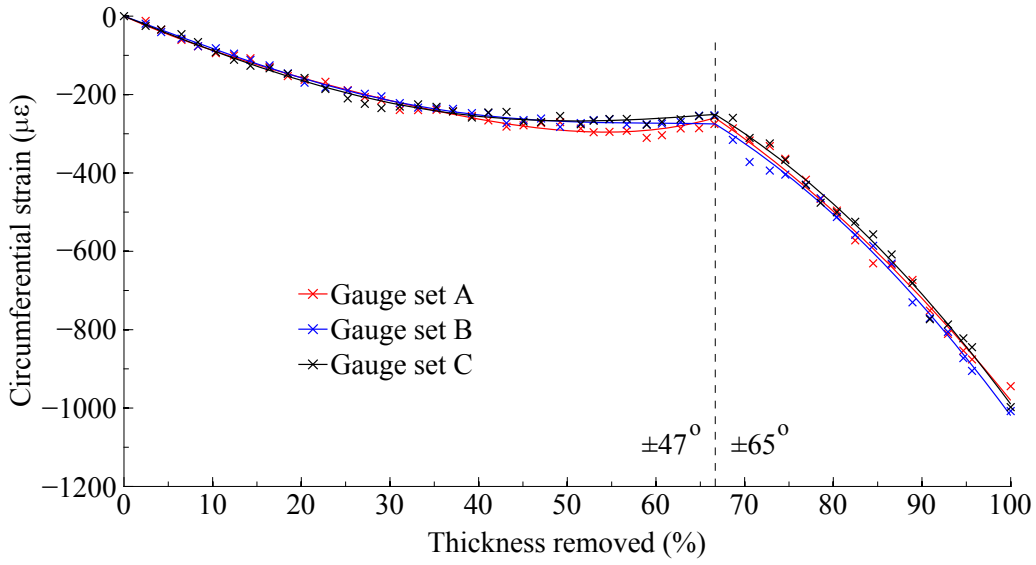

Figure 8.10: Measured circumferential strain response of the ±65°/±47° specimen

Over the range of material removal from the outer ±47° ply, the trends in the measured 45° strain variations of Fig. 8.11 are quite similar. Polynomials of 4th order were required to fit the responses measured by "Gauge set A" and "Gauge set C", while a polynomial of only 3rd order was required to fit the data of "Gauge set B" for this region. The largest difference over this region occurs between the polynomial fits of "Gauge set A" and "Gauge set C", for about 50% of the thickness removed. This difference has a magnitude of close to 40 $\mu\epsilon$. The polynomials fitted to the data measured by each gauge set, over the region corresponding to removal of material from the inner ply, were limited to 2nd order. The trends in the responses over this region are quite different. The difference between the fits of "Gauge set A" and "Gauge set C" increases from 20 $\mu\epsilon$, at the region corresponding to the ply interface, to roughly 200 $\mu\epsilon$ at 100% material removed. Over the entire range, there is generally an increase in the amount of scatter in the measured data, with the increase in the amount of material removed. Also, like the measured 45° strain variations of the ±55° pipe, seen in Fig. 8.3, there is an inherent waviness of the measured data of each gauge set about the polynomial fits. As has been discussed, the waviness is most likely a consequence of the spatial aliasing associated with the weave pattern of the filament winding. For each layer removal, there is most certainly removal of more material oriented in a particular direction. This uneven removal of material results in the release of non-equilibrating residual torque loads, that exist as a consequence of the meso-scale anisotropy of the material. Since the stacking sequence above each gauge set is different, different shear strains at the inner surface of the pipe are registered. This effect is amplified by the decrease in the level of orthotropy of the pipe as more material is removed.

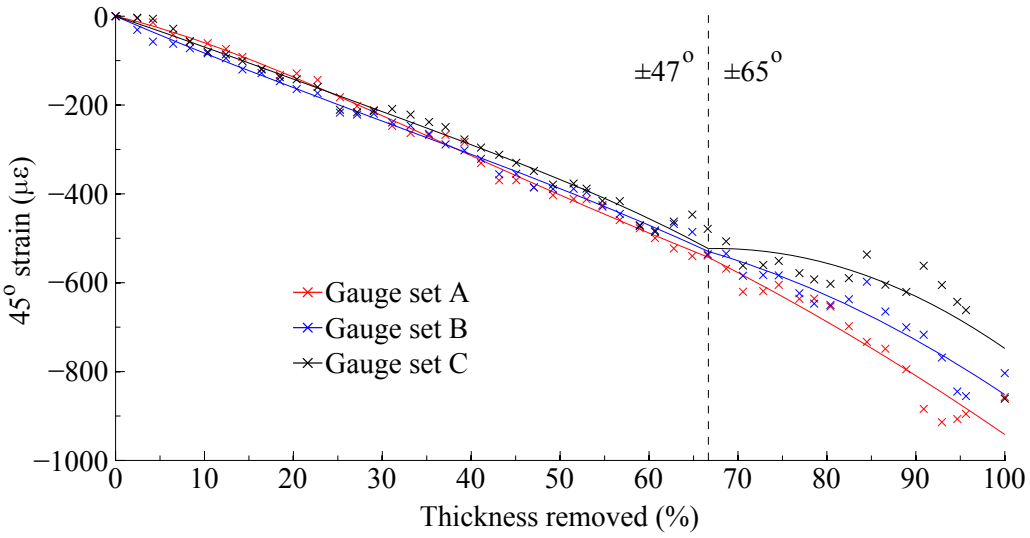

Figure 8.11: Measured 45° strain response of the ±65°/±47° specimen

8.2.2 Residual stress distributions

The axial residual stress distributions of the ±65°/±47° pipe, obtained using the polynomial fits of Figs. 8.9 to 8.11, are illustrated in Fig. 8.12. These comprise splines fitted to the stresses evaluated at the mid-radius of each removed layer, and are plotted together with the error bars estimated in the manner described in Section 5. Due to the presence of a residual strain discontinuity between the outer and inner plies, associated with the two-stage manufacturing process of this pipe, the results of the removed layer at the interface between the two plies and which comprises material from both plies were ignored. As discussed in Section 5, this was done to avoid inaccuracies associated with the averaging of the residual stresses across the ply interface. The residual stresses in this region were thus found through extrapolation of the stress distributions found to exist within the surrounding layers of the inner and outer plies, respectively. The residual stresses at the inner surface of the pipe were evaluated under the plane-stress assumption, using Eq. (8.1). The axial stress solutions of each gauge set are in excellent agreement with each other, and are largely linear over the thickness of the pipe. All three stress distributions satisfy the requirement of self-equilibrium when integrated over the wall thickness of the pipe. These distributions are compressive at the outer surface, with an average value of around -12 MPa, and become increasingly tensile toward the ply interface. The average stress found to exist at the inner surface of the pipe is roughly 13 MPa. A stress discontinuity at the ply interface occurs, with a magnitude of roughly 2 MPa. The stresses within this region are tensile in both the outer and inner plies. At the outer surface of the pipe, the largest difference in stress occurs between the results of “Gauge set A” and “Gauge set B”, with a magnitude of just more than 5 MPa. It would appear that the

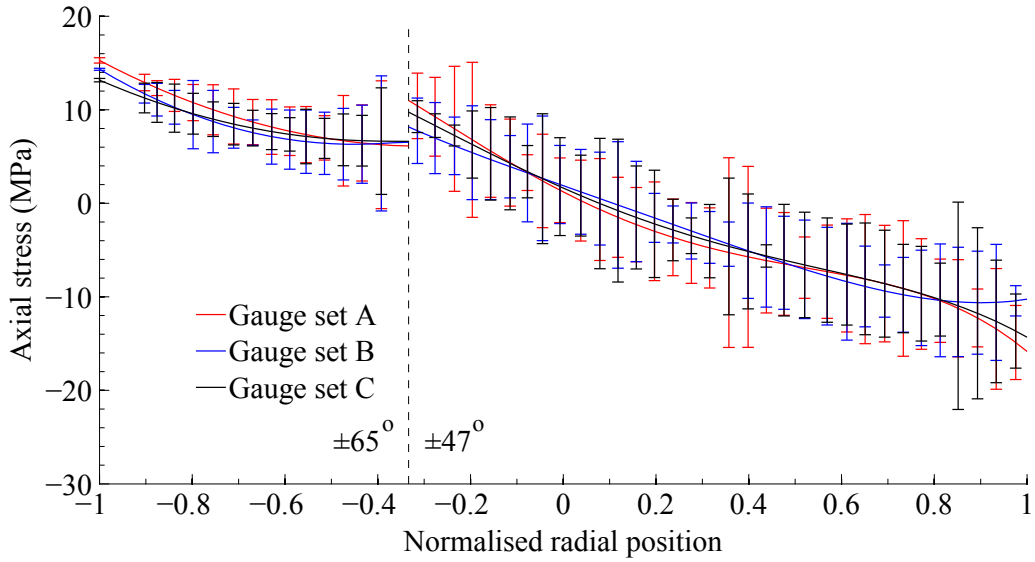

Figure 8.12: Axial stress distributions of the ±65°/±47° pipe

results of "Gauge set B" are most reasonable over the outer ply, since it is the least wavy of the solutions. The self-correcting nature of the current method is evident when the results of the other two gauge sets are compared to this, where overly compressive stresses between the normalised radial positions of -0.1 to 0.4 and 0.8 to 1 are countered by overly tensile regions between normalised radial positions from the ply interface to -0.1 and 0.4 to 0.8. As has been discussed, this self-correcting mechanism enforces the requirement of self-equilibrium. At the ply interface, the largest difference between the solutions of the three gauge sets is less than 4 MPa. This deviation is a direct result of the deviations in the measured axial strain responses of the gauge sets, for the region of material removal at the ply interface, seen in Fig. 8.9. Considering the differences in the measured strain variations of this figure, especially for the region of removal of material from the inner ply, one would expect significant differences in the axial stress solutions of Fig. 8.12. This is not the case, however, and the stress results for the inner ply are in good agreement with one another. The largest difference in the solutions over the inner ply occurs at the inner surface, with a magnitude of only around 3 MPa. Large differences between the solutions do not occur for a number of reasons. The axial stresses are not only dependant on the measured axial strain variations, but also depend on the measured circumferential strain responses. There are minor differences between the circumferential strain responses measured by each gauge set, illustrated in Fig. 8.10, and these presumably somewhat compensate for the effect caused by the differences in the measured axial strain variations. Additionally, as more material is removed the remaining pipe becomes increasingly sensitive to the release of the residual stresses. The large differences in the axial strain variations measured by each gauge set can be attributed to the release of stresses that are not truly axisymmetric. However, the inner ply of the ±65°/±47° pipe is wound with a

relatively high wind angle, and therefore the axial stiffness of this ply is relatively low. This low axial stiffness ensures that the differences in the residual loads determined for each gauge set, for a particular removed layer, are not very different, despite the large differences in the measured axial strain variations. As a consequence, the axial stress solutions of each gauge set are very similar, so similar that the axisymmetric assumption inherent in the current method can still be considered valid. As with the residual stress distributions of the $\pm 55^\circ$ pipe, the error bars of $\pm 65^\circ/\pm 47^\circ$ pipe are very large, but the magnitude of these somewhat decreases toward the inner surface of the pipe. It appears that the error bars are too large, and this is most apparent over the inner ply of the pipe. Since the differences between the polynomials fitted to the measured axial strain responses of Fig. 8.9 are much larger than the differences between the polynomials and the data to which they correspond for this region, one would expect the measurement error of each gauge set to not engulf the residual stresses determined for the other gauge sets. This is, however, not the case.

The hoop stress distributions of the $\pm 65^\circ/\pm 47^\circ$ pipe are illustrated in Fig. 8.13. Included in this figure are the error bars estimated for each removed layer. As with the axial stress distributions of Fig. 8.12, the results of the layer that comprises material from both the inner and outer plies were ignored, and the residual hoop stresses in the region of the ply interface was estimated by extrapolation of the stress distributions obtained for the surrounding layers of the inner and outer plies, respectively. The hoop stresses at the inner surface, associated with the parting-out procedure of the strain gauge rosettes, were calculated under the plane-stress assumption, using Eq. (8.1). The resulting hoop stress distributions of each gauge set are in excellent agreement with one another, and are near-linear over the much of the thickness of the pipe. As expected, each stress distribution satisfies the self-equilibrium requirement. The hoop stresses are compressive at the outer surface of the pipe, with an average value of around -22 MPa. These stresses become increasingly tensile away from the outer surface, until they reach a value of about 12 MPa at the ply interface. Within the inner ply, the average stress for this region is very close to zero, and this becomes increasingly tensile until it reaches a value of roughly 35 MPa at the inner surface. The magnitude and sense of the stress discontinuity at the ply interface is a direct result of the residual strain discontinuity that exists between the plies. As has been discussed, this strain discontinuity arises as a direct result of the two-stage manufacturing process of this pipe. During the first wind and cure procedure, residual stresses develop within the inner $\pm 65^\circ$ ply, and a residual strain exists at the outer surface of this ply prior to the wind and cure of the outer $\pm 47^\circ$ ply. Should no strain discontinuity have existed, the stress within the inner ply at the ply interface would not only have had the same sense as the stress within the outer ply for this region, but would also have been significantly larger in magnitude. Since the inner ply is significantly stiffer circumferentially than the

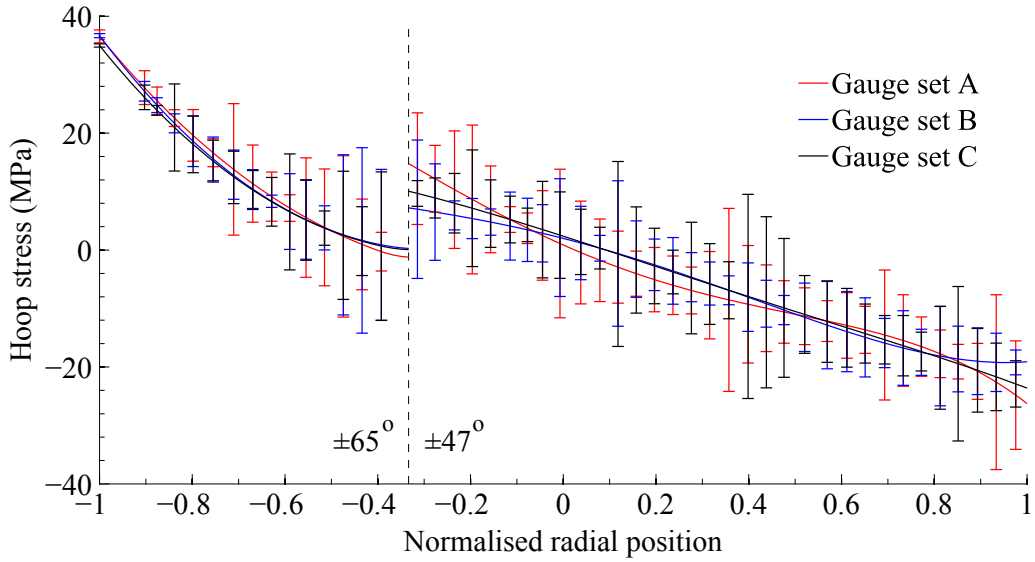

Figure 8.13: Hoop stress distributions of the ±65°/±47° pipe

outer ply, for the same residual strain, the stress within the inner ply would be larger than that within the outer ply by a factor similar to the ratio of the circumferential stiffnesses of the two plies, which is clearly not the case. Over the region of the outer ply, the results of "Gauge set C" are most convincing, as they are the least wavy of the stress distributions. The waviness in each stress distribution, as has been discussed, is a consequence of the self-correcting mechanism inherent in the current method of residual stress measurement. The largest differences in stress over the outer ply occur between the results of "Gauge set A" and "Gauge set B"at the outer surface and ply interface. The magnitudes of these differences are roughly 7 MPa and 8 MPa, respectively. Over the inner ply, the differences between the results of each gauge set never exceed 2 MPa. As with the previous stress distributions, the magnitude of the error bars of Fig. 8.13 are very large, and decrease toward the inner surface of the pipe. The largest error bound is in the region of ±16 MPa for the solution of "Gauge set C", at the normalised radial position of 0.4.

The corresponding radial stresses of the ±65°/±47° pipe are illustrated in Fig. 8.14. All of the radial stress distributions, as required, tend to zero at the inner and outer surfaces of the pipe, and are continuous across the ply interface. The radial stresses are roughly an order of magnitude lower than the axial stresses obtained for this pipe, shown in Fig. 8.12. Additionally, the solutions of each of gauge sets are in excellent agreement with one another, with a maximum difference of less than 0.3 MPa between the results of "Gauge set A" and "Gauge set B". This occurs at the normalised radial position of roughly -0.1. The magnitude of the error bars of these stress distributions are more reasonable than those determined for the axial and hoop stress distributions of Figs. 8.12 and 8.13,

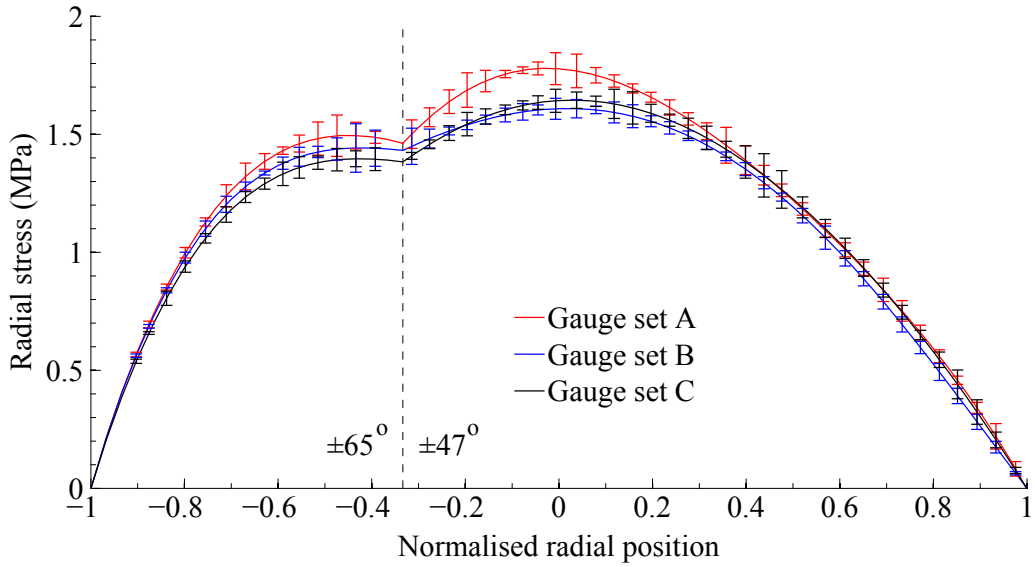

Figure 8.14: Radial stress distributions of the ±65°/±47° pipe

and are directly associated with the errors in residual pressure loads applied to the inner and outer surfaces of each removed layer. The influence of the two-stage manufacturing process is clearly evident in these stress distributions. The radial stresses that initially developed within the inner ±65° ply, after the first wind and cure, would have been very similar to those of the ±55° pipe, illustrated in Fig. 8.6. This stress state was then altered by the winding and cure of the outer ±47° ply. The influence of this process was to increase the residual radial stress of the inner ply from zero, in the region of the ply interface, to an average value of about 1.4 MPa. The location of maximum radial stress of the inner ply also appears to have moved from around the mid-radius of this ply, closer to the ply interface. This peak occurs at the normalised radial position of -0.5. The second stage of manufacture not only altered the residual stress state that initially formed within the inner ±65° ply, but also influenced the residual of stresses that formed within the outer ±47° ply. The peak of radial stress that developed within this ply resides very close to the mid-radius of the pipe, instead of the mid-radius of the ply itself. This peak has an average magnitude of roughly 1.7 MPa, and is the largest radial stress that occurs across the thickness of the pipe.

The bulk-scale in-plane shear stress distributions of the ±65°/±47° pipe are presented in Fig. 8.15. These distributions comprise splines fitted to the shear stresses evaluated at the mid-radius of each removed layer, based upon the polynomials fitted to the measured axial, circumferential and 45° strain responses of Figs. 8.9 to 8.11. The stresses at the inner surface were calculated under the plane-stress assumption, using Eq. (8.1). All resulting shear stress distributions adhere to the zero-torque requirement of self-equilibrium, associated with the self-correcting mechanism inherent in the current method of residual stress

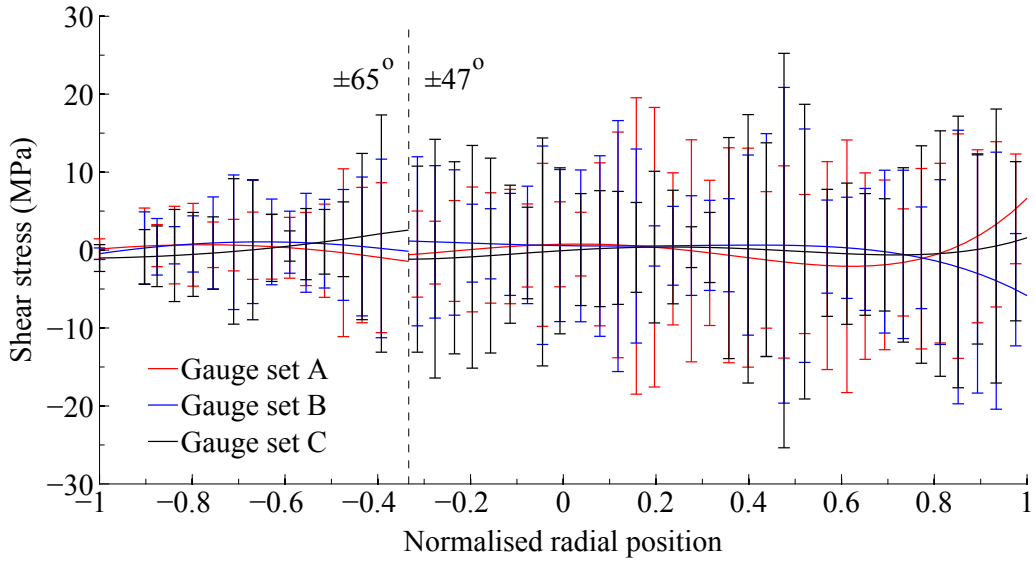

Figure 8.15: Shear stress distributions of the ±65°/±47° pipe

measurement. As has been discussed, the material properties of the filament-wound pipes can be considered orthotropic at the bulk scale. Under normal manufacturing conditions, the residual shear stresses that develop in a pipe or this nature should be zero. Although the residual shear stress distributions of Fig. 8.15 are non-zero, they all oscillate about the zero-stress state, and are of significantly lower magnitude than the axial and hoop stress distributions of Figs. 8.12 and 8.13, and can thus be considered negligible. The assumption of material orthotropy is therefore supported. As with the axial and hoop stress distribution, the magnitude of the error bars is very large, and is directly associated with the scatter of the measured strain distributions of Figs. 8.9 to 8.11. Additionally, the magnitude of the error bars clearly decreases toward the inner surface of the pipe. This is a direct result of the decreased sensitivity of the residual stress distributions to scatter as the wall thickness of the remaining pipe decreases.

The plies wound at ±65° and ±47° comprise laminae of which the fibre orientation and stacking sequence alternates with both axial and circumferential position. To maintain the bulk-scale orthotropic behaviour of the pipe, additional meso-scale shear stresses must exist, due to the local anisotropic nature of the material. Since the stacking sequence and material orientation above any of the gauge sets are unknown, only the bounds of these shear stresses can be estimated. The bounds of these stresses are illustrated in Fig. 8.16. Like the bounds of the meso-scale shear stresses of the ±55° pipe, shown in Fig. 8.8, the bounds of the stresses of the ±65°/±47° pipe were evaluated under the assumption of zero residual shear strain. In this sense, the shear stress distributions of Fig. 8.15 were assumed zero. First, the normal residual strains, ϵ_x, ϵ_θ, and ϵ_r, associated with the bulk-scale orthotropic material properties, were calculated at the mid-radius of each removed

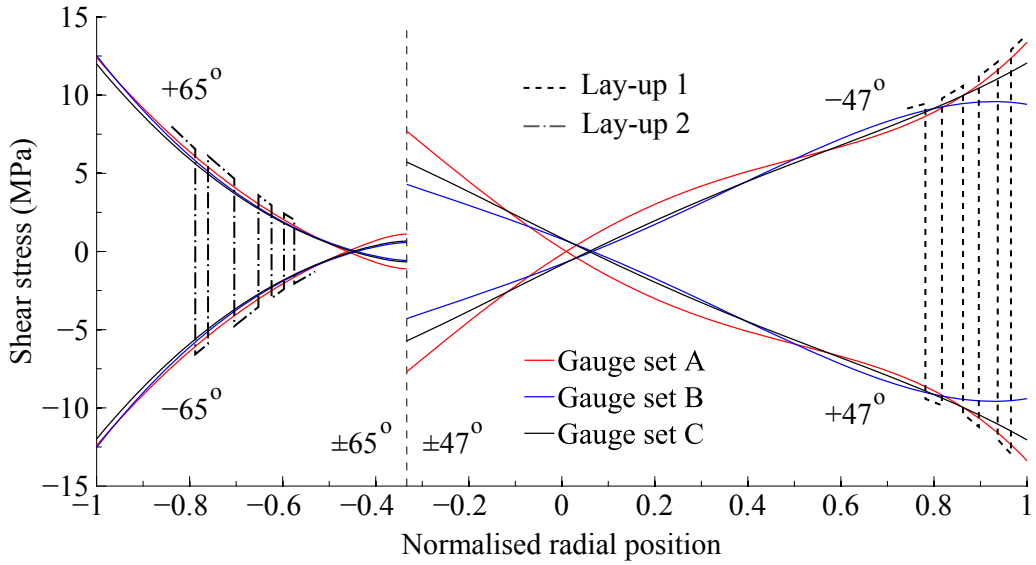

Figure 8.16: Bounds of meso-scale shear stresses of the ±65°/±47° pipe

layer. This was done utilising the stress distributions of Figs. 8.12 to 8.14, together with Eq. (5.31). This equation was then used to estimate the residual in-plane shear stresses for the monoclinic material properties, assuming both positive, ϕ, and negative, $-\phi$, wind angles over the thickness of each ply. Since the residual shear strains, $\gamma_{x\theta}$, were assumed zero, the meso-scale shear stresses that arise are a consequence only of the shear-coupling between the normal and in-plane shear components of the monoclinic material, and thus lie symmetrically about the zero-stress line. The bounds in stress of each gauge set are in excellent agreement with each other. The maximum stresses occur at the inner and outer surfaces, with magnitudes of close to 13 MPa, respectively. These are very similar to the maximum values obtained for the bounds of the the meso-scale shear stresses of the ±55° pipe. The largest deviations occur between the results of "Gauge set A" and "Gauge set B", at the outer surface of the pipe, and within the outer ply, at the region of the ply interface. The magnitude of these differences is around 5 MPa. The residual strain discontinuity present at the ply interface enhances the stress discontinuity associated with the change in material properties associated with the different wind angles of the inner and outer plies. For the purposes of clarity, two arbitrary stacking sequences of the inner and outer plies, namely "Lay-up 1" and "Lay-up 2", were assumed. These demonstrate how the meso-scale residual shear stresses would typically alternate with alternating material orientation between the wind angles of $+\phi$ and $-\phi$ over both plies. Over any particular cross section of the pipe, the shear stresses must adhere to the self-equilibrium requirement. The release of these alternating stresses amplifies the waviness within the measured 45° strain distributions of Fig. 8.11, since for each layer removal more material orientated at either $+\phi$ or $-\phi$ is most certainly removed. This results in a release in residual torque loads, which alternate with the stacking sequence of the laminae.

8.3 ±75°/±36° Filament-wound pipe

8.3.1 Measured strain response

The measured axial, circumferential, and 45° strain responses of the ±75°/±36° specimen, for the layer removal experiment, are illustrated in Figs. 8.17 to 8.19. These are plotted against the percentage thickness removed. The final measured strains, after parting-out of the respective strain gauge rosettes, were assigned to 100% thickness removed, under the assumption that these strains were exactly equal and opposite to the residual strains that existed at the inner surface of the specimen, prior to any machining process. A significant amount of scatter is present in the measured data, which increases with the amount of removed material. As has been discussed, the scatter is caused by both the manner in which the strain measurements were taken, as well as real geometric effects associated with the non-homogeneous nature of the material making up the thickness of the pipes. With the increase in the number of removed layers, the ratio of a particular lamina thickness, oriented at either $+\phi$ or $-\phi$, to the remaining wall thickness increases. This results in a decrease in the level of orthotropy above any particular gauge set, and local anisotropic properties therefore affect the measured strain response. As with the measured strain data of the ±65°/±47° pipe, the strain responses of Figs. 8.17 to 8.19 display clear changes in slope in the region corresponding to removal of material from ply interface. This is a consequence of laminated nature of the pipe. Two separate polynomials were fitted to the measured data, corresponding to removal of material from the outer and inner plies, respectively. As with the measured responses of the ±65°/±47° pipe, each pair of polynomials were forced to pass through the same value in strain at the region corresponding to removal of material from the ply interface. The method used for determining the value through which the polynomials were forced to pass is exactly as previously discussed.

The polynomials required to fit the axial strain data of the of the ±75°/±36° specimen, illustrated in Fig. 8.17, varied between 2nd and 4th order. The response of "Gauge set A" required a 4th order polynomial to sufficiently match the measured data, corresponding to material removal of the outer ply, and a 2nd order polynomial for removal of material from the inner ply. The data of "Gauge set B" required 3rd and 2nd order polynomials, while the data of "Gauge set C" required 4th and 3rd order polynomials, respectively. The trends in the strain responses of the three gauge sets are similar for the region of material removal from the outer ±36° ply but, like the axial strain responses of Fig. 8.9 of the ±65°/±47° pipe, these variations deviate from one another as the region corresponding to removal of material at the ply interface is approached. The largest difference in this region occurs between the responses of "Gauge set A" and "Gauge set B" with a magnitude of just more

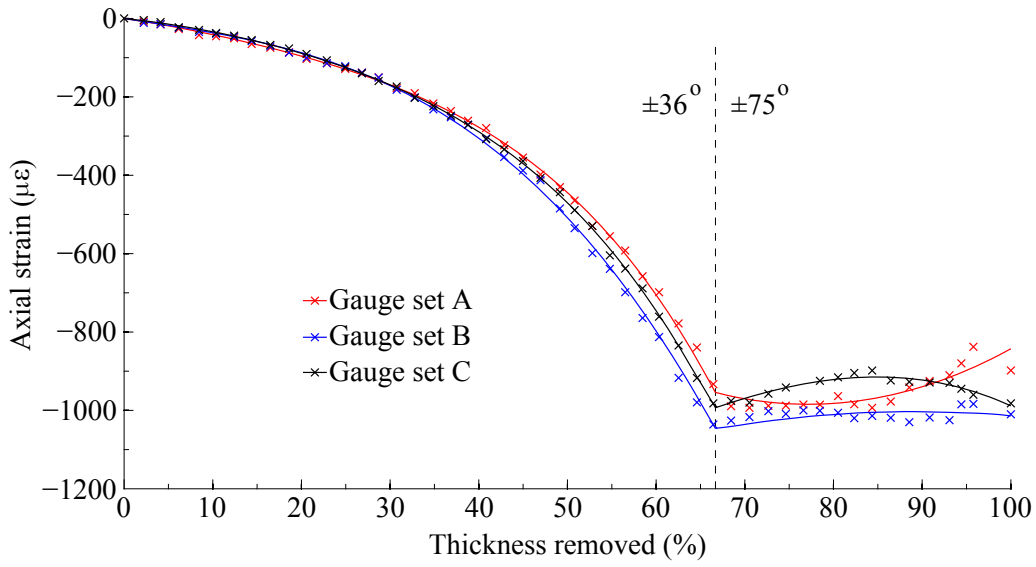

Figure 8.17: Measured axial strain response of the ±75°/±36° specimen

than 100 $\mu\epsilon$. The strain variations of each gauge set, for the removal of material from the inner ±75° ply, are quite different from one another. The strain response of "Gauge set A" decreases from a value of just less than -950 $\mu\epsilon$, for the region corresponding to removal of material from the ply interface, to around -980 $\mu\epsilon$ at about 78% thickness removed. Thereafter, the strain increases to value of about -840 $\mu\epsilon$ at 100% material removed. The strain response of "Gauge set B" increases gradually from about -1040 $\mu\epsilon$, at the region corresponding to removal of material at the ply interface, to around -1010 $\mu\epsilon$ for 100% material removed. The strain response of "Gauge set C", however, increases from just less than -1000 $\mu\epsilon$, for the region of material removal from the ply interface, to a value of roughly -915 $\mu\epsilon$ after the removal of about 84% of the wall thickness. This is followed by a decrease in strain to around -990 $\mu\epsilon$ at 100% material removed. The largest difference between the strain variations occurs for 100% material removed, between the responses of "Gauge set A" and "Gauge set B". The magnitude of this difference is around 170 $\mu\epsilon$. The deviation in the trends in the strain variations measured by each of the gauge sets is a consequence of the non-homogeneous nature of the material of the pipe. Like the axial strain variations of Fig. 8.9 for the ±65°/±47° pipe, the deviation between the measured responses of each gauge set are much larger than those seen by the axial strain responses of the ±55° pipe, illustrated in Fig. 8.1. As previously discussed, this is most likely caused by the decrease in the apparent axial stiffness of the ±75°/±36° pipe as more material is removed from the outer surface. The decrease in axial stiffness of the remaining pipe increases the sensitivity of the measured strain response to the release of residual stresses that are not truly axisymmetric. This behaviour is amplified by the decreased level of orthotropy above any particular gauge set as more material is removed.

For the circumferential strain responses of Fig. 8.18, the data of "Gauge set A" required 4th and 3rd order polynomials to be fitted to the regions corresponding to removal of material from the outer and inner plies, respectively. Polynomials of 4th and 2nd order were fitted to the data of "Gauge set B", while 5th and 2nd order polynomials were required to sufficiently fit the data measured by "Gauge set C". Over the entire range of material removal, the polynomial fits of each gauge set display near identical trends in strain. As has been discussed, the high apparent circumferential stiffness of the $\pm 75^{\circ}/\pm 36^{\circ}$ pipe, and the increase in this stiffness with the increase in the amount of removed material, is likely the reason for the relative insensitivity of the circumferential strain responses to the release of residual stresses that are not completely axisymmetric. For removal of material from the outer $\pm 36^{\circ}$ ply, the strain response is relatively small in comparison to the final measured magnitude, which was on average, about 650 $\mu\epsilon$ for 100% of the material removed. Initially, the strain response gradually decreased from zero at for 0% material removed, to a value of just less than -60 $\mu\epsilon$ at about 28% of the thickness removed. The strain then increases toward the region corresponding to the ply interface. Interestingly, this is the only response, across all three pipe configurations, that became positive. For the region of material removal from the ply interface, an average strain of just less then 80 $\mu\epsilon$ was measured. For most of the region corresponding to removal of between 0% and 40% of the thickness, the differences between the polynomials of the gauge sets are very similar to the differences between each polynomial and the measured data to which it corresponds. From 40% thickness removed, through to the region corresponding to the ply interface, there is evidently more scatter in the measured data, consequent of local anisotropic effect. Across the ply interface, there is a very significant change in slope in the strain variations. This change in slope is more pronounced than obtained for the circumferential strain responses of the $\pm 65^{\circ}/\pm 46^{\circ}$ pipe, illustrated in Fig. 8.10. This is most likely due to the higher difference in the circumferential stiffnesses of the plies wound at $\pm 75^{\circ}$ and $\pm 36^{\circ}$, as compared to the difference in stiffnesses between the plies of the other laminated pipe, wound at $\pm 65^{\circ}$ and $\pm 47^{\circ}$. The largest difference in the strain variations of Fig. 8.18 occurs between the data of "Gauge set A" and "Gauge set B", for 100% material removed. This has a magnitude of around 90 $\mu\epsilon$.

The measured 45° strain variations of "Gauge set A" and "Gauge set C" of Fig. 8.19 required polynomials of 4th and 2nd order to be fitted to the data corresponding to removal of material from the outer and inner plies, respectively. "Gauge set B" also required a polynomial of 2nd order to be fitted to the data for material removal from the inner $\pm 75^{\circ}$ ply, and a polynomial of 3rd order sufficiently matched the data corresponding to the removal of material from the outer $\pm 36^{\circ}$ ply. In the region between 85% and 100% thickness removed, there is a large amount of scatter in the measured data, especially in those measured by "Gauge set A" and "Gauge set B". On average, the trends in the

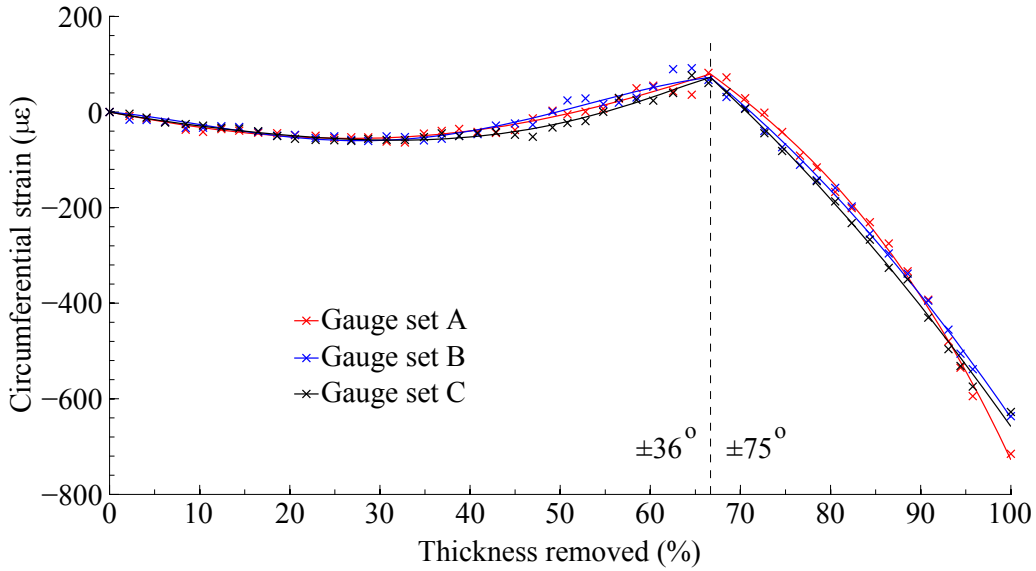

Figure 8.18: Measured circumferential strain response of the ±75°/±36° specimen

strain responses are the same, with relatively good agreement between the fits of each gauge set. Additionally, the change in slope of the strain responses, over the region corresponding to the ply interface, are more severe then those of the strain responses of the 45° gauges of the ±65°/±47° pipe, illustrated in Fig. 8.11. These changes in slope, however, are not as pronounced as those of the axial and circumferential strain responses of Figs. 8.17 and 8.18. The largest differences in the strain variations of Fig. 8.19 occurs at 100% material removed, between the fits of "Gauge set A" and "Gauge set C". The magnitude of this difference is roughly 60 $\mu\epsilon$. It is interesting to note that the waviness in the measured strain data is not as pronounced as the waviness of the measured 45° strain responses of the ±55° and ±65°/±47° pipes, seen in Figs. 8.3 and 8.11. The reason for this may lie with the meso-scale shear stresses that exist as a consequence of the local anisotropy of the pipes: It is feasible that the magnitude of the bounds of these stresses are significantly smaller than those of the ±55° and ±65°/±47° pipes, possibly due to the fact that the wind angles of both plies of the ±75°/±36° pipe are more different from the wind angle of ±45° (which would produce the highest shear stiffness) than the other two pipes. Therefore the ±75°/±36° pipe is the has the lowest shear stiffness of three pipe configurations, and the residual shear stresses that develop, as a consequence of the meso-scale anisotropy, will presumably be the smallest. Thus for each layer removal, smaller local residual torque loads above each gauge set would be released, resulting in a lower level of waviness in the measured data.

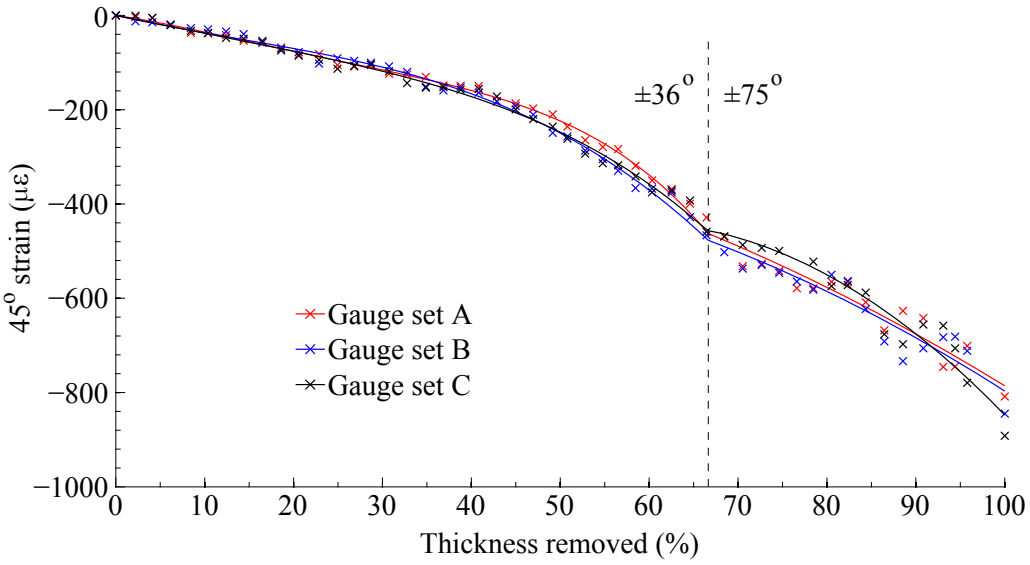

Figure 8.19: Measured 45° strain response of the ±75°/±36° specimen

8.3.2 Residual stress distributions

The residual axial stress distributions, evaluated using the polynomials fitted to the measured strain responses of the ±75°/±36° pipe, are illustrated in Fig. 8.20. These are plotted against the normalised through-thickness radial positions. Included in this figure are the error bars, evaluated at the mid-radius of each removed layer. The stresses at the inner surface of the pipe were determined under the plane-stress assumption, using Eq. (8.1). The results obtained for the layer comprising material from both the inner and outer plies was ignored. A strain discontinuity at the ply interface was expected, due to the two-stage manufacturing process of this pipe. The stresses in this region, were thus obtained by extrapolation of the stresses evaluated at the mid-radius of the surrounding layers. In the outer ±36° ply, the solutions of "Gauge set B"and "Gauge set C" are in excellent agreement with one another, and are the least wavy of the stress distributions. When the stress distribution of "Gauge set A" is compared to these, the effect of the self-correcting mechanism inherent in the current method of residual stress measurement is clear. Between the normalised radial positions of 0.8 to 1, the stress variation of this gauge set is clearly overly compressive. This overly compressive region is countered by an overly tensile region of stress between the normalised radial positions of 0 to 0.7. The location of the maximum tensile stresses for each of the gauge sets is interesting, as these do not occur at the inner surface of the pipe, but rather occur within the outer ply, in the region of the ply interface. The average stress obtained for this region is about 12 MPa. The minimum stress occurs at the outer surface of the pipe, with an average value of roughly -10 MPa. It is also interesting to note that the axial stress distributions that exist over

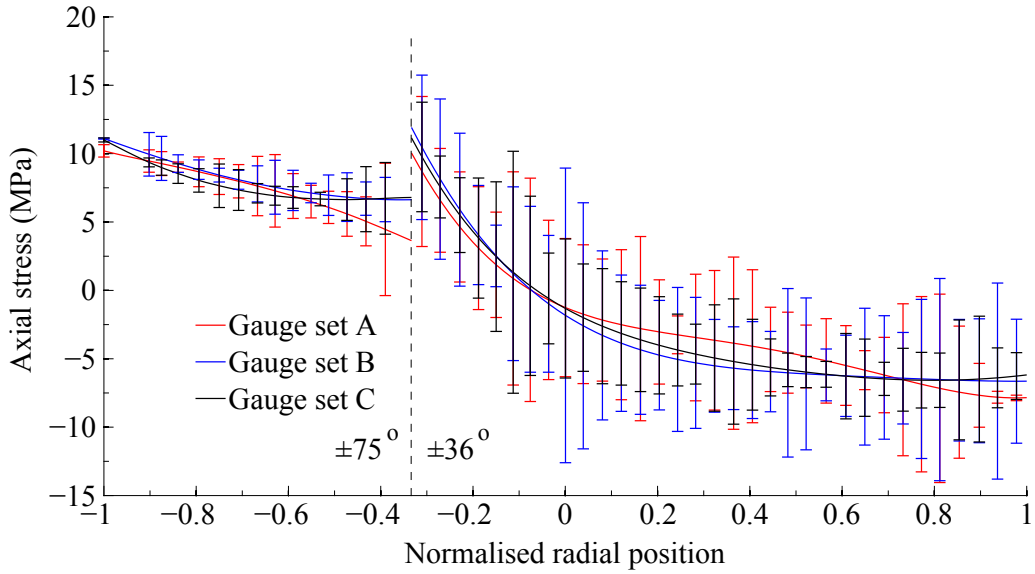

Figure 8.20: Axial stress distributions of the ±75°/±36° pipe

the outer ±36° ply, unlike those obtained for the outer ply of the ±65°/±47° pipe, seen in Fig. 8.12, are quite non-linear. Between the normalised radial position of 0.2 and the ply interface, the stress distributions rapidly change from a compressive state, with a value of roughly -5 MPa, to a tensile value of about 12 MPa. The non-linear nature of these stresses may arise because of the difference in material properties of the ±75° and ±36° plies of this pipe. The large mismatch between the axial stiffness of these plies possibly aided in the formation of the non-linear stress profile of the outer ply during the second curing process of the pipe. For the inner ply, the solutions of all the gauge sets are in good agreement between the normalised radial positions of -0.5 and -1. Despite this, only the trends in "Gauge set B" and "Gauge set C" are similar over this ply. The trend in the solution of "Gauge set A" almost mirrors these, resulting in a roughly 3 MPa difference at the region of the ply interface. The difference in the trend of this solution is solely due to the differences in the trends of the measured axial strain responses of the gauge sets, seen in Fig. 8.17. Additionally, the overly compressive region of the solution of "Gauge set A", between the radial positions corresponding to the ply interface and -0.6, is present as a result of the self-correcting mechanism inherent in the current method of residual stress measurement. The stress distributions of each gauge set consequently adhere to the zero-force equilibrium requirement. The error bars of the outer ply are seemingly very large, considering the agreement in the axial stress distributions of the gauge sets for this region. The largest bound in error occurs for the solution of "Gauge set B", at the mid-radius of the pipe. This has a magnitude of about ±11 MPa. The error bars of the inner ply are much smaller than those of the outer ply, associated with the lower axial stiffnesses of this ply. Additionally, the magnitude of the error bounds generally decrease toward the inner

surface of the pipe, since the strain response of the remaining pipe becomes more sensitive to the release of the residual stresses as the wall thickness decreases.

The corresponding hoop stress distributions of the $\pm 75^{\circ}/\pm 36^{\circ}$ pipe are illustrated in Fig. 8.21. The results of each gauge set are in excellent agreement with one another, and the stress distributions of both the outer and inner plies are largely linear. The maximum tensile stress, as expected, occurs at the inner surface of the pipe, with an average value of just less than 30 MPa. Interestingly, the maximum compressive stress, with a value of just less than -15 MPa, occurs within the inner ply, at the region of the ply interface. This is somewhat unexpected, since the maximum compressive stress would generally occur at the outer surface of a pipe of this nature. Additionally, this is quite different from the hoop stress results of the $\pm 65^{\circ}/\pm 47^{\circ}$ pipe, illustrated in Fig. 8.13, where the compressive stress that developed at the outer surface of the inner ply, during the initial wind and cure, shifted to an almost zero state of stress after the wind and cure of the outer $\pm 47^{\circ}$ ply. A possible explanation to these differences lies in the material properties of each ply. The wind angle of the two plies of the $\pm 65^{\circ}/\pm 47^{\circ}$ are not very different. In this case, the difference between the circumferential stiffnesses of both plies is not extreme, and the curing of the $\pm 47^{\circ}$ ply significantly altered the self-equilibrating residual stress state that initially existed within the $\pm 65^{\circ}$ ply. Since the inner ply of the $\pm 75^{\circ}/\pm 36^{\circ}$ pipe is much stiffer circumferentially than the outer ply, it had the ability to largely resist the influence of the curing of this ply. The self-equilibrating residual hoop stress distribution that initially developed within the $\pm 75^{\circ}$ ply thus likely changed only marginally during the wind and cure of the $\pm 36^{\circ}$ ply. The discontinuity in stress at the ply interface is clear indication of the discontinuity in residual strain that existed between the plies of the $\pm 75^{\circ}/\pm 36^{\circ}$ pipe. The stresses of the inner and outer plies for this region are opposite in sense, which would not be the case should the residual strains have been equivalent. The magnitude of the discontinuity in stress occurring in this region is roughly 25 MPa, and the average tensile stress in this region, within the outer ply, is around 10 MPa. The maximum difference between stresses in this region occurs between the results of "Gauge set B" and "Gauge set C", with a magnitude of roughly 6 MPa. The maximum difference that occurs at the outer surface of the pipe is between the results of "Gauge set A" and "Gauge set B", with a value of just less than 5 MPa. For the outer ply, the results of "Gauge set C" are most convincing, since it is the least wavy of the stress distributions for this region. When compared to this stress distribution, the solutions of "Gauge set A" are seemingly over compressive for the normalised radial positions between -0.33 and 0, and between roughly 0.7 and 1. This is countered by an overly tensile stress in the region between the normalised radial positions 0 and 0.7. The results of "Gauge set B" are overly compressive between the normalised radial positions of -0.33 to 0, and roughly 0.3 to 0.9. These are countered by overly tensile stresses between the

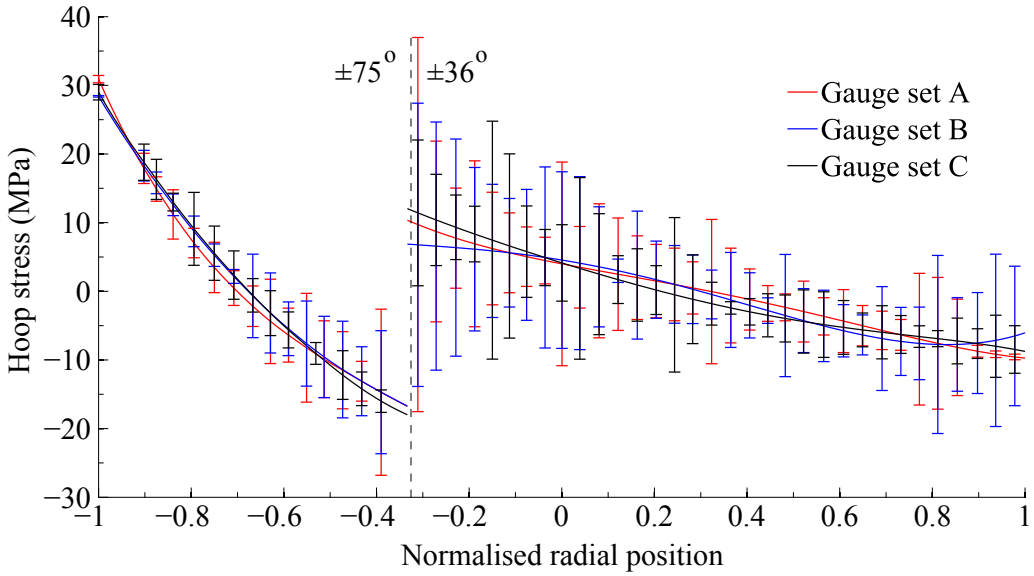

Figure 8.21: Hoop stress distributions of the ±75°/±36° pipe

normalised radial positions of around 0 to 0.3 and 0.9 to 1. As has been discussed, this is a consequence of the self-correcting mechanism inherent in the current method of residual stress measurement. As with the axial stress distributions of Fig. 8.20, the error bounds of the inner ±75° ply are generally much smaller than those of the outer ±36° ply. In light of the excellent agreement between the results of each gauge set, however, the magnitude of the error bounds over the entire wall thickness seem unreasonably large.

The radial stress distributions of the ±75°/±36° pipe are illustrated in Fig. 8.22. The solutions of each gauge set are in excellent agreement with one another. The maximum difference occurs in the region of the normalised radial position of 0.1, between the results of "Gauge set A" and "Gauge set C". This difference has a magnitude of roughly 0.1 MPa. Each of the distributions, as required, are continuous through the ply interface, and tends to zero at the outer and inner surfaces of the pipe. The two-stage manufacturing procedure of this pipe introduced two separate peaks in the radial stress distributions, each occurring close to the mid-radius of the two plies. The degree of the influence of the wind and cure of the outer ±36° ply, on the residual stress state that initially developed within the ±75° ply, is clearly evident in this figure. The residual radial stress that initially existed within the ±75° ply, would have been very similar to that of the ±55° pipe, illustrated in Fig. 8.6. In this sense, a state of zero radial stress existed at the outer surface of this ply. After the winding and curing of the outer ±36° ply, this stress only increased to an average of 0.15 MPa. This increase is much smaller than the 1.4 MPa shift in stress experienced by the inner ply of the ±65°/±47° pipe. This can be seen in Fig. 8.14. As previously discussed, it appears that the influence of winding and curing of the outer ply on the residual stress state within the inner ply is highly dependant on the differences in the material properties

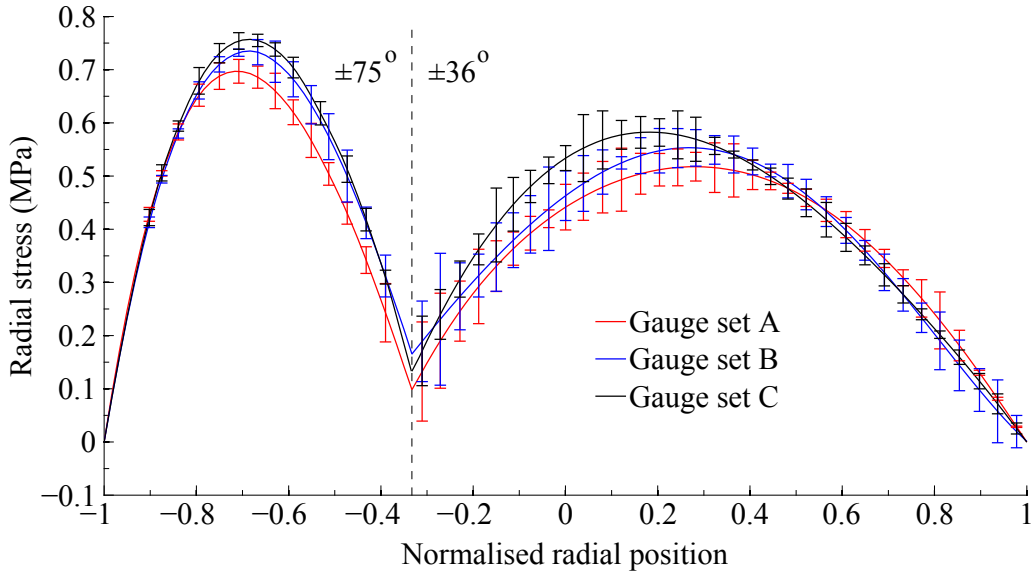

Figure 8.22: Radial stress distributions of the ±75°/±36° pipe

of the two plies. In the case of the ±65°/±47° pipe, these differences are not extreme, and therefore the curing of the outer ply significantly altered the residual stress state within the inner ply. The differences between the material properties of the inner and outer plies of the ±75°/±36° pipe are very large. The result is that, much like the hoop stress distributions seen in Fig. 8.21, the radial stress distribution that initially existed through the thickness of the inner ±75° ply changed only marginally during the wind and cure of the outer ±36° ply. The maximum radial stress occurs within the inner ply, with a value of less than 0.8 MPa. As with the error bars of the radial stress distributions of the ±55° and ±65°/±47° pipes, the error bounds in Fig. 8.22 are relatively small, and are quite reasonable with respect to the agreement of the solutions of the different gauge sets of this pipe. These error bounds are directly associated with the errors in residual pressure loads applied to the inner and outer surface of each layer.

Fig. 8.23 illustrates the residual in-plane shear stress distributions of the ±75°/±36° pipe. The magnitudes of these variations are very small in comparison to the measured axial and hoop stress distributions of this pipe, illustrated in Figs. 8.20 and 8.21. Additionally, like the bulk-scale shear stress distributions obtained for the ±55° and ±65°/±47° pipes, illustrated in Figs. 8.7 and 8.15, these variations all oscillate about the zero-stress line. Therefore these stresses can be considered negligible, validating the assumption of orthotropic material properties. As has been discussed, a zero-stress state of residual shear stresses are expected to exist through the thickness of a pipe of this nature. This is because the effects of the fibres orientated in a particular $+\phi$ direction are countered by the effect of the fibres orientated in the opposing $-\phi$ direction. These opposing effects limit any residual twisting of the pipe to occur, and thus at the orthotropic scale, limit the

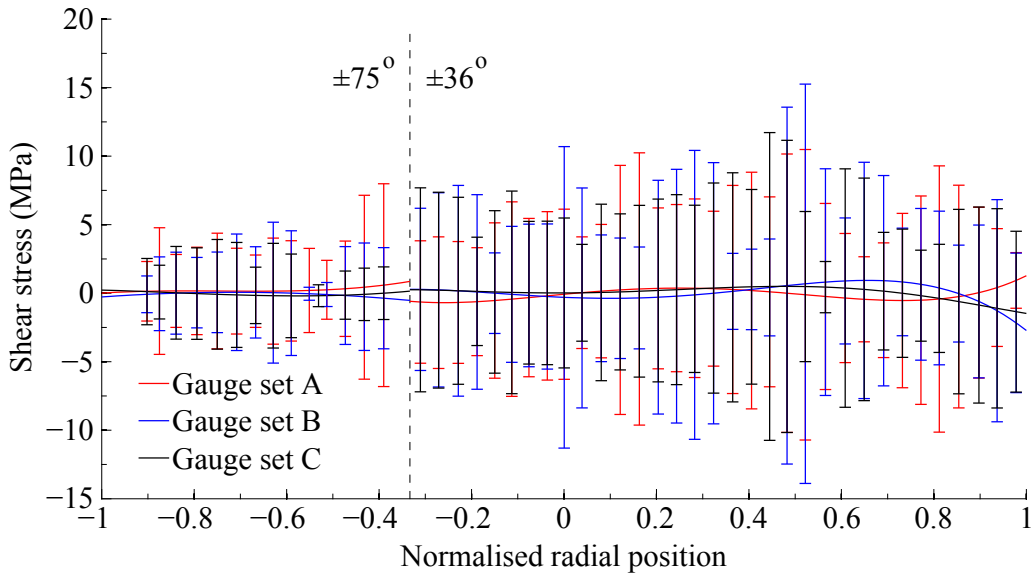

Figure 8.23: Shear stress distributions of the ±75°/±36° pipe

formation of any through-thickness residual shear stresses. The magnitude of the error bars, as expected, decrease toward the inner surface of the pipe. The general magnitude of these error bounds, although very large, are smaller than those determined for the ±55° and ±65°/±36° pipes. The reason for this is lies in the reduced level of waviness of the measured 45° strain data about the corresponding polynomial fits, as seen in Fig. 8.19.

The waviness of the measured 45° strain data about the corresponding polynomial fits arises due to the spatial aliasing above each of the gauge sets. This is associated with the weave pattern of the laminae as a product of the filament winding process. The stacking sequence of the laminae of each ply, orientated at both $+\phi$ and $-\phi$, changes with both axial and circumferential position. As a consequence, the pipe can be considered othotropic at the bulk-scale. Local anisotropic material properties across the thickness of each ply, however, give rise to the presence of residual shear stresses. These meso-scale shear stresses must exist to maintain the bulk-scale orthotropic behaviour of the pipe. Only the bounds of these stresses can, however, be estimated since the stacking sequence of the laminae above any gauge set is unknown. First, the through-thickness residual axial, ϵ_x, circumferential, ϵ_θ, and radial, ϵ_r, strain distributions associated with the results of the ±75°/±36° pipe were determined. This was done by substituting the respective orthotropic material properties, together with the normal residual stress distributions of Figs. 8.20 to 8.22 into Eq. (5.31). For the purposes of this work, it was assumed that the bulk-scale residual shear stress distributions of Fig. 8.23 were zero. This is a valid assumption, since the shear stress distributions presented in this figure are negligible. The consequence of this is that the residual in-plane shear strains, $\gamma_{x\theta}$, are exactly zero. The bounds of the meso-scale shear stresses were then found by substituting the residual

strain components back into Eq. (5.31), together with the monoclinic material properties associated with each of the $+\phi$ and $-\phi$ wind angles of both the inner and outer plies. These were evaluated over the entire thickness of the pipe. The resulting bounds of stress are presented in Fig. 8.24. The solutions of each gauge set are in good agreement with one another over both the inner and outer plies, particularly those of "Gauge set B" and "Gauge set C". Additionally, the bounds of each gauge set lie symmetrically about the line of zero stress. The reason for this is because the residual shear strain distribution is assumed zero, and hence the resulting bounds in meso-scale shear stress are dependant only upon the coupling between the shear stresses and the normal residual strain components. At the outer surface, the largest difference occurs between the solutions of "Gauge set A" and "Gauge set C". This has a magnitude just more than 1 MPa. A similar magnitude of deviation between the results of "Gauge set A" and "Gauge set B" is evident at the normalised radial position of about 0.3. A difference of about 1 MPa also occurs between the results of "Gauge set A" and "Gauge set C" within the inner ply, at the region of the ply interface. The magnitude of the bounds of shear stress are smaller than those obtained for the $\pm 55^\circ$ and $\pm 65^\circ/\pm 36^\circ$ pipes, seen in Figs. 8.8 and 8.16. The effect of this was to reduce the amount of waviness in the measured 45° strain data of Fig. 8.19. There is also a discontinuity in the bounds of the shear stresses of Fig. 8.24, which occurs at the ply interface. This discontinuity is a result of both the residual strain discontinuity that existed in this region, as well as the difference in material properties of the inner and outer plies. For illustrative purposes, two assumed stacking sequences namely "Lay-up 1" and "Lay-up 2", are included in Fig. 8.24. These demonstrate typical meso-scale shear stress distributions within each ply of the pipe. These shear stresses would alternate with the alternating stacking sequence of the laminae, and in this sense be continually discontinuous over the thickness of the pipe. Over any particular cross section, the resulting shear stress distributions must adhere to the requirement of self-equilibrium.

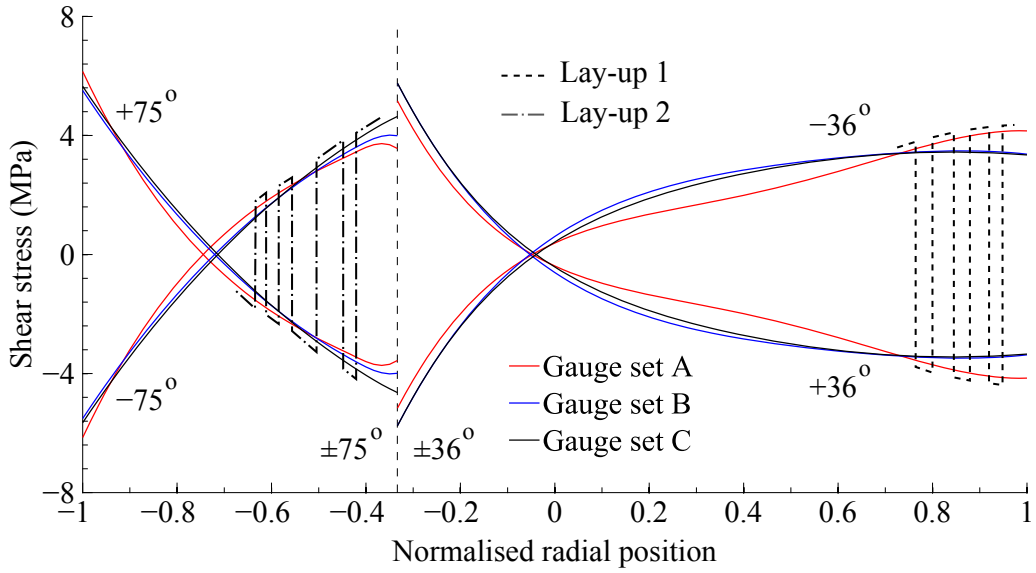

Figure 8.24: Bounds of meso-scale shear stresses of the ±75°/±36° pipe

9 Further investigation: Increasing the thickness of the removed layers

Increasing the thickness of the layers removed from the surface of a specimen is advantageous from an experimental standpoint. This ultimately reduces the time required to perform the experiment, and is therefore of some interest. A potential issue with increasing the thickness of the removed layers is a loss of resolution within the resulting residual stress distributions, as a consequence of loss of resolution within the measured strain variations. Additionally, there are potential inaccuracies associated with the manner in which the average residual stresses within each layer are determined. The residual axial strain, ϵ_x, and twist per unit length, $\gamma_{x\theta}/r$, that exist within any composite pipe likely vary through the wall thickness. The elastic solution of Section 4, however, requires these values be invariant when evaluating the residual stresses within any removed layer. These values can be considered constant, should the thickness of the layer be thin enough. It is feasible, however, that the thickness of the removed layers need not be very thin. The ϵ_x^0 and γ^0 values obtained through the elastic solution will be very similar to the average values of the residual ϵ_x and $\gamma_{x\theta}/r$ variations that existed through the thickness of this layer. Should these variations be near-linear, the constant ϵ_x^0 and γ^0 values will coincide with the average values of these variations at the mid-radius of the layer. Consequently, the residual stresses evaluated at this position will be very similar to the actual values in stress that existed in this region prior to any material removal. A smooth residual stress distribution, that does not change rapidly with radial position, could therefore be accurately measured with the removal of relatively thick layers. The purpose of this section is to investigate the validity of this hypothesis, based upon the measured stress distributions presented in the previous section. For each pipe configuration, only the measured strain variations of "Gauge set C" are considered. To simulate the removal of thicker layers, only every 5th measured datum point of each measured strain variation is considered. In reality this is equivalent to removal of layers 5 times thicker than those removed in the original experiment.

9.1 ±55° Filament-wound pipe

Fig. 9.1 illustrates the measured axial, circumferential, and 45°, strain variations of the reduced data set of the ±55° pipe. These comprise every 5th datum point of the measured strain variations of "Gauge set C", illustrated Figs. 8.1 to 8.3, and thereby simulate the removal of layers of roughly 1.5 mm thickness. Included in this figure are the least-squares polynomials fitted to each of the strain variations. These are all of 2nd order, as opposed to the 3rd and 4th order polynomial fits originally required for strain responses of Figs. 8.1 to 8.3.

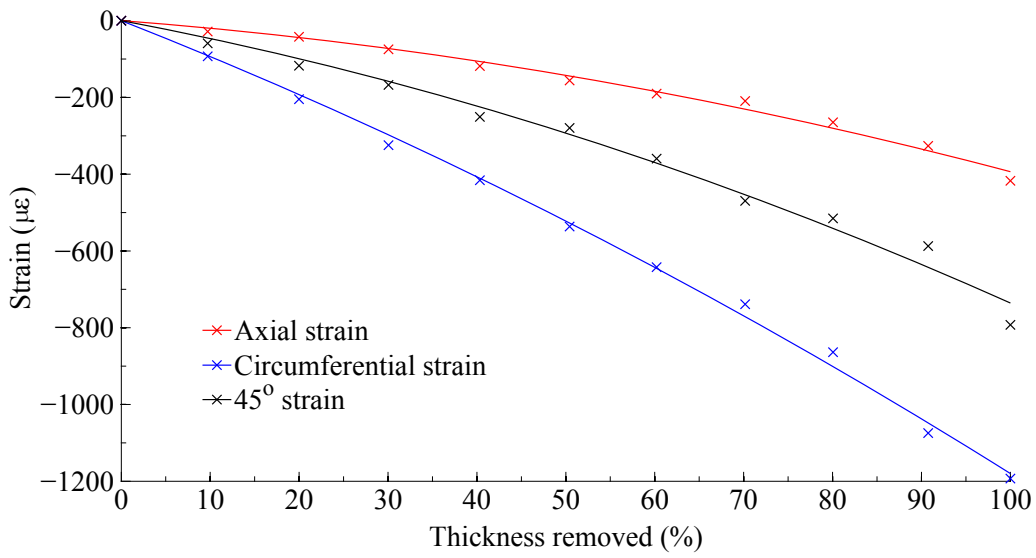

Figure 9.1: Strain responses of the ±55° specimen for the reduced data set

The corresponding axial stress distribution of the reduced data set is presented in Fig. 9.2. As with the previous stress distributions of Section 8, this solution comprises splines fitted to the stresses evaluated at the mid-radius of each removed layer, as well as the stress at the inner surface of the pipe, which was calculated under the plane-stress assumption, using Eq. (8.1). Included in this figure is the axial stress distribution of the full data set, which was originally presented in Fig. 8.4. These distributions are plotted together with the error bars estimated for the mid-radius of each removed layer. Based upon the projected values of the splines describing each of the stress distributions, the largest difference between the solutions of the full and reduced data sets occurs at the outer surface of the pipe, with a magnitude of less than 2 MPa. Since the stress distributions are almost identical between the normalised radial positions of -1 to 0.7, these differences must be a consequence only of minor variations between the polynomials fitted to the strain variations the two data sets, as opposed to errors associated with the application of the elastic solution to the thick layers. The magnitude of the error bars of the reduced

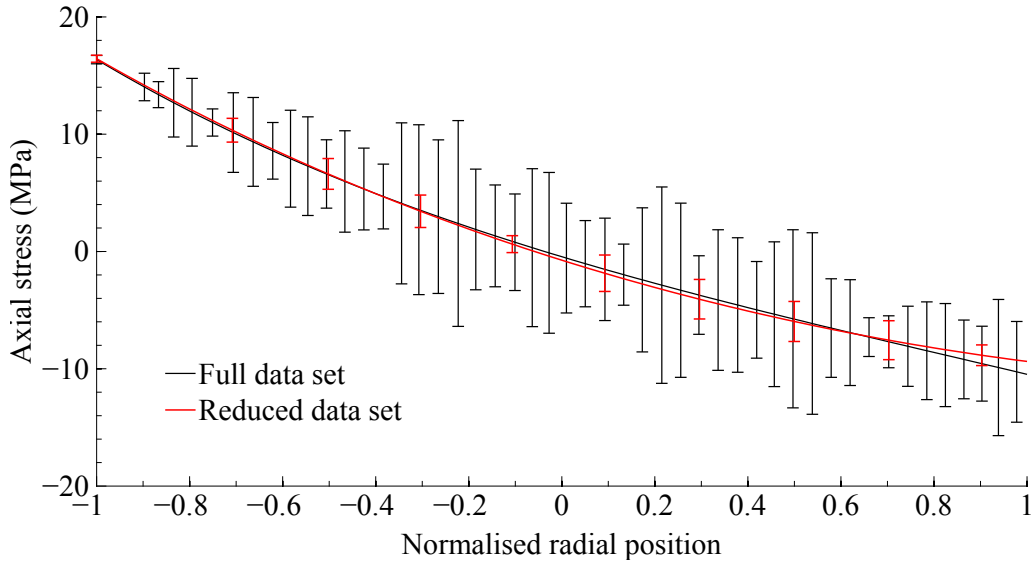

Figure 9.2: Comparison of the axial stress distributions of the ±55° pipe

data set are much smaller, and much more convincing, than those originally found for the full data set. This is an unexpected result, since the error bars corresponding to the stress distributions of both data sets were estimated in the same manner, described in Section 5. First, the differences between the measured strain data and the corresponding polynomial fits were used to determine the errors in the residual loads released by each layer. In this sense, the errors in the residual loads depend only on the elastic response of the remaining pipe, and not the thickness of the removed layers. The errors in residual stresses are estimated by application of the errors in the residual loads, associated with the removal a particular layer, to the layer itself. Applying identical errors in the residual loads to layers of different thickness produce errors of different magnitudes. Since the thicker layers of the reduced data set comprise more area over which the errors in the residual loads are distributed, the resulting errors in stress are smaller in magnitude.

The hoop stress distributions of the full and reduced data sets of the ±55° pipe are plotted in Fig. 9.3. Included in this figure are the error bars of each data set. As with the axial stress distributions of Fig. 9.2, the stress distributions of the full and reduced data sets are almost identical to each other, with only minor deviation between the solutions. This deviation is also less than 2 MPa at the outer surface, based upon the projected values of the splines fitted to each set of results. These differences are purely a consequence of the differences between the polynomials fitted to the strain data of the two data sets. No apparent error associated with the used of the elastic solution to the thicker layers of the reduced data set occurs, because the solutions of this data set is almost identical to that of the full data set over most of the wall thickness of the pipe. As with the results of Fig. 9.2, the error bars of the reduced data set are much smaller than those estimated for the full

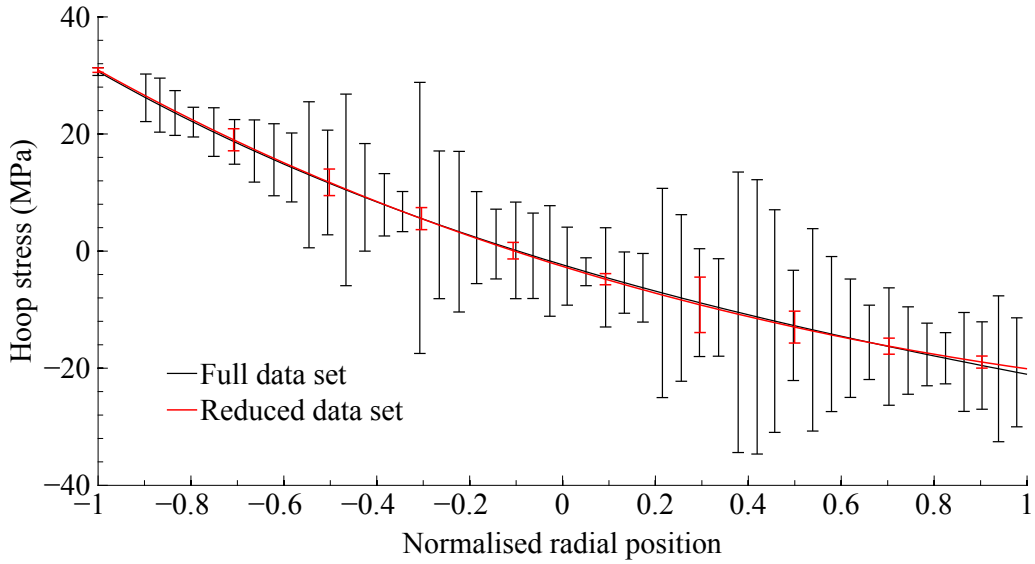

Figure 9.3: Comparison of the hoop stress distributions of the ±55° pipe

data set. As has been discussed, this is solely due to the differences between the thickness of the removed layers, where the errors in stress decrease with increased thickness of the layers. Considering the excellent agreement between the results of all the gauge sets of Fig. 8.5, the magnitude of the error bounds of the reduced data set are seemingly a more accurate indication of the actual experimental error.

The radial stress distributions of both the full and reduced data sets, illustrated in Fig. 9.4, are virtually indistinguishable from one another. The largest deviation between these solutions occurs in the region of the normalised radial position of around 0.6, with a magnitude of around 0.05 MPa. Fig. 9.4 also includes the error bars obtained for each data set. Interestingly, the magnitude of these are very similar for both data sets. The reason for this is quite simple: The radial stresses evaluated at the mid-radius of each removed layer will be very similar to the average of the residual pressure loads applied to the inner and outer surfaces of this layer. Since the errors in the pressure loads do not depend on the thickness of the removed layers, the resulting errors in the radial stresses also do not depend on the thickness of these layers.

The corresponding in-plane shear stress distributions of the full and reduced data sets of the ±55° pipe are illustrated in Fig. 9.5. These are plotted together with the error bounds evaluated at the mid-radius of each removed layer. Deviations between the stress distributions occur across the entire wall thickness of the pipe, but these are all less than 2 MPa. These differences are directly associated with the differences between the polynomials fitted to the strain variations of both of the data sets. As a consequence of the self-correcting mechanism inherent in the current method of residual stress measurement,

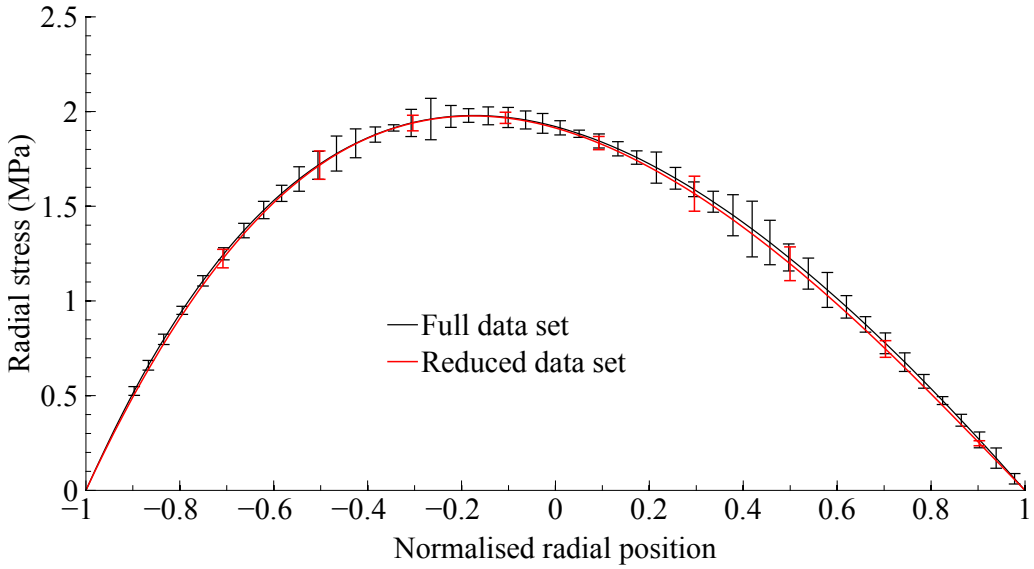

Figure 9.4: Comparison of the radial stress distributions of the ±55° pipe

the shear stress distribution of the reduced data set satisfies the requirement of self-equilibrium. More importantly, the magnitude of the shear stress distribution of this data set is very small in comparison to axial and hoop stress distributions of this pipe. The results of the reduced data set therefore support the assumed orthotropic bulk-scale behaviour of the pipe, and like those of the full data set, can be considered negligible. As with the axial and hoop stress distributions of Figs. 9.2 and 9.3, the magnitude of the error bars of the reduced data set are much smaller than those corresponding to the solution of the full data set. As has been discussed, this is directly associated with the thickness of the removed layers, and the manner in which the errors in the residual stresses are estimated.

It is clear that the through-thickness residual stress distributions of the ±55° pipe could have been accurately measured by considering layers that were considerably thicker than those removed during the experimental component of this work. This is a positive result, and implies that the time required to perform the experiment could have been drastically reduced. The reason for this lies within the nature of the residual stress distributions themselves. These are all relatively simple, and do not vary rapidly through the thickness of the pipe. As a consequence, the measured strain responses are also relatively simple, and can be described by only a few data points. There is therefore virtually no loss in resolution in the strain variations when the number of measured data points is reduced, and consequently the polynomials fitted to the measured variations of the reduced data set are very similar to those originally fitted to the measured strain variations of the full data set. Additionally, the through-thickness residual strain distributions are directly associated with the residual stress distributions, and therefore also do not vary rapidly through the

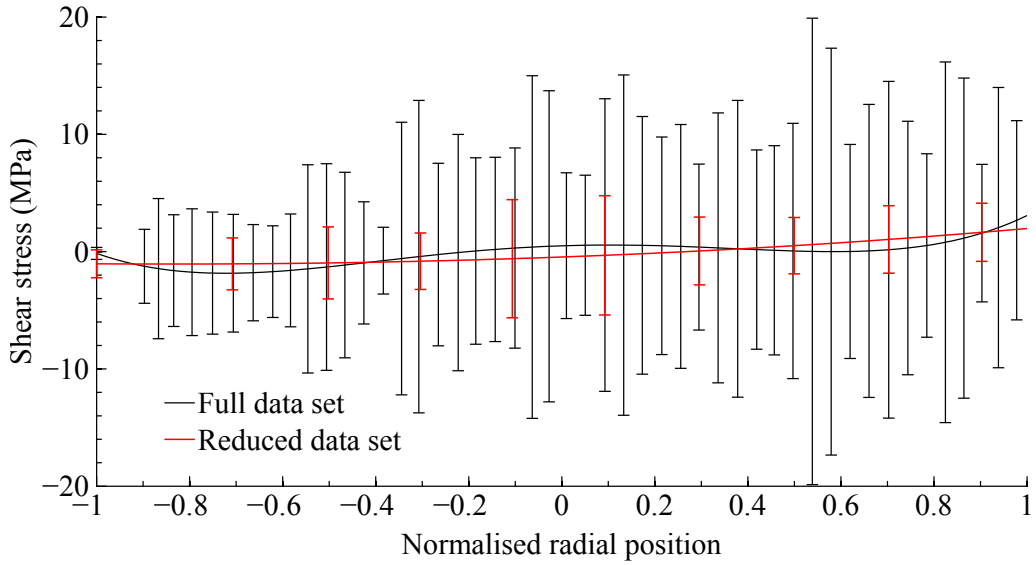

Figure 9.5: Comparison of the shear stress distributions of the ±55° pipe

thickness of the pipe. As a consequence, the average value of the residual strain within any removed layer resides very close to the mid-radius of the layer. This is because the strain variation through this layer can be considered near-linear. It was hypothesised that the constant ϵ_x^0 and γ^0 values evaluated for this layer, utilising the elastic solution, would be very similar to the average values in the variations in ϵ_x and $\gamma_{x\theta}/r$ of this layer, and would therefore coincide with these variations at the mid-radius. Fig. 9.6 illustrates the residual axial strain variation through the thickness of the ±55° pipe, determined from the results of the full data set, along with the ϵ_x^0 values obtained for the removed layers of the reduced data set. The $\gamma_{x\theta}/r$ distribution is not considered, since it is negligible through the thickness of this pipe. It is clear from Fig. 9.6 that the ϵ_x^0 values do indeed match closely with the values of the axial residual strain distribution in the regions of the mid-radius of each removed layer (For clarity these are marked with the dashed lines). There is, however, a minor deviation between the ϵ_x^0 value and the axial strain distribution at mid-radius of the the first removed layer, corresponding to the normalised radial position of 0.9. This deviation is merely the result of the minor differences between the polynomials fitted to the strain variations of the full and reduced data sets. Since the axial strain distribution is accurately described by the ϵ_x^0 values at the mid-radius of each removed layer, the residual stresses obtained for these locations are also accurate, and therefore can be used to describe the state of stress through the entire thickness of the pipe. It is believed that similar results would be obtained even for very large slopes in residual strain, provided they do not vary rapidly though the thickness of the pipe. If the slope in residual strain varied rapidly, then the average strain within a removed layer will not occur in the region of the mid-radius, introducing inaccuracies in the resulting residual stress distributions. Under normal curing conditions, however, the slopes in residual strain through the thickness of

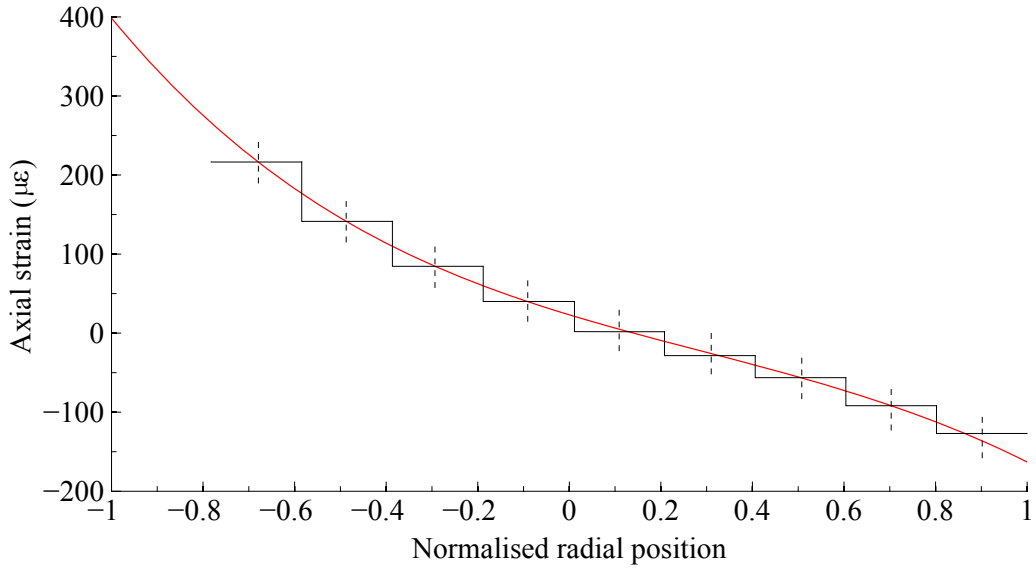

Figure 9.6: Axial strain distribution ±55° pipe

FRP pipes would generally not rapidly vary. Such a condition though, could potentially exist under special circumstances. For instance, if a pipe were intensely ground at the outer or inner surface, additional residual stresses would be introduced and the slope in the residual strains would vary quite rapidly within these regions. Another example is the surface of an isotropic pipe that has been peened. Under these conditions, however, the measured strain responses for the removal of material would also require more data points, since the more complex stress distribution would cause the strain responses to also be more complex. In this sense the thickness of the removed layers would need to be reduced anyway, and the rapid variation in ϵ_x and $\gamma_{x\theta}/r$ values better described at the mid-radius of the thinner layers.

9.2 ±65°/±47° Filament-wound pipe

The reduced data set of the measured axial, circumferential, and 45° strain variations of the ±65°/±47° pipe is presented in Fig. 9.7. These comprise every 5th datum point of the measured strain variations of "Gauge set C", presented in Figs. 8.9 to 8.11. Included in Fig. 9.7 are the least-squares polynomials fitted to each of the reduced strain variations. As with the variations of Figs. 8.9 to 8.11, two separate polynomials were fitted to the strain data corresponding to removal of layers from the outer and inner plies, respectively. The fitting procedure of these was identical to that described in Section 8, where each pair of polynomials was forced through the same value in strain for the region corresponding to removal of material at the ply interface. The polynomials fitted to the strain variations

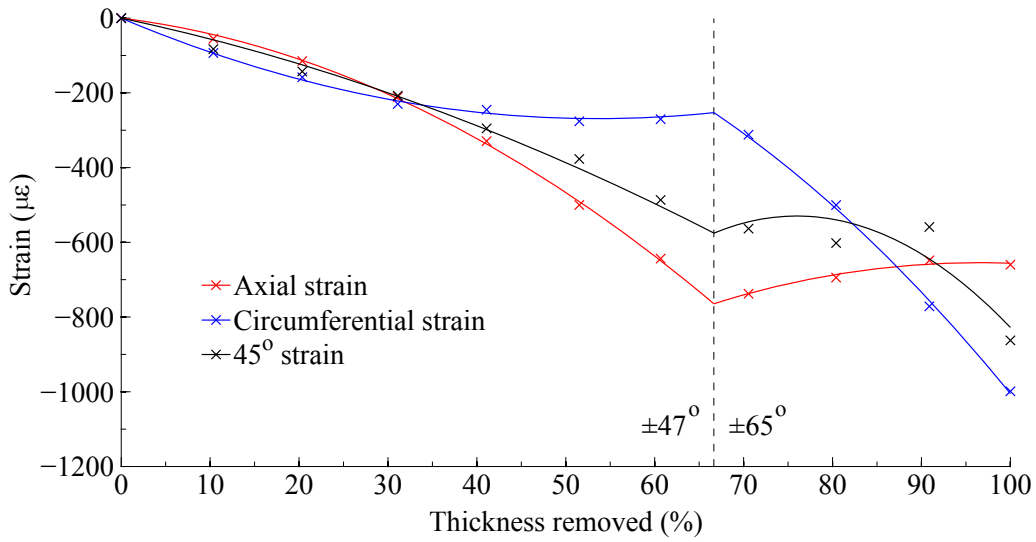

Figure 9.7: Strain responses of the ±65°/±47° specimen for the reduced data set

of the reduced data set, illustrated in Fig. 9.7, were all limited to 2nd order, for removal of material from both the outer and inner plies. The order of these polynomial pairs are quite different to those originally required to fit the strain variations of the full data set of Figs. 8.9 to 8.11, particularly for removal of material from the outer ply.

The corresponding axial stress distribution of the reduced data set is illustrated in Fig. 9.8. Included in this figure is the axial stress distribution of the full data set, which was originally presented in Fig. 8.12. These stress distributions comprise splines fitted to the stresses evaluated at the mid-radius of the removed layers. Due to the inaccuracies associated with the residual strain discontinuity across the ply interface, the value in stress obtained for the layer containing material from both the inner and outer plies was ignored. Included in Fig. 9.8 are the error bars determined for each data set, a consequence of the misfit between the strain data and the corresponding polynomial fits. Over the outer ±47° ply, there are minor differences between the results of the two data sets, the largest occurring at the outer surface of the pipe, with a magnitude of less than 4 MPa. These differences are a direct result of the different order polynomial fits between the full and reduced axial and circumferential strain variations for removal of material from the outer ply. For the region corresponding to the inner ply, the axial stress distributions of the full and reduced data sets are almost indistinguishable from one another. The reason for this is because the polynomial fitted to the axial and circumferential strain variations of the two data sets are virtually identical. The magnitude of the error bars for the reduced data set are significantly smaller than those of the full data set. As has been discussed, these are directly associated with the thickness of the removed layers, and the manner by which the errors are estimated.

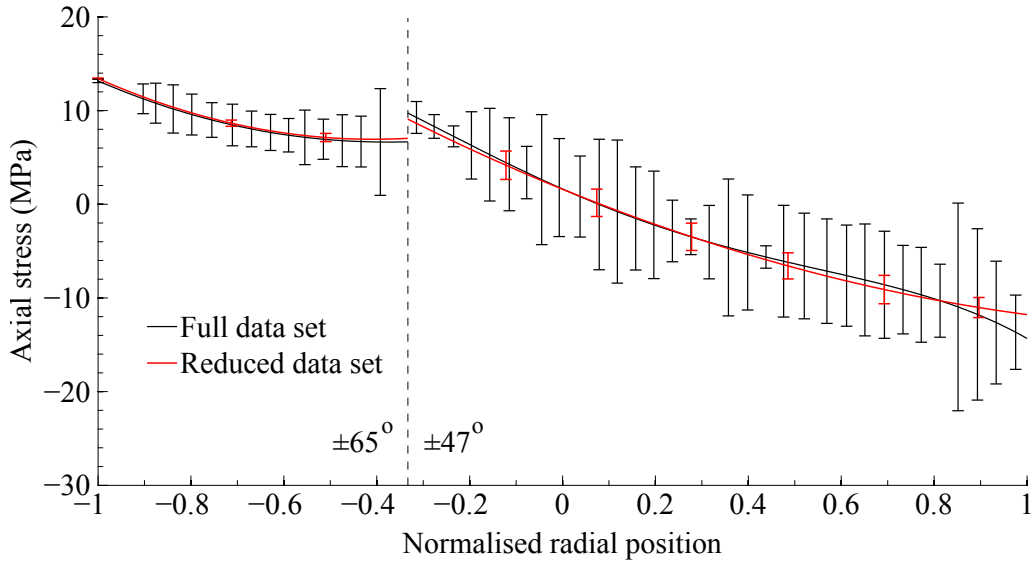

Figure 9.8: Comparison of the axial stress distributions of the ±65°/±47° pipe

The hoop stress distribution of the reduced data set of the ±65°/±47° pipe is illustrated in Fig. 9.9. For comparison purposes, the residual hoop stress distribution of the full data set, presented in Fig. 8.13, is included in this figure. Both stress distributions are plotted together with the the error bars evaluated at the mid-radius of the removed layers. Once again, the results obtained for the layer comprising material of both the inner and outer plies was ignored, due to the presence of a residual strain discontinuity across the ply interface. The hoop stress distributions of both the full and reduced data sets are in excellent agreement with one another, and share almost identical trends. Based on the spline fits, the largest mismatch between the stress distributions occurs at the outer surface of the pipe, as well as in the inner ±65° ply, at the ply interface. These differences are both less than 2 MPa. The magnitude of the error bars of the reduced data set are much smaller than those determined for the solutions of the full data set, owing to the differences in the thickness of the removed layers of these data sets.

The radial stress distributions of the ±65°/±47° pipe, obtained for both the full and reduced data sets, are illustrated in Fig. 9.10. Despite the presence of the discontinuity in residual strain at the ply interface, the stress distribution of the reduced data set includes the result for the mid-radius of the layer comprising material of both plies. This was included since the radial stresses across the ply interface must be continuous, a requirement enforced by the elastic solution. The strain discontinuity thus has little effect on the resulting radial stress determined for this region. It is clear from Fig. 9.10 that the trends in the radial stress distributions of both the full and reduced data sets are very similar. There is, however, some loss in the resolution of the stress distribution of the reduced data set, specifically for the region corresponding to the ply interface. Based on the

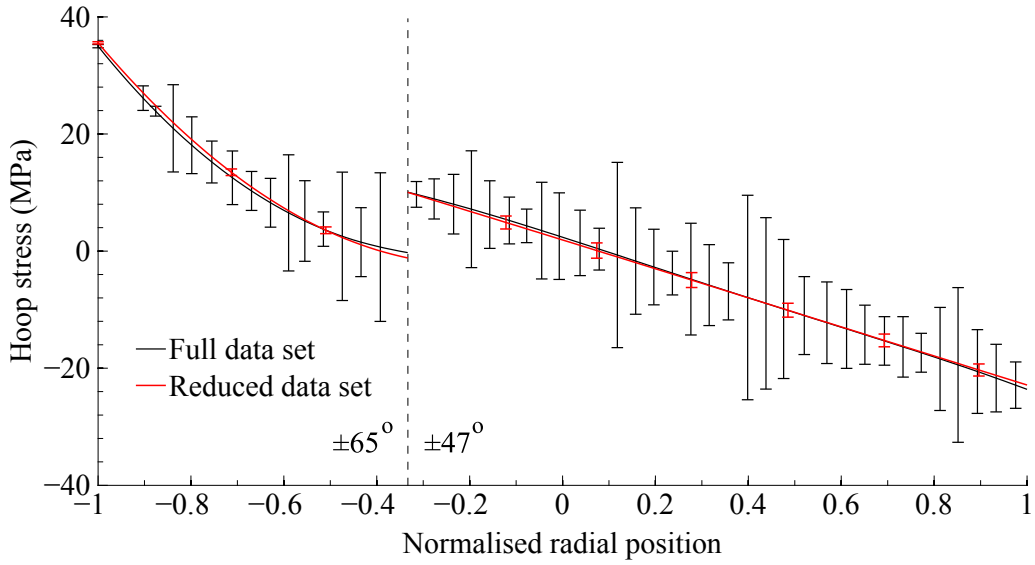

Figure 9.9: Comparison of the hoop stress distributions of the ±65°/±47° pipe

spline fits, the magnitude of the difference between the stress distributions in this region is about 0.15 MPa. This difference, is very small and can be considered negligible. As has been discussed, the magnitude of the bounds of error of the radial stresses are independent of the thickness of the removed layers. As a consequence, the magnitude of the error bars of both data sets are very similar.

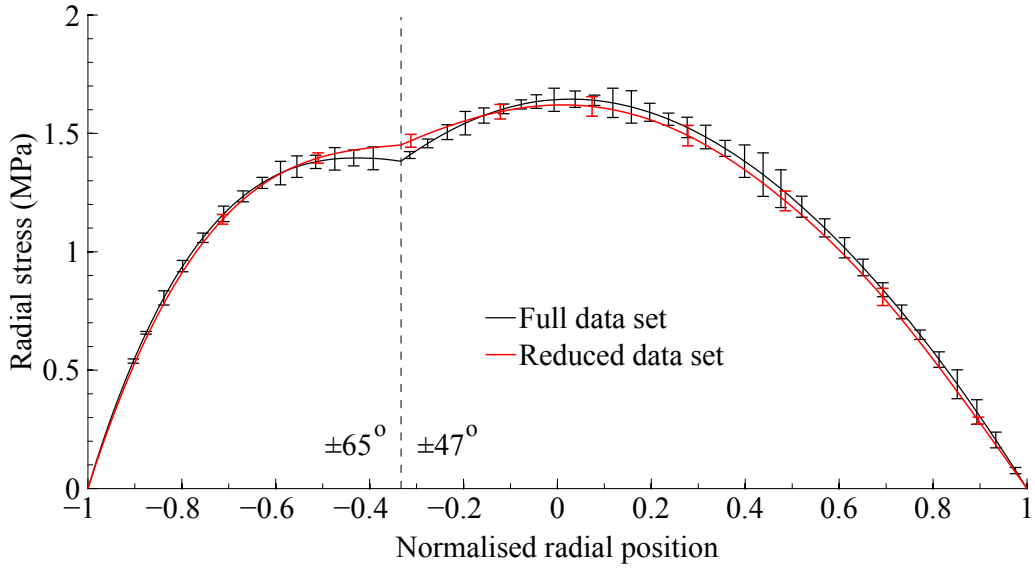

Figure 9.10: Comparison of the radial stress distributions of the ±65°/±47° pipe

The bulk-scale shear stress distributions of both the full and reduced data sets of the ±65°/±47° pipe are illustrated in Fig. 9.11. Over the outer ±47° ply, the largest difference

between both stress distributions occurs at a normalised radial position of roughly 0.2, with a value of less the 2.5 MPa. For the inner ply, the largest difference between the distributions of both data sets occurs in the region of the ply interface, with a magnitude of roughly 5 MPa. This deviation is a direct result of the scatter in the measured 45° strain response for removal of material from the inner ±65° ply, which causes considerable differences between the least-squares polynomials fitted to the strain variations of full and reduced data sets of Figs. 8.11 and 9.7, respectively. The shear stress distribution of the reduced data set, however, still oscillates about the zero stress line, and has an average magnitude much smaller than those of the axial and hoop stress distributions of this pipe. Therefore this stress distribution can still be considered negligible, and these results still support the assumed orthotropic nature of this pipe. The magnitude of the error bars of the reduced data set are considerably smaller than those obtained for the full data set. As has been discussed, this is simply due to the differences in the thickness of the removed layers of these data sets, and the manner by which these are found.

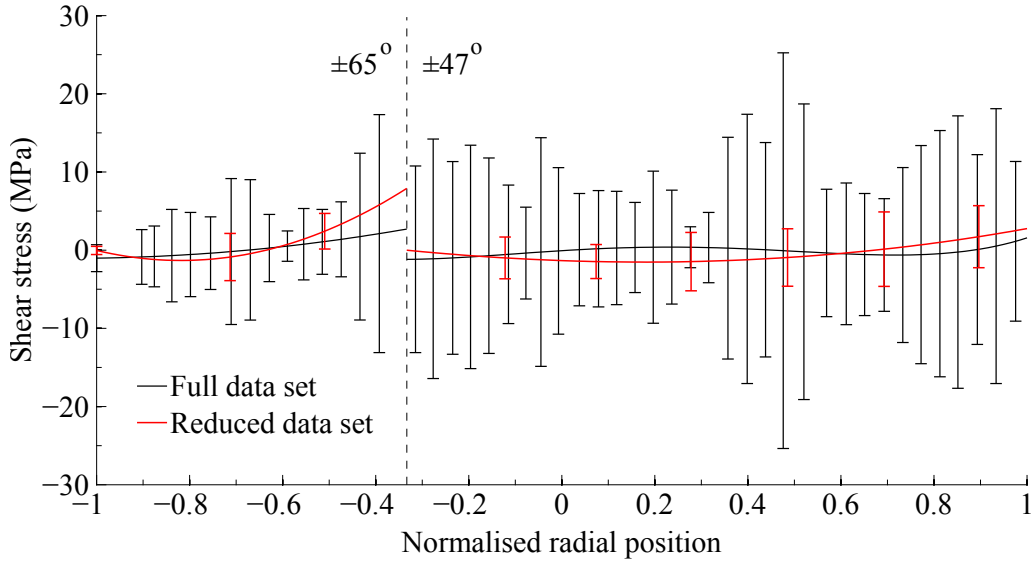

Figure 9.11: Comparison of the shear stress distributions of the ±65°/±47° pipe

The excellent agreement between the axial and hoop residual stress distributions of the full and reduced data sets of the ±65°/±47° pipe, illustrated in Figs. 9.8 and 9.9, indicates that the measured axial and circumferential strain responses are adequately described by the strain variations of the reduced data set. Additionally, the residual axial strain distribution does not vary rapidly through the thickness of the ±65°/±47° pipe. In this sense, the stresses calculated at the mid-radius of each removed layer, under the assumption of constant axial strain, ϵ_x^0, align well with the actual residual stresses that were present, prior to any material removal. This was previously demonstrated in Fig. 9.6 for the ±55° pipe. The radial stress distributions of both data sets are also in good agreement, with

negligible differences. It does, however, appear that some resolution in the region of the ply interface is lost when thick layers are removed. Although the resulting shear stresses still indicate a zero-shear stress state at the bulk scale, significant differences in the results of the two data sets in the region of the ply interface, within the inner ±65° ply do occur. As discussed, this is purely a result of the scatter seen by the 45° strain gauge for removal of material from the inner ply of the pipe, causing significant differences between the polynomial fits of the full and reduced data sets to arise.

9.3 ±75°/±36° Filament-wound pipe

The reduced axial, circumferential and 45° strain variations of the ±75°/±36° pipe, along with the respective least-squares polynomial fits, are presented in Fig. 9.12. As with the measured strain variations of the full data set of this pipe, presented in Figs. 8.17 to 8.19, two separate polynomials were required to fit the data corresponding to removal of material from the outer and inner plies. The polynomials required to adequately describe the axial and 45° strain variations for removal of material from the outer ply were of 4th and 3rd order, respectively. All other polynomials were limited to 2nd order. Generally, the least-squares polynomials fitted to the strain data of the reduced data set are of lower order than those fitted to the strain variations of the full data set, as a consequence of the reduced number of data points. As with the previous strain fits of the laminated pipes, the pairs of polynomials corresponding to removal of material from the outer and inner plies were forced to pass through the same value in strain for the region of material removal from the ply interface. The process followed to ensure this has already been discussed in depth.

The corresponding axial stress distribution of the reduced data set of the ±75°/±36° pipe is illustrated in Fig. 9.13. Due to the presence of the residual strain discontinuity at the ply interface, the axial stress obtained for the layer comprising material from both the inner and outer plies was ignored. Included in this figure is the axial stress distribution of the full data set, which was originally presented in Fig. 8.20. These distributions are plotted together with the error bars estimated, using the method described in Section 5. The stress distributions of both data sets are in excellent agreement with one another over the entire thickness of the pipe. Based on the spline fits, the maximum deviation between these distributions occurs within the inner ply, in the region of the ply interface. The magnitude of this difference is about 1.5 MPa. For the outer ±36° ply, the stress distribution of the reduced data set is seemingly more wavy than that of the full data set, but the extent of this waviness results in negligible differences between the two distributions. The largest difference between these occurs in the region of the ply interface, with a magnitude of just more than 1 MPa. The trends in stress distributions over the inner ±75° ply are very

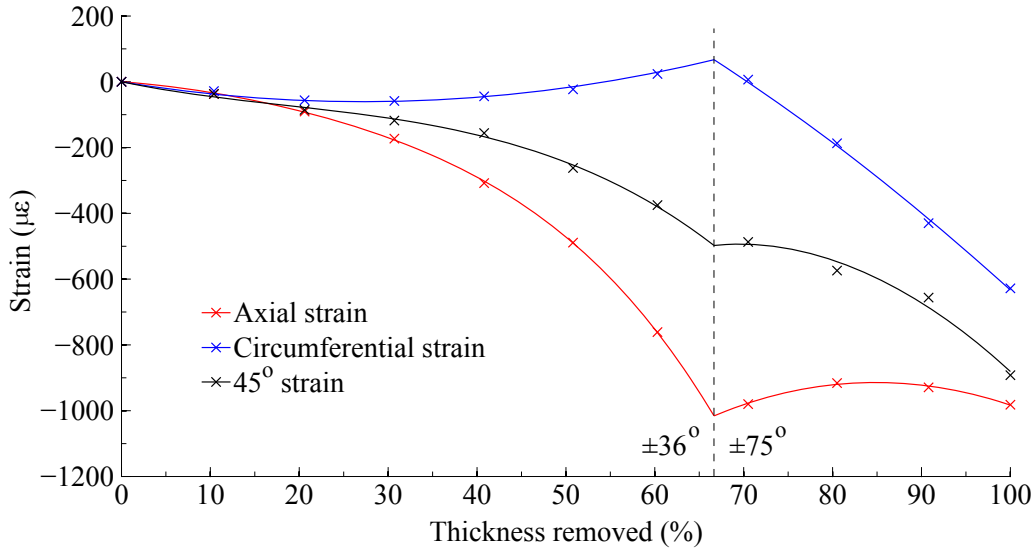

Figure 9.12: Strain responses of the ±75°/±36° specimen for the reduced data set

similar, and are almost identical between the normalised radial positions of -1 and -0.7. As expected, the magnitude of the error bars of the reduced data set are significantly smaller than those of the full strain data set. The bounds of these error bars are seemingly more accurate, considering the good agreement in the stress distributions determined for the three different gauge sets of this pipe, which can be seen in Fig. 8.20.

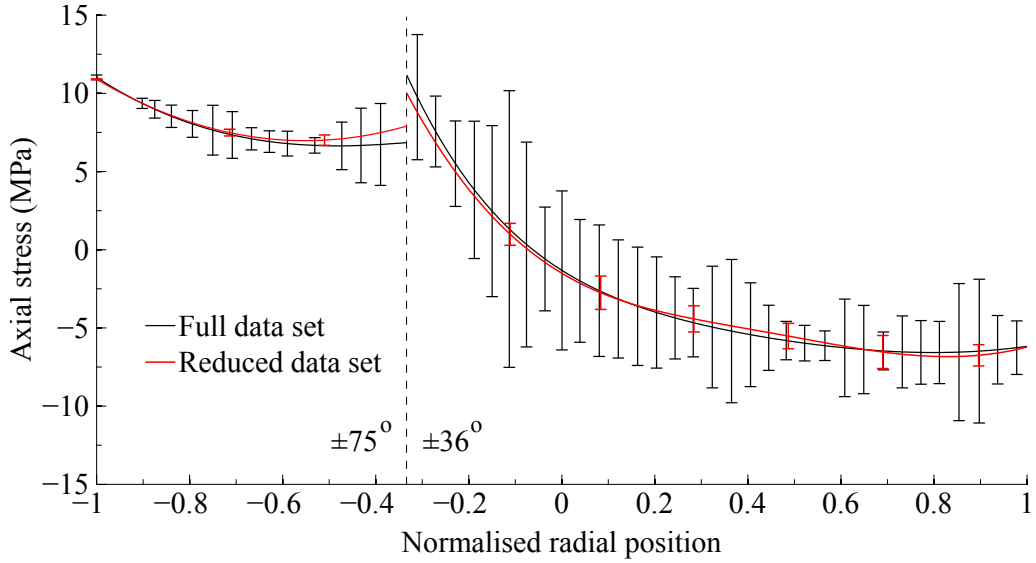

Figure 9.13: Comparison of the axial stress distributions of the ±75°/±36° pipe

The hoop stress distributions of the full and reduced data sets of the ±75°/±36° pipe are presented in Fig. 9.14. These distributions comprise splines fitted to the stresses evaluated at the mid-radius of the removed layers. Due to the presence of a residual strain

discontinuity across the ply interface, the hoop stress determined for the layers comprising material from both the outer and inner plies was ignored. Included in this figure are the error bars estimated for the solutions of each data set. The stress distributions of these data sets are in excellent agreement with one another. The largest differences between these distributions occurs over the outer ±47° ply, at the normalised radial positions of -0.33, 0.4, and 1. The magnitude of these differences are all roughly 2 MPa, which amounts to less than 8% of the maximum stress, which occurs at the inner surface of the pipe. The minor differences in the stress distributions are directly associated with the differences in the polynomials fitted to the axial and circumferential strain variations of the two data sets. It cannot be said that there is a loss of resolution in the results of the reduced data set, since both stress distributions are equally feasible solutions. Over the inner ply, the stress distributions of both data sets are almost identical. The maximum difference between the distributions for this ply occurs at the ply interface, with a magnitude of around 1 MPa. The magnitude of the error bounds of the reduced data set is significantly smaller than that obtained for the full data set, due to the differences in the thickness of the removed layers of these data sets, and the manner in which these errors are estimated.

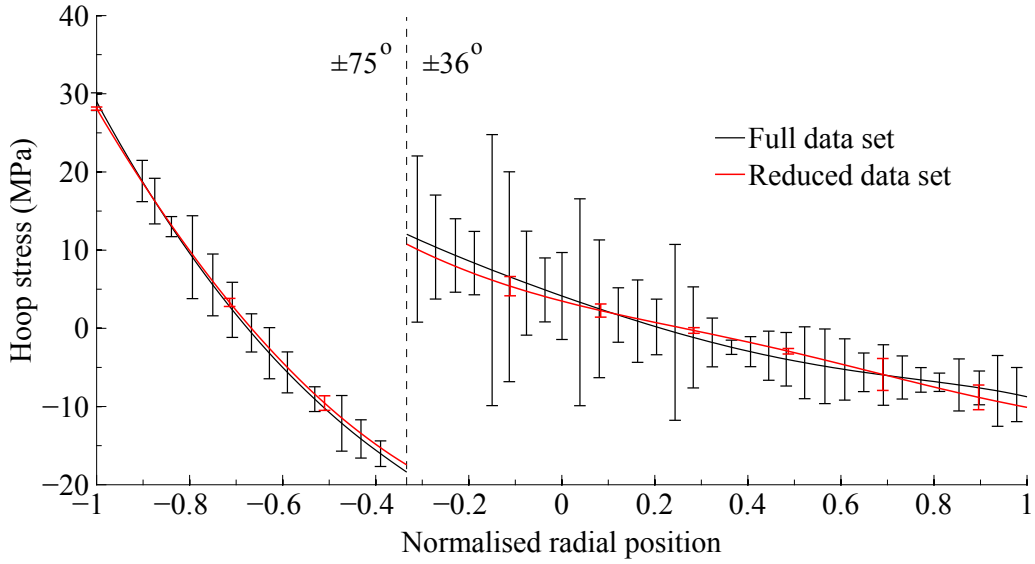

Figure 9.14: Comparison of the hoop stress distributions of the ±75°/±36° pipe

The corresponding in-plane shear stress distributions of the full and reduced data sets of the ±75°/±36° pipe are illustrated in Fig. 9.15. Over the wall thickness, the shear stress distributions obtained for both data sets are quite different. Based upon the spline fits, the largest difference between these occurs at the outer surface of the pipe, with a magnitude of just less than 3 MPa. Over the inner ply, the largest difference between the stress distributions occurs at the ply interface, with a magnitude of less than 2 MPa. It would appear from these results that there is a loss in the resolution of this stress when the

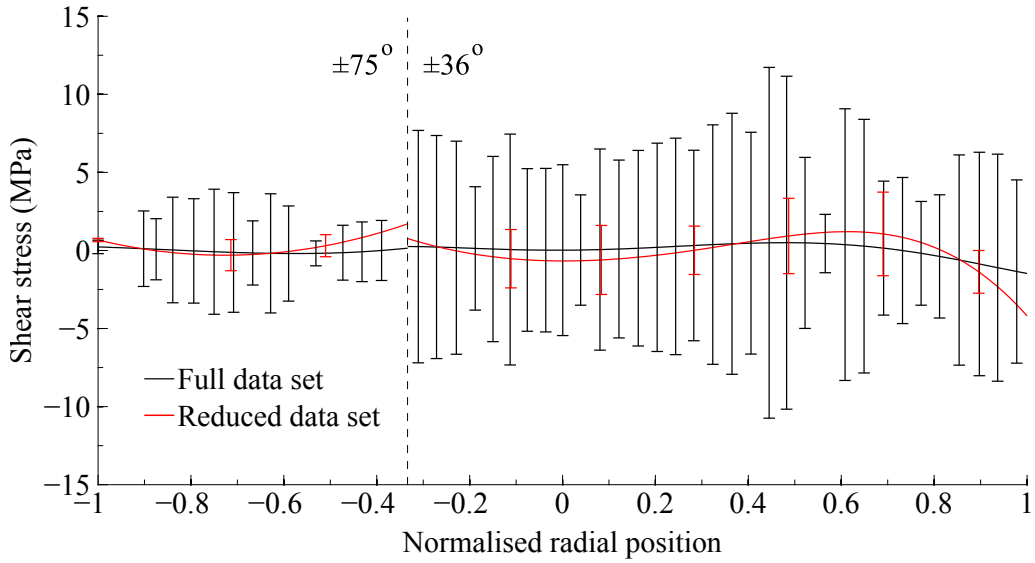

Figure 9.15: Comparison of the shear stress distributions of the ±75°/±36° pipe

thickness of the removed layers is increased, since these lie further from the expected zero-stress line. Over the entire wall thickness, however, the stress distribution of this data set still oscillates about the zero-stress line, and is of relatively low magnitude. These results therefore still support the assumption of orthotropic material properties, and the consequent absence of these stresses through the thickness of the pipe. The differences between the distributions of the full and reduced data sets may seem large, but this is only with respect to the expected zero-stress state. In relation to the magnitude of the axial an hoop stress distributions of this pipe, illustrated in Figs. 9.13 and 9.14, these differences can be considered negligible, and thus the loss of resolution in the results of the reduced data set is also negligible. The error bars of the reduced data set are significantly smaller than those of the full strain data set, due to the manner by which these are estimated.

The radial stress distributions of the full and reduced data sets are presented in Fig. 9.16. For reasons already discussed, the radial stress distribution of the reduced data set includes the stress evaluated at the mid-radius of the layer comprising material from both plies. The stress distributions of both data sets are quite different. It is clear that the results of the reduced data set do not sufficiently resolve the radial stress distribution of this pipe. This loss in resolution is significantly more severe than obtained for the radial stress distribution of ±65°/±47° pipe, illustrated in Fig. 9.10. Although the maximum difference in magnitude in the residual stress distributions of Fig. 9.16 is less than 0.2 MPa, this is significant compared to the maximum value around of 0.8 MPa, which occurs at the normalised radial position of -0.7. The loss in the resolution is directly associated with the form of this stress distribution. As has been discussed, the radial stress determined at the mid-radius of a particular removed layer will be the somewhat averaged value of the

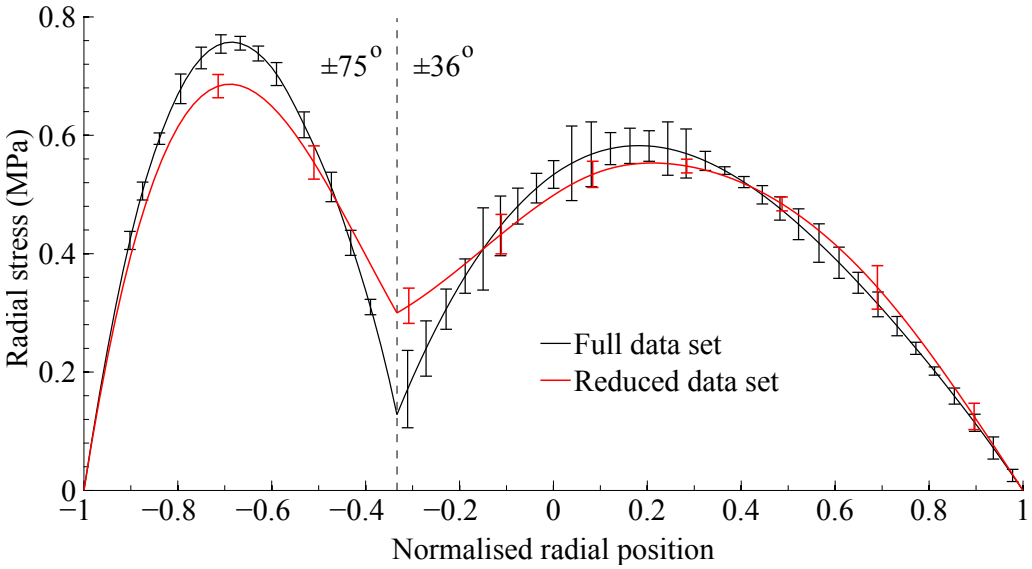

Figure 9.16: Comparison of the radial stress distributions of the ±75°/±36° pipe

residual pressure loads applied to the outer and inner surfaces of this layer. Since the radial stress distribution of this pipe varies rapidly through the wall thickness, particularly in the region of the ply interface and within the inner ply, it cannot be accurately resolved by considering the removal of thick layers, simulated by the reduced data set. The magnitude of the error bars obtained for both data sets are similar, and are directly associated with the error in the residual pressure loads applied to the outer and inner surfaces of each layer. These error bounds, therefore, do not highlight the loss of resolution in the results of the reduced data set.

The excellent agreement between the axial and hoop stress distributions of Figs. 9.13 and 9.14 indicates that the trends in the measured axial and circumferential strain variations of this pipe are adequately described by the strain variations of the reduced data set. Also, as discussed for the ±55° pipe, the axial strain response does not rapidly change through the wall thickness of the pipe. In this sense, the assumption of constant axial strain of the elastic solution produces results that are accurate for the mid-radius of each removed layer. The differences between the in-plane shear stress distributions of the full and reduced data sets, illustrated in Fig. 9.15, are negligible with respect to the magnitude of the axial and hoop stress distributions of this pipe. Additionally, the shear stress distribution obtained for the reduced data set oscillates about the zero-stress line, which supports the assumed orthotropy of this pipe. Unfortunately, the results of the reduced data set do not accurately describe the radial stress distribution of this pipe, and the thickness of the removed layers would need to be decreased to resolve this issue. Since the strain variations of this pipe are accurately defined by the reduced data set, this can be done numerically. Based on the polynomials fitted to the strain variations of the reduced

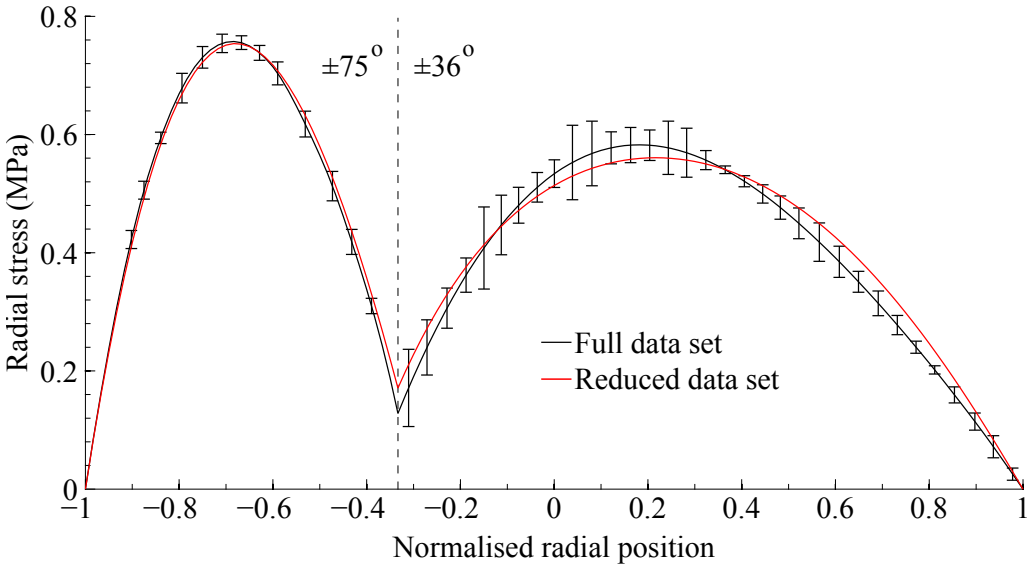

Figure 9.17: Comparison of the radial stress distributions of the ±75°/±36° pipe, based upon numerically decreased layer thickness

data set, shown in Fig. 9.12, a total number of 50 layers was simulated to be removed. The resulting radial stress distribution is presented in Fig. 9.17, along with the stress distribution originally obtained for the full data set. It is clear from this figure there has been a significant improvement in the results of the reduced data set. The radial stress distributions of both data sets are now in excellent agreement, and maximum deviation between these has been reduced to less than 0.08 MPa. No error bars are presented for the improved reduced data set solution, as these cannot be estimated for the simulated layers, using the manner presented in Section 5. In this case, however, the error bounds originally found for this data set, illustrated in Fig. 9.16, could be used.

It can be concluded from this investigation that the residual stresses within all of the GFRP pipes considered could have been accurately measured by removing thicker layers from the outer surface of the pipes. Consequently, the time required to perform such an experiment can be significantly reduced.

10 Further investigation: Error analysis

Section 9 demonstrates that the residual stress state within any typical filament-wound pipe can be accurately measured by removal of relatively thick layers, provided that there is no loss in resolution in the measured strain variations. This is a positive result, since the time required to perform the layer removal experiment can be significantly reduced. In addition to this result, the investigation of Section 9 also highlights an issue with the current method of error analysis. This issue is the direct dependence of the error bounds on the thickness of the removed layers. As the thickness of the removed layers increases, so the magnitude of the errors in axial, hoop and in-plane shear stress decreases. Although the method of error analysis, presented in Section 5, is mathematically sound, one could infer from this behaviour that the removal of thicker layers results in stress distributions that are more accurate than those measured by the removal of thinner layers. This conclusion, however, defies any logic, and in reality one would expect a lower level of error associated with the measurement of more experimental data points. In this sense the bounds of error presented for both the full and reduced data sets of Sections 8 and 9 are not true indications of the error in the measured residual stress distributions. For this reason, the uncertainty analysis needs to be reformulated, so that the true bounds in experimental error can be estimated. The present section deals with this issue, and presents a new method of error analysis. This method is based upon a sensitivity analysis of the stress distributions to the level of scatter in the measured strain data. As has been discussed, this scatter exists not only as a consequence of the inherent error associated with the measurement procedure, but also due to real effects associated with the meso-scale anisotropy that locally affect the strain response measured by each gauge set.

10.1 Basis of error analysis

A sensitivity analysis is an investigation whereby the uncertainty of the output of a model can be attributed to variations in the inputs of the model. In the case of the current method of residual stress measurement, the input parameters are the measured strain

variations, and the output parameters are the residual stress distributions. By varying the input strain responses, the variation of the resulting residual stress distributions, and thus the uncertainties, can be quantified. Variations in strain were generated by addition of scatter to the "exact" strain responses, which were taken as the least-squares polynomials fitted to the experimentally measured strain data. To eliminate the effect of any single set of scatter simulated using this technique, a total of 100 sets of scatter were generated for each data set. Least-squares polynomials were fitted to each simulated strain response, and the corresponding residual stresses associated with these polynomials were determined. The standard deviation (SD) of the stress distributions were used to estimate the error bounds. The thickness of the removed layers of each data set was maintained as identical to those removed from the pipes during the experiment. The scatter added to each "exact" strain datum point took the form of a random value, constrained by the normal distribution [233]. The magnitude of the scatter was governed by the variation in the SD of the experimentally measured data about the corresponding "exact" polynomial fits. These were determined for each strain gauge orientation of each pipe configuration, and are presented in Appendix L. Constraining the scatter added to the "exact" strain variations in this sense ensures that the levels of uncertainty in the simulated data points remain similar those of the experimentally measured strain data. Since the thickness of the removed layers was maintained, and the level of scatter generated similar to the scatter in the experimentally measured data, the error bounds presented in this section can be considered an estimate of the actual error in the measured stress distributions.

Since the order of polynomial fitted to a specific strain variation relies solely on the discretion of the researcher performing the analysis, a range of polynomial fits and combinations of fits needed to be considered for each simulation. Therefore, for each simulated strain variation, a range of possible residual stress distributions exist, each a plausible solution. The order of each strain fit, however, was still kept relatively low to avoid excess waviness within the resulting stress distributions. The range of polynomials chosen varied between 2nd and 4th order for the $\pm 55^{\circ}$ and $\pm 65^{\circ}/\pm 47^{\circ}$ pipes, and between 2nd and 5th order for the $\pm 75^{\circ}/\pm 36^{\circ}$ pipe. As with Section 9, only the results of "Gauge set C" of each pipe configuration are considered, and 100 simulations performed for both the full and reduced data sets of the pipes. All of the simulated strain variations and corresponding stress distributions of the $\pm 55^{\circ}$ pipe are presented in this section, while the majority of those corresponding to the other two pipe configurations are presented in Appendix M. These distributions were used to estimate the magnitude of the error of each stress component. In this section, the improved error bars are plotted together with the experimentally measured stress distributions of both the full and reduced data sets of each pipe configuration, and compared to those originally determined using the manner described in Section 5.

Previously, error bars were estimated by considering the difference between each measured datum point and the value of the polynomial fitted to the strain variation, and the error in stress evaluated directly from these differences. Therefore, all scatter within the strain data was considered to correspond with real possible solutions. The analysis of this section finds an estimate of the error bars by considering the solutions obtained from the polynomial fits, for a large number of simulated strain variations. The error associated with a particular datum point is therefore found, not by considering the possible solutions associated with the scatter in the datum point itself, but rather by considering the influence of the scatter on the polynomial strain fits. The error bounds are therefore somewhat smoothed in a similar sense to the way that Prime and Hill [173] use "covariances" to estimate the errors in stresses measured using the crack compliance method. Additionally, considering a range of polynomials fitted to each strain variation to estimate the error bounds takes into account what Prime and Hill [173] refer to as "model error". These authors estimate the model error of the crack compliance method by considering the differences in the stress solutions associated with different series expansion orders [173].

10.2 $\pm 55^{\circ}$ Filament-wound pipe

The sensitivity analysis of the $\pm 55^{\circ}$ pipe was performed on both the full and reduced data sets of "Gauge set C". For each simulation, scatter was added to the baseline "exact" strain variations, taken as the least-squares polynomials originally fitted to the measured strain responses of both data sets. As previously discussed, the scatter added to the "exact" strain response took the form of random values, constrained by the normal distribution with a variable SD, dependant on the amount of material removed. The SD values governing the magnitude of the scatter added to the "exact" strain responses were obtained from polynomials fitted to the SD variations determined for the experimentally measured strain data. These SD variations are presented in Appendix L. The general trend in these variations is an increase in SD, and thus an increase in scatter, with increased material removal. As already mentioned, the thickness of the layers removed from this pipe during the experiment were maintained in the simulated strain variations, so that the errors estimated from the corresponding stress distributions can be considered the actual error of the measured stress distributions. For this pipe configuration, the polynomials fitted to each simulated strain response were constrained to between 2nd and 4th order. Since the material is considered orthotropic, the polynomials fitted to the simulated 45° strain data do not affect the resulting axial, hoop and radial stress distributions. Thus, for a single simulation, there exists 9 possible solutions in axial, hoop and radial stress, owing to the different combinations of each of the 2nd to 4th order polynomials fitted to the simulated axial and circumferential strain variations. Since the shear strain response depends on the

polynomials fitted to the responses of all three gauge orientations, there exist 27 different possible solutions in shear stress. MATLAB software was used to generate 100 different strain variations, producing a total of 900 different axial, hoop, and radial stress distributions, and 2700 different shear stress distributions. This was done for both the full and reduced data sets of this pipe.

10.2.1 Full data set

Strain simulations

The 100 simulated axial strain variations of the full data set of the $\pm 55^{\circ}$ pipe, along with the 2nd to 4th least-squares polynomials fitted to each variation, are presented in Fig. 10.1. The order of each polynomial fit is denoted by "n". Included in this figure is the "exact" 3rd order polynomial, originally fitted to the measured data of "Gauge set C", presented in Fig. 8.1. This strain response is plotted in Fig. 10.1 as the thick black continuous line, and is the response upon which the scatter was added to generate the simulated strain variations. It is clear from this figure that the scatter in the simulated data increases with increased removal of material, as defined by the SD variations of Appendix L. All polynomials were, as required, forced to pass through a value of zero strain for 0% material removed. There is a distinct difference between the 2nd and 4th order polynomial fits, while the 3rd and 4th order fits seem to bunch together with similar trends. For about 20% of the wall thickness removed, the differences between the upper and lower bounds of the polynomial fits is roughly 40 $\mu\epsilon$. The upper bounds of within this region are defined by 2nd order polynomial fits, while the lower bounds are defined by the 3rd and 4th order polynomial fits. The difference between the upper and lower bounds of the fits then decreases slightly to about 30 $\mu\epsilon$ for 40% thickness removed, and this range is more of less maintained through to about 60% of the thickness removed. From this point, the difference between the upper and lower bounds of the polynomial fits increases gradually to approximately 70 $\mu\epsilon$ for 100% material removed. Over most of the range of material removal, the upper and lower bounds of the simulated data points lie well beyond the upper and lower bounds of the polynomial fits, and these fits are thus constrained to lie close to the "exact" strain response. The reason for this lies within the number of data points describing each simulated strain variation. Since the number of data points is high, the probability that of all these data points lie either well above or below the "exact" strain response is very low. The result is that the least-squares polynomials fitted to each simulated variation lie relatively close to the "exact" strain response. This type of behaviour can be expected in any experimental situation, and is the reason why a lower level of uncertainty can be expected with the measurement of more experimental data

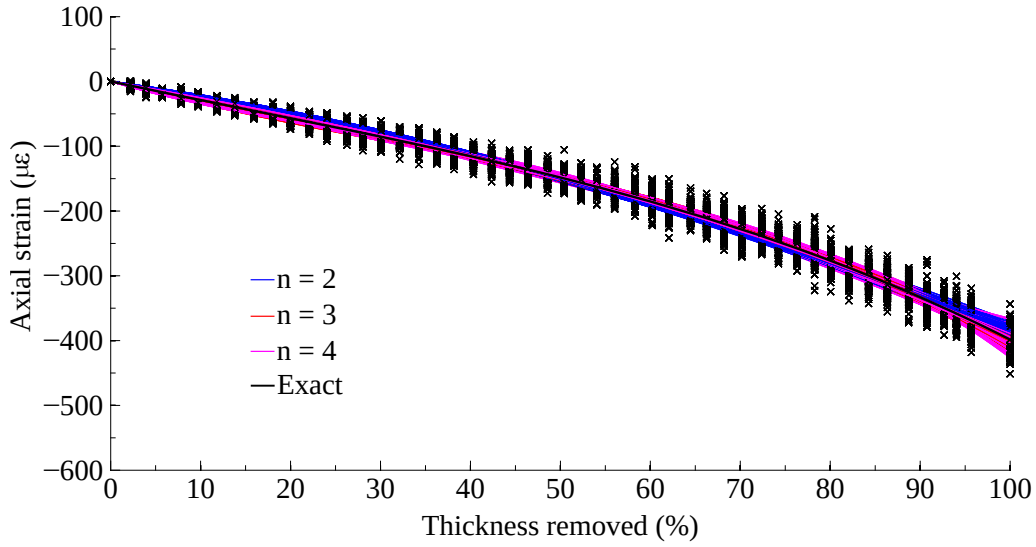

Figure 10.1: Simulated axial strain variations and polynomial fits for the full data set of the ±55° pipe

points.

The simulated circumferential strain variations for the full data set of the ±55° pipe, along with the corresponding 2nd to 4th order least-squares polynomial fits, are presented in Fig. 10.2. Included in this figure is the "exact" 2nd order polynomial, originally fitted to the measured strain data "Gauge set C", seen in Fig. 8.2. This is the response that served as the basis upon which the scatter was added to generate the simulated data points. As with the axial strain simulations of Fig. 10.1, it is clear that the scatter in the simulated data increases with increased removal of material, a consequence of the experimental SD variation determined for this gauge orientation, presented in Appendix L. The difference between the upper and lower bounds of the polynomial fits increases gradually from zero at 0% thickness removed to about 100 $\mu\epsilon$ at 100% thickness removed. Over the entire range of material removal, the upper and lower bounds of the simulated data points lie well beyond the upper and lower bounds of the fits. The region where this is most severe corresponds to roughly 94% thickness removed, where the maximum difference between the simulated data points is about 200 $\mu\epsilon$, while the difference between the upper and lower bounds of the polynomial fits for this region is approximately 70 $\mu\epsilon$. As has been discussed, the fits are somewhat constrained to lie relatively close to the "exact" strain variation, as a consequence of the large number of data points describing each strain variation. Unlike the polynomial fits of Fig. 10.1, there appears to be no particular distinction between the different order polynomials over most of the range of material removal. The highest order polynomials do, however, clearly define the upper and lower bounds of the fits between 65% and 100% of the thickness removed.

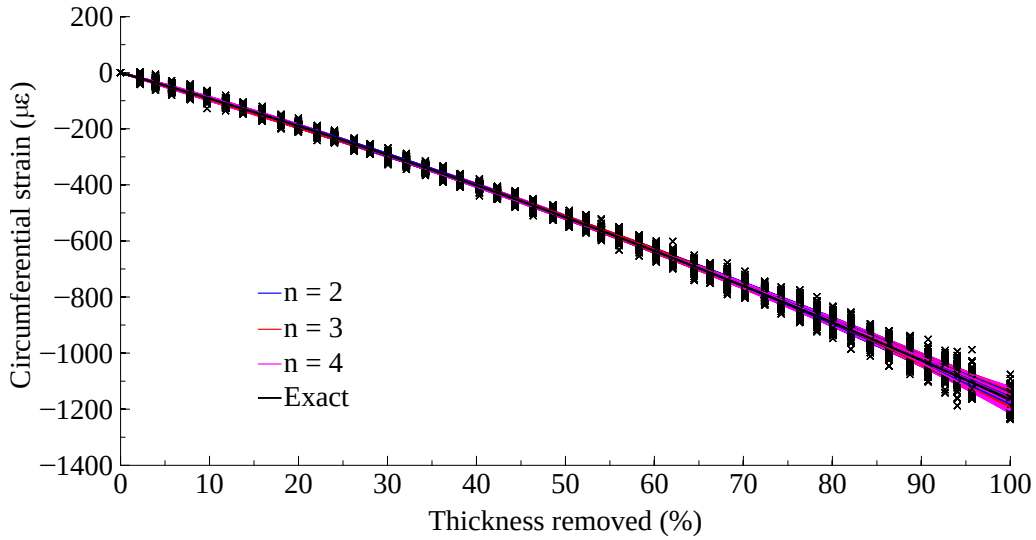

Figure 10.2: Simulated circumferential strain variations and polynomial fits for the full data set of the ±55° pipe

The 100 simulated 45° strain variations of the full data set of the ±55° pipe, together with the corresponding 2nd to 4th order polynomials fitted to these data, are presented in Fig. 10.3. The "exact" 4th order polynomial originally fitted to the measured 45° response of "Gauge set C", illustrated in Fig. 8.3, is included in Fig. 10.3. This response is represented by the thick black line, and formed the basis upon which scatter was added to produce the simulated strain variations. The increase in scatter in the simulated 45° strain variations with material removal is noticeably larger than that obtained for the axial and circumferential strain simulations of Figs. 10.1 and 10.2. This behaviour is a consequence of the experimental SD variation for this gauge orientation, presented in Appendix L. The largest difference between any two simulated data points occurs for about 96% thickness removed, with a magnitude of more than 250 $\mu\epsilon$. Across the entire range of material removal, there is a clear distinction between the trends of the different order polynomial fits, and the upper and lower bounds of these lie well within the upper and lower bounds of the simulated data points over most of this region. The difference between the upper and lower bounds of the polynomial fits increases from zero at 0% thickness removed to around 35 $\mu\epsilon$ for 15% thickness removed. This range then gradually decreases to around 28 $\mu\epsilon$ towards 50% thickness removed. Thereafter, the difference between the upper and lower bounds of the fits gradually increases to roughly 75 $\mu\epsilon$ at 90% thickness removed, followed by a rapid increase to approximately 200 $\mu\epsilon$ at 100% material removed.

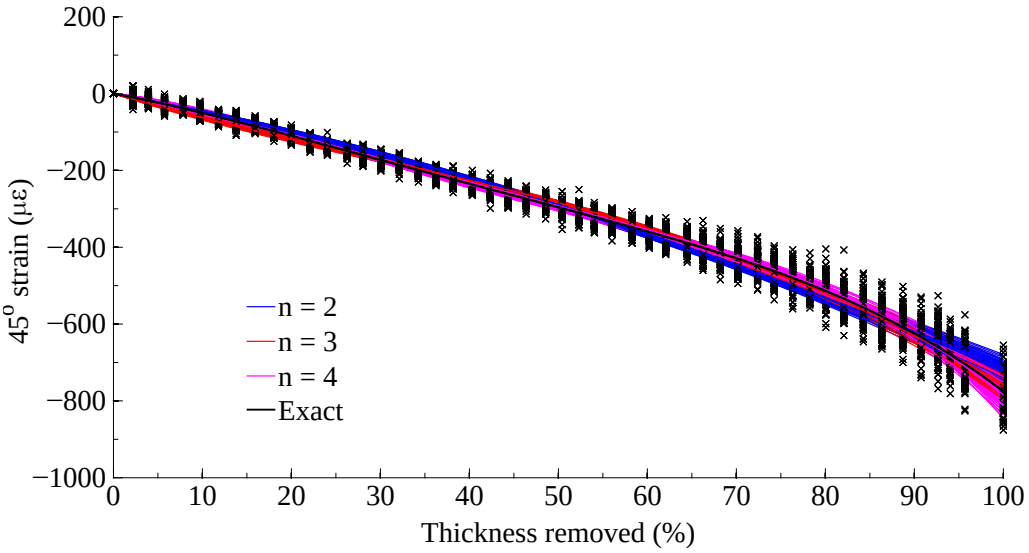

Figure 10.3: Simulated 45° strain variations and polynomial fits for the full data set of the ±55° pipe

Residual stress distributions

The 900 axial residual stress distributions of the full data set of the ±55° pipe, associated with all the combinations of the 2nd to 4th order polynomials fitted to the simulated axial and circumferential strain variations of Figs. 10.1 and 10.2, are plotted in Fig. 10.4. Each stress distribution comprises splines fitted to the axial residual stress determined at the mid-radius of each layer, and is colour coded according to the order of polynomial fitted to the simulated strain variation to which it corresponds. The upper and lower bounds of the stress solutions lie almost completely symmetrically about the "exact" stress distribution. The 2nd order solutions are clearly distinguishable from the 4th solutions, while the stress distributions corresponding to 3rd order polynomial fits follow similar trends as the 4th order solutions. The largest difference between the upper and lower bounds of the stress distributions occurs at the outer surface of the pipe, with a magnitude of close to 4 MPa. This range decreases to around 0.8 MPa toward the normalised radial position of 0.75, and then increases slightly to roughly 1.3 MPa as the normalised radial position of 0.5 is approached. From this point, the difference between the upper and lower bounds of the stress solutions gradually decreases to a value of about 0.6 MPa at the normalised radial position of -0.9. Thereafter the polynomial solutions somewhat fan out, such that the difference between the upper and lower bounds increases to more or less 1.3 MPa for the region corresponding to the inner surface of the pipe.

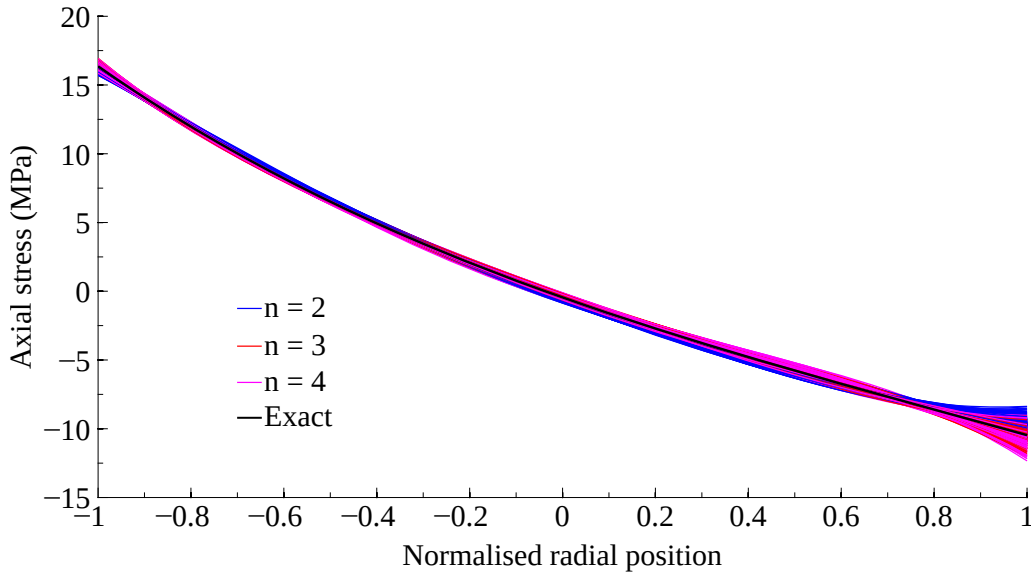

Figure 10.4: Axial stress variations for the full data set of the ±55° pipe

The corresponding residual hoop stress distributions of the full data set of the ±55° pipe, associated with the possible combinations of the polynomials fitted to the simulated axial and circumferential strain data of Figs. 10.1 and 10.2, are illustrated in Fig. 10.5. These stress distributions are colour coded according to the order of polynomial fitted to the circumferential strain variations to which they correspond. As with the axial stress distributions of Fig. 10.4, the bounds of the hoop stress solutions lie almost completely symmetrically about the "exact" stress distribution. Additionally, the trends in these bounds are very similar to those seen in Fig. 10.4. The largest difference between the upper and lower bounds in stress occurs at the outer surface of the pipe, with a magnitude of around 7 MPa. This range decreases to approximately 1.3 MPa, toward the normalised radial position of 0.77, and then increases again to about 2.5 MPa as the normalised radial position of 0.55 is approached. From this point, this range decreases gradually until a minimum value of 1 MPa, at the normalised radial position of -0.45, is reached. Like the axial stress distributions of Fig. 10.4, the stress solutions fan out toward the inner surface, and the difference between the upper and lower bounds in stress for this region is close to 2.5 MPa. As with the circumferential strain variations of Fig. 10.2, the different order solutions do not form trends that are clearly distinguishable from one another. The 2nd order solutions, however, seem to all lie close to the "exact" stress distribution. This is an expected result, since the "exact" stress distribution is based upon a 2nd order polynomial that was fitted to the measured circumferential strain response.

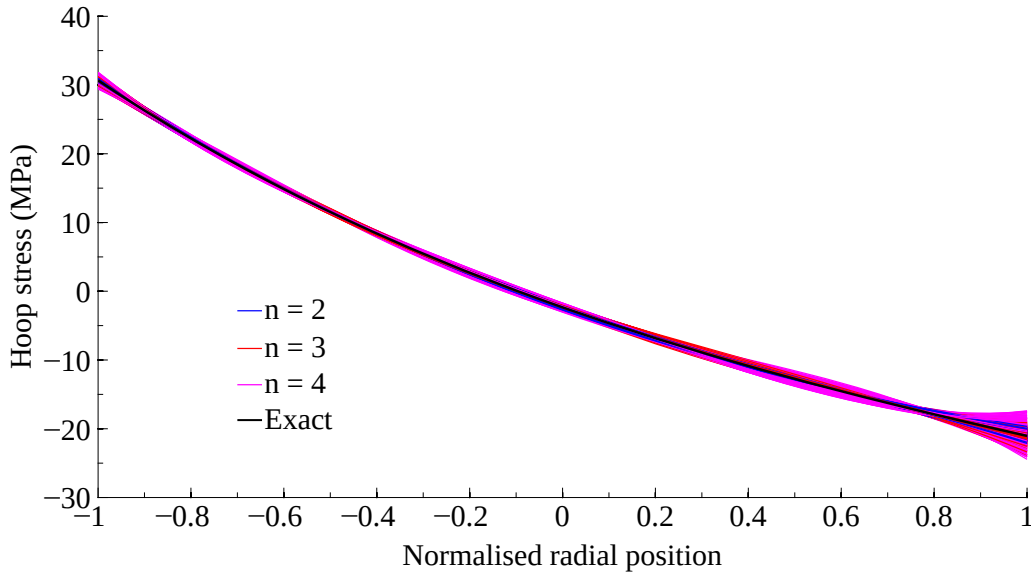

Figure 10.5: Hoop stress variations for the full data set of the ±55° pipe

The residual radial stress distributions of the full data set of the ±55° pipe, associated with every combination of the polynomials fitted to the simulated strain data of Figs. 10.1 and 10.2, are plotted in Fig. 10.6. These are all colour coded according to the order of polynomial fitted to the circumferential strain data, seen in Fig. 10.2, to which they correspond. As with the stress distributions of Figs. 10.4 and 10.5, the bounds of radial stress are located almost completely symmetrically about the "exact" stress variation, denoted by the thick black line. The difference between these bounds is very small over the entire wall thickness of the pipe, and never exceeds 0.15 MPa.

Since the material can be considered orthotropic at the bulk-scale, the shear distributions of the ±55° pipe depend only on the shear strain response of the pipe to removal of material. By Eq. (5.1), this strain response is dependant on the axial, circumferential and 45° strain variations. This translates to 27 different possible solutions in shear stress for the different combinations of the 2nd to 4th order least-squares polynomials fitted to each strain variation for a particular simulation. Fig. 10.7 illustrates the 2700 residual shear stress distributions associated with the 100 simulated strain variations of the full data set, illustrated in Figs. 10.1 to 10.3. Included in this figure is the "exact" stress variation of this data set, associated with the "exact" strain variations. The stress distributions are colour coded according to the order of polynomials fitted to the simulated 45° strain variations, to which they correspond. Unlike the axial and hoop stress distributions of Figs. 10.4 and 10.5, the bounds of these stress solutions do not lie symmetrically about the "exact" stress distribution. Similar to the polynomial fits of Fig. 10.3, there is a clear distinction between the solutions of the different order. All solutions oscillate about the

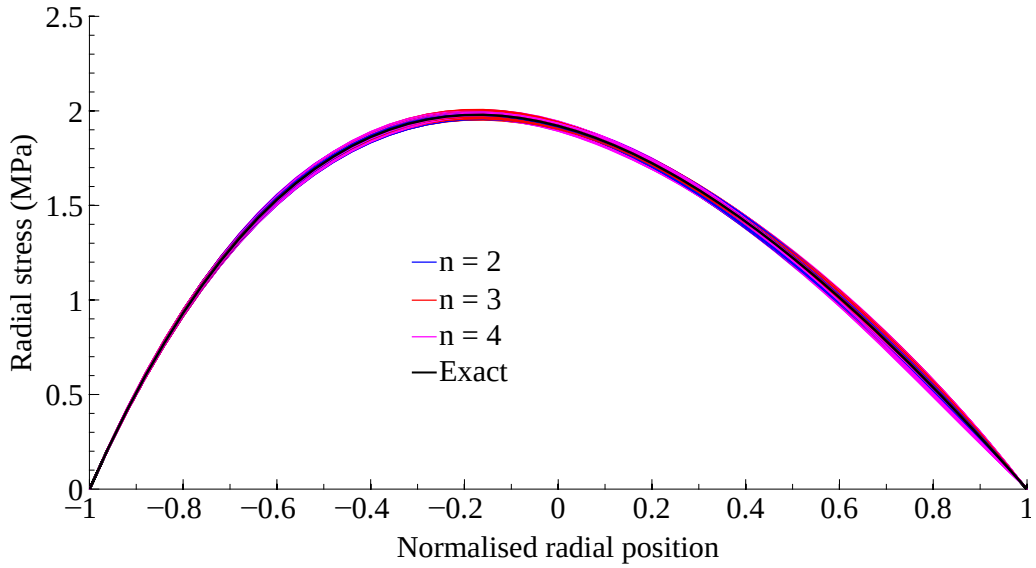

Figure 10.6: Radial stress variations for the full data set of the ±55° pipe

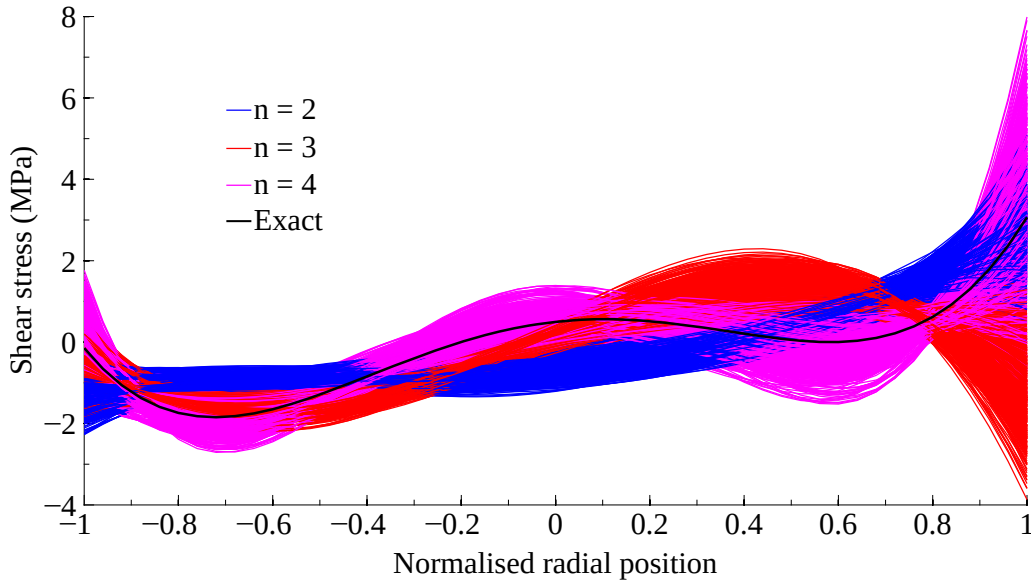

Figure 10.7: Shear stress variations for the full data set of the ±55° pipe

zero-stress state expected to exist through the thickness of a filament-wound pipe, and have a zero-torque resultant as required. From this figure it appears that the 2nd order solutions might be best, since they lie closest to the zero-stress line. The largest discrepancy between the results occurs at the outer surface, with a magnitude of about 12 MPa between the upper and lower bounds of the stress distributions. This range rapidly decreases away from the outer surface, to a value of marginally greater than 2 MPa, at the normalised radial position of 0.8. Over the remaining thickness of the pipe, the difference between the upper and lower bounds varies with the waviness of the different order solutions, but never exceeds 4 MPa. Although these differences seem large in comparison to the expected zero-stress state, they are only slightly larger than the differences between the upper and lower bounds of the hoop stress solutions of Fig. 10.5. The sensitivity to the presence of scatter in strain measurements of the shear stress distributions is thus similar to that of the hoop stress component.

10.2.2 Reduced data set

Strain simulations

Fig. 10.8 illustrates the 100 simulated axial strain variations of the reduced data set of the $\pm 55^{\circ}$ pipe, along with the corresponding 2nd to 4th order least-squares polynomials fitted to each variation. Included in this figure is the "exact" 2nd order polynomial originally fitted to the axial strain variation of the reduced data set, seen in Fig. 9.1. As required, each of the polynomial fits were forced to pass through a value of zero strain for 0% material removed. It is clear from this figure that the scatter in the simulated data increases with increased material removal, governed by the SD variation determined for the axial strain response of this pipe, presented in Appendix L. This is the same SD variation utilised for the axial strain simulations of the full data set, illustrated in Fig. 10.1. Compared to the polynomials fitted to these strain variations, it is evident that the fits of Fig. 10.8 lie over a significantly wider range, and the upper and lower bounds of these fits reside quite close to the upper and lower bounds of the simulated data points. Additionally, there is no clear distinction between the trends of the different order fits. The magnitude of the difference between the upper and lower bounds of the fits increases rapidly from zero at 0% thickness removed to about 40 $\mu\epsilon$ for 10% thickness removed. This range then gradually increases until it reaches a value of roughly 100 $\mu\epsilon$ for 100% thickness removed. The reason for the increased range of polynomial fits of this data set lies in the number of simulated data points. Since the reduced data set comprises significantly fewer data points than the strain variations of the full data set, there is an increased probability that all the data for a particular simulation lie either above or below the "exact" strain response

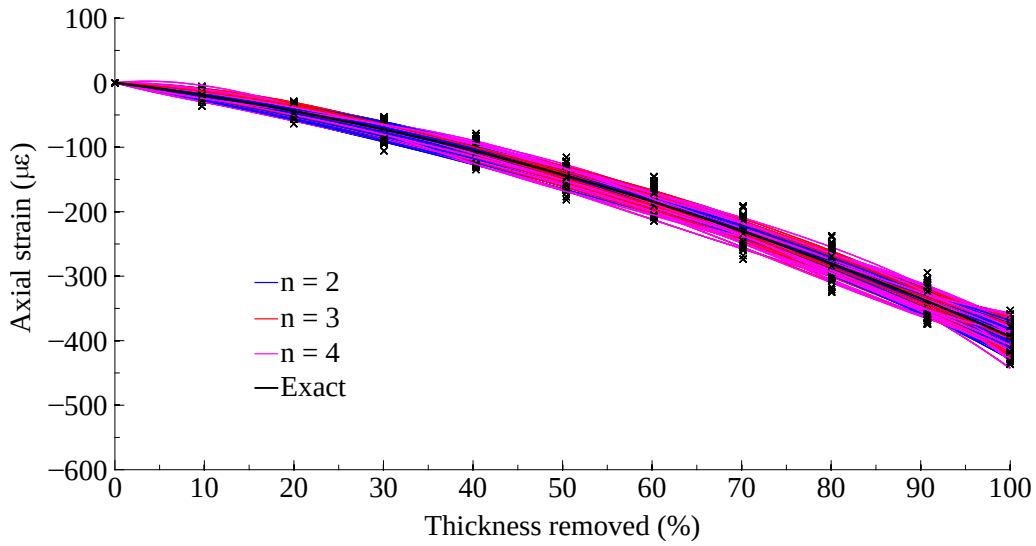

Figure 10.8: Simulated axial strain variations and polynomial fits for the reduced data set of the ±55° pipe

upon which they are based. In this sense the bounds of the polynomial fits increase for the same amount of scatter, since the fits are less constrained to lie close to the "exact" strain response. This behaviour can be expected in any real experiment, and is an indication that the error associated with removal of thicker layers should be higher than that associated with the removal of thin layers.

The simulated circumferential strain variations and corresponding 2nd to 4th order polynomial fits of the reduced data set of the ±55° pipe are illustrated in Fig. 10.9. Included in this figure is the "exact" 2nd order polynomial originally fitted to the circumferential strain variation of this data set, illustrated in Fig. 9.1, and is the strain response upon which scatter was added to produce each of the strain variations. The magnitude of the scatter increases with increased material removal, governed by the same SD variation used for the circumferential strain simulations of the full data set, seen in Fig. 10.2. As with those of Fig. 10.8, the different order polynomial fits of Fig. 10.9 do not demonstrate distinctive trends over the majority of the range of material removal. The upper and lower bounds of these fits lie close to the bounds of the simulated data points, and encompass the majority of these points. The difference between the bounds of the fits is significantly larger than obtained for the polynomial fits of Fig. 10.2 over the full range of material removal. As has been discussed, this is a direct result of the amount of simulated data points upon which each polynomial fit is based. Fewer data points increases the probability of a particular polynomial fit lying further from the "exact" strain solution. The difference between the upper and lower bounds of the fits rapidly increases from zero at 0% thickness removed to slightly less than 60 $\mu\epsilon$ for 10% thickness removed. This is clearly a consequence of

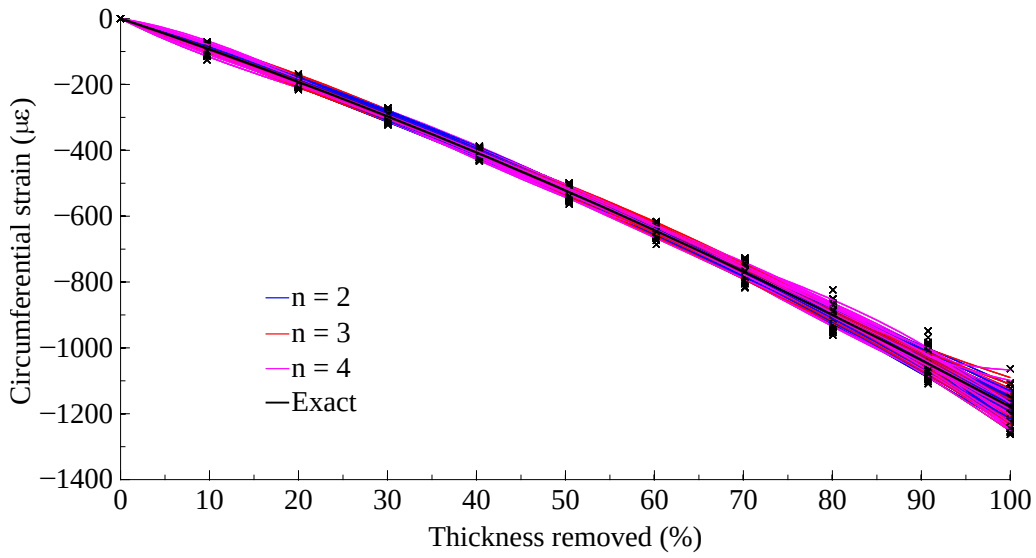

Figure 10.9: Simulated circumferential strain variations and polynomial fits for the reduced data set of the ±55° pipe

the presence of the 4th order polynomial fits. This range then decreases to around 40 $\mu\epsilon$ toward 30% thickness removed, and this is roughly maintained to about 50% thickness removed. From this point, the difference between the upper and lower bounds of the polynomial fits increases gradually until it reaches a value of slightly less than 200 $\mu\epsilon$ at 100% material removed.

The 100 simulated 45° strain variations of the ±55° pipe, and corresponding 2nd to 4th order least-squares polynomials fitted to the data, are illustrated in Fig. 10.10. Included in this figure is the "exact" 2nd order least-squares polynomial originally fitted to the 45° strain response of this data set, illustrated in Fig. 9.1. The SD variation governing the magnitude of the simulated scatter, which is presented in Appendix L, is exactly that used to generate the 45° strain variations of the full data set, illustrated in Fig. 10.3. As with all strain simulations and fits, the least-squares polynomial fits were forced to pass through a value of zero for 0% material removed. Due to the reduced number of data points describing the strain variations of this data set, the upper and lower bounds of the fits form a much wider range over the entire range of material removal than the fits to the simulated 45° strain variations of the full data set. The difference between the upper and lower bounds of the polynomial fits of Fig. 10.10 rapidly increases from zero, at 0% material removed, to marginally greater than 50 $\mu\epsilon$ at 10% thickness removed, a consequence of the presence of the 4th order polynomial fits. This range is roughly maintained through to 30% thickness removed. Between this point and 40% thickness removed, the range formed by the majority of the polynomial fits decreases to approximately 40 $\mu\epsilon$, and then increases gradually to about 200 $\mu\epsilon$ for 100% material removed. The combination of the

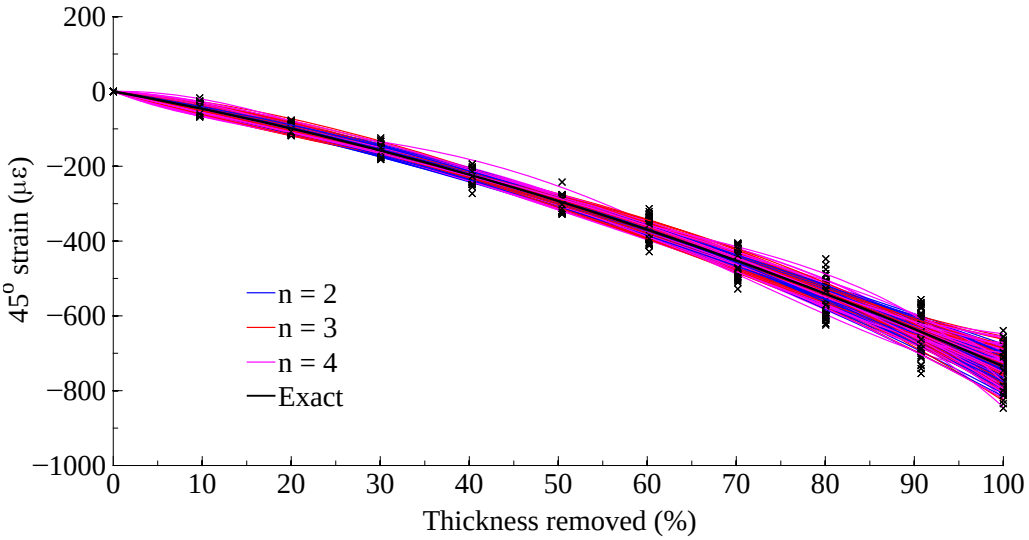

Figure 10.10: Simulated 45° strain variations and polynomial fits for the reduced data set of the ±55° pipe

reduced number of data points and use of 4th order polynomials results in some outlying fits, which occur between the regions of 30% to 55% thickness removed, and 70% to 90% thickness removed. The extent by which these polynomial deviate from the majority of the fits is, however, relatively small.

Residual stress distributions

It has been demonstrated in Section 9, that numerically simulating the removal of thinner layers for the reduced data set allows the radial residual stress distributions of the laminated pipes to be accurately resolved. Although each strain variation of the reduced data set comprises only 10 data points associated with the thickness of the physically removed layers, the residual stresses arising from these variations can be evaluated for any number of layers. This is because the residual stresses at any particular position are dependant on the polynomials fitted to the strain variations, which can be evaluated for any removed layer thickness. To maintain congruence between the sensitivity analyses of all the pipe configurations, the residual stresses of the reduced data set of the ±55° pipe were evaluated at the mid-radius of 50 numerically simulated layers. The stress distributions presented in this section comprise splines fitted to these data. Although this procedure was not required for the ±55° pipe, it does allow a better representation of the variation in the residual stress distributions to be obtained. Where higher order polynomials are fitted to the strain data, these variations can be quite significant.

The resulting residual axial stress distributions are presented in Fig. 10.11. As with Fig. 10.4, this figure comprises 900 different stress distributions, corresponding to the possible combinations of the 2nd to 4th order least-squares polynomials fitted to the simulated axial and circumferential strain variations of Figs. 10.8 and 10.9. These distributions are colour coded according to the order of polynomial fitted to the axial strain data to which they correspond. Included in this figure is the "exact" stress distribution associated with the "exact" strain variations of the reduced data set. As with the axial stress distributions of the full data set, seen in Fig. 10.4, the bounds of the stress solutions of Fig. 10.11 lie almost symmetrically about the "exact" stress distribution. These bounds, however, lie further apart than those of Fig. 10.4, over the entire wall thickness of the pipe. This is a direct result of the increased range of the polynomials fitted to the simulated strain variations of this data set. The largest difference between the upper and lower bounds occurs at the outer surface, with a magnitude of around 10 MPa. This is roughly 6 MPa larger than the difference between the bounds in stress of Fig. 10.4 for the same region. This range then rapidly decreases to approximately 2.5 MPa, at the normalised radial position of 0.8, followed by an increase to about 3.5 MPa at the normalised radial position of 0.6. Between the normalised radial position of 0.3 and the region of the inner surface, the difference between the upper and lower bounds in stress does not exceed 2.5 MPa. Unlike those of the full data set, the 2nd order solutions do not form distinctly separate trends in stress. Rather, the stress distributions corresponding to the range of polynomial orders coexist over the entire range of possible solutions.

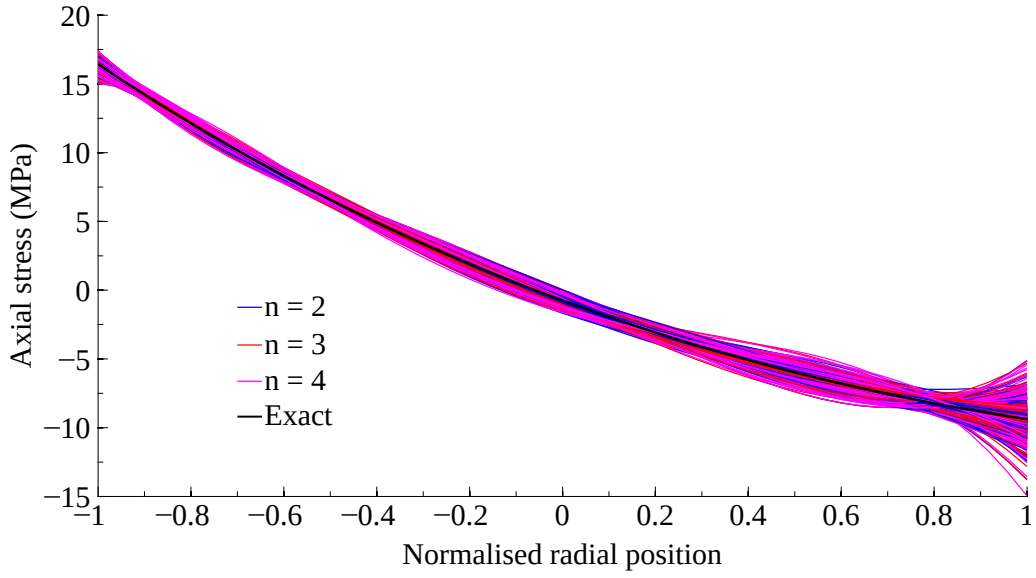

Figure 10.11: Axial stress variations for the reduced data set of the ±55° pipe

The 900 residual hoop stress distributions of the reduced data set of the ±55° pipe, associated with the different combinations of the 2nd to 4th order polynomials fitted to the simulated strain variations of Figs. 10.8 and 10.9, are plotted in Fig. 10.12. Each solution in stress is colour coded according to the order of polynomial fitted to the circumferential strain variation, seen in Fig. 10.9, to which it corresponds. As with the hoop stress distributions of the full data set, illustrated in Fig. 10.5, the bounds of the stress solutions of Fig. 10.12 lie almost symmetrically about the "exact" stress solution. The magnitude of the difference between the bounds of the stress distributions of the reduced data set are, however, significantly larger than those obtained for the full strain data set, over the entire thickness of the pipe. This is directly associated with the increased range over which the least-squares polynomials fitted to the simulated axial and circumferential strain variations exist, a result of the reduced number of data points of the reduced data set. The magnitude of the difference in the bounds in stress is larger than 20 MPa at the outer surface, about 13 MPa larger than the difference between the upper and lower bounds in stress of Fig. 10.5 for the same region. This range decreases to roughly 5 MPa, at the normalised radial position of 0.8, and then increases again to roughly 7 MPa, at the normalised radial position of 0.6. Between the normalised radial positions of 0.3 and -1, the difference between the upper and lower bounds in stress does not exceed 4 MPa. Over the entire wall thickness, the bounds in stress are almost entirely defined by 4th order solutions, and like Fig. 10.5, the 2nd order solutions appear to all lie relatively close to the "exact" stress distribution.

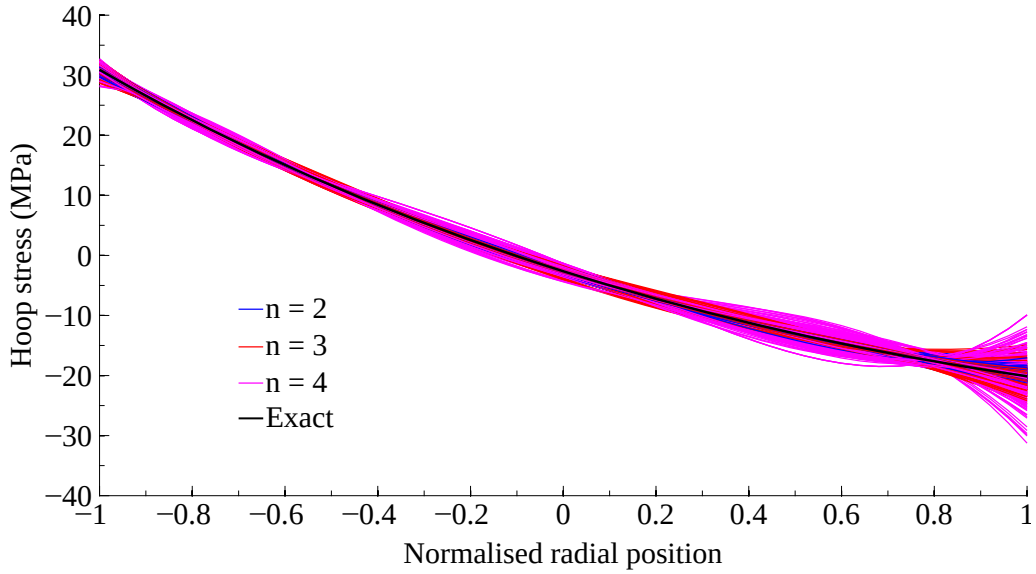

Figure 10.12: Hoop stress variations for the reduced data set of the ±55° pipe

The residual radial stress distributions which result from the different combinations of the polynomials fitted to the simulated axial and circumferential strain variations of the reduced data set, seen in Figs. 10.8 and 10.9, are presented in Fig. 10.13. These stress distributions are colour coded according to the order of polynomial fitted to the circumferential strain variation of Fig. 10.9. The upper and lower bounds in stress lie almost symmetrically about the "exact" solution, and these are defined by the 3rd and 4th order solutions. The magnitude of the difference between these bounds, over the entire wall thickness of the pipe, is about twice that obtained for the radial stress distributions of the full data set, illustrated in Fig. 10.6. As has been discussed, this is a consequence of the reduced number of data points describing each simulated strain variation of this data set, which results in an increased range defined by the corresponding polynomial fits. The difference between the upper and lower bounds of the radial stress distributions of Fig. 10.13 never exceeds 0.3 MPa, which is roughly 15% of the maximum value of 2 MPa obtained for the "exact" stress distribution, at the normalised radial position of -0.2.

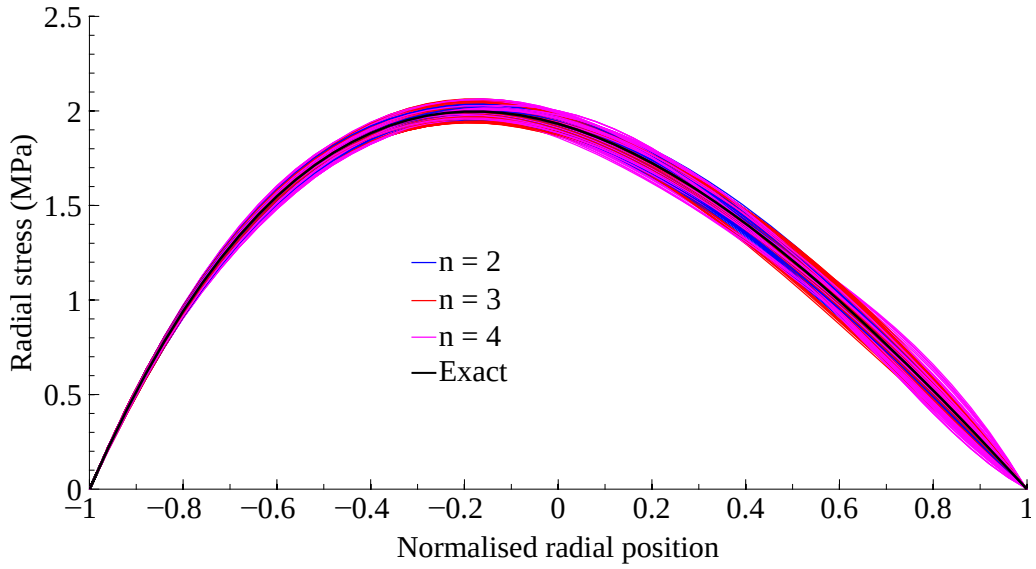

Figure 10.13: Radial stress variations for the reduced data set of the ±55° pipe

The in-plane residual shear stress distributions resulting from the simulated strain data of the reduced data set are presented in Fig. 10.14. This figure comprises 2700 different stress distributions, a consequence of the different possible combinations of the 2nd to 4th polynomials fitted to the simulated axial, circumferential and 45° strain variations of Figs. 10.8 to 10.10. Included in this figure is the "exact" stress distribution, associated with the "exact" strain variations of this data set. As with those of Fig. 10.7, the stress distributions of Fig. 10.14 are colour coded according to the order polynomial fitted to the 45° strain response to which they correspond. Over most of the wall thickness of the

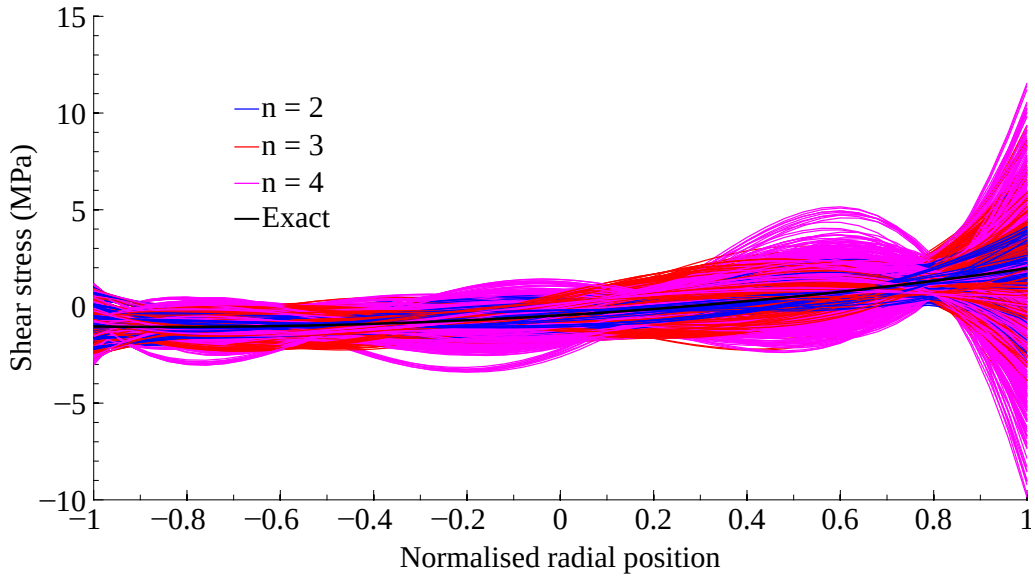

Figure 10.14: Shear stress variations for the reduced data set of the ±55° pipe

pipe, the bounds in stress are defined by 4th order solutions, and these do not lie symmetrically about the "exact" stress distribution. The magnitude of the difference between the bounds in stress is close to 22 MPa at the region of the outer surface of the pipe. This is significantly larger than the 12 MPa range obtained for the shear stress distributions of the full data set, shown in Fig. 10.7, for the same region. This range, however, rapidly decreases to about 4 MPa, as the normalised radial position of 0.8 is approached, and then increases to approximately 8 MPa, towards the normalised radial position of roughly 0.6. Thereafter, the difference between the upper and lower bounds varies with the waviness of the stress distributions, but never exceeds 5 MPa. The waviness in shear stress distributions increases with increased polynomial order, but all solutions oscillate about the zero-stress line expected to exist through the thickness of this pipe. The 2nd order solutions seem most reasonable, as they lie closest to the expected zero-stress line.

10.2.3 Error bar estimation

An analysis of the sensitivity to the level of scatter in the experimental data has been performed on both the full and reduced data sets of "Gauge set C" of the ±55° pipe. It is clear from the results presented that, in general, the bounds of each component of residual stress of the reduced data set lie further apart than those determined for the full data set. As has been discussed, this is a direct result of the reduction in the number of data points describing each simulated strain variation of this data set, resulting in a larger range of possible polynomial fits. This behaviour can be expected under normal experimental conditions, and consequently the error bars of the reduced data set should

be larger than those of the full data set. Additionally, the error bars should almost entirely encompass any feasible solution associated with the level of experimental scatter, and these can therefore be estimated directly from the residual stresses evaluated for the simulated strain variations. For each component in stress, the variations in SD were found through the wall thickness, using MATLAB software. These SD variations were then utilised to generate error bars at the radial locations of the mid-radius of each removed layer, as well as at the inner surface of the pipe. The magnitude of each error bar was estimated by multiplying the SD by a factor of three. Assuming that the residual stress distributions arising from the simulated strain variations are normally distributed about the "exact" solutions, this ensures a 99.7% confidence level [233] that all possible stress distributions, associated with the level of simulated scatter (and thus the level of scatter in the experimental data) and the order of polynomial fits considered, lie within the resulting error bounds.

The "exact" axial stress distributions of both the full and reduced data sets of the ±55° pipe are illustrated in Fig. 10.15. Included in this figure are the error bars determined for each data set, based upon the SD variations of the stress distributions of Figs. 10.4 and 10.11. The magnitude of the resulting error bounds of the reduced data set are larger than those of the full data set, a consequence of the increased sensitivity of this solution to scatter. Despite the larger uncertainties, the stress distribution of the reduced data set lies within the error bounds of the full data set, over the entire thickness of the pipe. The magnitude of the error bars of the full data set have been significantly reduced in comparison to those presented for this data set in Fig. 9.2. The error bounds of the reduced set, however, are of similar magnitude to those originally presented for this data set. Additionally, the magnitudes of the error bars of both data sets are no longer random, but vary smoothly over the wall thickness, highlighting the regions that are most sensitive to measurement scatter. Interestingly, the magnitude of the new error bounds at the inner surface of the pipe, for both data sets, are larger than those presented in Fig. 9.2 for this region. Since the error bars of Fig. 9.2 for this surface were estimated under the plane stress assumption of the parting out procedure, they were independent of the thickness of any removed layers, and dependant solely on the differences between the measured strain data and corresponding polynomial fits for 100% material removed. These error bars are of smaller magnitude than those presented in Fig. 10.15 for this surface, because the differences between the measured data and polynomial fits of Figs. 8.1, 8.2, and 9.1 are smaller than the range in the polynomial fits of Figs. 10.1, 10.2, 10.8 and 10.9 in the region of 100% material removed.

The "exact" hoop stress distributions of both the full and reduced data sets of the ±55° pipe are illustrated in Fig. 10.16. Included in this figure are the error bars of each data set,

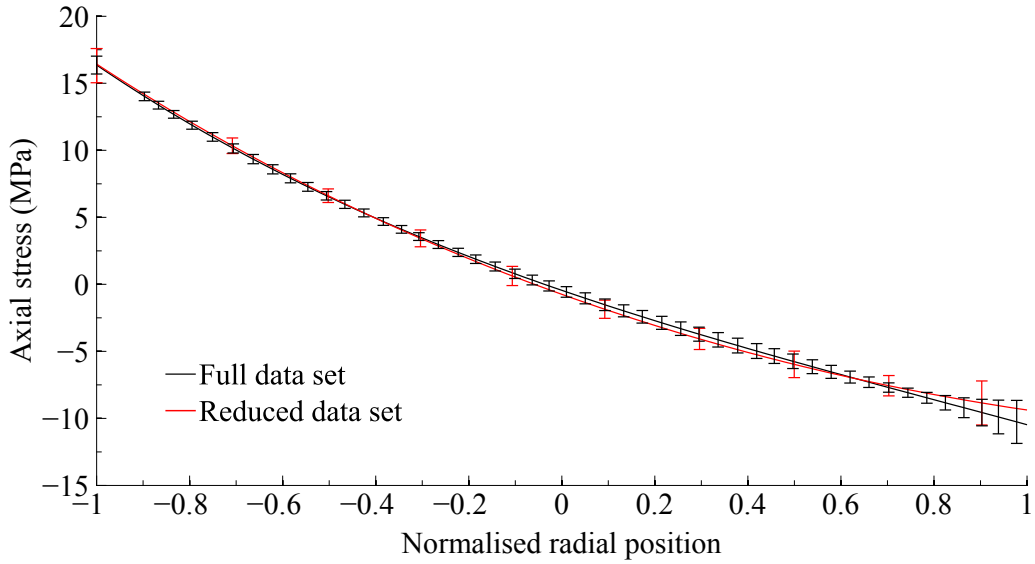

Figure 10.15: Improved error bars of the axial stress distributions for both data sets of the ±55° pipe

estimated from the SD variations of the stress distributions of Figs. 10.5 and 10.12. As with Fig. 10.15, the error bars of the reduced data set are larger than those of the full data set at similar through-thickness positions, despite the near perfect agreement between the stress distributions. As has been discussed, this is a direct result of the increased sensitivity of this data set to measurement scatter. The magnitude of the error bars of the full data set have been significantly reduced in comparison to those originally obtained for this data set, seen in Fig. 9.3. In some cases the extent of this reduction is twenty fold. Additionally, unlike those presented in Fig. 9.3, the magnitude of the error bars of Fig. 10.16 varies smoothly over the thickness of the pipe, and highlights the regions most sensitive to scatter in the measured data. In some regions of Fig. 10.16, the magnitude of the error bounds of the reduced data are larger than those presented in Fig. 9.3 for this data set. Since the error bars are no longer dependant on the thickness of the removed layers, they accurately represent the errors associated with the level of scatter obtained in the measured strain distributions.

The “exact” radial stress distributions of both data sets of the ±55° pipe, together with the error bars estimated from the SD variations of the stress distributions of Figs. 10.6 and 10.13, are illustrated in Fig. 10.17. The error bounds of the reduced data set are the largest, with a magnitude, on average, of twice that of those determined for the full data set. Despite this, the radial stress distribution of the reduced data lies within all of the error bounds of the full data set. The magnitude of the error bounds of the full data set are generally smaller than those presented in Fig. 9.4 for this data set. This magnitude differs by as much as a factor of two in some cases. The error bounds originally presented

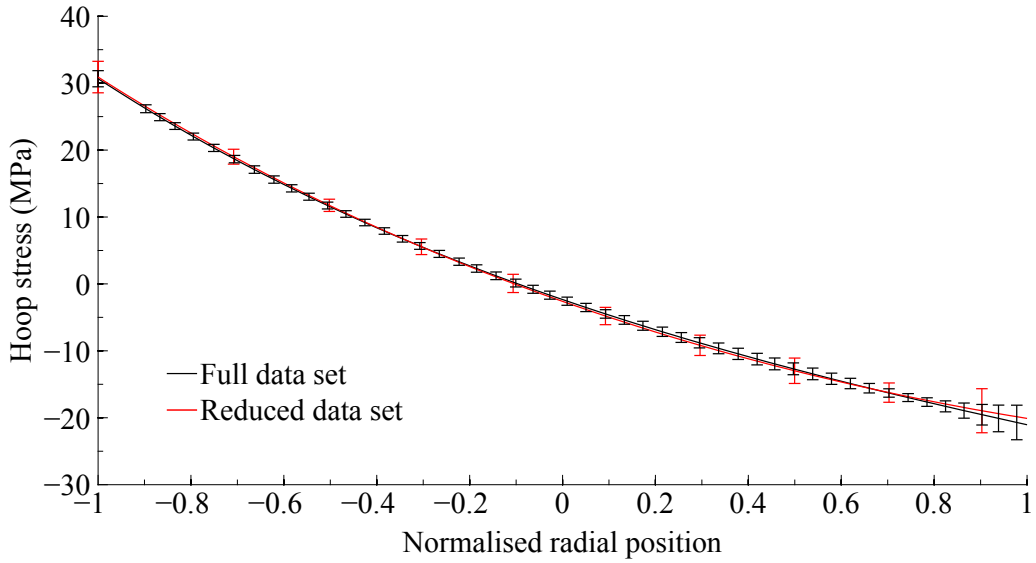

Figure 10.16: Improved error bars of the hoop stress distributions for both data sets of the ±55° pipe

for the reduced data set in this figure, on the other hand, underestimate the error in the region where the radial stress reaches its maximum, while the error bounds of Fig. 10.17 accurately demonstrate the sensitivity in this region.

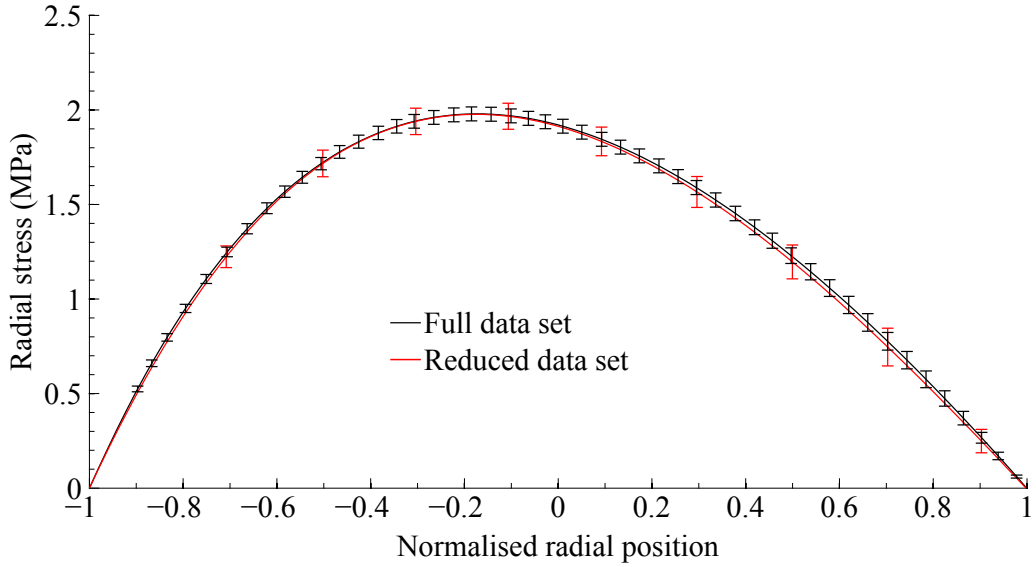

Figure 10.17: Improved error bars of the radial stress distributions for both data sets of the ±55° pipe

Fig. 10.18 illustrates the "exact" in-plane shear stress distributions of both the full and reduced data sets of the ±55° pipe. Included in this figure are the error bars, determined

from the SD variations of the shear stress distributions of Figs. 10.7 and 10.14. In general, the magnitude of the error bounds of the reduced data set are larger than those obtained for the full data set for similar through-thickness positions. These magnitudes, however, are very similar between the normalised radial positions of -0.1 to 0.3. Additionally, the residual shear stress distribution of the reduced data set lies within all of the error bounds of the full data set. Interestingly, almost all the error bars of the full and reduced data sets encompass the line of zero stress, which is expected to exist through the thickness of filament-wound pipes. Although the bounds in error are large in comparison to the magnitude of the expected shear stress, these are of similar magnitude to those obtained for the hoop stress distributions of Fig. 10.16. In this sense the accuracy of the current method to measurement of shear stresses is similar to that of normal stress components. Towards the outer surface of the pipe, the magnitude of the error bars of both data sets seem to approach one another. The error bars of the reduced data set are not, however, numerous enough to reflect the severity of the sensitivity of the shear stress to measurement that occurs for this data set between the normalised radial positions of 0.9 and 1. This sensitivity is clearly demonstrated in Fig. 10.14. In relation to the shear stress distributions of Fig. 9.5, the error bounds of the full data set have been reduced tremendously. These now vary smoothly across the wall thickness, as opposed to the random variation in magnitude illustrated in Fig. 9.5. The error bounds of the reduced data set have also, in general, reduced over the thickness of the pipe. For reasons already discussed, the error bounds of Fig. 10.18, at the inner surface of the pipe, are significantly larger than those presented in Fig. 9.5 at this position.

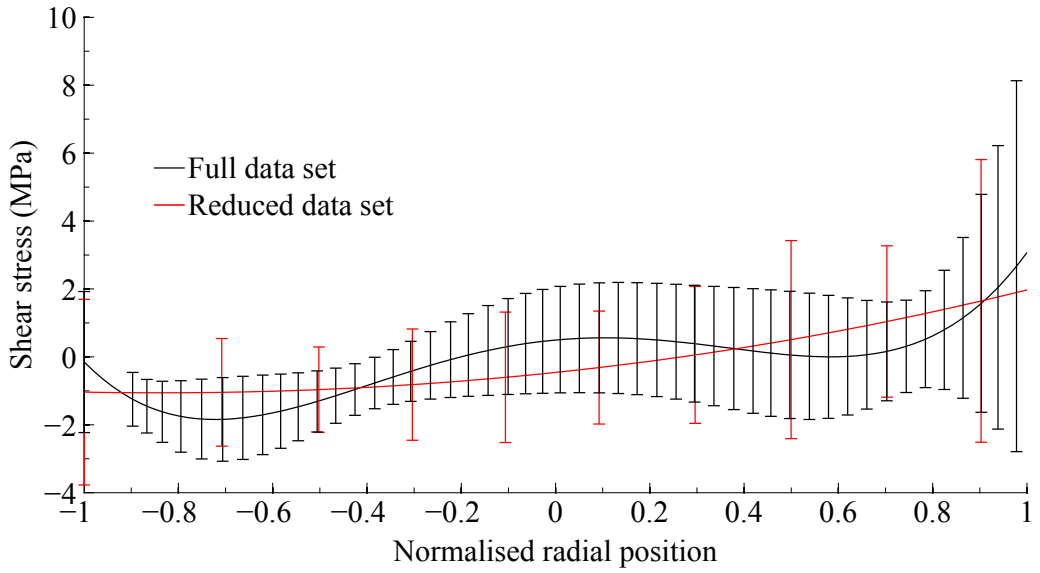

Figure 10.18: Improved error bars of the shear stress distributions for both data sets of the ±55° pipe

10.3 ±65°/±47° Filament-wound pipe

The sensitivity analysis of the ±65°/±47° pipe was performed for both the full and reduced data sets of "Gauge set C". Once again, the "exact" strain variations were taken as the polynomials fitted to the measured data of each of the data sets. The scatter added to these variations was governed by the normal distribution, and the magnitude of the scatter was constrained by the SD variations of the measured data about the polynomial fits. These were determined for each strain gauge orientation, and are presented in Appendix L. As has been discussed, the thickness of the removed layers of each data set was maintained for the simulated strain variations, to ensure that the error bounds obtained using the current uncertainty analysis represent the actual errors in the experimentally measured stress distributions.

10.3.1 Full data set

All of the simulated strain variations of the full data set of the ±65°/±47° pipe, together with the polynomials fitted to the data, are presented and discussed in Appendix M. Like the sensitivity analysis of the ±55° pipe, the least-squares polynomials fitted to the simulated strain variations were constrained between 2nd and 4th order, but only for material removal from the outer ±47° ply. Only 2nd order polynomials were considered for removal of material from the inner ±65° ply. Different order fits were not considered for this region, since the remaining pipe is relatively thin once the inner ply is reached. Therefore minor variations between different order polynomials fitted to any particular simulated strain variation over this region do not result in any significant differences in the corresponding residual stress distributions. The fitting procedure was identical to that described in Section 8, where each pair of polynomials were forced to pass through the same value of strain when material was removed at the ply interface. Bearing this in mind, for each simulation there are still 3 possible 2nd order least-squares polynomial fits for material removal from the inner ply, each paired with the 2nd to 4th order fits to the data corresponding to removal of material from the outer ply. The simulated strain variations of the full data set of the ±65°/±47° pipe, together with the polynomials fitted to these data, are presented in Appendix M. For illustrative purposes the axial strain variations are also considered in this section, and these are presented in Fig. 10.19. The scatter in the simulated data clearly increases with increased material removed, as governed by the SD variation of the measured data of this gauge orientation about the "exact" polynomial fit, presented in Appendix L. Additionally, the magnitude of this scatter is similar to that of the simulated axial strain variations of the ±55° pipe, illustrated in Fig. 10.1. Much like the polynomial fits of Fig. 10.1, the polynomials fitted to the data of Fig. 10.19 are constrained to

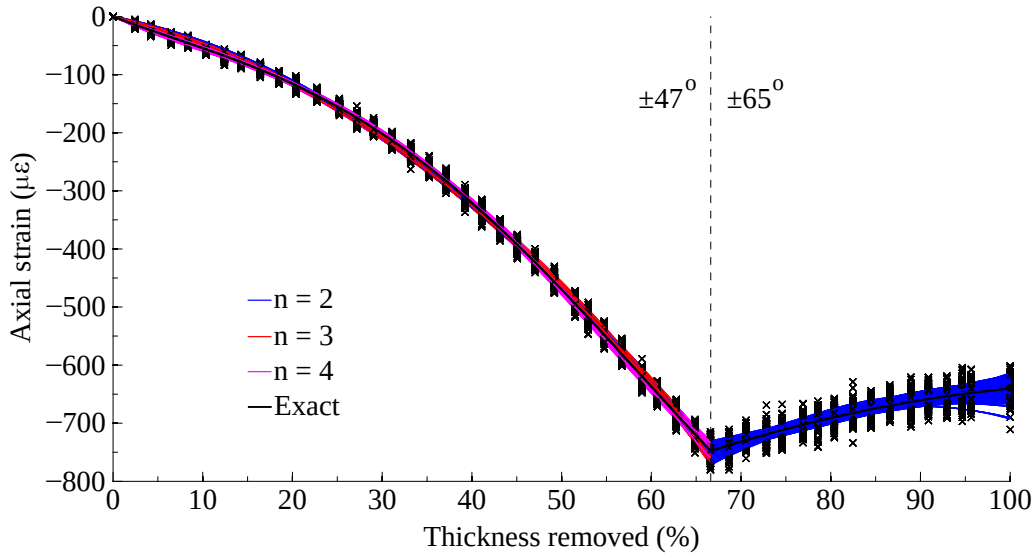

Figure 10.19: Simulated axial strain variations and polynomial fits for the full data set of the ±65°/±47° pipe

lie quite close to the "exact" strain variation, a consequence of the large number of data points describing each strain variation of this data set. For the region when material was removed at the ply interface, however, the difference between the upper and lower bounds of the polynomial fits of the ±65° pipe are is significantly greater than the range formed by the polynomials fitted to the axial variations of the ±55° pipe for the same amount of material removed. This is a direct result of the of the requirement for two polynomials to be fitted to the data for removal of material from the two separate plies of the ±65°/±47° pipe. Although each pair of polynomials were forced to pass through the same value in strain at the region corresponding to the ply interface, the lowered stability, associated with the end points of each polynomial, lowers the level of constraint on the resulting fits to lie close to the "exact" variation in this region. Consequently, the level of sensitivity in the residual stresses at the location of the ply interface of the ±65°/±47° pipe can be expected to be higher than the uncertainty obtained in the residual stresses of the ±55° for the same radial location.

Due to the bulk-scale orthotropy of the material, there exist 9 different axial, hoop, and radial stress distributions for the full data set of this pipe, corresponding to the possible combinations of the 2nd to 4th order polynomial pairs fitted to each simulated axial and circumferential strain variation. Due to the dependence of the shear strain variation on the measured strain responses in the three gauge orientations, there exist 27 possible shear stress distributions for each simulation. The residual stress distributions of the full data set of the ±65°/±47° pipe, arising from the 100 sets of simulated scatter, are presented in Appendix M. For the sake of clarity, the axial residual stress distributions are considered

in this section, and are presented in Fig. 10.20. Similar to the axial stress distributions of the ±55° pipe, illustrated in Fig. 10.4, the stress distributions of Fig. 10.20 demonstrate a considerable level of sensitivity to scatter at the outer surface, and this generally decreases toward the inner surface of the pipe. The axial stresses of the ±65°/±47° pipe are, however, quite sensitive to scatter in the region of the ply interface. At the same radial location, this level of sensitivity does not occur for the ±55° pipe. This behaviour is a direct result of the lowered level of constraint applied to the polynomial fits when material is removed from region of the ply interface of the ±65°/±47° pipe. In the case of the axial stresses of this data set, however, the uncertainty in the region of the ply interface is not as severe as that at the outer surface of the pipe.

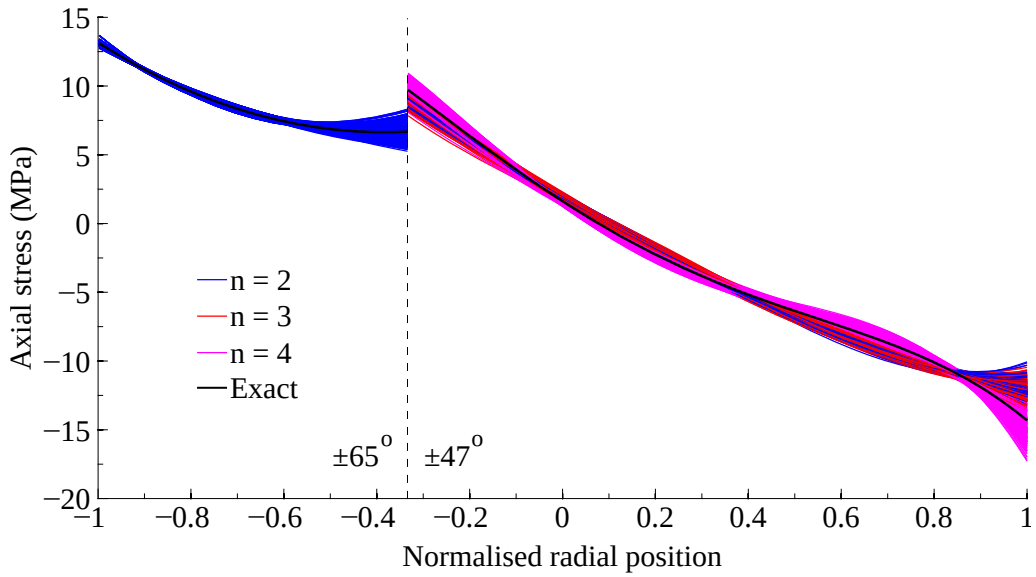

Figure 10.20: Axial stress variations for the full data set of the ±65°/±47° pipe

10.3.2 Reduced data set

The polynomials fitted to the simulated data of the reduced data set of the ±65°/±47° filament-wound pipe were maintained between 2nd and 4th order. More specifically the range of polynomials fitted to the data corresponding to removal of material from the outer ±47° ply was limited between 2nd and 4th order. For reasons already discussed, only 2nd order fits were considered for removal of material from the inner ±65° ply. The scatter added to the "exact" strain responses of this data set took the form of random values constrained by the normal distribution. The SD values applied to the scatter at each depth of material removal were found using the same polynomials fitted to the SD variation determined for the full data set, across all three strain gauge rosettes of this pipe, presented in Appendix L. In this sense, the level of scatter applied to the reduced data set was identical to that applied to the strain variations of the full data set, which are discussed in Appendix M. The simulated strain variations and corresponding polynomial fits of the reduced data set of the ±65°/±47° pipe are presented in Appendix M. For illustrative purposes, the simulated axial strain variations of this data set are presented in Fig. 10.21. Included in this figure are the "exact" 2nd order polynomial pair fitted to the measured axial response of this data set, seen in Fig. 9.7. It is clear from Fig. 10.21 that the level of scatter of the simulated data points increases with increased removal of material, as governed by the SD variation of the experimental scatter for this gauge orientation. This variation is presented in Appendix L, and is the same variation which constrained the scatter of the simulated axial strain variations of the full data set, presented in Fig. 10.19. Compared to the polynomial pairs fitted to these strain variations, the bounds of the polynomials fitted to the simulated data of Fig. 10.21 lie significantly further apart, and almost entirely engulf the range of simulated data points. This behaviour, as has been discussed, is a direct result of the reduced number of data points describing each strain variation and can be expected in any real experiment. Additionally, the use of separate polynomials to define the strain response for the removal of material from the two plies further reduces the level of constraint on the polynomials in the region of the interface and consequently a significant level of uncertainty in the stress distributions is expected here.

As with the results of the ±55° pipe, the range formed by the polynomials fitted to the simulated strain variations of the reduced data set of the ±65°/±47° is significantly larger than that of the polynomials fitted to the strain distributions of the full data set. Consequently, the residual stress distributions of the reduced data set are more sensitive to scatter in the measured data than those of the full data set. The residual stress distributions, associated with the combinations of the different order polynomial pairs fitted to the strain variations of the reduced data set of the ±65°/±47° pipe are presented in

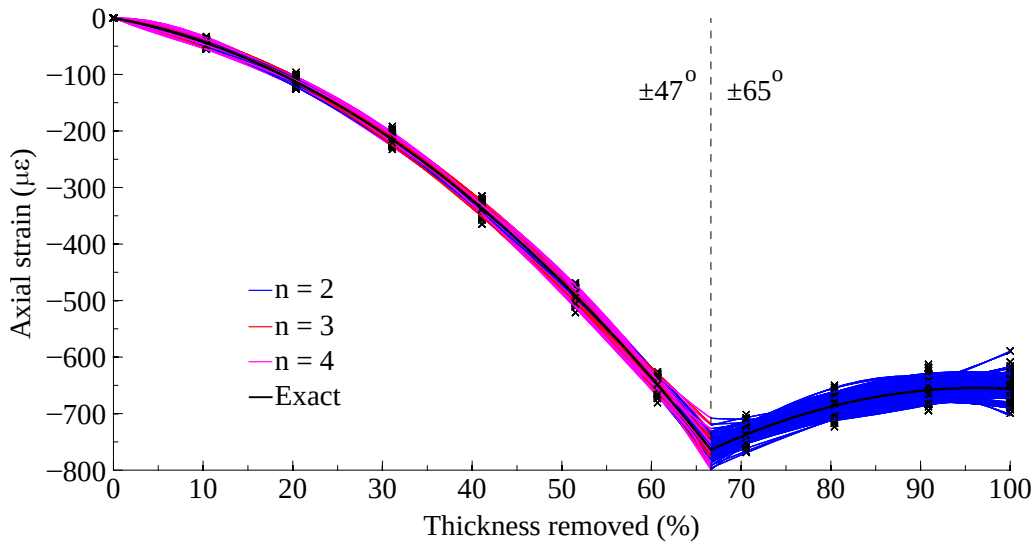

Figure 10.21: Simulated axial strain variations and polynomial fits for the reduced data set of the ±65°/±47° pipe

Appendix M. These stresses were evaluated at the mid-radius of 50 numerically simulated layers, based upon the polynomials fitted to the strain variations of this data set. As has been discussed, although each strain variation comprises only 10 data points associated with the removal of layers that are approximately 1.5 mm thick, any number of layers can be simulated to evaluate the residual stresses, since these are based upon the polynomials fitted to the strain data. Increasing the number of layers for which the residual stresses are evaluated not only allows the radial residual stresses of the laminated pipes to be accurately resolved, but also provides a better representation of the other stress components that may vary significantly in regions through the thickness of the pipes. For illustrative purposes the resulting axial stress distributions are discussed in the current section, and are presented in Fig. 10.22. Compared to the axial stress distributions of the full data set, illustrated in Fig. 10.20, the axial stresses of the reduced data set lie over a much more widespread range. This is a direct result of the increased range formed by the polynomial fits of this data set, as compared to those fitted to the simulated data of the full data set. The stress distributions of Fig. 10.22 are most sensitive to scatter at the outer surface of the pipe and the ply interface. Unlike the results of the full data set, the difference between the upper and lower bounds of the solutions of the reduced data set at the ply interface, particularly the solutions for the inner ply, are very similar to the range formed by the solutions at the outer surface. Consequently, the error bars found around the ply interface can be expected to be of similar magnitude to those at outer surface.

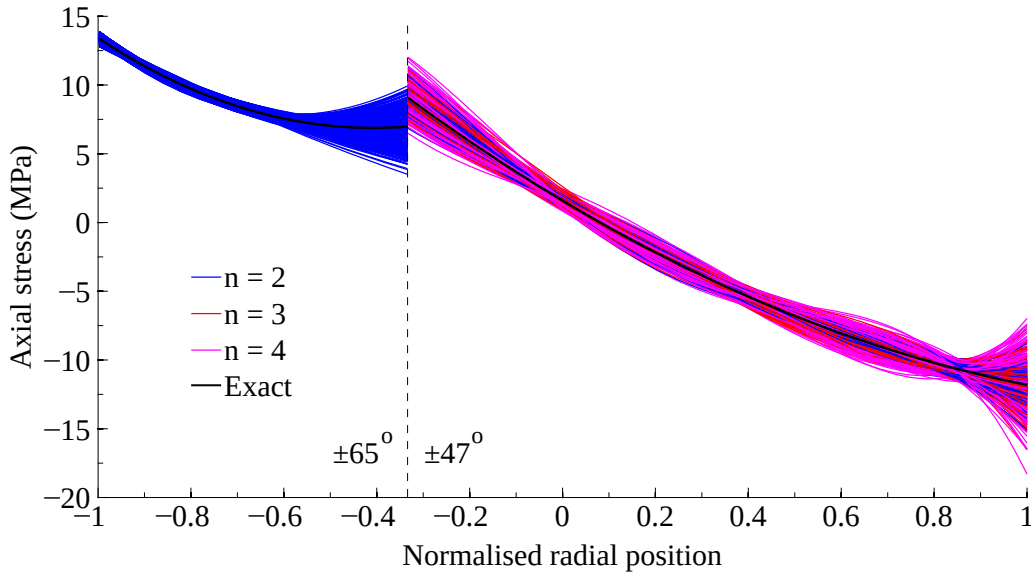

Figure 10.22: Axial stress variations for the reduced data set of the ±65°/±47° pipe

10.3.3 Error bar estimation

The error bars of both data sets of the ±65°/±47° pipe, presented in this section, were estimated in the same manner as described for the ±55° pipe. These are plotted at the mid-radius of each removed layer, as well as at the inner surface of the pipe, associated with the parting-out procedure of the strain gauge rosettes. The magnitude of each error bar was found by multiplying the appropriate SD variation in stress by a factor of three. Assuming that the residual stress distributions associated with the simulated strain variations are normally distributed about the "exact" stress solutions, multiplying the SD values by this factor ensures a 99.7% confidence level [233] that any feasible solution in stress, associated with the level of simulated scatter (and therefore experimental scatter) and the range of polynomial orders considered, lies within the bounds of the resulting error bars.

The "exact" axial stress distributions of the full and reduced data sets of "Gauge set C" of the ±65°/±47° pipe, together with the associated error bars, are illustrated in Fig. 10.23. These were estimated from the variation in the SD of the axial stress distributions of Figs. 10.20 and 10.22. The magnitude of the error bars of the reduced data set are larger than those of the full data set for similar though-thickness positions, associated with the increased sensitivity to scatter when thicker layers are removed. On average, the magnitude of the error bars of the full data set have been significantly reduced, as compared to those originally presented in Fig. 9.8 for this data set, and no longer vary randomly across the wall thickness. Rather, these error bars increase in magnitude in the regions where the sensitivity of this stress distribution is highest, and decrease in magnitude where

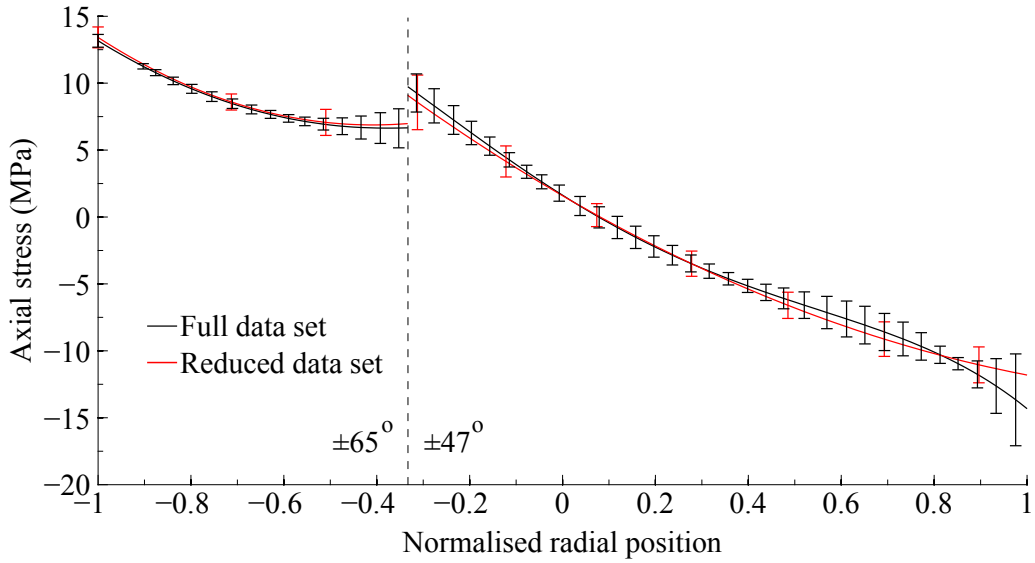

Figure 10.23: Improved error bars of the axial stress distributions for both data sets of the ±65°/±47° pipe

all feasible solutions lie close together. The effectiveness of this is evident when the "exact" stress distributions of both data sets of this figure are compared: In the regions where these distributions lie farthest apart (at the outer surface of the pipe, the normalised radial position of around 0.65, and at the ply interface), the error bounds of the full data set reach their largest magnitude, and the reduced data set solution lies within these bounds. Within the outer ±47° ply, the magnitude of the error bars of the reduced data set are similar to those originally determined for this data set, illustrated in Fig. 9.8. The same cannot be said, however, for the error bars of the inner ±65° ply. Unfortunately, the reduced number of error bars of this data set does not effectively highlight some of the regions of highest sensitivity seen in Fig. 10.22. In particular, these regions correspond with the outer surface of the pipe and within the inner ply at the ply interface. For this reason, it is useful to produce figures such as Fig. 10.22, so that the bounds of plausible stresses over the entire wall thickness can be found. It is interesting to note that the previous method of uncertainty analysis did not allow for the estimation of an error bar for the removed layer comprising material from both the inner and outer plies of a laminated pipe, due to the averaging issue associated with the presence of a residual strain discontinuity in this region. Since the error bars estimated using the current uncertainty analysis depend only on the variations in SD of the stress distributions resulting from the simulated strain variations, this issue is no longer a problem, and an error bar for this layer can be found.

The "exact" residual hoop stress distributions of the full and reduced data sets of the ±65°/±47° pipe are illustrated in Fig. 10.23. Compared to those presented in Fig. 9.9, the magnitude of the error bars of the full data set, in general, have been significantly

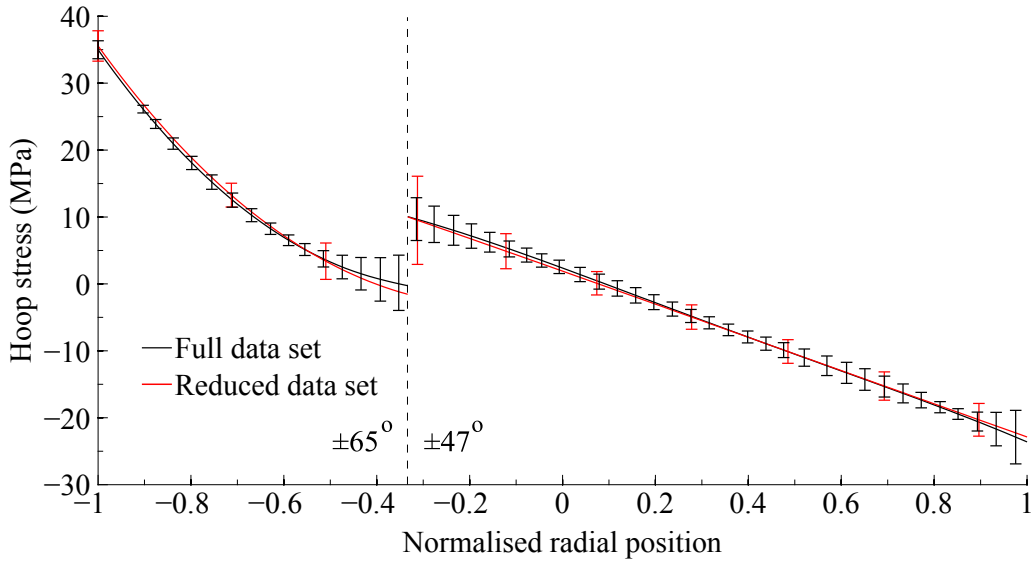

Figure 10.24: Improved error bars of the hoop stress distributions for both data sets of the ±65°/±47° pipe

reduced. Additionally, these error bars now vary smoothly over the wall thickness, and highlight the regions most sensitive to measurement scatter. As illustrated for the axial stress results, the residual stress distributions of the reduced data set are significantly more sensitive to measurement scatter than those of the full data set. As a consequence, the error bars of the reduced data set of Fig. 10.24 are larger than those of the full data set at similar through-thickness positions. The small number of error bounds plotted for the reduced data set does not, however, effectively highlight some of the regions most sensitive to measurement scatter such as the outer surface of the pipe, and within the inner ply near the ply interface. The only region where the sensitivity to scatter is adequately highlighted is within the outer ply, at the normalised radial position of about -0.1. This error bar is roughly double the magnitude of the error bar of the full data set in the same region. It is important to understand the effect of measurement scatter on the residual stress distributions over the entire thickness of the pipe, and it is thus advisable to create figures such as Fig. 10.22 so that this can clearly be demonstrated.

The "exact" radial residual stress distributions of the ±65°/±47° pipe are illustrated in Fig. 10.25. The residual stress distributions of the reduced data set presented in this section comprise the values in stress determined at mid-radius of 50 numerically simulated layers, as opposed to the mid-radius of the thicker layers simulated to be physically removed. This was done to better resolve the radial stress distribution of this pipe. As a consequence, the stress distribution of the reduced data set of Fig. 10.25 is slightly different to that presented for this data set in Fig. 9.10 where this was not done. Included in Fig. 10.25 are the error bars of both data sets, estimated from the SD of the radial stress distributions of

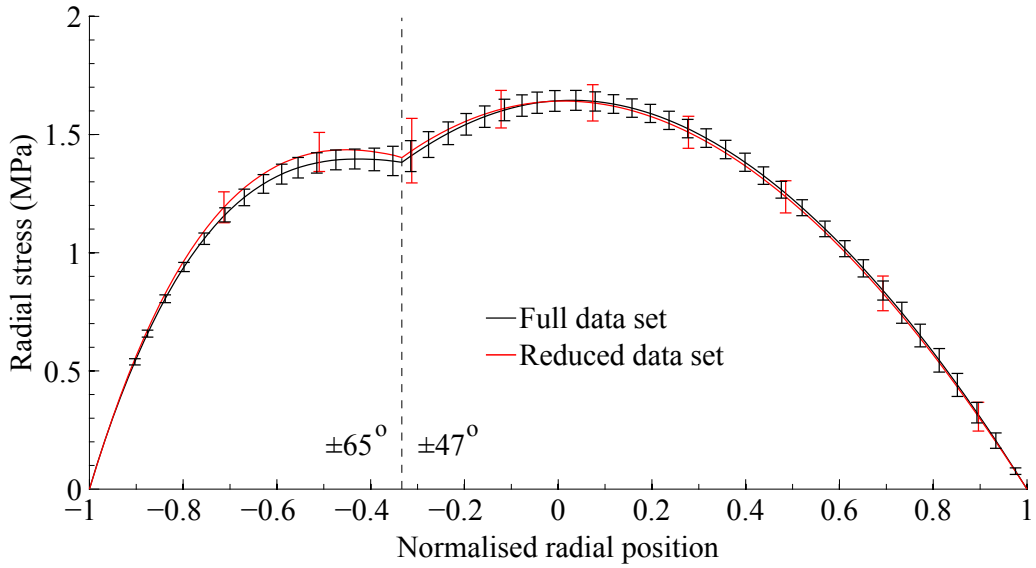

Figure 10.25: Improved error bars of the radial stress distributions for both data sets of the ±65°/±47° pipe

this pipe which can be found in Appendix M. As has come to be expected, the magnitude of the error bars of the reduced data set are significantly larger than those of the full data set, at similar through-thickness radial positions. The error bars of both data sets vary smoothly over the thickness of the pipe, and define the bounds of the most feasible solutions, associated with the level of simulated scatter. The stress distributions of both data sets are nearly identical over the outer ±47° ply, but demonstrate different trends over the inner ±65° ply. The extent of these differences are not severe, however, and the stress distribution of the full data set lies well within the error bounds of the reduced data set over the entire wall thickness of the pipe.

The "exact" in-plane residual shear stress distributions of "Gauge set C" of the ±65°/±47° pipe are illustrated in Fig. 10.26. As expected, the magnitude of the error bars of the reduced data set are much larger than those determined for the full data set. In comparison to those of Fig. 9.11, the magnitude of the error bars of the full data set have been significantly reduced. Additionally, these error bars now vary smoothly across the thickness of the pipe, highlighting the regions most sensitive to measurement scatter. It is interesting to note that nearly all of the error bounds of this data set encompass the zero-stress line expected to exist through the thickness of this pipe which is associated with its being filament-wound. The same can be said for the error bars of the reduced data set. Unfortunately, as for the results of the axial and hoop stress distributions, there are not enough error bars plotted for this data set to highlight the regions most sensitive to measurement error. This is a clear illustration that although the reduced number of layer removals can give a good representation of the stress distribution, it does not properly highlight areas

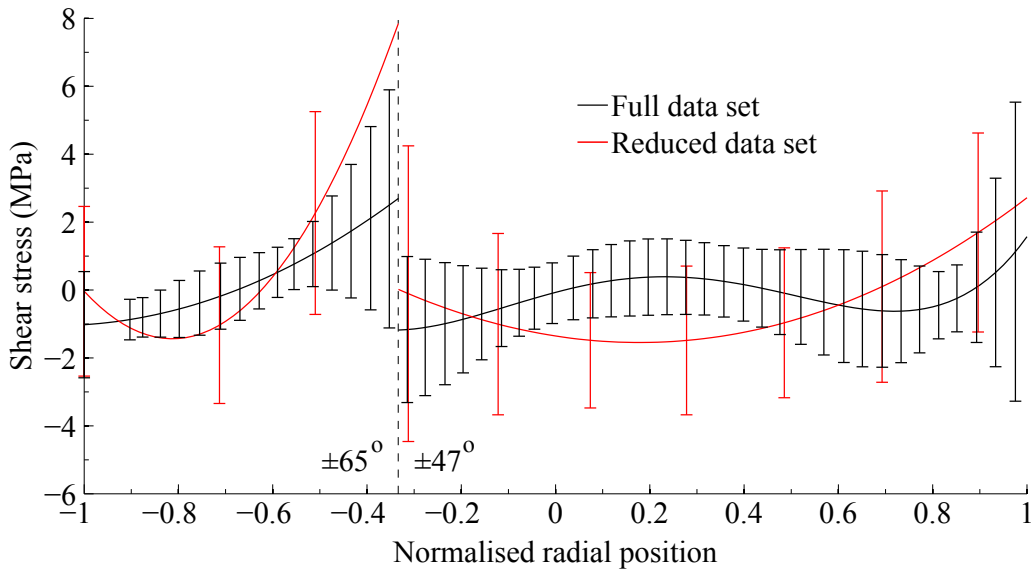

Figure 10.26: Improved error bars of the shear stress distributions for both data sets of the ±65°/±47° pipe

where the error bounds may become very large. These regions correspond with the outer surface of the pipe, and within the inner ply at the ply interface. It is therefore useful to produce plots such as Fig. 10.22, so that the sensitivity of the stress distributions to measurement scatter, across the full thickness of the pipe, can be demonstrated. Although the error bars of Fig. 10.26 are large in comparison to the state of stress, they are of similar magnitude to the error bars of the hoop stress distributions of this pipe, illustrated in Fig. 10.24. This is a positive result, and implies that this level of accuracy has been maintained.

10.4 ±75°/±36° Filament-wound pipe

The sensitivity analysis of the ±75°/±36° filament-wound pipe was performed for both the full and reduced data sets of "Gauge set C". For each simulation, scatter was added to the "exact" strain variations. These, once again, were taken as the polynomials fitted to the measured data of each data set. The scatter added to generate each simulated strain variation took the form of random values, governed by the normal distribution. The magnitude of the random values was constrained by SD variations determined from the scatter of the measured data about the "exact" polynomial fits. These SD variations were obtained for each gauge orientation, and are presented in Appendix L. As with the ±55° and ±65°/±47° pipes, the original thickness of the removed layers of both the full and reduced data sets was maintained. Removal of layers the same thickness, and the

addition of scatter of magnitude similar to that of the experimental data allows the true error in the measured stress distributions to be estimated. For each data set, 100 sets of scatter were generated and least-squares polynomials fitted to each variation. Since the pipe is laminated, a distinct change in slope occurs in the strain data when material is removed at the ply interface, and two separate polynomials were therefore required, one for the removal of each ply. Each pair of polynomials was forced to pass through the same value in strain when material was removed at the ply interface. This was done in the same manner as described in Section 8.

10.4.1 Full data set

The least-squares polynomials fitted to the simulated strain variations of the full data set varied between 2nd and 5th order. As with the strain variations of the $\pm 55^{\circ}$ and $\pm 65^{\circ}/\pm 47^{\circ}$ pipes, the polynomials fitted to the full data set of the $\pm 75^{\circ}/\pm 36^{\circ}$ pipe are constrained to lie relatively close to the "exact" strain distributions, and the bounds of these fits generally lie well within the bounds of the scatter. As has been discussed, this is purely a result of the large number of data points describing each variation. As with the strain variations of the $\pm 65^{\circ}/\pm 47^{\circ}$ pipe, however, the presence of two separate polynomials somewhat reduces the level of constraint on the fits in the region when material is removed at the ply interface and is associated with the end point stability of these fits. Therefore the polynomial fits of the $\pm 75^{\circ}/\pm 36^{\circ}$ pipe are spread over a wider range than the polynomial fits of the full data set of the $\pm 55^{\circ}$ pipe in this region. This behaviour translates directly into considerable scatter in the stress distributions at the ply interface of the $\pm 75^{\circ}/\pm 36^{\circ}$ pipe. For the simulated axial strain variations, polynomials of 3rd and 4th order were fitted to the data corresponding to the removal of material from the outer ply. Polynomials of 2nd order were not considered for this region as these did not adequately fit the strain variations. Polynomials of 3rd order were fitted to the axial strain data corresponding to removal of material from the inner ply, as this is the same order as the "exact" variation of the full data set for this region. For the circumferential distributions, polynomials of 2nd to 5th order were fitted to the each set of simulated data corresponding to the removal of material from the outer ply. Polynomials of 5th order were included in this case as this is the same order of the "exact" variation for this region. Only 2nd order polynomials were considered for removal of material from the inner ply. For the variations in the 45° strain measurements of the full data set, polynomials of 3rd and 4th order were fitted for the outer ply, and 2nd order polynomials fitted for the inner ply. As with the axial strain variations, 2nd order polynomial fits were not considered for the region of the outer ply, since these did not adequately fit the strain variations. All of the simulated strain variations of the full data set of the $\pm 75^{\circ}/\pm 36^{\circ}$ pipe are presented in

Appendix M. For each simulation of scatter, there exist 8 corresponding residual axial, hoop, and radial stress distributions, associated with the different combinations of the polynomials fitted to the axial and circumferential strain data. Since the shear strain is dependant on the strain response of all three orientations, for each simulation there exist 16 different in-plane shear stress distributions. Since 100 different strain variations were generated for each gauge orientation, there exist a total of 800 possible axial, hoop, and radial stress distributions, and 1600 residual shear stress distributions. The residual stress distributions are presented in Appendix M. For illustrative purposes, the residual axial stresses are also discussed in this section and are presented in Fig. 10.27. Due to the self-correcting nature of the current method of residual stress measurement, all solutions of Fig. 10.27 adhere to the requirement of self-equilibrium. Over the outer $\pm 36^{\circ}$ ply, there is a clear distinction between the trends of the 3rd and 4th order solutions and these solutions somewhat mirror one another. Consequently one might argue that for a number of simulations, the optimal solution lies somewhere between those of the two different distributions. This type of solution can be achieved by altering the polynomials fitted to the strain variations, possibly by applying a weighting to the strain data [150] or utilising Thikhonov regularisation [163, 173]. Regularisation is often applied to the strain variations measured using the crack compliance [173] and hole-drilling methods [239], allowing the strain fits to be somewhat smoothed by minimising the effect of measurement error. Optimising the solutions of the current method using a similar approach would not only allow more reasonable stress distributions to be obtained, but also reduce the uncertainty associated with the presence of scatter in the strain measurements. For the purposes of this work, however, these techniques are not considered.

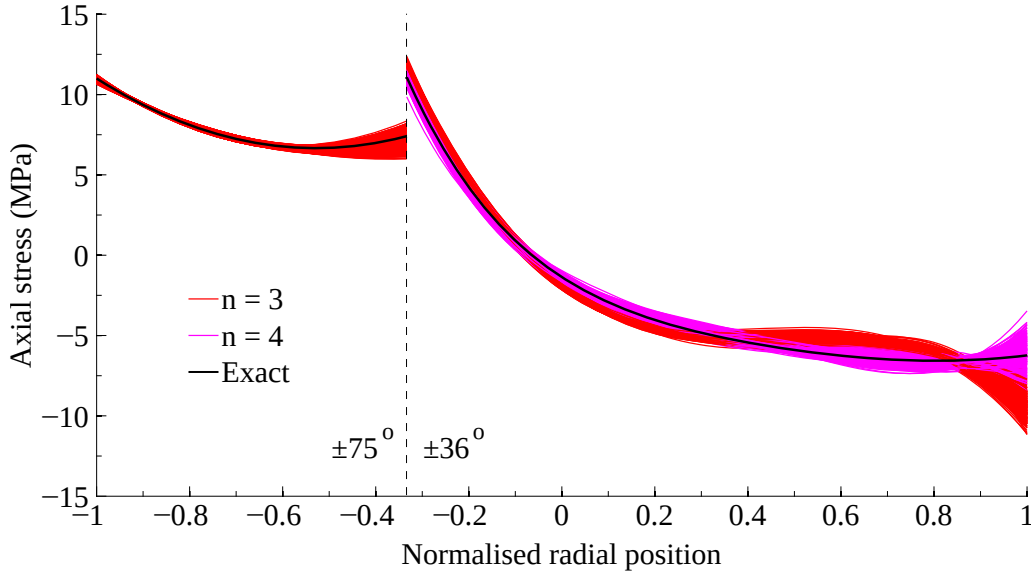

Figure 10.27: Axial stress variations for the full data set of the $\pm 75^{\circ}/\pm 36^{\circ}$ pipe

10.4.2 Reduced data set

As with the axial strain variations of the full data set, the polynomials fitted to the strains of the reduced data set of the $\pm75^\circ/\pm36^\circ$ pipe were limited to 3rd and 4th order, but the polynomials fitted for removal of material from the inner ply were of 2nd order, the same order as that of "exact" variation for this region. Polynomial pairs of 2nd to 4th order were considered for the circumferential strain variations, and 3rd and 4th order pairs were fitted to the 45° strain data. The scatter added to each "exact" variation (taken as the polynomials fitted to the measured data of this data set, illustrated in Fig 9.12) was constrained by the same SD variations used to generate the scatter in the strain variations of the full data set. These can be found in Appendix L. The simulated strain variations and corresponding polynomial fits for all three gauge orientations of the reduced data set are presented in Appendix M. Due to the reduced number of data points describing each strain variation, the bounds of the polynomial fits of the reduced data set, for each gauge orientation, lie significantly further apart than those of the polynomials fitted to the strain variations of the full data set. Owing to the different combinations of the polynomials fitted to the axial and circumferential strain data, for 100 sets of scatter there exist 600 different residual axial, hoop, and radial stress distributions. Since the shear strain response is dependant on the response in all three gauge orientations, there exist 1200 possible residual in-plane shear stress distributions. All of the residual stress distributions arising from the simulated strain variations of the reduced data set are presented in Appendix M. The stress distributions of the reduced data set of the $\pm75^\circ/\pm36^\circ$ pipe were found in the same manner as those of the reduced data sets of the $\pm55^\circ$ and $\pm65^\circ/\pm47^\circ$ pipes whereby the number of layers for which the residual stresses were evaluated was numerically increased to 50. As has been discussed, this was done to ensure that the radial stress distributions of this pipe were accurately resolved. Additionally, evaluating the stresses at more points through the thickness also allows a better representation of the other stress components to be obtained, particularly when these vary significantly through the wall thickness. The stress distributions of this data set, like those of the reduced data sets of the $\pm55^\circ$ and $\pm65^\circ/\pm47^\circ$ pipes, are significantly more sensitive to scatter in the strain measurements than the stress distributions of the full data set. This is a consequence of the increased range defined by the bounds of the polynomial fits, a result of the reduced number of data points. Additionally, like the $\pm65^\circ/\pm47^\circ$ pipe, the stress distributions of the $\pm75^\circ/\pm36^\circ$ pipe are most sensitive to measurement scatter in the regions of the outer surface and the ply interface.

10.4.3 Error bar estimation

This section presents the "exact" stress distributions of both the full and reduced data sets of the ±75°/±36° pipe, together with the improved error bars which are estimated using the spread in the stress distributions as a result of measurement scatter. As with the ±55° and ±65°/±47° pipes, the error bars are plotted at the radial positions corresponding to the mid-radius of the removed layers and their magnitude corresponds with a factor of three times the SD of the stress variation. Under the assumption that the stress distributions associated with the simulated strain variations are normally distributed about the "exact" solutions, this ensures a 99.7% confidence level [233] that all possible solutions in the residual stresses of each data set lie within the bounds of the error bars. This is of course, limited by the level of simulated scatter (and thus experimental scatter) and the range of the least-squares polynomial fits considered.

The "exact" axial residual stress distributions of the full and reduced data sets of the ±75°/±36° pipe, together with the associated error bars, are illustrated in Fig. 10.28. Compared to those presented in Fig. 9.13, the magnitude of the error bars of the full data set have been significantly reduced. Additionally, these error bounds now vary smoothly over the thickness of the pipe, and highlight the regions most sensitive to measurement error. It is clear from this figure that the solution is most sensitive to measurement scatter at the outer surface of the pipe, and the uncertainty in this region is close to ±4 MPa. This is quite large, considering that the "exact" stress at the outer surface has a magnitude of only about 7 MPa. The large value of the uncertainty is a direct result of the variation between the 3rd and 4th order solutions, seen in Fig. 10.27. Referring back to Fig. 10.28, the magnitude of the error bounds of the full data set rapidly decrease away from the outer surface, and fluctuate over the remaining thickness of the outer ply. Over the entire wall thickness of the pipe, the axial stress distribution of the reduced data set lies within the error bars of the full data set. At similar through-thickness radial positions, the magnitude of the error bars of the reduced data set are significantly larger than those of the full data set. The error bars of the reduced data set, however, are not numerous enough to adequately highlight the uncertainty of this solution at the outer surface of the pipe. There is thus merit in producing figures such as Fig. 10.27 so that the sensitivity of the stress solutions to measurement error over the entire wall thickness can be demonstrated, particularly when the number of removed layers is minimised.

The "exact" hoop residual stress distributions of both the full and reduced data sets of the ±75°/±36° pipe are illustrated in Fig. 10.29. Included in this figure are the error bars, determined for each data set. Compared to those presented in Fig. 9.14, the magnitude of most of the error bars of the full data set have been significantly reduced. Additionally,

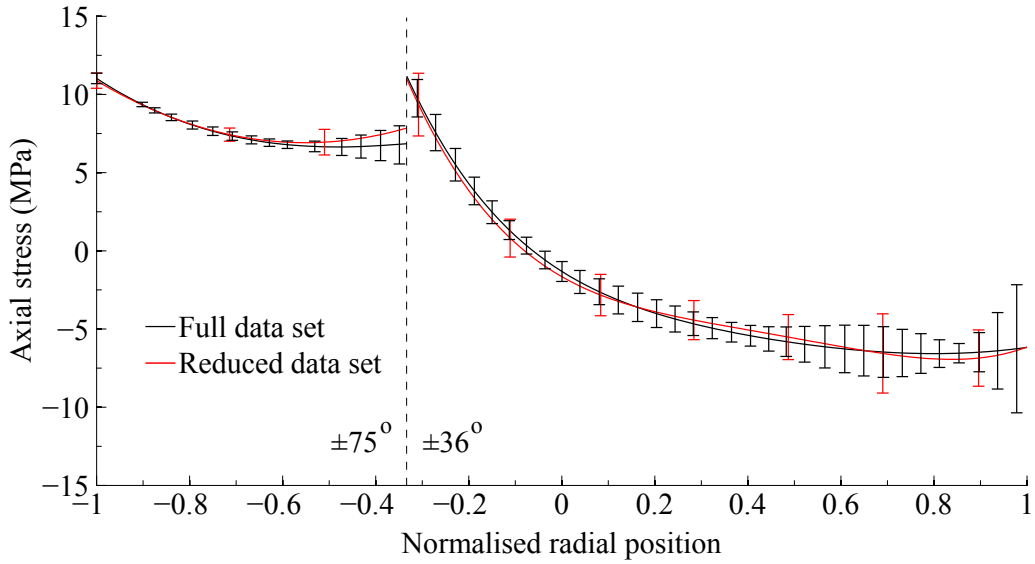

Figure 10.28: Improved error bars of the axial stress distributions for both data sets of the ±75°/±36° pipe

these error bars no longer vary randomly in magnitude, but form a smooth, continuous band of uncertainty, where the regions most sensitive to measurement error are highlighted. Over the entire wall thickness of the pipe, the stress distribution of the reduced data set lies within the error bounds of the full data set. Between the normalised radial positions of 0.9 and 0.3, the magnitude of the error bars of the reduced data set are quite similar to those obtained for the full data set. Over the remaining wall thickness, however, the error bars of the reduced data set are significantly larger, particularly in the region the ply interface. Despite this, we know that the error bars of this data set are not numerous enough to adequately highlight the uncertainty of the this stress solution in the region of the outer surface of the pipe.

The "exact" radial stress distributions of the ±75°/±36° pipe are illustrated in Fig. 10.30. The error bars corresponding to the full data set are of similar magnitude to those presented for this data set in Fig. 9.16. Unlike those of Fig. 9.16, however, the error bars of Fig. 10.30 vary smoothly over the wall thickness of the pipe. The largest uncertainty occurs at the ply interface, and the closest error bound to this region, at the normalised radial position of about -0.3, has a magnitude of roughly ±0.06 MPa. Over the entire thickness of the pipe, the stress distribution corresponding to the reduced data set lies within all the uncertainty bounds of the full data set. This distribution is identical to the variation presented in Fig. 9.17 for this data set, which demonstrates the advantage of numerically increasing the number of removed layers, addressing the issue of the loss of resolution of this stress component. Referring back to Fig. 10.30, the magnitude of the error bounds of this data set are significantly larger than those of the full data set, a result

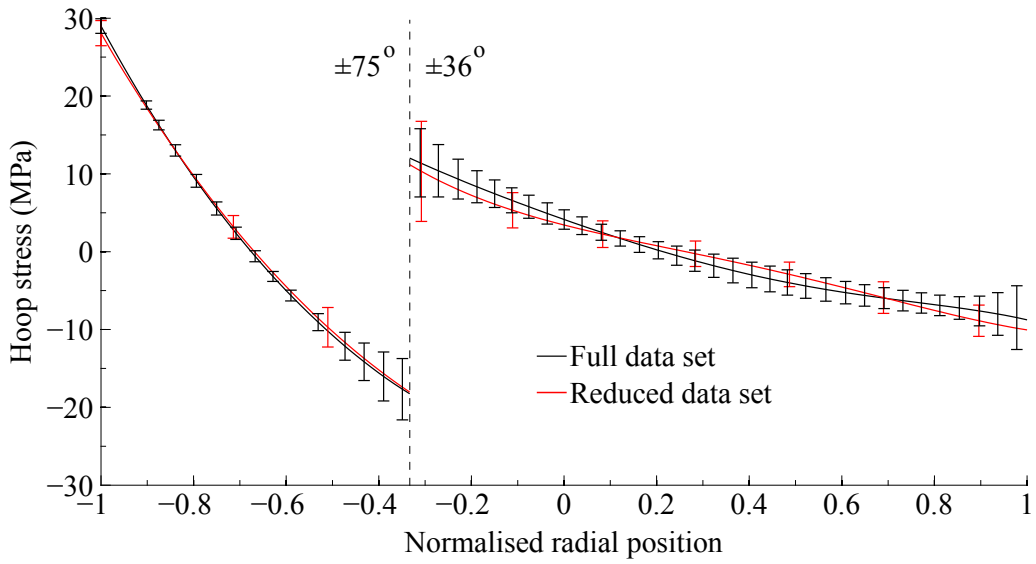

Figure 10.29: Improved error bars of the hoop stress distributions for both data sets of the ±75°/±36° pipe

of the increased sensitivity of this solution with the reduction in the number of physically removed layers. The largest uncertainty in this stress distribution, like that of the full data set, occurs at the ply interface. The magnitude of the error bar closest to this region, around the normalised radial position of -0.3, is just larger than ±0.12 MPa.

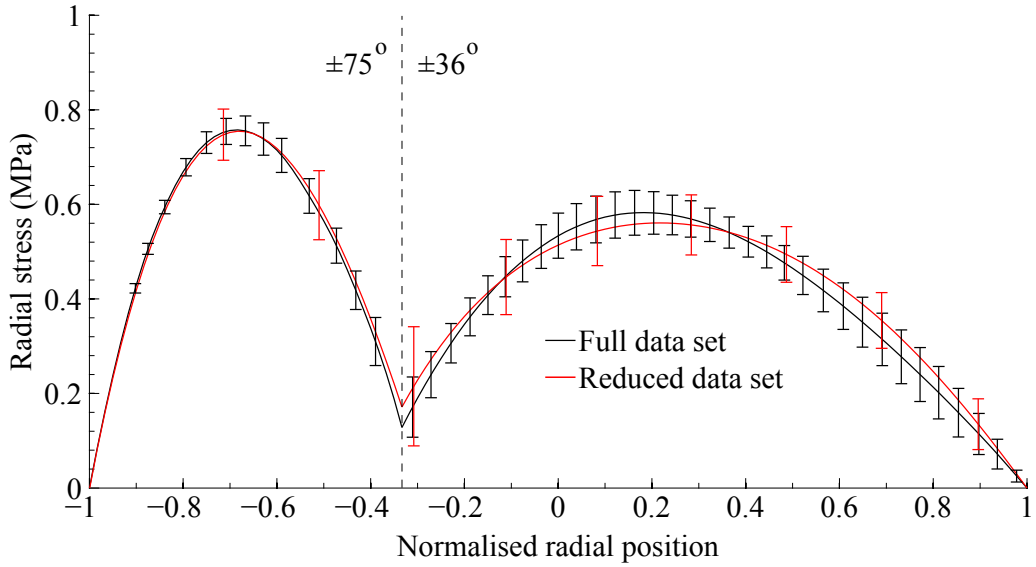

Figure 10.30: Improved error bars of the radial stress distributions for both data sets of the ±75°/±36° pipe

The "exact" in-plane residual shear stress distributions of the ±75°/±36° pipe are illustrated in Fig. 10.31. Compared to those of Fig. 9.15, the magnitude of the error bars of the full data set have been significantly reduced over the majority of the wall thickness of the pipe. In some cases, the extent of this reduction is by a factor of more than 10. Despite this, the error bounds of this data set are quite large in relation to the zero-stress state expected to exist. This is not very concerning, however, since these uncertainties are of similar magnitude to those obtained for the axial stress distribution of the full data set, shown in Fig. 10.28. This implies that a similar level of accuracy has been maintained. Additionally, over the entire wall thickness of the pipe, every error bar of Fig. 10.31 encompasses the zero-stress line. At similar through-thickness radial positions, the error bars of the reduced data set are significantly larger than those determined for the full data set, a consequence of the increased sensitivity associated with the reduction in the number of removed layers. These do not, however, adequately highlight the severe sensitivity of this solution at the outer surface of the pipe which we know exist and which can be seen in Appendix M, if desired. Thus, if the number of removed layers is minimised, figures such as Fig. 10.27 should be utilised to demonstrate the uncertainty in the resulting stress distributions over the entire wall thickness of the pipe.

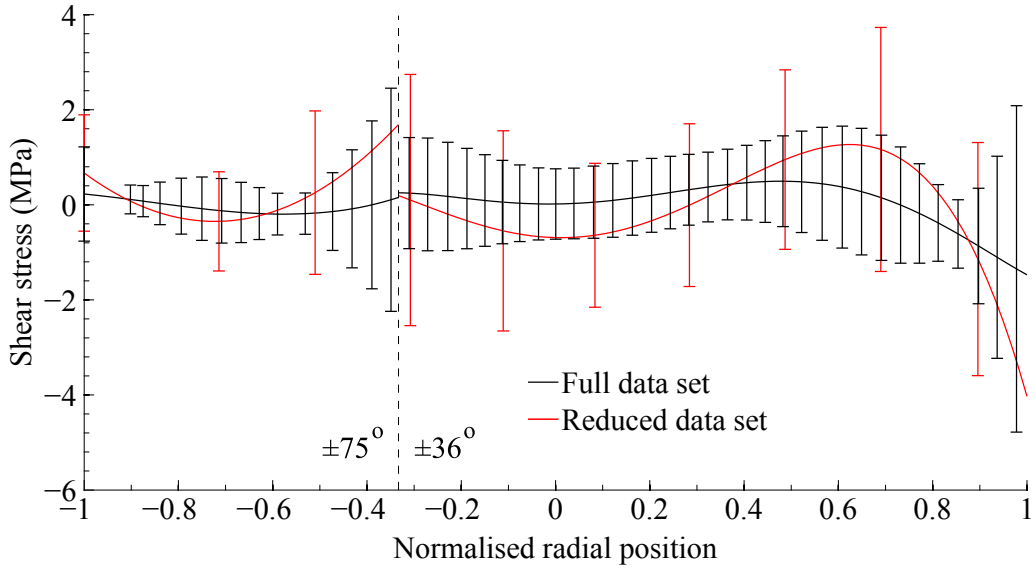

Figure 10.31: Improved error bars of the shear stress distributions for both data sets of the ±75°/±36° pipe

It is clear from the results presented in this section that the new method of uncertainty analysis is far superior to the original method of error analysis presented in Section 5. Unlike those found using the technique of Section 5, the error bounds determined using the method presented in this section do not vary randomly through the wall thickness of

the pipes but rather form smooth bands of uncertainty, highlighting the regions of the stress distributions that are most sensitive to scatter in the measured strain variations. In addition to this, the error bounds found using the new method of uncertainty analysis are not directly dependant on the thickness of the removed layers, which is a serious issue with the original method of error analysis. As has been discussed, one would expect more accurate results with an increase in the amount of measured data points. This behaviour is directly associated with the level of constraint that the number of measured data points has on the polynomials fitted to the data, and is accurately represented by the error bounds found using the new technique of error analysis.

Using this technique, error bounds were determined for the measured residual stress distributions of both the full and reduced data set of each pipe configuration. Since the level of scatter governing the simulated strain variations was very similar to the scatter observed the in the experimentally measured data and the thickness of the removed layers was maintained, the error bounds presented in this section can be considered an accurate estimate of the error in the stress distributions measured using the current method of residual stress measurement. Compared to those determined using the previous method of uncertainty analysis, the error bars have significantly reduced in magnitude. Considering the level of scatter in the simulated strain variations, this is a positive result and highlights the ability of the current method of residual stress measurement to give good results, even if large amounts of scatter are present in the measured data.

11 Conclusions

From the work presented in this thesis, the following conclusions can be drawn:

- No previously published works extend the capabilities of Sachs' method to allow the measurement of the residual stresses within layered FRP pipes of anisotropic lay-up.
- Previous extensions of Sachs' method to cylindrically orthotropic pipes are accurate only for relatively thin-walled structures.
- A method that addresses these deficiencies has been presented. This method utilises the exact elastic solution of layered anisotropic pipes under axisymmetric loading conditions, and produces residual stress distributions that always adhere to the self-equilibrium requirement.
- Additionally, a method for estimating the bounds of the meso-scale residual in-plane shear stresses within filament-wound pipes has been presented.
- The current method has been validated against Sachs' method for a thick-walled isotropic pipe, as well as against a previous solution for a thin-walled orthotropic pipe. In addition to this, the application of the current method to thick-walled orthotropic, and layered anisotropic pipes has been validated using FE simulations.
- Using the current method, the residual stresses within three thick-walled filament-wound GFRP pipes were measured.
- The current method was applied to the pipes and three separate sets of residual stress measurements were obtained for each pipe. These results are in excellent agreement with one another, despite a significant level of scatter in the measured data. The agreement of these results validates the assumed axisymmetric state of the residual stresses.
- The measured residual in-plane shear stress distributions of all the GFRP pipes are of relatively low magnitude, and oscillate about the zero-stress line. This supports the assumed bulk-scale orthotropic material properties of filament-wound pipes.

- The effect of increasing the removed layer thickness from each of these pipes has been investigated, and it has been demonstrated that little or no loss in the resolution of the measured residual stress distributions occurs under these conditions.

- The initial method of uncertainty analysis, based upon the standard linearised differential relationships, produces error bars that are highly dependant on the thickness of the layers removed from the pipes. As a result, the error bounds estimated for the removal of thinner layers are significantly larger that those estimated for the removal of thicker layers.

- To deal with this issue, a new method of error analysis has been presented. This makes use of an analysis of the sensitivity of the residual stress distributions to the level of scatter in the measured strain variations.

- A sensitivity analysis using the new technique was performed which considered the removal of both thin and thick layers from the three GFRP pipes. Improved error bounds, based on these results, were estimated. As required, these results indicate that the uncertainties in residual stress increase with an increase in the thickness of the removed layers. This effect is associated with a reduction in the level of constraint on the polynomials fitted to the measured strain distributions as the amount of data decreases.

12 Recommendations

The method of residual stress measurement proposed in this thesis focusses on the removal of material from the outer surface, while measuring the strain change at the inner surface of a pipe. The boring out of material from the inner surface of a pipe has not been considered. Consequently, it is recommended that the equations for this type of test be derived. These can be determined in a similar manner as those presented in this work.

The current method can be applied to layered anisotropic pipes of any wall thickness. Although this has been demonstrated through simulation, it has not been used experimentally in this manner, since no anisotropic pipes of suitable quality could be sourced. It is therefore recommended that this method be utilised to experimentally measure the residual stress state within layered pipes that are cylindrically anisotropic at the bulk-scale.

It has been discussed that the residual stress solutions obtained using the current method could be optimised by altering the polynomials fitted to the measured strain variations, possibly by applying a weighting to the data, or employing Thikhonov regularisation. Application of these techniques was not, however, considered in this work. This is consequently recommended for future study.

REFERENCES

[1] P.J. Hogg and D. Hull. Role of matrix properties on the stress corrosion of GRP. *BPF Reinforced Plastics Congress*, paper 29, 1983.

[2] P.J. Hogg. A model for stress corrosion crack growth in glass reinforced plastics. *Composites Science and Technology*, 38(1):23 – 42, 1990.

[3] J.N. Price and D. Hull. Effect of Matrix Toughness on Crack Propagation during Stress Corrosion of Glass Reinforced Composites. *Composites Science and Technology*, 28(3):193–210, 1987.

[4] George Marsh. Manipulating matrices. *Reinforced Plastics*, 47(7):22–24, 2003.

[5] Amanda Jacob. Vinyl esters lead the corrosion challenge. *Reinforced Plastics*, 47(6):32–35, 2003.

[6] British Standards Institution. Design and construction of vessels and tanks in reinforced plastics. BS 4994, 1987.

[7] British Standards Institution. GRP tanks and vessels for use above ground-Part 2: Composite materials-Chemical resistance. BS EN 13121-2, 2003.

[8] British Standards Institution. GRP tanks and vessels for use above ground-Part 3: Design and workmanship. BS EN 13121-3, 2008.

[9] R.F. Regester. Behavior of Fiber Reinforced Plastic Materials in Chemical Service. *Corrosion*, 25(4):157–167, 1969.

[10] Q. Qiu and M. Kumosa. Corrosion of E-glass fibers in acidic environments. *Composites Science and Technology*, 57(5):497 – 507, 1997.

[11] P.J. Hogg. Factors affecting the stress corrosion of GRP in acid environments. *Composites*, 14(3):254 – 261, 1983.

[12] P. J. Hogg and D. Hull. Micromechanisms of crack growth in composite materials under corrosive enviroments. *Metal Science*, 14:441–449, 1980.

[13] F.R. Jones, J.W. Rock, and A.R. Wheatley. Stress corrosion cracking and its implications for the long-term durability of E-glass fibre composites. *Composites*, 14(3):262 – 269, 1983.

[14] L.S. Norwood and A.F. Millman. Strain limited design criteria for reinforced plastic process equipment. *Composites*, 11(1):39 – 45, 1980.

[15] M.A. Stone, I.F. Schwartz, and H.D. Chandler. Residual stresses associated with post-cure shrinkage in GRP tubes. *Composites Science and Technology*, 57(1):47 – 54, 1997.

[16] M.M. Shokrieh. *Residual Stresses in Composite Materials*. Woodhead Publishing, Limited, 1st edition, 2014.

[17] R.G. Reid. *The Measurement of Longitudinal Residual Stresses in Unidirectional Glass Fibre Reinforced Plastic*. PhD thesis, University of the Witwatersrand, Johannesburg, 2009.

[18] P.P. Parlevliet, H.E.N. Bersee, and A. Beukers. Residual stresses in thermoplastic composites – a study of the literature. Part III: Effects of thermal residual stresses. *Composites Part A: Applied Science and Manufacturing*, 38(6):1581 – 1596, 2007.

[19] Yu.M. Tarnopol'skii, G.G. Portnov, and Yu.B. Spridzans. Compensation of thermal stresses in glass-fiber-reinforced plastic articles by the layerwise winding method. *Polymer Mechanics*, 8(4):553–557, 1972.

[20] A.I. Beil', G.G. Portnov, I.V. Sanina, and V.A. Yakushin. Elimination of the initial thermal stresses in wound articles made from composites by varying the winding angle over the thickness. *Mechanics of Composite Materials*, 16(6):715–720, 1981.

[21] H. Lü, M. Schlottermüller, N. Himmel, and R. Schledjewski. Effects of Tape Tension on Residual Stress in Thermoplastic Composite Filament Winding. *Journal of Thermoplastic Composite Materials*, 18(6):469–487, 2005.

[22] S.R. White and H.T. Hahn. Cure Cycle Optimization for the Reduction of Processing-Induced Residual Stresses in Composite Materials. *Journal of Composite Materials*, 27(14):1352–1378, 1993.

[23] D.H. Lee, S.K. Kim, W.I. Lee, S.K. Ha, and S.W. Tsai. Smart cure of thick composite filament wound structures to minimize the development of residual stresses. *Composites Part A: Applied Science and Manufacturing*, 37(4):530 – 537, 2006.

[24] S.R. White and Z. Zhang. The Effect of Mandrel Material on the Processing-Induced Residual Stresses in Thick Filament Wound Composite Cylinders. *Journal of Reinforced Plastics and Composites*, 12(6):698–771, 1993.

[25] W.K. Binienda and Y. Wang. Residual stresses Reduction in Filament Wound Composite Tubes. *Journal of Reinforced Plastics and Composites*, 18(8):684–701, 1999.

[26] V.M. Indenbaum. Calculation of stresses in multilayer cylindrical articles made of variously combined composite materials. *Polymer Mechanics*, 10(1):48–52, 1974.

[27] Y.K. Kim and S.R. White. Cure-dependent viscoelastic residual stress analysis of filament-wound composite cylinders. *Mechanics of Composite Materials and Structures*, 5(4):327–354, 1999.

[28] E.P. Calius and G.S. Springer. A model of filament-wound thin cylinders. *International Journal of Solids and Structures*, 26(3):271 – 297, 1990.

[29] S.C. Mantell and G.S. Springer. Manufacturing process models for thermoplastic composites. *Journal of Composite Materials*, 26(16):2348–2377, 1992.

[30] S.C. Mantell and G.S. Springer. Filament winding process models. *Composite Structures*, 27(1–2):141 – 147, 1994.

[31] S.R. White and H.T. Hahn. Process Modeling of Composite Materials: Residual Stress Development during Cure. Part I. Model Formulation. *Journal of Composite Materials*, 26(16):2402–2422, 1992.

[32] P. Rangaswamy, M.B. Prime, M. Daymond, M.A.M. Bourke, B. Clausen, H. Choo, and N. Jayaraman. Comparison of residual strains measured by X-ray and neutron diffraction in a titanium (Ti-6Al-4V) matrix composite. *Materials Science and Engineering: A: Structural Materials: Properties, Microstructure and Processing*, A259(2):209–219, 1999.

[33] F. Fiori, G. Albertini, E. Girardin, A. Giuliani, A. Manescu, and F. Rustichelli. Neutron and synchrotron radiation non-destructive methods for the characterisation of materials for different applications. *Journal of Alloys and Compounds*, 382(1-2):39–45, 2004.

[34] S.H. Li, G. Zeng, Y.F. Ma, Y.J. Guo, and X.M. Lai. Residual stresses in roll-formed square hollow sections. *Thin-Walled Structures*, 47(5):505–513, 2009.

[35] B.N. Cox, M.R. James, D.B. Marshall, and R.C. Addison. Determination of residual stresses in thin sheet titanium aluminide composites. *Metallurgical Transactions A*, 21(10):2701–2707, 1990.

[36] K.L. Kendig, W.O. Soboyejo, and D.B. Miracle. Measurement of residual stresses in Ti-15-3 SCS-9 continuously reinforced composites using X-ray diffraction and a matrix etching technique. *Scripta Metallurgica et Materialia*, 32(5):669–674, 1995.

[37] T. Adachi, T. Sekino, T. Nakayama, T. Kusunose, and K. Niihara. Measurement of microscopic stress distribution of multilayered composite by X-ray stress analysis. *Materials Letters*, 57(20):3057–3062, 2003.

[38] F. Rotundo and A.M. Korsunsky. Synchrotron XRD study of residual stress in a shot peened Al/SiCp composite. *Procedia Engineering*, 1(1):221–224, 2009.

[39] M.B. Prime. Residual stress measurement by successive extension of a slot: The crack compliance method. *Applied Mechanics Reviews*, 52(2):75–96, 1999.

[40] Paul Predecki and Charles S. Barrett. Stress measurement in graphite/epoxy composites by X-ray diffraction from fillers. *Journal of Composite Materials*, 13(1):61–71, 1979.

[41] R.H. Fenn and A.M. Jones. Measurements of Residual Stress in Carbon Fibre Composite Materials Using X-Ray Diffraction. In G. Beck, S. Denis, and A. Simon, editors, *International Conference on Residual Stresses*, pages 160–165. Springer Netherlands, 1989.

[42] R.H. Fenn, A.M. Jones, and G.M. Wells. X-ray diffraction investigation of triaxial residual stresses in composite materials. *Journal of Composite Materials*, 27(14):1338–1351, 1993.

[43] R. Meske and E. Schnack. Particular adaptation of X-ray diffraction to fiber reinforced composites. *Mechanics of Materials*, 35(1):19–34, 2003.

[44] R. Meske and E. Schnack. A micromechanical model for X-ray stress analysis of fiber reinforced composites. *Journal of Composite Materials*, 35(11):972–998, 2001.

[45] G. Albertini, G. Bruno, A. Carrado, F. Fiori, M. Rogante, and F. Rustichelli. Determination of residual stresses in materials and industrial components by neutron diffraction. *Measurement Science and Technology*, 10(3):R56–R73, 1999.

[46] J. Mathar. Determination of initial stresses by measuring the deformation around drilled holes. *Transactions of the ASME*, 56:249–254, 1934.

[47] ASTM E837-13a. Standard Test Method for Determining Residual Stresses by the Hole-Drilling Strain-Gage Method. ASTM International, West Conshohocken, PA, 2013, www.astm.org.

[48] G.S. Schajer. Advances in Hole-Drilling Residual Stress Measurements. *Experimental Mechanics*, 50(2):159–168, 2010.

[49] G.S. Schajer. Hole-Drilling Residual Stress Measurements at 75: Origins, Advances, Opportunities. *Experimental Mechanics*, 50(2):245–253, 2010.

[50] O. Sicot, X.L. Gong, A. Cherouat, and J. Lu. Influence of experimental parameters on determination of residual stress using the incremental hole-drilling method. *Composites Science and Technology*, 64(2):171–180, 2004.

[51] P.P. Parlevliet, H.E.N. Bersee, and A. Beukers. Residual stresses in thermoplastic composites—A study of the literature—Part II: Experimental techniques. *Composites Part A: Applied Science and Manufacturing*, 38(3):651 – 665, 2007.

[52] Gianni Nicoletto. Moiré interferometry determination of residual stresses in the presence of gradients. *Experimental Mechanics*, 31(3):252–256, 1991.

[53] Z. Wu, J. Lu, and B. Han. Study of Residual Stress Distribution by a Combined Method of Moiré Interferometry and Incremental Hole Drilling, Part I: Theory. *Journal of Applied Mechanics*, 65(4):837–843, 1998.

[54] Z. Wu, J. Lu, and B. Han. Study of Residual Stress Distribution by a Combined Method of Moiré Interferometry and Incremental Hole Drilling, Part II: Implementation. *Journal of Applied Mechanics*, 65(4):844–850, 1998.

[55] Y. Min, M. Hong, Z. Xi, and L. Jian. Determination of residual stress by use of phase shifting moiré interferometry and hole-drilling method. *Optics and Lasers in Engineering*, 44(1):68–79, 2006.

[56] D.V. Nelson and J.T. McCrickerd. Residual-stress determination through combined use of holographic interferometry and blind-hole drilling. *Experimental Mechanics*, 26(4):371–378, 1986.

[57] A. Makino and D. Nelson. Residual-stress determination by single-axis holographic interferometry and hole drilling—Part I: Theory. *Experimental Mechanics*, 34(1):66–78, 1994.

[58] D.R. Schmitt and Y. Li. Three-dimensional stress relief displacement resulting from drilling a blind hole in acrylic. *Experimental Mechanics*, 36(4):412–420, 1996.

[59] G. Focht and K. Schiffner. Determination of residual stresses by an optical correlative hole-drilling method. *Experimental Mechanics*, 43(1):97–104, 2003.

[60] F.M. Furgiuele, L. Pagnotta, and A. Poggialini. Measuring Residual Stresses by Hole-Drilling and Coherent Optics Techniques: A Numerical Calibration. *Journal of Engineering Materials and Technology*, 113(1):41–50, 1991.

[61] E. Ponslet and M. Steinzig. Residual Stress Measurement using the Hole Drilling Method and Laser Speckle Interferometry Part II: Analysis Technique. *Experimental Techniques*, 27(4):17–21, 2003.

[62] F.V. Díaz, G.H. Kaufmann, and O. Möller. Residual stress determination using blind-hole drilling and digital speckle pattern interferometry with automated data processing. *Experimental Mechanics*, 41(4):319–323, 2001.

[63] S.Y. Wu and Y.W. Qin. Determination of residual stresses using large shearing speckle interferometry and the hole drilling method. *Optics and Lasers in Engineering*, 23(4):233–244, 1995.

[64] D.R. Schmitt and R.W. Hunt. Inversion of Speckle Interferometer Fringes for Hole-drilling Residual Stress Determinations. *Experimental Mechanics*, 40(2):129–137, 2000.

[65] M.J. McGinnis, S. Pessiki, and H. Turker. Application of three-dimensional digital image correlation to the core-drilling method. *Experimental Mechanics*, 45(4):359–367, 2005.

[66] D.V. Nelson, A. Makino, and T. Schmidt. Residual Stress Determination Using Hole Drilling and 3D Image Correlation. *Experimental Mechanics*, 46(1):31–38, 2006.

[67] C.W. Bert and G.L. Thompson. A method for measuring planar residual stresses in rectangularly orthotropic materials. *Journal of Composite Materials*, 2(2):244–253, 1968.

[68] B.R. Lake, F.J. Appl, and C.W. Bert. An investigation of the hole-drilling technique for measuring planar residual stress in rectangularly orthotropic materials. *Experimental Mechanics*, 10(6):233–239, 1970.

[69] O. Sicot, X.L. Gong, A. Cherouat, and J. Lu. Determination of residual stress in composite laminates using the incremental hole-drilling method. *Journal of Composite Materials*, 37(9):831–844, 2003.

[70] G.S. Schajer and L. Yang. Residual-stress Measurement in Orthotropic Materials Using the Hole-drilling Method. *Experimental Mechanics*, 34(4):324–333, 1994.

[71] P. Pagliaro and B. Zuccarello. Residual Stress Analysis of Orthotropic Materials by the Through-hole Drilling Method. *Experimental Mechanics*, 47(2):217–236, 2007.

[72] C.B. Prasad, R. Prabhakaran, and S. Tompkins. Determination of calibration constants for the hole-drilling residual stress measurement technique applied to orthotropic composites—Part II: Experimental evaluations. *Composite Structures*, 8(3):165 – 172, 1987.

[73] G.S. Schajer. Application of Finite Element Calculations to Residual Stress Measurements. *Journal of Engineering Materials and Technology*, 103(2):157–163, 1981.

[74] M.T. Flaman and B.H. Manning. Determination of residual-stress variation with depth by the hole-drilling method. *Experimental Mechanics*, 25(3):205–207, 1985.

[75] M.M. Shokrieh and A.R. Ghasemi K. Simulation of Central Hole Drilling Process for Measurement of Residual Stresses in Isotropic, Orthotropic, and Laminated Composite Plates. *Journal of Composite Materials*, 41(4):435–452, 2007.

[76] M. Safarabadi. Prediction of calibration factors of the hole-drilling method for orthotropic composites including hybrid interphase region. *Journal of Composite Materials*, DOI: 10.1177/0021998314529680, 2014.

[77] C.B. Prasad and R. Prabhakaran. Determination of calibration constants for the hole-drilling residual stress measurement technique applied to orthotropic composites—Part I: Theoretical Considerations. *Composite Structures*, 8(2):105–118, 1987.

[78] M.M. Shokrieh and A.R. Ghasemi K. Determination of Calibration Factors of the Hole Drilling Method for Orthotropic Composites using an Exact Solution. *Journal of Composite Materials*, 41(19):2293–2311, 2007.

[79] J.F. Cárdenas-García, S. Ekwaro-Osire, J.M. Berg, and W.H. Wilson. Non-linear least-squares solution to the moiré hole method problem in orthotropic materials. Part 1: Residual stresses. *Experimental Mechanics*, 45(4):301–313, 2005.

[80] M.M. Shokrieh and S.M. Kamali. Theoretical and Experimental Studies on Residual Stresses in Laminated Polymer Composites. *Journal of Composite Materials*, 39(24):2213–2225, 2005.

[81] I.M. Zhandanov and A.K. Gonchar. Determining the residual welding stresses at depth in metals. *Automatic Welding*, 31:22–24, 1978.

[82] E.M. Beaney. Measurement of Sub-Surface Stress. CEGB Report Rd/B/N4325, 1978.

[83] M. Jesensky and J. Vargova. Calculation and measurement of stresses in thick-walled pressure vessels. *Svaracske Spravy*, 4:79–87, 1981.

[84] E. Procter and E.M. Beaney. Trepan or ring-core method, centre-hole method, Sach's method, blind hole methods, deep hole technique. In *Advances in Surface Treatment: Technology - Application - Effects*, volume 4: Residual Stresses, pages 165–198. Pergamon Press, New York, 1987.

[85] A. Mirzaee-Sisan, A.J. Fookes, C.E. Truman, D.J. Smith, T.B. Brown, and T.A. Dauda. Residual stress measurement in a repair welded header in the as-welded condition and after advanced post weld treatment. *International Journal of Pressure Vessels and Piping*, 84(5):265–273, 2007.

[86] R.H. Leggatt, D.J. Smith, S.D. Smith, and F. Faure. Development and experimental validation of the deep hole method for residual stress measurement. *The Journal of Strain Analysis for Engineering Design*, 31(3):177–186, 1996.

[87] D.J. Smith, P.J. Bouchard, and D. George. Measurement and prediction of residual stresses in thick-section steel welds. *Journal of Strain Analysis for Engineering Design*, 35(4):287–305, 2000.

[88] R.C Wimpory, P.S May, N.P O'Dowd, G.A Webster, D.J. Smith, and E. Kingston. Measurement of residual stresses in T-plate weldments. *The Journal of Strain Analysis for Engineering Design*, 38(4):349–365, 2003.

[89] P.J. Bouchard, D. George, J.R. Santisteban, G. Bruno, M. Dutta, L. Edwards, E. Kingston, and D.J. Smith. Measurement of the residual stresses in a stainless steel pipe girth weld containing long and short repairs. *International Journal of Pressure Vessels and Piping*, 82(4):299–310, 2005.

[90] D. George and D.J. Smith. Through thickness measurement of residual stresses in a stainless steel cylinder containing shallow and deep weld repairs. *International Journal of Pressure Vessels and Piping*, 82(4):279–287, 2005.

[91] T.B. Brown, T.A. Dauda, C.E. Truman, D.J. Smith, D. Memhard, and W. Pfeiffer. Predictions and measurements of residual stress in repair welds in plates. *International Journal of Pressure Vessels and Piping*, 83(11-12):809–818, 2006.

[92] D. Stefanescu, C.E. Truman, and D.J. Smith. Residual stress measurement using integrated drilling techniques. In *SEM Annual Conference & Exposition on Experimental and Applied Mechanics*, pages 1–8, 2003.

[93] D. Stefanescu, P. Browne, C.E. Truman, and D.J. Smith. Residual stress measurement within a european UIC60 rail using integrated drilling techniques. *Materials Science Forum*, 440-441:85–92, 2003.

[94] E. Kingston and D.J. Smith. Residual stress measurements in rolling mill rolls using deep hole drilling technique. *Ironmaking and Steelmaking*, 32(5):379–380, 2005.

[95] D. George and D.J. Smith. The application of the deep hole technique for measuring residual stresses in an autofrettaged tube. In *Proceedings ASME Pressure Vessels and Piping*, volume 4, pages 1–7. Seattle, Washington, 2000.

[96] M.G. Bateman, O.H. Miller, T.J. Palmer, C.E.P. Breen, E.J. Kingston, D.J. Smith, and M.J. Pavier. Measurement of residual stress in thick section composite laminates using the deep-hole method. *International Journal of Mechanical Sciences*, 47(11):1718–1739, 2005.

[97] S.G. Lekhnitskii. *Anisotropic plates, 2nd edn.* Gordon and Breach, 1968.

[98] D. George, E. Kingston, and D.J. Smith. Measurement of through-thickness stresses using small holes. *The Journal of Strain Analysis for Engineering Design*, 37(2):125–139, 2002.

[99] M.R. Hill. *Determination of residual stress based on the estimation of eigenstrain.* PhD thesis, Stanford University, California, 1996.

[100] N. Tebedge, G. Alpsten, and L. Tall. Residual-stress measurement by the sectioning method. *Experimental Mechanics*, 13(2):88–96, 1973.

[101] C.C. Weng and R.N. White. Residual stresses in cold-bent thick steel plates. *Journal of Structural Engineering*, 116(1):24–39, 1990.

[102] M. Kovač. A method for residual stress measurement in welded seams. *Journal of Materials Processing Technology*, 52(2–4):503 – 514, 1995.

[103] E.F. Rybicki, J.R. Shadley, and W.S. Shealy. A consistent-splitting model for experimental residual-stress analysis. *Experimental Mechanics*, 23(4):438–446, 1983.

[104] W.S. Shealy, J.R. Shadley, and E.F. Rybicki. An improved back computation procedure for the parting-out step of a destructive method for measuring residual stresses in pipes. *Strain*, 20(3):117–122, 1984.

[105] E.F. Rybicki and J.R Shadley. A Three-Dimensional Finite Element Evaluation of a Destructive Experimental Method for Determining Through-Thickness Residual Stresses in Girth Welded Pipes. *Journal of Engineering Materials and Technology*, 108(2):99–106, 1986.

[106] P. Casari, F. Jacquemin, and P. Davies. Characterization of residual stresses in wound composite tubes. *Composites Part A: Applied Science and Manufacturing*, 37(2):337 – 343, 2006.

[107] Y. Ueda, K. Nakacho, and S. Endo. A New Measuring Method of Residual Stresses With The Aid of Finite Element Method And Reliability of Estimated Values. *Trans. Japan Welding Research Institute*, 4(2):123–131, 1975.

[108] M.R. Hill and D.V. Nelson. Inherent strain method for residual stress determination and its application to a long welded joint. In *Proceedings of the 1995 Joint ASME/JSME Pressure Vessels and Piping Conference*, pages 343–352. Honolulu, USA, 1995.

[109] M.R. Hill and D.V. Nelson. Determining residual stress through the thickness of a welded plate. In *Proceedings of the 1996 ASME Pressure Vessels and Piping Conference*, pages 29–36. Montreal, Canada, 1996.

[110] J.A.E. Manson and J.C. Seferis. Process Simulated Laminate (PSL), a methodology to internal stress characterization in advanced composite materials. *Journal of Composite Materials*, 26(3):405–431, 1992.

[111] T.J. Chapman, J.W. Gillespie, R.B. Pipes, J.-A.E. Manson, and J.C. Seferis. Prediction of Process-Induced Residual Stresses in Thermoplastic Composites. *Journal of Composite Materials*, 24(6):616–643, 1990.

[112] D. Joh, K.Y. Byun, and J. Ha. Thermal residual stresses in thick graphite/epoxy composite laminates—uniaxial approach. *Experimental Mechanics*, 33(1):70–76, 1993.

[113] H.E. Gascoigne. Residual surface stresses in laminated cross-ply fiber-epoxy composite materials. *Experimental Mechanics*, 34(1):27–36, 1994.

[114] T.L. Andersen and A. Lystrup. Room temperature filament winding of thermoplastic composites. *Plastics, Rubber and Composites Processing and Applications*, 19(3):143–149, 1993.

[115] D. Cohen. Influence of filament winding parameters on composite vessel quality and strength. *Composites Part A: Applied Science and Manufacturing*, 28(12):1035–1047, 1997.

[116] M.A. Seif and S.R. Short. Determination of residual stresses in thin-walled composite cylinders. *Experimental Techniques*, 26(2):43–46, 2002.

[117] J.W. Kim, J.H. Lee, H.G. Kim, H.S. Kim, and D.G. Lee. Reduction of residual stresses in thick-walled composite cylinders by smart cure cycle with cooling and reheating. *Composite Structures*, 75(1–4):261–266, 2006.

[118] A.S. Kaddour, S.T.S. Al-Hassani, and M.J. Hinton. Residual Stress Assessment in Thin Angle Ply Tubes. *Applied Composite Materials*, 10(3):169–188, 2003.

[119] M.A. Seif, U.A. Khashaba, and R. Rojas-oviedo. Residual stress measurements in CFRE and GFRE composite missile shells. *Composite Structures*, 79(2):261–269, 2007.

[120] J.W. Kim and D.G. Lee. Measurement of residual stresses in thick composite cylinders by the radial-cut-cylinder-bending method. *Composite Structures*, 77(4):444–456, 2007.

[121] G. Aleong and M. Munro. Evaluation of the radial-cut method for determining residual strains in fiber composite rings. *Experimental Techniques*, 15(1):55–58, 1991.

[122] A.K. Roy. Response of thick laminated composite rings to thermal stresses. *Composite Structures*, 18(2):125 – 138, 1991.

[123] S.K. Ha, H.-T. Kim, and T.-H. Sung. Measurement and Prediction of Process-induced Residual Strains in Thick Wound Composite Rings. *Journal of Composite Materials*, 37(14):1223–1237, 2003.

[124] S.K. Ha, H.-T. Kim, and S.C. Han. Effects of Rotor Sizes and Epoxy System on the Process-Induced Residual Strains within Multi-Ring Composite Rotors. *Journal of Composite Materials*, 38(10):871–885, 2004.

[125] S.K. Ha and J.Y. Jeong. Effects of winding angles on through-thickness properties and residual strains of thick filament wound composite rings. *Composites Science and Technology*, 65(1):27–35, 2005.

[126] M.B. Prime. Cross-Sectional Mapping of Residual Stresses by Measuring the Surface Contour After a Cut. *Journal of Engineering Materials and Technology*, 123(2):162–168, 2000.

[127] M.B. Toparli, M.E. Fitzpatrick, and S. Gungor. Improvement of the Contour Method for Measurement of Near-Surface Residual Stresses from Laser Peening. *Experimental Mechanics*, 53(9):1705–1718, 2013.

[128] S. Zabeen, M. Preuss, and P.J. Withers. Residual stresses caused by head-on and 45° foreign object damage for a laser shock peened Ti–6Al–4V alloy aerofoil. *Materials Science and Engineering: A*, 560:518–527, 2013.

[129] S.D. Cuellar, M.R. Hill, A.T. DeWald, and J.E. Rankin. Residual stress and fatigue life in laser shock peened open hole samples. *International Journal of Fatigue*, 44:8–13, 2012.

[130] A.T. DeWald and M.R. Hill. Eigenstrain-based model for prediction of laser peening residual stresses in arbitrary three-dimensional bodies Part 2: Model verification. *The Journal of Strain Analysis for Engineering Design*, 44(1):13–27, 2009.

[131] A. Evans, G. Johnson, A. King, and P.J. Withers. Characterization of laser peening residual stresses in Al 7075 by synchrotron diffraction and the contour method. *Journal of Neutron Research*, 15(2):139–146, 2007.

[132] W. Woo, H. Choo, M.B. Prime, Z. Feng, and B. Clausen. Microstructure, texture and residual stress in a friction-stir-processed AZ31B magnesium alloy. *Acta Materialia*, 56(8):1701–1711, 2008.

[133] M.B. Prime, T. Gnäupel-Herold, J.A. Baumann, R.J. Lederich, D.M. Bowden, and R.J. Sebring. Residual stress measurements in a thick, dissimilar aluminum alloy friction stir weld. *Acta Materialia*, 54(15):4013–4021, 2006.

[134] C. Liu, H.-Y. Zhu, and C.-L. Dong. Internal residual stress measurement on inertia friction welding of nickel-based superalloy. *Science and Technology of Welding and Joining*, 19(5):408–415, 2014.

[135] P. Carlone and G.S. Palazzo. Longitudinal Residual Stress Analysis in AA2024-T3 Friction Stir Welding. *The Open Mechanical Engineering Journal*, 7:18–26, 2013.

[136] R.G. Citarella, P. Carlone, M. Lepore, and G.S. Palazzo. A FEM-DBEM Investigation of the Influence of Process Parameters on Crack Growth in Aluminum Friction Stir Welded Butt Joints. *Key Engineering Materials*, 554-557:2118–2126, 2013.

[137] C. Liu and X. Yi. Residual stress measurement on AA6061-T6 aluminum alloy friction stir butt welds using contour method. *Materials & Design*, 46:366–371, 2013.

[138] M. Kerr, M.B. Prime, and H. Swenson. Residual Stress Characterization in a Dissimilar Metal Weld Nuclear Reactor Piping System Mock up. *Journal of Pressure Vessel Technology*, 135(4):041205, 2013.

[139] T.G. Hicks, W.R. Mabe, J.R. Miller, and J.V. Mullen. Residual Stress Evaluation of Small Diameter Stainless Steel Piping by Experimental Measurements and Finite Element Analysis. In *ASME 2014 Pressure Vessels and Piping Conference*, volume 6B: Materials and Fabrication, page V06BT06A077. Anaheim, California, USA, 2014.

[140] W. Woo, G.B. An, V.T. Em, A.T. De Wald, and M.R. Hill. Through-thickness distributions of residual stresses in an 80 mm thick weld using neutron diffraction and contour method. *Journal of Materials Science*, 50(2):784–793, 2015.

[141] A. Elmesalamy, J.A. Francis, and L. Li. A comparison of residual stresses in multi pass narrow gap laser welds and gas-tungsten arc welds in AISI 316L stainless steel. *International Journal of Pressure Vessels and Piping*, 113:49–59, 2014.

[142] D.F.O. Braga, H.E. Coules, T. Pirling, V. Richter-Trummer, P. Colegrove, and P.M.S.T. de Castro. Assessment of residual stress of welded structural steel plates with or without post weld rolling using the contour method and neutron diffraction. *Journal of Materials Processing Technology*, 213(12):2323–2328, 2013.

[143] F. Hosseinzadeh and P.J. Bouchard. Mapping Multiple Components of the Residual Stress Tensor in a Large P91 Steel Pipe Girth Weld Using a Single Contour Cut. *Experimental Mechanics*, 53(2):171–181, 2013.

[144] M.E. Kartal. Analytical solutions for determining residual stresses in two-dimensional domains using the contour method. *Proceedings of the Royal Society of London A: Mathematical, Physical and Engineering Sciences*, 469(2159), 2013.

[145] P. Pagliaro, M.B. Prime, H. Swenson, and B. Zuccarello. Measuring Multiple Residual-Stress Components using the Contour Method and Multiple cuts. *Experimental Mechanics*, 50(2):187–194, 2010.

[146] A.T. DeWald and M.R. Hill. Measurement of Bulk Residual Stress Distributions in Thick-section Components using the Contour Method. In *Engineering Applications of Residual Stress, Volume 8*, Conference Proceedings of the Society for Experimental Mechanics Series, T. Proulx (ed.), pages 29–31. Springer New York, 2011.

[147] P. Pagliaro, M.B. Prime, J.S. Robinson, B. Clausen, H. Swenson, M. Steinzig, and B. Zuccarello. Measuring Inaccessible Residual Stresses Using Multiple Methods and Superposition. *Experimental Mechanics*, 51(7):1123–1134, 2011.

[148] D.W. Brown, T.M. Holden, B. Clausen, M.B. Prime, T.A. Sisneros, H. Swenson, and J. Vaja. Critical comparison of two independent measurements of residual stress in an electron-beam welded uranium cylinder: Neutron diffraction and the contour method. *Acta Materialia*, 59(3):864–873, 2011.

[149] J.C. Rebelo, M. Kornmeier, A.C. Batista, and A.M. Dias. Residual Stress after EDM–FEM Study and Measurement Results. *Materials Science Forum*, 404-407:159–164, 2002.

[150] W. Cheng and I. Finnie. *Residual Stress Measurement and the Slitting Method.* Springer, 2007.

[151] S. Vaidyanathan and I. Finnie. Determination of Residual Stresses From Stress Intensity Factor Measurements. *Journal of Fluids Engineering*, 93(2):242–246, 1971.

[152] S. Güngör. Residual stress measurements in fibre reinforced titanium alloy composites. *Acta Materialia*, 50(8):2053–2073, 2002.

[153] A. Neubrand, T.-J. Chung, J. Rödel, E.D. Steffler, and T. Fett. Residual stresses in functionally graded plates. *Journal of Materials Research*, 17:2912–2920, 2002.

[154] K.-J. Kang, S. Darzens, and G.-S. Choi. Effect of geometry and materials on residual stress measurement in thin films by using the focused ion beam. *Journal of Engineering Materials and Technology*, 126(4):457–464, 2004.

[155] N. Sabaté, D. Vogel, A. Gollhardt, J. Keller, C. Cané, I. Gràcia, J.R. Morante, and B. Michel. Measurement of residual stress by slot milling with focused ion-beam equipment. *Journal of Micromechanics and Microengineering*, 16(2):254–259, 2006.

[156] N. Sabaté, D. Vogel, A. Gollhardt, J. Keller, B. Michel, C. Cané, I. Gràcia, and J.R. Morante. Measurement of residual stresses in micromachined structures in a microregion. *Applied Physics Letters*, 88(7):071910, 2006.

[157] W.-L. Lim, J.-H. Song, and B.V. Sankar. Effect of ring indentation on fatigue crack growth in an aluminum plate. *International Journal of Fatigue*, 25(9–11):1271–1277, 2003.

[158] M.B. Prime. Measuring residual stress and the resulting stress intensity factor in compact tension specimens. *Fatigue & Fracture of Engineering Materials & Structures*, 22(3):195–204, 1999.

[159] N. Ersoy and Ö. Vardar. Measurement of Residual Stresses in Layered Composites by Compliance Method. *Journal of Composite Materials*, 34(7):575–598, 2000.

[160] J.M. Ganley, A.K. Maji, and S. Huybrechts. Explaining Spring-In in Filament Wound Carbon Fibre/Epoxy Composites. *Journal of Composite Materials*, 34(14):1216–1239, 2000.

[161] D. Ritchie and R.H. Leggatt. The measurement of the distribution of residual stresses through the thickness of a welded joint. *Strain*, 23(2):61–70, 1987.

[162] W. Cheng and I. Finnie. A Method for Measurement of Axisymmetric Residual Stresses In Circumferentially Welded Thin-Walled Cylinders. *Journal of Engineering Materials and Technology*, 107(3):181–185, 1985.

[163] G.S. Schajer and M.B. Prime. Use of Inverse Solutions for Residual Stress Measurement. *Journal of Engineering Materials and Technology*, 128(3):375–382, 2006.

[164] W. Cheng and I. Finnie. A Comparison of the Strains due to Edge Cracks and Cuts of Finite Width in a Semi-Infinite Elastic Plate. *Journal of Engineering Materials and Technology*, 115(2):220–226, 1993.

[165] M.B. Prime and I. Finnie. Surface Strains Due to Face Loading of a Slot in a Layered Half-space. *Journal of Engineering Materials and Technology*, 118(3):410–418, 1996.

[166] W. Cheng and I. Finnie. The Crack Compliance Method for Residual Stresses Measurement. *Welding in the World*, 28:103–110, 1990.

[167] W. Cheng and I. Finnie. Measurement of residual stress distributions near the toe of an attachment welded on a plate using the crack compliance method. *Engineering Fracture Mechanics*, 46(1):79–91, 1993.

[168] T. Fett. Determination of residual stresses in components using the fracture mechanics weight function. *Engineering Fracture Mechanics*, 55(4):571–576, 1996.

[169] T. Fett and G. Thun. Residual stresses in PVC-cylinders determined with the weight function method. *Engineering Fracture Mechanics*, 55(5):859–863, 1996.

[170] D. Nowell, S. Tochilin, and D.A. Hills. The Crack Compliance Method for Measurement of Residual Stress: Dislocation Density Analysis. In *The Fifth Int Conference on Residual Stresses*, volume 2, pages 664–669. Ericsson T. et al. (ed.), Linköping, Sweden, June 1997.

[171] M. Gremaud, W. Cheng, I. Finnie, and M.B. Prime. The Compliance Method for Measurement of Near Surface Residual Stresses—Analytical Background. *Journal of Enigineering Materials and Technology*, 116(4):550–555, 1994.

[172] M.B. Prime and Ch. Hellwig. Residual Stresses in a Bi-Material Laser Clad Measured Using Compliance. In *The Fifth Int Conference on Residual Stresses*, volume 1, pages 127–132. Linköping, Sweden, Ericsson T et al. (eds), June 1997.

[173] M.B. Prime and M.R. Hill. Uncertainty analysis, model error, and order selection for series-expanded, residual stress inverse solutions. *Journal of Engineering Materials and Technology*, 128(2):175–185, 2006.

[174] A. Sharma and C.E. Bakis. C-Shape Specimen for Tensile Radial Strength of Thick, Filament-wound Rings. *Journal of Composite Materials*, 40(2):97–117, 2006.

[175] G.S. Schajer and M.B. Prime. Residual stress solution extrapolation for the slitting method using equilibrium constraints. *Journal of Engineering Materials and Technology*, 129(2):227–232, 2007.

[176] S. Finnie, W. Cheng, I. Finnie, J. M. Drezet, and M. Gremaud. The Computation and Measurement of Residual Stresses in Laser Deposited Layers. *Journal of Engineering Materials and Technology*, 125(3):302–308, 2003.

[177] B. Ekbote, P. Kwon, and M. B. Prime. Micromechanics-based Design and Processing of Efficient Meso-scale Heat Exchanger. In *21st Annual Technical Conference of the American Society for Composites.*, Dearborn, MI, September 17-20, 2006.

[178] M.B. Prime and M.R. Hill. Measurement of fiber-scale residual stress variation in a metal-matrix composite. *Journal of Composite Materials*, 38(23):2079–2095, 2004.

[179] N. Ersoy and Ö. Vardar. Measurement of residual stresses in layered composites by compliance method. *Journal of Composite Materials*, 34(7):575–598, 2000.

[180] M.M. Shokrieh, S. Akbari, and A. Daneshvar. A comparison between the slitting method and the classical lamination theory in determination of macro-residual stresses in laminated composites. *Composite Structures*, 96:708–715, 2013.

[181] S. Akbari, F. Taheri-Behrooz, and M.M. Shokrieh. Slitting Measurement of Residual Hoop Stresses Through the Wall-Thickness of a Filament Wound Composite Ring. *Experimental Mechanics*, 53(9):1509–1518, 2013.

[182] M.M. Shokrieh and S. Akbari. Simulation of slitting method for calculation of compliance functions of laminated composites. *Journal of Composite Materials*, 46(9):1101–1109, 2011.

[183] M.M. Shokrieh and S. Akbari. Effect of Residual Shear Stresses on Released Strains in Isotopic and Orthotropic Materials Measured by the Slitting Method. *Journal of Engineering Materials and Technology*, 134(1):011006, 2011.

[184] W. Cheng and I. Finnie. Measurement of Residual Hoop Stress in Cylinders Using the Compliance Method. *Journal of Engineering Materials and Technology*, 108(2):87–92, 1986.

[185] W. Cheng and I. Finnie. Determination of Stress Intensity Factors for Partial Penetration Axial Cracks in Thin-Walled Cylinders. *Journal of Engineering Materials and Technology*, 108(2):83–86, 1986.

[186] W. Cheng and I. Finnie. An Experimental Method for Determining Residual Stresses in Welds. In *Modeling of Casting, Welding, and Advanced Solidification Processes*, pages 245–252. The Minerals, Metals, and Materials Society, Warrendale, PA, USA, 1991.

[187] M. Perl and R. Aroné. An Axisymmetric Stress Release Method for Measuring the Autofrettage Level in Thick-Walled - Parts I & II. *Journal of Pressure Vessel Technology*, 116:384–395, 1994.

[188] A. M. Venter, R. R. Swardt, and S. Kyriacou. Comparative measurements on autofrettaged cylinders with large Bauschinger reverse yielding zones. *Journal of Strain Analysis for Engineering Design*, 35(6):495–469, 2000.

[189] H.J. Schindler. Determination of residual stress distributions from measured stress intensity factors. *International Journal of Fracture*, 74(2):R23–R30, 1995.

[190] K.J. Kang and S.Y. Seol. Measurement of Residual Stresses in a Circular Ring Using the Successive Cracking Method. *Journal of Engineering Materials and Technology*, 118(2):217–223, 1996.

[191] P. Rangaswamy M.B. Prime, V.C. Prantil and F.P. Garcia. Residual Stress Measurement and Prediction in a Hardened Steel Ring. *Materials Science Forum*, 347-349:223–228, 2000.

[192] M.W. Joerms. Calculation of Residual Stresses in Railroad Rails and Wheels from Sawcut Displacement. In W. Young B., editor, *Proceedings of ASM's Conference in Residual Stress in Design, Process and Material Selection*, pages 205–209. Cincinnati, Ohio, USA, 27-29 April 1987.

[193] W. Cheng, G. Stevick, and I. Finnie. Predictions of Stress Intensity Factor for an Internal Circumferential Crack at a Butt-Weld Between Cylinders Using the Plane Strain Solutions. *Journal of Engineering Materials and Technology*, 106(1):21–24, 1984.

[194] W. Cheng and I. Finnie. A New Method of Measurement of Residual Axial Stresses Applied to a Multi-Pass Butt Welded Cylinder. *Journal of Engineering Materials and Technology*, 109(4):337–342, 1987.

[195] W. Cheng, I. Finnie, and Ö. Vardar. Estimation of Axisymmetric Residual Stresses in a Long Cylinder. *Journal of Engineering Materials and Technology*, 114(2):137–140, 1992.

[196] W. Cheng and I. Finnie. The Single Slice Method for Measurement of Axisymmetric Residual Stresses in Solid Rods or Hollow Cylinders in the Region of Plane Strain. *Journal of Engineering Materials and Technology*, 120(2):170–176, 1998.

[197] W. Cheng. Measurement of the Axial Residual Stresses Using the Initial Strain Approach. *Journal of Engineering Materials and Technology*, 122(1):135–140, 2000.

[198] G. Sachs. Der nachweiss innerer spannungen in stangen und rohren. *Zeitschrift für Metallkinde*, 19:352–357, 1927.

[199] M. Kovač, Y. Miyano, and T.C. Woo. Residual-stress measurement in SS304 seamless tube. *Experimental Mechanics*, 29(2):209–213, 1989.

[200] B.M. Botros. Residual stresses in cold ironed tubes. *International Journal of Mechanical Sciences*, 2(3):195–205, 1960.

[201] A. Stacey and G.A. Webster. Determination of residual stress distributions in autofrettaged tubing. *International Journal of Pressure Vessels and Piping*, 31(3):205–220, 1988.

[202] J. Perry and J. Aboudi. Elasto-Plastic Stresses in Thick Walled Cylinders. *Journal of Pressure Vessel Technology*, 125(3):248–252, 2003.

[203] V.D. Lacarac, M.J. Pavier, D.J. Smith, J. Keltjenz, and D. Lemmens. Complete Determination of the State of Residual Stress in Solid and Hollow Metal Cylinders. In *Measurement and Prediction of Residual Stresses in Autofrettage High Pressure Tubing Incorporating Temperature and Bauschinger Effect*. PVP conference, Seattle, USA, 2000.

[204] T. Kuboki, M. Akiyama, Y. Neishi, and K. Kuroda. Effect of final drawing with light reduction on the levelling of residual stress distribution in cold bar drawing. *Proceedings of the Institution of Mechanical Engineers, Part C: Journal of Mechanical Engineering Science*, 214(11):1389–1400, 2000.

[205] D.R. Mack. Measurement of residual stress in disks from turbine-rotor forgings. *Experimental Mechanics*, 2(5):155–158, 1962.

[206] B.K. Jones and J.W. Martin. Residual stress distribution in nitrided En41B steel as function of case depth. *Metals Technology*, 4(1):520–523, 1977.

[207] A.T. Özdemir and L. Edwards. Measurement of the three-dimensional residual stress distribution around split-sleeve cold-expanded holes. *The Journal of Strain Analysis for Engineering Design*, 31(6):413–421, 1996.

[208] D.J. Smith, C.G.C. Poussard, and M.J. Pavier. An assessment of the Sachs method for measuring residual stresses in cold worked fastener holes. *The Journal of Strain Analysis for Engineering Design*, 33(4):263–274, 1998.

[209] A.A. Garcia-Granada, V.D. Lacarac, P. Holdway, D.J. Smith, and M.J. Pavier. Creep relaxation of residual stresses around cold expanded holes. *Journal of Engineering Materials and Technology*, 123(1):125–131, 2001.

[210] H. Bühler. Complete Determination of the State of Residual Stress in Solid and Hollow Metal Cylinders. In *Residual Stresses in Metals and Metal Construction*, pages 305–329. (ed) W.R. Osgoodi, Reinhold Publ. Corp., 1954.

[211] J. Druez and A. Bazergui. Through-thickness measurement of residual stresses in thin tubes. *Experimental Mechanics*, 23(2):211–216, 1983.

[212] D.A. Ignat'kov. Determination of residual stresses in multilayer cylindrical parts. *Strength of Materials*, 11(10):1097–1100, 1979.

[213] D.A. Ignat'kov. Determination of residual stresses in piecewise-inhomogeneous cylinders. *Strength of Materials*, 16(6):832–837, 1984.

[214] T. Nishimura. Analysis of axially symmetrical residual stresses in bars and tubes. *Experimental Mechanics*, 18(5):180–184, 1978.

[215] D.J. Sharman, H.L. Stark, and D.W. Kelly. Benchmarking of a destructive technique to determine residual stresses in thick-walled axisymmetric components. *The Journal of Strain Analysis for Engineering Design*, 32(2):87–96, 1997.

[216] A.A. Garcia-Granada, D.J. Smith, and M.J. Pavier. A new procedure based on Sachs' boring for measuring non-axisymmetric residual stresses. *International Journal of Mechanical Sciences*, 42(6):1027–1047, 2000.

[217] T. Terasaki, T. Akiyama, and T. Ishimura. New Method for Estimating Residual Stresses in Pipe Made by Surfacing Weld. *Journal of Manufacturing Science and Engineering, Transactions of the ASME*, 117(3):365–371, 1995.

[218] J. Chen, T. Terasaki, T. Akiyama, and K. Kishitake. New Concept of Equivalent Inherent Strain for Measuring Axisymmetric Residual Stresses. *Journal of Manufacturing Science and Engineering*, 122(2):304–309, 2000.

[219] W.A. Olson and C.W. Bert. Analysis of Residual Stresses in Bars and Tubes of Cylindrically Orthotropic Materials. *Experimental Mechanics*, 6(9):451–457, 1966.

[220] G.Z. Voyiadjis, P.D. Kiousis, and C.S. Hartley. Analysis of residual stresses in cylindrically anisotropic materials. *Experimental Mechanics*, 25(2):145–147, 1985.

[221] N.P. Hung. The use of an automatic data-acquisition system for the Sachs' residual stress measurement method. *Experimental Techniques*, 13(4):24–26, 1989.

[222] J. Rasty, X. Le, M. Baydogan, and J.F. Cárdenas-García. Measurement of residual stresses in nuclear-grade Zircaloy-4(R) tubes - Effect of heat treatment. *Experimental Mechanics*, 47(2):185–199, 2007.

[223] G.Z. Voyiadjis and C.S. Hartley. Residual-stress determination of concentric layers of cylindrically orthotropic materials. *Experimental Mechanics*, 27(3):290–297, 1987.

[224] C.T. Herakovich. *Mechanics of Fibrous Composites*. John Wiley & Sons, Inc., 1998.

[225] S.G. Lekhniitski. *Theory of Elasticity of an Anisotropic Elastic Body*. Holden-Day, Inc., San Francisco, 1963.

[226] R.E. Scherrer. Filament-Wound Cylinders with Axial-Symmetric Loads. *Journal of Composite Materials*, 1:344–355, 1967.

[227] E. Reissner. On axially uniform stress and strain in axially homogeneous cylindrical shells. *International Journal of Solids and Structures*, 6(1):133–138, 1970.

[228] N.J. Pagano. Stress Gradients in Laminated Composite Cylinders. *Journal of Composite Materials*, 5:257–265, 1971.

[229] E. Reissner and W.T. Tsai. Pure Bending, Stretching, and Twisting of Anisotropic Cylindrical Shells. *Journal of Applied Mechanics*, 4:168–174, 1974.

[230] G. Orgill and J.F. Wilson. Finite Deformations of Nonlinear, Orthotropic Cylindrical Shells. *Journal of Applied Mechanics*, 53(2):257–265, 1986.

[231] Y.K. Kim and S.R. White. Cure-Dependent Viscoelastic Residual Stress Analysis of Filament-Wound Composite Cylinders. *Mechanics of Composite Materials and Structures*, 5(4):327–354, 1999.

[232] R.C. Hibbeler. *Mechanics of Materials*. Pearson Prentice Hall, 2005.

[233] J.P. Holman. *Experimental Methods for Engineers.* McGraw-Hill, eighth edition, 2012.

[234] Kyowa Electronic Instruments. Strain Gages for General Stress Measurement. KFG Series Strain Gage catalogue.

[235] Texas Instruments. *LM35 Precision Centigrade Temperature Sensors.* August 1999-Revised October 2013.

[236] ASM International. *Engineered Materials Handbook - Desk Edition.* Materials Park, Ohio, 1995.

[237] Technical Information. *EPIKOTE Resin L 1100-set.* HEXION speciality chemicals, 2006.

[238] ASTM Standard D 638-10, 2010. *Standard Test Method for Tensile Properties of Plastics.* ASTM International, West Conshohocken, PA, 2010, DOI: 10.1520/D0638-10, www.astm.org.

[239] T. Tjhung and K.Y. Li. Measurement of in-Plane Residual Stresses Varying with Depth by the Interferometric Strain/Slope Rosette and Incremental Hole-Drilling. *Journal of Engineering Materials and Technology*, 125(2):153–162, 2003.

[240] A.K. Kaw. *Mechanics of Composite Materials, Second Edition.* Mechanical and Aerospace Engineering Series. Taylor & Francis, 2005.

[241] B. Harris. *Engineering Composite Materials.* Institute of Materials (Great Britain). IOM, 1999.

[242] B.A. Mansfield. Analysis of Finite Length, Orthotropic Composite Cylinders Including Through-thickness Shear Effects. Master's thesis, University of the Witwatersrand, Johannesburg, 2006.

[243] C.W. Bert. Analysis of residual stresses in cylindrically anisotropic materials. *Experimental Mechanics*, 26(1):112, 1986.

[244] H. Fox and W. Bolton. *Mathematics for Engineers and Technologists.* Elsevier, Burlington, 2002.

[245] *Linear Static, Normal Modes, and Buckling Analysis Using MSC.Nastran and MSC.Patran.* NAS 120 Course Notes. MSC. Software Corporation, 2006.

APPENDIX A Determination of material and transformed stiffness matrices

The constitutive equation, in the material coordinate system, for an orthotropic material can be written [224] in matrix form as

$$\begin{bmatrix} \epsilon_1 \\ \epsilon_2 \\ \epsilon_3 \\ \gamma_{23} \\ \gamma_{31} \\ \gamma_{12} \end{bmatrix} = \begin{bmatrix} S_{11} & S_{12} & S_{13} & 0 & 0 & 0 \\ S_{12} & S_{22} & S_{23} & 0 & 0 & 0 \\ S_{13} & S_{23} & S_{33} & 0 & 0 & 0 \\ 0 & 0 & 0 & S_{44} & 0 & 0 \\ 0 & 0 & 0 & 0 & S_{55} & 0 \\ 0 & 0 & 0 & 0 & 0 & S_{66} \end{bmatrix} \begin{bmatrix} \sigma_1 \\ \sigma_2 \\ \sigma_3 \\ \tau_{23} \\ \tau_{31} \\ \tau_{12} \end{bmatrix} \tag{A.1}$$

For clarity, the γ_{ij} terms of Eq. (A.1) are taken as the engineering shear strains [224], associated with the respective τ_{ij} shear stresses. The terms of the compliance matrix [224], $\boldsymbol{S}$, are determined by utilising the material properties of the lamina:

$$\begin{aligned} S_{11} &= \tfrac{1}{E_1} \quad & S_{12} &= -\tfrac{\nu_{21}}{E_2} \quad & S_{13} &= -\tfrac{\nu_{31}}{E_3} \\ S_{21} &= -\tfrac{\nu_{12}}{E_1} \quad & S_{22} &= \tfrac{1}{E_2} \quad & S_{23} &= -\tfrac{\nu_{32}}{E_3} \\ S_{31} &= -\tfrac{\nu_{13}}{E_1} \quad & S_{32} &= -\tfrac{\nu_{23}}{E_2} \quad & S_{33} &= \tfrac{1}{E_3} \\ S_{44} &= \tfrac{1}{G_{23}} \quad & S_{55} &= \tfrac{1}{G_{13}} \quad & S_{66} &= \tfrac{1}{G_{12}} \end{aligned} \tag{A.2}$$

The terms E_i, ν_{ij} and G_{ij} of Eq. (A.2) are the Young's modulus, Poisson's ratio and shear modulus of the lamina, in the respective material directions. These can be estimated using micromechanics [224]. Using *rule of mixtures* relationships [224], the terms E_1, E_2, G_{12} and ν_{12} can be estimated using Eqs. (A.3) to (A.6).

$$E_1 = E_f V_f + E_m V_m \tag{A.3}$$

$$E_2 = \frac{E_f E_m}{E_f V_m + E_m V_f} \tag{A.4}$$

$$G_{12} = \frac{G_f G_m}{G_m V_f + G_f V_m} \tag{A.5}$$

$$\nu_{12} = \nu_f V_f + \nu_m V_m \tag{A.6}$$

where E_f and E_m are the respective fibre and resin Young's moduli, G_f and G_m are fibre and resin Shear moduli, ν_f and ν_m are the fibre and resin Poisson's ratios, and V_f and V_m are respective fibre and resin volume fractions. Assuming the absence of voids, the fibre and resin volume fractions can be estimated using Eqs. (A.7) and (A.8) [240]:

$$V_f = \frac{\frac{M_f}{\rho_f}}{\frac{M_f}{\rho_f} + \frac{M_m}{\rho_m}} \tag{A.7}$$

$$V_m = 1 - V_f \tag{A.8}$$

where M_f and M_m are the masses, and ρ_f and ρ_m the densities of the fibres and resin of the lamina, respectfully. For the purposes of this work, Eq. (A.4) was modified to take the form of Eq. (A.9):

$$E_2 = \frac{E_f \frac{E_m}{1-\nu_m^2}}{E_f V_m + \frac{E_m}{1-\nu_m^2} V_f} \tag{A.9}$$

This modification takes into account the effect of the Poisson's ratio of the resin system [241], and provides a more accurate estimation of this material property. The minor Poisson's ratio, ν_{23}, can be found utilising Eq. (A.10) [242]:

$$\nu_{23} = \frac{\frac{V_f \nu_f}{E_f} + \frac{V_m \nu_m}{E_m}}{\frac{V_f}{E_f} + \frac{V_m}{E_m}} \tag{A.10}$$

In the material coordinate system, the properties of a lamina are what is referred to as transversely isotropic [224]. In this sense, the material properties transverse to the fibre

orientation are all identical, thus:

$$E_2 = E_3 \tag{A.11}$$

$$G_{12} = G_{13} \tag{A.12}$$

$$\nu_{12} = \nu_{13} \tag{A.13}$$

The remaining Poisson's ratio terms are found from the reciprocal relations [224] of Eq. (A.14):

$$E_1\nu_{21} = E_2\nu_{12}; \quad E_1\nu_{31} = E_3\nu_{13}; \quad E_3\nu_{23} = E_2\nu_{32} \tag{A.14}$$

The last required shear modulus, G_{23}, is obtained using Eq. (A.15) [224]:

$$G_{23} = \frac{E_2}{2(1+\nu_{23})} \tag{A.15}$$

Once all the required material property terms have been calculated, they can be substituted into Eq. (A.2) to determine the material compliance matrix, $\boldsymbol{S}$. The material stiffness matrix [224], $\boldsymbol{C}$, is obtained through inversion of the compliance matrix of the material, and the constitutive equations can thus be modified to Eq. (A.16):

$$\begin{bmatrix} \sigma_1 \\ \sigma_2 \\ \sigma_3 \\ \tau_{23} \\ \tau_{31} \\ \tau_{12} \end{bmatrix} = \begin{bmatrix} C_{11} & C_{12} & C_{13} & 0 & 0 & 0 \\ C_{12} & C_{22} & C_{23} & 0 & 0 & 0 \\ C_{13} & C_{23} & C_{33} & 0 & 0 & 0 \\ 0 & 0 & 0 & C_{44} & 0 & 0 \\ 0 & 0 & 0 & 0 & C_{55} & 0 \\ 0 & 0 & 0 & 0 & 0 & C_{66} \end{bmatrix} \begin{bmatrix} \epsilon_1 \\ \epsilon_2 \\ \epsilon_3 \\ \gamma_{23} \\ \gamma_{31} \\ \gamma_{12} \end{bmatrix} \tag{A.16}$$

Rotation of this ply through an angle, ϕ, measured from the axial orientation, the elastic constitutive equations of Eq. (A.16) are transformed into those of a monoclinic material in the cylindrical coordinate system (r, θ, x) [224]:

$$\begin{bmatrix} \sigma_x \\ \sigma_\theta \\ \sigma_r \\ \tau_{\theta r} \\ \tau_{xr} \\ \tau_{x\theta} \end{bmatrix} = \begin{bmatrix} \bar{C}_{11} & \bar{C}_{12} & \bar{C}_{13} & 0 & 0 & \bar{C}_{16} \\ \bar{C}_{12} & \bar{C}_{22} & \bar{C}_{23} & 0 & 0 & \bar{C}_{26} \\ \bar{C}_{13} & \bar{C}_{23} & \bar{C}_{33} & 0 & 0 & \bar{C}_{36} \\ 0 & 0 & 0 & \bar{C}_{44} & \bar{C}_{45} & 0 \\ 0 & 0 & 0 & \bar{C}_{45} & \bar{C}_{55} & 0 \\ \bar{C}_{16} & \bar{C}_{26} & \bar{C}_{36} & 0 & 0 & \bar{C}_{66} \end{bmatrix} \begin{bmatrix} \epsilon_x \\ \epsilon_\theta \\ \epsilon_r \\ \gamma_{\theta r} \\ \gamma_{xr} \\ \gamma_{x\theta} \end{bmatrix} \tag{A.17}$$

The transformed stiffness matrix, $\bar{\boldsymbol{C}}$, is obtained through the transformation equation:

$$[\bar{\boldsymbol{C}}] = [\boldsymbol{T}_1]^{-1}[\boldsymbol{C}][\boldsymbol{T}_2] \tag{A.18}$$

The transformation matrices [224], $\boldsymbol{T}_1$ and $\boldsymbol{T}_2$ are defined by Eqs. (A.19) and (A.20):

$$\boldsymbol{T}_1 = \begin{bmatrix} m^2 & n^2 & 0 & 0 & 0 & 2mn \\ n^2 & m^2 & 0 & 0 & 0 & -2mn \\ 0 & 0 & 1 & 0 & 0 & 0 \\ 0 & 0 & 0 & m & -n & 0 \\ 0 & 0 & 0 & n & m & 0 \\ -mn & mn & 0 & 0 & 0 & m^2 - n^2 \end{bmatrix} \tag{A.19}$$

$$\boldsymbol{T}_2 = \begin{bmatrix} m^2 & n^2 & 0 & 0 & 0 & mn \\ n^2 & m^2 & 0 & 0 & 0 & -mn \\ 0 & 0 & 1 & 0 & 0 & 0 \\ 0 & 0 & 0 & m & -n & 0 \\ 0 & 0 & 0 & n & m & 0 \\ -2mn & 2mn & 0 & 0 & 0 & m^2 - n^2 \end{bmatrix} \tag{A.20}$$

where $m = \cos\phi$ and $n = \sin\phi$.

APPENDIX B Theoretical derivation

The derivation presented in this section proves the absence of through-thickness shear stresses for the prescribed loading in the regions of a composite pipe, free from edge effects. It is also shown that, as a consequence, the elastic response is that of constant axial strain, ϵ_x^0, and twist per unit length, γ^0, through the wall thickness, irrespective of the laminated nature of the pipe. This derivation is adapted directly from that presented in the textbook of Herakovich [224], with thermal components, which are not used in the context of this analysis, ignored. The strain-displacement equations for an axisymmetric tube loaded uniformly along its length [224] are:

$$\begin{gathered} \epsilon_x = \frac{\partial u}{\partial x} \qquad \epsilon_\theta = \frac{w}{r} \qquad \epsilon_r = \frac{\partial w}{\partial r} \\ \gamma_{\theta r} = \frac{\partial v}{\partial r} - \frac{v}{r} \quad \gamma_{xr} = \frac{\partial u}{\partial r} \quad \gamma_{x\theta} = \frac{\partial v}{\partial x} \end{gathered} \tag{B.1}$$

where $u = u(x, r)$, $v = v(x, r)$ and $w = w(r)$ are the axial, tangential and radial displacements. The equilibrium equations can be written as [224] :

$$\frac{d\tau_{\theta r}}{dr} + \frac{2\tau_{\theta r}}{r} = 0 \tag{B.2}$$

$$\frac{d\tau_{xr}}{dr} + \frac{\tau_{xr}}{r} = 0 \tag{B.3}$$

These equilibrium equations also apply to a laminated pipe [224]. Integration of Eq. (B.2) and (B.3), for ply k, produces the result [224]:

$$\tau_{\theta r}^k = \frac{H^k}{r^2} \tag{B.4}$$

$$\tau_{xr}^k = \frac{I^k}{r} \tag{B.5}$$

where H^k and I^k are the integration constants. The compatibility equations [224] are:

$$\frac{d^2\epsilon_x}{dr^2} = 0 \tag{B.6}$$

$$\frac{1}{r}\frac{d\epsilon_x}{dr} = 0 \tag{B.7}$$

$$\frac{1}{2}\frac{d}{dr}\left[\frac{1}{r}\frac{d}{dr}(r\gamma_{x\theta})\right] = 0 \tag{B.8}$$

where total derivatives are used since the strains are a function of r only [224]. Integration of Eqs. (B.6) and (B.7) shows that the axial strain is constant in the ply:

$$\epsilon_x^k = \epsilon_x^{0^k} \tag{B.9}$$

The constitutive equations of a monoclinic material are [224]:

$$\begin{bmatrix} \epsilon_x \\ \epsilon_\theta \\ \epsilon_r \\ \gamma_{\theta r} \\ \gamma_{xr} \\ \gamma_{x\theta} \end{bmatrix} = \begin{bmatrix} \bar{S}_{11} & \bar{S}_{12} & \bar{S}_{13} & 0 & 0 & \bar{S}_{16} \\ \bar{S}_{12} & \bar{S}_{22} & \bar{S}_{23} & 0 & 0 & \bar{S}_{26} \\ \bar{S}_{13} & \bar{S}_{23} & \bar{S}_{33} & 0 & 0 & \bar{S}_{36} \\ 0 & 0 & 0 & \bar{S}_{44} & \bar{S}_{45} & 0 \\ 0 & 0 & 0 & \bar{S}_{45} & \bar{S}_{55} & 0 \\ \bar{S}_{16} & \bar{S}_{26} & \bar{S}_{36} & 0 & 0 & \bar{S}_{66} \end{bmatrix} \begin{bmatrix} \sigma_x \\ \sigma_\theta \\ \sigma_r \\ \tau_{\theta r} \\ \tau_{xr} \\ \tau_{x\theta} \end{bmatrix} \tag{B.10}$$

Using Eqs. (B.4) and (B.5) with the constitutive equation for γ_{xr} from Eq. (B.10), the strain-displacement Eq. (B.1) gives the shear strain of ply k as [224]:

$$\gamma_{xr}^k = \frac{\partial u}{\partial r} = \bar{S}_{45}^k \frac{H^k}{r^2} + \bar{S}_{55}^k \frac{I^k}{r} \tag{B.11}$$

Integration of Eq. (B.11) with respect to r gives the axial displacement:

$$u(x,r) = -\bar{S}_{45}^k \frac{H^k}{r} + \bar{S}_{55}^k I^k \ln r + f(x) \tag{B.12}$$

Substitution of Eqs. (B.9) and (B.12) into the first strain-displacement equation of Eq. (B.1) shows that $f(x)$ must be equal to $\epsilon_x^{0^k} x$ plus a constant, F_1. Thus the final form of axial displacement is [224]:

$$u(x,r) = \epsilon_x^{0^k} x - \bar{S}_{45}^k \frac{H^k}{r} + \bar{S}_{55}^k I^k \ln r + F_1 \tag{B.13}$$

The tangential displacements, v, can be found by integration of Eq. (B.8) to give the shear

strain:

$$\gamma_{x\theta}^{k} = K_1 r + \frac{K_2}{r} \tag{B.14}$$

where K_1 and K_2 are constants of integration. Combining Eq. (B.14) with the strain-displacement relationship of Eq. (B.1) the tangential displacement takes the form [224]:

$$v = \left(K_1 r + \frac{K_2}{r} \right) x + g(r) \tag{B.15}$$

where $g(r)$ is an arbitrary function. From Eq. (B.1) we have

$$\gamma_{\theta r}^{k} = \frac{\partial v}{\partial r} - \frac{v}{r} = g'(r) - \frac{2K_2 x}{r^2} - \frac{g(r)}{r} \tag{B.16}$$

The shear strain $\gamma_{\theta r}^{k}$ can also be found be combining Eqs. (B.10), (B.4) and (B.5) to give:

$$\gamma_{\theta r}^{k} = \bar{S}_{44}^{k} \frac{H^k}{r^2} + \bar{S}_{45}^{k} \frac{I^k}{r} \tag{B.17}$$

Equating Eqs. (B.16) and (B.17) shows that $K_2 = 0$ and that [224]

$$g(r) = -\frac{\bar{S}_{45}^{k} H^k}{2r} - \bar{S}_{45}^{k} I^k + G_1 r \tag{B.18}$$

where G_1 is a constant of integration associated with rotational rigid body motion. Substituting Eq. (B.18) into Eq. (B.15), with $K_2 = 0$ and defining $K_1 = \gamma^{0^k}$, the angle of twist per unit length of ply k, the final form of v is [224]:

$$v(x, r) = \gamma^{0^k} x r - \bar{S}_{44}^{k} \frac{H^k}{2r} - \bar{S}_{45}^{k} I^k + G_1 r \tag{B.19}$$

Finally, traction continuity between plies requires that the two through-thickness shear stresses, τ_{xr} and $\tau_{\theta r}$ be continuous from ply to ply. Writing these continuity conditions using Eqs. (B.4) and (B.5), starting from either the inner or outer surface of the pipe, where the shear stresses are zero, shows that the constants $H^k = I^k = 0$ in all plies. This leads to the result that for an infinitely long laminated pipe, the through-thickness shear stresses, τ_{xr}^{k} and $\tau_{\theta r}^{k}$, are zero throughout the pipe thickness. The axial and shear strains in each layer can be determined from the strain-displacement relations of Eq. (B.1) and Eqs. (B.13) and (B.19), bearing in mind the constants H^k and I^k are zero. We therefore find:

$$\epsilon_x^k = \frac{\partial u}{\partial x} = \epsilon_x^{0^k} \tag{B.20}$$

$$\gamma_{x\theta}^k = \frac{\partial v}{\partial x} = \gamma^{0^k} r \tag{B.21}$$

Eq. (B.20) is exactly the same as Eq. (B.9) obtained from integration of the compatibility conditions of Eqs. (B.6) and (B.7), and implies that the axial strain of each ply must be constant. For perfectly bonded plies, all displacements must be continuous from ply to ply. For the axial displacements, the general expression of Eq. (B.13), with the constants $H^k = I^k = 0$ for all plies, requires that the axial strain be constant throughout all plies of a laminated pipe of N layers, therefore [224]:

$$\epsilon_x^{0^k} = \epsilon_x^0 \qquad (k = 1, ..., N) \tag{B.22}$$

The tangential displacements, v, must also be continuous from ply to ply. Thus the general expression of Eq. (B.19) requires that the angle of twist per unit length be constant for all layers, thus [224]:

$$\gamma^{0^k} = \gamma^0 \qquad (k = 1, ..., N) \tag{B.23}$$

APPENDIX C Issues with the current extensions of Sachs' method for determining residual stresses in cylindrically orthotropic pipes

An extension of the Sachs' method [198] to cylindrically orthotropic materials was first published by Olson and Bert [219]. The equations that these authors presented are only applicable for the case of the removal of material from the inner surface of a pipe. Voyaidjis et al. [220] later published a paper that is titled *"Analysis of Residual Stresses in Cylindrically Anisotropic Materials"*. This paper presents equations for material removal from both the inner and outer surfaces of a pipe, and also considers the case where the residual in-plane shear stresses, $\tau_{x\theta}$, can be calculated. Bert [243] later pointed out that the paper of Voyiadjis et al. [220] does not, as the title would suggest, apply to materials of cylindrical anisotropy, but rather, like Olson and Bert's [219] paper, applies only to cylindrically orthotropic materials. Voyiadjis and Hartley [223] later extended the work of Voyaidjis et al. [220] to allow the residual stresses within layered cylindrically orthotropic pipes to be measured. A common assumption made in all of these works [219, 220, 223] is that the residual hoop and radial stresses within the pipe can be determined independent of the axial stresses by applying the residual pressure loads determined from the measured strain response to the inner and outer surface of each removed layer. This is done by utilising the plane-stress equations developed by Lekhnitskii [97], for cylindrically orthotropic annular plates. This assumption is acceptable for thin-walled orthotropic pipes, where the hoop stresses that develop are many orders of magnitude larger than axial stresses that arise for a pressure load, applied under the open-end condition. In thick-walled sections, however, the presence of axial stresses becomes more relevant. Fig. C.1 illustrates the through-thickness axial and hoop stresses that develop in both thin-walled ($t/d_i = 0.001875$) and thick-walled ($t/d_i = 0.375$) orthotropic pipes, for both internal and external applied pressures. The orthotropic properties used for this investigation correspond with those of a filament-wound GFRP pipe, wound entirely at a wind angle of $\pm 55°$. The compliance matrix of this material was found, utilising the equations presented in Appendix A, and the

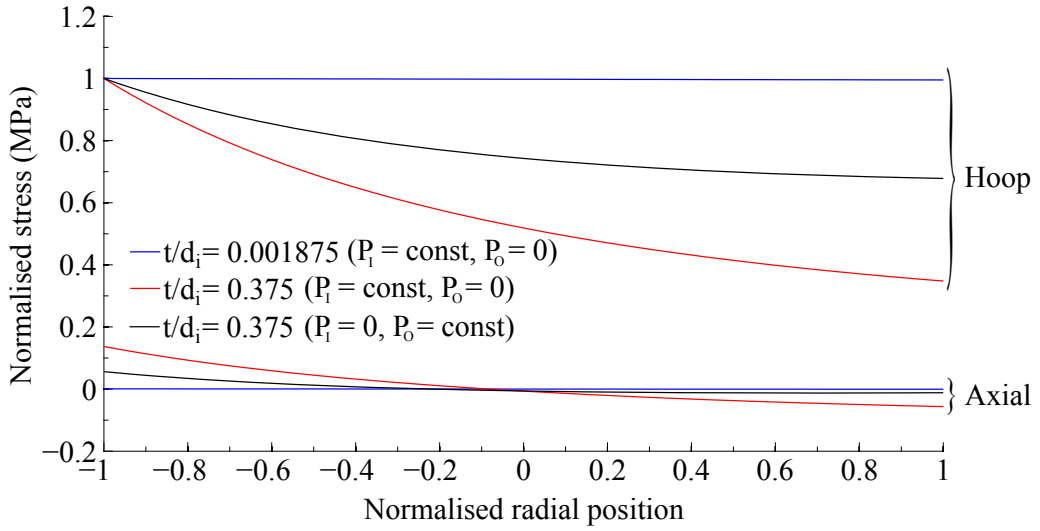

Figure C.1: Comparison of the axial and hoop stress distributions for thin and thick-walled orthotropic pipes under internally and externally applied pressures

lamina properties presented in Appendix F. The orthotropic compliance matrix is absent of any shear-coupling terms, and was found by averaging the compliance matrices determined for both $+55^\circ$ and -55° wind angles. For presentation purposes, the through-thickness radial positions of Fig. C.1 are normalised, such that the inner and outer surfaces of the pipes coincide with -1 and 1, respectively. The through-thickness stress distributions were found by utilising the exact elastic solution, presented in Section 4. For each case, the stresses are normalised with respect to the largest hoop stress, which develops at the inner surface of the pipes. The normalised through-thickness axial stresses of the thin-walled pipe, for an internally applied pressure, are very close to zero. This aligns well with the plane-stress assumption made by Olson and Bert [219] and Voyaidjis et al. [220, 223], for the determination of the residual hoop and radial stresses. The normalised axial stresses of the thick-walled pipe, however, are not negligible. For an internally applied pressure (associated with the change in radial stress resulting from the boring-out of material from the inner surface of the pipe), the axial stress that develops at the inner surface of the pipe is roughly of 13% of the hoop stress value for this region. Also, the magnitude of the axial stress that occurs at the outer surface of the pipe, where the strain response would be measured, is close to 17% of the magnitude of the hoop stress for this region. For an externally applied pressure (when material from the outer surface is removed), the axial stress of the thick-walled pipe is in the region of 6% of the hoop stress value at the inner surface. The axial stress at the outer surface for this case, is within 3% of the hoop stress that occurs in this region. The plane-stress assumption made by Olson and Bert [219] and Voyaidjis et al. [220, 223] does not align well with the response of a thick-walled orthotropic pipe to applied pressure loads. Therefore these methods will produce inaccurate

results, since the coupled nature between the residual hoop and radial stresses, with the axial stresses, is not fully accounted for. It appears, however, that the turning-down of layers from the outer surface of a pipe will produce less erroneous hoop and radial stresses than those obtained by the boring-out procedure. This is due to the fact that an applied external pressure load induces less severe axial stresses in a thick-walled orthotropic pipe, as compared to those induced by an internal pressure.

The works of Olson and Bert [219] and Voyaidjis et al. [220,223] also assume that the axial force, F_x, released by the removal of a layer, is uniformly distributed over the thickness of the remaining pipe, and therefore assume that the axial stress change over the wall thickness is uniform. For thin-walled pipes, the through-thickness axial stress response to an applied axial load can be considered constant. This, however, is not the case when thick-walled pipes are considered. The reason for this is that the axial strain response, under any applied load, must be constant through the wall thickness [224], and this does not necessary result in uniform through-thickness axial stresses. The normalised axial and hoop stress distributions in thin-walled ($t/d_i = 0.001875$) and thick-walled ($t/d_i = 0.375$) orthotropic pipes, obtained for an applied axial load, are presented in Fig. C.2. These distributions were, once again, determined using the elastic solution presented in Section 4, assuming the orthotropic material properties of the $\pm 55^\circ$ filament-wound GFRP pipe. The stresses are normalised by the maximum axial stress, which develops at the outer surface of the pipes. It is apparent from this figure that the axial stress distribution of the thin-walled pipe is approximately uniform over the entire wall thickness, and the resulting hoop stresses are very close to zero. This condition aligns itself well with the assumption made in the previous works [219,220,223]. The axial stresses within the thick-walled pipe, however, are clearly not constant through the thickness. Additionally, non-negligible hoop stresses arise within this pipe. The residual axial stresses determined using the methods of Olson and Bert [219] and Voyaidjis et al. [220, 223] will be inaccurate under these conditions. This is because axial stresses that arise through the thickness of a thick-walled pipe, for an applied axial load, are not uniform. Additionally, the coupled nature between these and the hoop stresses that also arise are not properly accounted for. It appears however, that the inaccuracies arising from this would be less severe for the case of boring-out from the inner surface of the pipe. At the outer surface, the hoop stress that arises is approximately 16% of the axial stress within this region. At the inner surface, however, the the magnitude of the hoop stress is around 27% of the magnitude of axial stress of this region. Therefore the inaccuracies associated with the couple nature of the axial and hoop stresses will be more severe if the strain response at the inner surface is measured.

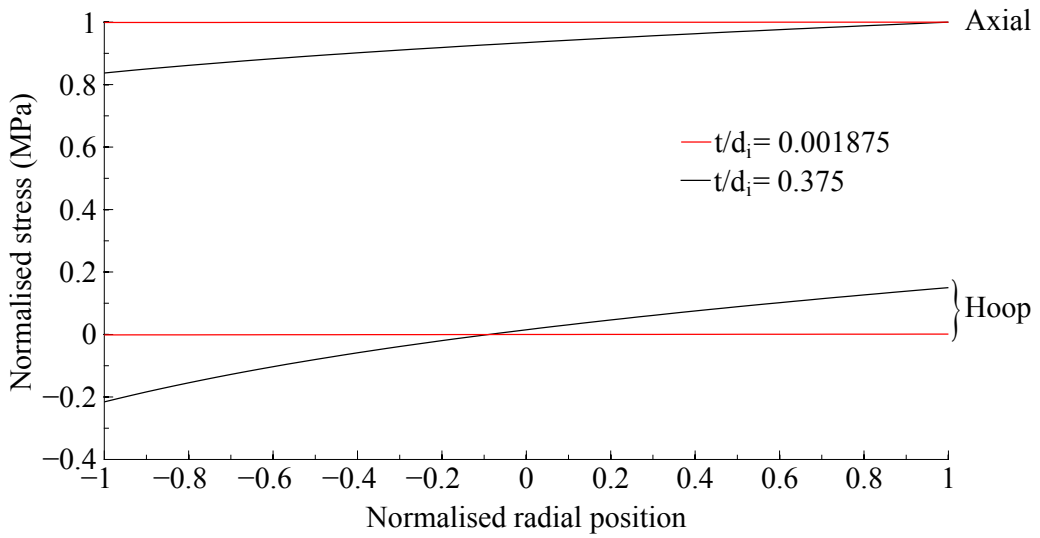

Figure C.2: Comparison of the axial and hoop stress distributions for thin and thick-walled orthotropic pipes under applied axial load

The current work only considers the removal of layers from the outer surface of a pipe. For this reason, only this condition is considered from the work of Voyiadjis et al. [220]. The equations presented by Voyiadjis et al. [220] for calculation of the hoop, σ_θ, radial, σ_r, axial, σ_x, and in-plane shear, $\tau_{x\theta}$, residual stresses, in terms of measured axial, ϵ_x, circumferential, ϵ_θ, and shear, $\gamma_{x\theta}$, strain responses at the inner surface of the pipe of inner radius a, and remaining outer radius r, are illustrated in Eqs. (C.1) to (C.3).

$$\sigma_\theta(U) = E'_\theta \left\{ -\left[\frac{(1-U^{2k})}{2kU^k} \left(\frac{d\theta_i}{dU} \right) \right] + \left[\frac{1+U^{2k}}{2U^{k+1}} \right] \theta_i \right\} U^2 \tag{C.1}$$

$$\sigma_r(U) = E'_\theta \left[\frac{(1-U^{2k})}{2kU^{k-1}} \right] \theta_i \tag{C.2}$$

$$\sigma_x(U) = -E'_x \left\{ -\left[\frac{(1-U^2)}{2} \right] U \left(\frac{d\phi_i}{dU} \right) + \phi_i \right\} \tag{C.3}$$

$$\tau_{x\theta}(U) = -G_{x\theta} \left\{ -\left[\frac{(1-U^4)}{4} \right] \left(\frac{d\gamma_{x\theta}}{dU} \right) + \frac{1}{U} \gamma_{x\theta} \right\} \tag{C.4}$$

where

$$\theta_i = \epsilon^i_\theta + \nu_{x\theta} \epsilon^i_x \tag{C.5}$$

$$\phi_i = \epsilon_x^i + \nu_{\theta x}\epsilon_\theta^i \tag{C.6}$$

$$E'_\theta = \frac{E_\theta}{1 - \nu_{x\theta}\nu_{\theta x}} \tag{C.7}$$

$$E'_x = \frac{E_x}{1 - \nu_{x\theta}\nu_{\theta x}} \tag{C.8}$$

$$k = \sqrt{E_\theta / E_r} \tag{C.9}$$

$$U = a/r \tag{C.10}$$

It has been found, as originally pointed out by Rasty et al. [222], that there is a small discrepancy in the equations presented by Voyiadjis et al. [220] for the determination of the residual hoop and radial stresses, specifically in Eqs. (C.1) and (C.2). The corrected equations are presented in Eqs. (C.11) and (C.12).

$$\sigma_\theta(U) = -E'_\theta \left\{ -\left[\frac{(1 - U^{2k})}{2kU^k} \frac{d\theta_i}{dU} \right] + \left[\frac{1 + U^{2k}}{2U^{k+1}} \right] \theta_i \right\} U^2 \tag{C.11}$$

$$\sigma_r(U) = -E'_\theta \left[\frac{(1 - U^{2k})}{2kU^{k-1}} \right] \theta_i \tag{C.12}$$

These equations differ from those presented by Voyiadjis et al. [220] only by a negative sign. Although Rasty et al. [222] determined the radial stress equation to be exactly Eq. (C.12), they presented a different equation for the evaluation of the residual hoop stresses. This is equation is presented in Eq. (C.13):

$$\sigma_\theta(U) = E'_\theta \left\{ \left[\frac{(1 - U^{2k})}{2kU^k} \frac{d\theta_i}{dU} \right] + \left[\frac{2 - k - (k+2)U^{2k}}{2kU^{k+1}} \right] \theta_i \right\} U^2 \tag{C.13}$$

Eqs. (C.11) and (C.12) can be shown correct by considering isotropic material properties. Under these conditions it can be demonstrated that these equations become exactly the equations presented by Sachs [198]. Eq. (C.13) does not, however, become the Sachs equation for the determination of the residual hoop stresses. For an isotropic material:

$$E'_\theta = E'_x = \frac{E}{1 - \nu^2} \tag{C.14}$$

$$k = 1 \tag{C.15}$$

Eq. (C.11) therefore becomes

$$\begin{aligned}\sigma_\theta(U) &= -\frac{E}{1-\nu^2}\left\{-\left[\frac{(1-U^2)}{2U}\frac{d\theta_i}{dU}\right]+\left[\frac{1+U^2}{2U^2}\right]\theta_i\right\}U^2 \\ &= -\frac{E}{1-\nu^2}\left\{-\left[\frac{U(1-U^2)}{2}\left(\frac{d\theta_i}{dU}\right)\right]+\left[\frac{1+U^2}{2}\right]\theta_i\right\}\end{aligned} \tag{C.16}$$

Sachs equations [198, 200] are defined in terms of inner bore area, F_a, and remaining pipe area (including inner bore area), F. These can be written in the form of Eqs. (C.17) and (C.18).

$$F_a = \pi a^2 \tag{C.17}$$

$$F = \pi r^2 \tag{C.18}$$

With $U = a/r$ [220], Eq. (C.18) can be rewritten as:

$$F = \pi\frac{a^2}{U^2} \tag{C.19}$$

Using the chain rule of differentiation [244], the derivative term, $\frac{d\theta_i}{dU}$, can be written as:

$$\frac{d\theta_i}{dU} = \frac{d\theta_i}{dF}\frac{dF}{dU} \tag{C.20}$$

Derivation of Eq. (C.19) and substitution into Eq. (C.20) produces the result:

$$\frac{d\theta_i}{dU} = -2\pi\frac{a^2}{U^3}\frac{d\theta_i}{dF} \tag{C.21}$$

Substituting Eqs. (C.19) and (C.21) into Eq. (C.16) yields:

$$\sigma_\theta(F) = -\frac{E}{1-\nu^2}\left\{-\left[\frac{\pi^{\frac{1}{2}}a}{2F^{\frac{1}{2}}}\left(1-\frac{\pi a^2}{F}\right)\frac{d\theta_i}{dF}\left(-2\pi a^2\frac{F^{\frac{3}{2}}}{\pi a^3}\right)\right]+\left[\frac{1+\frac{\pi a^2}{F}}{2}\right]\theta_i\right\} \tag{C.22}$$

Finally, substituting Eq. (C.17) into Eq. (C.22):

$$\begin{aligned}\sigma_\theta(F) &= -\frac{E}{1-\nu^2}\left\{-\left[\frac{a}{2F^{\frac{1}{2}}}\left(\frac{F-F_a}{F}\right)\frac{d\theta_i}{dF}\left(-2F_a\frac{F^{\frac{3}{2}}}{F_a a}\right)\right]+\left[\frac{F+F_a}{2F}\right]\theta_i\right\} \\ &= -\frac{E}{1-\nu^2}\left\{(F-F_a)\frac{d\theta_i}{dF}+\left(\frac{F+F_a}{2F}\right)\theta_i\right\}\end{aligned} \tag{C.23}$$

Similarly it can be shown that Eqs. (C.12) and (C.3) become Eqs. (C.24) and (C.25):

$$\sigma_r(F) = -\frac{E}{1-\nu^2}\left[\frac{F-F_a}{2F}\theta_i\right] \tag{C.24}$$

$$\sigma_x(F) = -\frac{E}{1-\nu^2}\left\{(F-F_a)\,\frac{d\phi_i}{dF} + \phi_i\right\} \tag{C.25}$$

Eqs. (C.23) to (C.25) are the exact Sachs [198,200] equations for removal of material from the outer surface of a cylinder. The equivalence of both methods for isotropic material properties implies that the method of Sachs is based upon the same assumptions that result in the inaccuracies of the method of Voyiadjis et al. [220] for thick-walled pipes. These assumptions, however, hold true for isotropic pipes of any wall thickness and thus the method of Sachs [198] is correct. This is illustrated in Fig. C.3, for application of a pure internal pressure, as well as for application of an axial load to a thick-walled ($t/d_i = 0.375$) isotropic pipe. The material properties were assumed to be those of steel, with $E = 200$ GPa and $\nu = 0.3$. As with Figs. C.1 and C.2, the through-thickness stress distributions are normalised by the maximum stress determined in each case. The stress distributions were obtained using the elastic solution presented in Section 4. For an isotropic material, the constant terms of Eqs. (4.9) to (4.11) are defined as:

$$\lambda = 1 \tag{C.26}$$

$$\Gamma = 1 \tag{C.27}$$

$$\Omega = 0 \tag{C.28}$$

Under these conditions, Eq. (4.24) becomes

$$\begin{aligned} F_x =& 2\pi\Bigg[\left(\bar{C}_{11}+\bar{C}_{13}+\bar{C}_{12}\right)\epsilon_x^0\left(\frac{R_O^2-R_I^2}{2}\right) + \bar{C}_{16}\gamma^0\left(\frac{R_O^3-R_I^3}{3}\right) \\ &+ \frac{\left(\bar{C}_{12}+\bar{C}_{13}\right)}{2}A_1\left(R_O^2-R_I^2\right) + \left(\bar{C}_{12}-\bar{C}_{13}\right)A_2\left\{\ln(R_O)-\ln(R_I)\right\}\Bigg] \end{aligned} \tag{C.29}$$

while all other applicable equations remain the same. Referring to Fig. C.3, when an internal pressure is applied, under the open-end condition, only hoop stresses develop, while axial stresses are exactly zero. Thus the plane-stress assumption for determining hoop and radial stresses is completely correct. For the application of an axial force, only axial stresses develop, while through thickness hoop stresses are exactly zero. More

importantly, the axial stresses that develop are uniform through the wall thickness, aligning directly with the manner by which the axial stresses are determined.

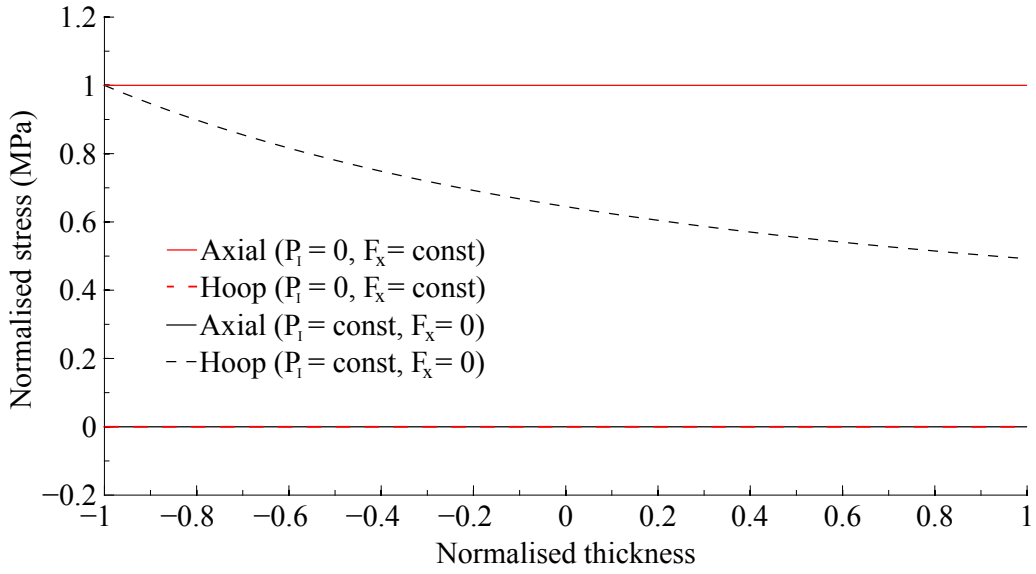

Figure C.3: Comparison of the axial and hoop stress distributions for a thick-walled isotropic pipe $(t/d_i) = 0.375$

APPENDIX D Derivation of matrix-form equations for determination of the pipe constants

D.1 Finding pipe constants of remaining pipe after the removal of m layers

Consider a pipe of N remaining plies, with measured axial, ϵ_x^m, circumferential, ϵ_θ^m, and shear strain, $\gamma_{x\theta}^m$, responses associated with the removal of m layers. These strain responses, together with the boundary condition of zero radial stress at the inner surface, and the requirement of equivalent radial stress and radial displacement at each ply interface, allow for constants A_1^k, A_2^k of each ply to be found. The axial strain must be constant, ϵ_x^0, through the remaining pipe thickness, as well as the angle of twist per unit length, γ^0 in response to the the removal of outer m layers. These can thus be found directly from the strains measured at the inner surface:

$$\epsilon_x^0 = \epsilon_x^m \tag{D.1}$$

$$\gamma^0 = \gamma_{x\theta}^m / R_I \tag{D.2}$$

where R_I is the inner radius of the pipe. At the inner surface of the pipe, the radial stress must always be zero (since no external pressure load is applied to this surface). At this surface, $R_I = r_0$, and k=1. Thus from Eq. (4.18):

$$\begin{aligned}\sigma_r(r_0) = 0 = \left[\bar{C}_{13}^1 + \left(\bar{C}_{23}^1 + \bar{C}_{33}^1\right)\Gamma^1\right]\epsilon_x^0 + \left[\left(\bar{C}_{23}^1 + 2\bar{C}_{33}^1\right)\Omega^1 + \bar{C}_{36}^1\right]\gamma^0 r_0 \\ + \left[\bar{C}_{23}^1 + \lambda^1\bar{C}_{33}^1\right]A_1^1 r_0^{\left(\lambda^1-1\right)} + \left[\bar{C}_{23}^1 - \lambda^1\bar{C}_{33}^1\right]A_2^1 r_0^{\left(-\lambda^1-1\right)}\end{aligned} \tag{D.3}$$

Defining the terms β^k, δ^k, η^k and κ^k as:

$$\beta^k = \bar{C}^k_{23} + \lambda^k \bar{C}^k_{33} \tag{D.4}$$

$$\delta^k = \bar{C}^k_{23} - \lambda^k \bar{C}^k_{33} \tag{D.5}$$

$$\eta^k = \bar{C}^k_{13} + \left[\bar{C}^k_{23} + \bar{C}^k_{33}\right] \Gamma^k \tag{D.6}$$

$$\kappa^k = \left[\bar{C}^k_{23} + 2\bar{C}^k_{33}\right] \Omega^k + \bar{C}^k_{36} \tag{D.7}$$

Eq. (D.3) can be rearranged to:

$$\beta^1 r_0^{(\lambda^1 - 1)} A^1_1 + \delta^1 r_0^{(-\lambda^1 - 1)} A^1_2 = -\eta^1 \epsilon^0_x - \kappa^1 \gamma^0 r_0 \tag{D.8}$$

The measured circumferential strain, ϵ^m_θ, at the inner surface can be expressed in terms of the pipe constants using Eq. (4.13). This equation is reproduced in Eq (D.9):

$$\epsilon^m_\theta = A^1_1 r_0^{(\lambda^1 - 1)} + A^1_2 r_0^{(-\lambda^1 - 1)} + \Gamma^1 \epsilon^0_x + \Omega^1 \gamma^0 r_0 \tag{D.9}$$

which can be rearranged to:

$$A^1_1 r_0^{(\lambda^1 - 1)} + A^1_2 r_0^{(-\lambda^1 - 1)} = -\epsilon^m_\theta - \Gamma^1 \epsilon^0_x - \Omega^1 \gamma^0 r_0 \tag{D.10}$$

For a pipe made up of a single ply, $N = 1$, Eqs. (D.8) and (D.10) can be solved simultaneously to obtain the constants A^1_1 and A^1_2. This can be written matrix form:

$$\begin{bmatrix} \beta^1 r_0^{(\lambda^1 - 1)} & \delta^1 r_0^{(-\lambda^1 - 1)} \\ r_0^{(\lambda^1 - 1)} & r_0^{(-\lambda^1 - 1)} \end{bmatrix} \begin{bmatrix} A^1_1 \\ A^1_2 \end{bmatrix} = \begin{bmatrix} -\eta^1 \epsilon^0_x - \kappa^1 \gamma^0 r_0 \\ -\epsilon^m_\theta - \Gamma^1 \epsilon^0_x - \Omega^1 \gamma^0 r_0 \end{bmatrix} \tag{D.11}$$

For a pipe of numerous plies, $N > 1$, additional A^k_1 and A^k_2 constants need to be found for each additional ply. This is done considering each ply interface. Within these regions, traction continuity [224] requires that the radial stress be continuous from ply to ply. This boundary condition is given by Eq. (4.21) and repeated in Eq. (D.12):

$$\sigma^k_r(r_k) \quad = \quad \sigma^{k+1}_r(r_k) \qquad \text{(Interface at } r_k \quad k = 1, \ldots, N-1) \tag{D.12}$$

Substitution of Eq. (4.18) into Eq. (D.12), with the terms β^k, δ^k, η^k and κ^k as defined by Eqs. (D.4) to (D.7), produces Eq. (D.13):

$$\begin{aligned}\beta^k r_k^{(\lambda^k-1)} A_1^k + \delta^k r_k^{(-\lambda^k-1)} A_2^k + \eta^k \epsilon_x^0 + \kappa^k \gamma^0 r_k = \beta^{k+1} r_k^{(\lambda^{k+1}-1)} A_1^{k+1} \\ + \delta^{k+1} r_k^{(-\lambda^{k+1}-1)} A_2^{k+1} + \eta^{k+1} \epsilon_x^0 + \kappa^{k+1} \gamma^0 r_k\end{aligned} \tag{D.13}$$

Which can be rewritten as:

$$\begin{aligned}\beta^k r_k^{(\lambda^k-1)} A_1^k + \delta^k r_k^{(-\lambda^k-1)} A_2^k - \beta^{k+1} r_k^{(\lambda^{k+1}-1)} A_1^{k+1} - \delta^{k+1} r_k^{(-\lambda^{k+1}-1)} A_2^{k+1} \\ = -\eta^k \epsilon_x^0 - \kappa^k \gamma^0 r_k + \eta^{k+1} \epsilon_x^0 + \kappa^{k+1} \gamma^0 r_k\end{aligned} \tag{D.14}$$

Displacement continuity between plies requires that the radial displacement, w, be continuous from ply to ply [224], thus:

$$w^k(r_k) \quad = \quad w^{k+1}(r_k) \qquad (\text{Interface at } r_k \quad k = 1, \ldots, N-1) \tag{D.15}$$

The radial displacement within ply k, evaluated at r can be determined using Eq. (4.8). The radial displacement of ply k, at the interface between ply k and ply $k+1$ can therefore be written as:

$$w^k(r_k) = A_1^k r_k^{\lambda^k} + A_2^k r_k^{-\lambda^k} + \Gamma^k \epsilon_x^0 r_k + \Omega^k \gamma^0 r_k^2 \tag{D.16}$$

Substituting Eq. (D.16) into Eq. (D.15), and rearranging:

$$\begin{aligned}A_1^k r_k^{\lambda^k} + A_2^k r_k^{-\lambda^k} - A_1^{k+1} r_k^{\lambda^{k+1}} - A_2^{k+1} r_k^{-\lambda^{k+1}} \\ = -\Gamma^k \epsilon_x^0 r_k - \Omega^k \gamma^0 r_k^2 + \Gamma^{k+1} \epsilon_x^0 r_k + \Omega^{k+1} \gamma^0 r_k^2\end{aligned} \tag{D.17}$$

For a pipe comprising two plies, $N = 2$, the A_1^1, A_2^1,A_1^2 and A_2^2 constants are determined by simultaneously solving Eqs. (D.8), (D.10), (D.14) and (D.17). The matrix-form notation of this is presented in Eq. (D.18):

$$\begin{aligned}&\begin{bmatrix} \beta^1 r_0^{(\lambda^1-1)} & \delta^1 r_0^{(-\lambda^1-1)} & 0 & 0 \\ r_0^{(\lambda^1-1)} & r_0^{(-\lambda^1-1)} & 0 & 0 \\ \beta^1 r_1^{(\lambda^1-1)} & \delta^1 r_1^{(-\lambda^1-1)} & -\beta^2 r_1^{(\lambda^2-1)} & -\delta^2 r_1^{(-\lambda^2-1)} \\ r_1^{\lambda^1} & r_1^{-\lambda^1} & -r_1^{\lambda^2} & -r_1^{-\lambda^2} \end{bmatrix} \begin{bmatrix} A_1^1 \\ A_2^1 \\ A_1^2 \\ A_2^2 \end{bmatrix} \\ &= \begin{bmatrix} -\eta^1 \epsilon_x^0 - \kappa^1 \gamma^0 r_0 \\ \epsilon_\theta^m - \Gamma^1 \epsilon_x^0 - \Omega^1 \gamma^0 r_0 \\ -\eta^1 \epsilon_x^0 - \kappa^1 \gamma^0 r_1 + \eta^2 \epsilon_x^0 + \kappa^2 \gamma^0 r_1 \\ -\Gamma^1 \epsilon_x^0 r_1 - \Omega^1 \gamma^0 r_1^2 + \Gamma^2 \epsilon_x^0 r_1 + \Omega^2 \gamma^0 r_1^2 \end{bmatrix}\end{aligned} \tag{D.18}$$

This can be extended to a pipe of N remaining plies, where the remaining A_1^k and A_2^k constants are obtained by utilising Eqs. (D.14) and (D.17) at each ply interface. This produces the matrix form equation:

$$\boldsymbol{DA} = \boldsymbol{M} \tag{D.19}$$

The non-zero terms of the square matrix $\boldsymbol{D}$ are determined as

$$\left.\begin{array}{rcl} D_{1,1} &=& \beta^1 r_0^{(\lambda^1-1)} \\ D_{1,2} &=& \delta^1 r_0^{(-\lambda^1-1)} \\ D_{2,1} &=& r_0^{(\lambda^1-1)} \\ D_{2,2} &=& r_0^{(-\lambda^1-1)} \end{array}\right\} \text{For } k=1 \tag{D.20}$$

which are related directly to Eqs. (D.8) and (D.10). The terms of the $\boldsymbol{D}$ matrix related to boundary conditions at each ply interface of Eqs. (D.14) and (D.17) are:

$$\left.\begin{array}{rcl} D_{2k+1,2k-1} &=& \beta^k r_k^{(\lambda^k-1)} \\ D_{2k+1,2k} &=& \delta^k r_k^{(-\lambda^k-1)} \\ D_{2k+1,2k+1} &=& -\beta^{k+1} r_k^{(\lambda^{k+1}-1)} \\ D_{2k+1,2k+2} &=& -\delta^{k+1} r_k^{(-\lambda^{k+1}-1)} \\ D_{2k+2,2k-1} &=& r_k^{\lambda^k} \\ D_{2k+2,2k} &=& r_k^{-\lambda^k} \\ D_{2k+2,2k+1} &=& -r_k^{\lambda^{k+1}} \\ D_{2k+2,2k+2} &=& -r_k^{-\lambda^{k+1}} \end{array}\right\} \text{For } 1 \le k \le N-1 \tag{D.21}$$

The terms of vector $\boldsymbol{A}$ in Eq. (D.19) are

$$\left.\begin{array}{rcl} A_{2k-1} &=& A_1^k \\ A_{2k} &=& A_2^k \end{array}\right\} \text{For } 1 \le k \le N \tag{D.22}$$

The vector $\boldsymbol{M}$ in Eq. (D.19) is expressed in terms of the measured strain ϵ_θ^m and constant strain terms ϵ_x^0 and γ^0, which are found directly from the measured axial, ϵ_x^m, and shear strain, $\gamma_{x\theta}$, responses, using Eqs. (D.1) and (D.2).

$$\left.\begin{array}{rcl} M_1 &=& -\eta^1 \epsilon_x^0 - \kappa^1 \gamma^0 r_0 \\ M_2 &=& \epsilon_\theta^m - \Gamma^1 \epsilon_x^0 - \Omega^1 \gamma^0 r_0 \end{array}\right\} \text{For } k=1 \tag{D.23}$$

which are related directly to Eqs. (D.8) and (D.10). The terms of the $\boldsymbol{M}$ matrix associated with the boundary conditions at each ply interface of Eqs. (D.14) and (D.17) are:

$$\left.\begin{array}{rcl} M_{2k+1} & = & -\eta^k \epsilon_x^0 - \kappa^k \gamma^0 r_k \\ & & +\eta^{k+1} \epsilon_x^0 + \kappa^{k+1} \gamma^0 r_k \\ M_{2k+2} & = & -\Gamma^k \epsilon_x^0 r_k - \Omega^k \gamma^0 r_k^2 \\ & & +\Gamma^{k+1} \epsilon_x^0 r_k + \Omega^{k+1} \gamma^0 r_k^2 \end{array}\right\} \text{For } 1 \leq k \leq N-1 \qquad \text{(D.24)}$$

D.2 Finding constants of the layer m

To determine the average residual stresses that existed within removed layer m, the constant ϵ_x^0, γ^0, and A_1^k and A_2^k terms of this layer need to be found. These can be found directly using the loads calculated for the removal of $m-1$ and m layers, respectively. Two cases are considered for the determination of these layer constants. The first of these cases is that when layer m comprises the material from a single ply, k. The second case corresponds to that when the this layer comprises material from two plies, k and $k+1$.

D.2.1 Finding the constants when layer m comprises material of ply k

When layer m is made up entirely of material of ply k, the layer constants can be determined directly from the loads calculated for the removal of $m-1$ and m layers, respectively. As discussed in Section 5, the radial residual stresses that existed at the inner surface of layer m is exactly the external pressure, P_m, calculated to exist at the outer surface of the remaining pipe after the removal of all m layers. Using Eq. (4.18), the radial stress at the inner surface of layer m, at the radial position, r_m, is:

$$\sigma_r(r_m) = P_m = \eta^k \epsilon_x^0 + \kappa^k \gamma^0 r_m + \beta^k A_1^k r_m^{(\lambda^k - 1)} + \delta^k A_2^k r_m^{(-\lambda^k - 1)} \qquad \text{(D.25)}$$

Where β^k, δ^k, η^k and κ^k are as defined in Eqs. (D.4) to (D.7). Similarly, the radial residual stress required to exist at the outer surface of layer m, at the radial position r_{m-1}, is exactly the external pressure, P_{m-1}, calculated as a consequence of the induced stress in the remaining pipe after the removal of $m-1$ layers. This requirement is presented in Eq. (D.26).

$$\sigma_r(r_{m-1}) = P_{m-1} = \eta^k \epsilon_x^0 + \kappa^k \gamma^0 r_{m-1} + \beta^k A_1^k r_{m-1}^{(\lambda^k - 1)} + \delta^k A_2^k r_{m-1}^{(-\lambda^k - 1)} \qquad \text{(D.26)}$$

Defining the terms ζ^k, ξ^k, ψ^k and χ^k as:

$$\zeta^k = \frac{\bar{C}^k_{12} + \lambda^k \bar{C}^k_{13}}{\lambda^k + 1} \tag{D.27}$$

$$\xi^k = \frac{\bar{C}^k_{12} - \lambda^k \bar{C}^k_{13}}{-\lambda^k + 1} \tag{D.28}$$

$$\psi^k = \bar{C}^k_{11} + \left[\bar{C}^k_{13} + \bar{C}^k_{12}\right] \Gamma^k \tag{D.29}$$

$$\chi^k = \bar{C}^k_{16} + \left[\bar{C}^k_{12} + 2\bar{C}^k_{13}\right] \Omega^k \tag{D.30}$$

The residual axial force, $F_x^{\overline{m}}$, required to exist at the ends of layer m can be described by Eq. (D.31). This equation is obtained using Eq. (4.24), with substitution of Eqs. (D.27) to (D.30), together with the calculated axial load $F_x^{\overline{m}}$, determined using Eq. (5.12).

$$\begin{aligned}\frac{F_x^{\overline{m}}}{2\pi} =& \psi^k \epsilon_x^0 \left(\frac{r_{m-1}^2 - r_m^2}{2}\right) + \chi^k \gamma^0 \left(\frac{r_{m-1}^3 - r_m^3}{3}\right) \\ &+ \zeta^k A_1^k \left(r_{m-1}^{(\lambda^k+1)} - r_m^{(\lambda^k+1)}\right) + \xi^k A_2^k \left(r_{m-1}^{(-\lambda^k+1)} - r_m^{(-\lambda^k+1)}\right)\end{aligned} \tag{D.31}$$

Similarly, the residual torque load required to exist at the ends of layer m can be described by Eq. (D.32):

$$\begin{aligned}\frac{T_x^{\overline{m}}}{2\pi} =& \varrho^k \epsilon_x^0 \left(\frac{r_{m-1}^3 - r_m^3}{3}\right) + \vartheta^k \gamma^0 \left(\frac{r_{m-1}^4 - r_m^4}{4}\right) \\ &+ \iota^k A_1^k \left(r_{m-1}^{(\lambda^k+2)} - r_m^{(\lambda^k+2)}\right) + \omega^k A_2^k \left(r_{m-1}^{(-\lambda^k+2)} - r_m^{(-\lambda^k+2)}\right)\end{aligned} \tag{D.32}$$

where the term $T_x^{\overline{m}}$ is found using Eq. (5.13), and is the residual torque load released by the removal of layer m. The terms ι^k, ω^k, ϱ^k and ϑ^k are defined as:

$$\iota^k = \frac{\bar{C}^k_{26} + \lambda^k \bar{C}^k_{36}}{\lambda^k + 2} \tag{D.33}$$

$$\omega^k = \frac{\bar{C}^k_{26} - \lambda^k \bar{C}^k_{36}}{-\lambda^k + 2} \tag{D.34}$$

$$\varrho^k = \bar{C}_{16}^k + \left[\bar{C}_{26}^k + \bar{C}_{36}^k\right]\Gamma^k \tag{D.35}$$

$$\vartheta^k = \bar{C}_{66}^k + \left[\bar{C}_{26}^k + 2\bar{C}_{36}^k\right]\Omega^k \tag{D.36}$$

The layer constants ϵ_x^0, γ^0 and A_1^k and A_2^k can be found by simultaneously solving Eqs. (D.25), (D.26), (D.31) and (D.32). This can be done in matrix form:

$$\boldsymbol{Y}\boldsymbol{X} = \boldsymbol{Z} \tag{D.37}$$

The terms of matrix $\boldsymbol{Y}$ are described by Eq. (D.38):

$$\begin{array}{lllllll}
Y_{11} & = & \beta^k r_m^{\left(\lambda^k-1\right)} & Y_{31} & = & \zeta^k\left(r_{m-1}^{\left(\lambda^k+1\right)} - r_m^{\left(\lambda^k+1\right)}\right) \\
Y_{12} & = & \delta^k r_m^{\left(-\lambda^k-1\right)} & Y_{32} & = & \xi^k\left(r_{m-1}^{\left(-\lambda^k+1\right)} - r_m^{\left(-\lambda^k+1\right)}\right) \\
Y_{13} & = & \eta^k & Y_{33} & = & \psi^k\left(\frac{r_{m-1}^2 - r_m^2}{2}\right) \\
Y_{14} & = & \kappa^k r_m & Y_{34} & = & \chi^k\left(\frac{r_{m-1}^3 - r_m^3}{3}\right) \\
Y_{21} & = & \beta^k r_{m-1}^{\left(\lambda^k-1\right)} & Y_{41} & = & \iota^k\left(r_{m-1}^{\left(\lambda^k+2\right)} - r_m^{\left(\lambda^k+2\right)}\right) \\
Y_{22} & = & \delta^k r_{m-1}^{\left(-\lambda^k-1\right)} & Y_{42} & = & \omega^k\left(r_{m-1}^{\left(-\lambda^k+2\right)} - r_m^{\left(-\lambda^k+2\right)}\right) \\
Y_{23} & = & \eta^k & Y_{43} & = & \varrho^k\left(\frac{r_{m-1}^3 - r_m^3}{3}\right) \\
Y_{24} & = & \kappa^k r_{m-1} & Y_{44} & = & \vartheta^k\left(\frac{r_{m-1}^4 - r_m^4}{4}\right)
\end{array} \tag{D.38}$$

The layer constants to be solved make up the values of the vector $\boldsymbol{X}$, as seen in Eq. (D.39).

$$\begin{array}{lll}
X_1 & = & A_1^k \\
X_2 & = & A_2^k \\
X_3 & = & \epsilon_x^0 \\
X_4 & = & \gamma^0
\end{array} \tag{D.39}$$

The vector $\boldsymbol{Z}$ comprises the residual loading released by layer m, and is described by Eq. (D.40).

$$\begin{array}{lll}
Z_1 & = & P_m \\
Z_2 & = & P_{m-1} \\
Z_3 & = & \frac{F_x^{\overline{m}}}{2\pi} \\
Z_4 & = & \frac{T_x^{\overline{m}}}{2\pi}
\end{array} \tag{D.40}$$

D.2.2 Finding the constants when layer m comprises material of two plies

When layer m comprises material from two different plies, k and $k+1$, two additional constants, A_1^{k+1} and A_2^{k+1}, need to be found. To maintain consistency in the defined ply numbering of Fig. 4.1, the inner ply material of layer m is assumed that from ply k, and the outer material form ply $k+1$. The radial position corresponding to the interface of each ply is r_k, and the inner and outer layer radial positions are r_m and r_{m-1} respectively. At the layer inner surface, the required radial stress is exactly P_m and can be described by Eq. (D.25). This equation is repeated in Eq. (D.41) for clarity:

$$\sigma_r(r_m) = P_m = \eta^k \epsilon_x^0 + \kappa^k \gamma^0 r_m + \beta^k A_1^k r_m^{(\lambda^k - 1)} + \delta^k A_2^k r_m^{(-\lambda^k - 1)} \tag{D.41}$$

The radial stress required to exist at the outer surface of layer m, as with Eq. (D.26), is exactly P_{m-1}. The outer surface of layer m, in this case, is made up of material of ply $k+1$, therefore Eq. (D.26) becomes Eq (D.42):

$$\sigma_r(r_{m-1}) = P_{m-1} = \eta^{k+1} \epsilon_x^0 + \kappa^{k+1} \gamma^0 r_{m-1} + \beta^{k+1} A_1^{k+1} r_{m-1}^{(\lambda^{k+1} - 1)} + \delta^{k+1} A_2^{k+1} r_{m-1}^{(-\lambda^{k+1} - 1)} \tag{D.42}$$

The axial force, $F_x^{\overline{m}}$, required to exist at the ends of layer m is exactly the integral of axial stress over the layer thickness, as seen in Eq. (D.43).

$$\begin{aligned}
\frac{F_x^{\overline{m}}}{2\pi} =& \psi^k \epsilon_x^0 \left(\frac{r_k^2 - r_m^2}{2} \right) + \chi^k \gamma^0 \left(\frac{r_k^3 - r_m^3}{3} \right) \\
&+ \zeta^k A_1^k \left(r_k^{(\lambda^k + 1)} - r_m^{(\lambda^k + 1)} \right) + \xi^k A_2^k \left(r_k^{(-\lambda^k + 1)} - r_m^{(-\lambda^k + 1)} \right) \\
&+ \psi^{k+1} \epsilon_x^0 \left(\frac{r_{m-1}^2 - r_k^2}{2} \right) + \chi^{k+1} \gamma^0 \left(\frac{r_{m-1}^3 - r_k^3}{3} \right) \\
&+ \zeta^{k+1} A_1^{k+1} \left(r_{m-1}^{(\lambda^{k+1} + 1)} - r_k^{(\lambda^{k+1} + 1)} \right) + \xi^{k+1} A_2^{k+1} \left(r_{m-1}^{(-\lambda^{k+1} + 1)} - r_k^{(-\lambda^{k+1} + 1)} \right)
\end{aligned} \tag{D.43}$$

Similarly, the torque, $T_x^{\overline{m}}$, required to exist in layer m can be described by Eq. (D.44):

$$\begin{aligned}\frac{T_x^{\overline{m}}}{2\pi} =& \varrho^k \epsilon_x^0 \left(\frac{r_k^3 - r_m^3}{3}\right) + \vartheta^k \gamma^0 \left(\frac{r_k^4 - r_m^4}{4}\right) \\ &+ \iota^k A_1^k \left(r_k^{\left(\lambda^k+2\right)} - r_m^{\left(\lambda^k+2\right)}\right) + \omega^k A_2^k \left(r_k^{\left(-\lambda^k+2\right)} - r_m^{\left(-\lambda^k+2\right)}\right) \\ &+ \varrho^{k+1} \epsilon_x^0 \left(\frac{r_{m-1}^3 - r_k^3}{3}\right) + \vartheta^{k+1} \gamma^0 \left(\frac{r_{m-1}^4 - r_k^4}{4}\right) \\ &+ \iota^{k+1} A_1^{k+1} \left(r_{m-1}^{\left(\lambda^{k+1}+2\right)} - r_k^{\left(\lambda^{k+1}+2\right)}\right) + \omega^{k+1} A_2^{k+1} \left(r_{m-1}^{\left(-\lambda^{k+1}+2\right)} - r_k^{\left(-\lambda^{k+1}+2\right)}\right)\end{aligned} \tag{D.44}$$

To determine the additional A_1^{k+1} and A_2^{k+1} constants, the boundary conditions that exist at the interface of plies k and $k+1$ need to be accounted for. This is done by invoking the boundary condition of Eqs. (4.20) and (4.21). The second of these boundary conditions is the requirement of continuous radial stresses from ply to ply. Applying Eq. (4.18) at the radial position of the ply interface, r_k, to the boundary condition, and substitution of Eqs. (D.4) to (D.7) results in Eq. (D.13), repeated in Eq. (D.45).

$$\begin{aligned}\beta^k r_k^{(\lambda^k-1)} A_1^k + \delta^k r_k^{(-\lambda^k-1)} A_2^k + \eta^k \epsilon_x^0 + \kappa^k \gamma^0 r_k = \beta^{k+1} r_k^{(\lambda^{k+1}-1)} A_1^{k+1} \\ + \delta^{k+1} r_k^{(-\lambda^{k+1}-1)} A_2^{k+1} + \eta^{k+1} \epsilon_x^0 + \kappa^{k+1} \gamma^0 r_k\end{aligned} \tag{D.45}$$

The final boundary condition of Eq. (4.20) requires that the radial displacement be continuous from ply to ply. At the radial position between plies k and $k+1$, this requirement can be written in the form of Eq. (D.46). This equation can be found by invoking Eq. (4.20), and substituting the constants defined by Eqs. (D.4) to (D.7).

$$\begin{aligned}A_1^k r_k^{\lambda^k} + A_2^k r_k^{-\lambda^k} + \Gamma^k \epsilon_x^0 r_k + \Omega^k \gamma^0 r_k^2 = A_1^{k+1} r_k^{\lambda^{k+1}} + A_2^{k+1} r_k^{-\lambda^{k+1}} \\ + \Gamma^{k+1} \epsilon_x^0 r_k + \Omega^{k+1} \gamma^0 r_k^2\end{aligned} \tag{D.46}$$

Solving Eqs. (D.41) to (D.46) allows for the required layer constants to be found. This can be done simultaneously in the matrix form of Eq. (D.37). For this case, the terms of the matrix $\boldsymbol{Y}$ are calculated using Eq. (D.47):

$$
\begin{aligned}
Y_{11} &= \beta^k r_m^{\left(\lambda^k-1\right)} & Y_{41} &= \iota^k\left(r_k^{\left(\lambda^k+2\right)} - r_m^{\left(\lambda^k+2\right)}\right)\\
Y_{12} &= \delta^k r_m^{\left(-\lambda^k-1\right)} & Y_{42} &= \omega^k\left(r_k^{\left(-\lambda^k+2\right)} - r_m^{\left(-\lambda^k+2\right)}\right)\\
Y_{13} &= \eta^k & Y_{43} &= \varrho^k\left(\tfrac{r_k^3-r_m^3}{3}\right) + \varrho^{k+1}\left(\tfrac{r_{m-1}^3-r_k^3}{3}\right)\\
Y_{14} &= \kappa^k r_m & Y_{44} &= \vartheta^k\left(\tfrac{r_k^4-r_m^4}{4}\right) + \vartheta^{k+1}\left(\tfrac{r_{m-1}^4-r_k^4}{4}\right)\\
Y_{15} &= 0 & Y_{45} &= \iota^{k+1}\left(r_{m-1}^{\left(\lambda^{k+1}+2\right)} - r_k^{\left(\lambda^{k+1}+2\right)}\right)\\
Y_{16} &= 0 & Y_{46} &= \omega^{k+1}\left(r_{m-1}^{\left(-\lambda^{k+1}+2\right)} - r_k^{\left(-\lambda^{k+1}+2\right)}\right)\\
Y_{21} &= 0 & Y_{51} &= \beta^k r_k^{\left(\lambda^k-1\right)}\\
Y_{22} &= 0 & Y_{52} &= \delta^k r_k^{\left(-\lambda^k-1\right)}\\
Y_{23} &= \eta^{k+1} & Y_{53} &= \eta^k - \eta^{k+1}\\
Y_{24} &= \kappa^{k+1} r_{m-1} & Y_{54} &= (\kappa^k - \kappa^{k+1}) r_k\\
Y_{25} &= \beta^{k+1} r_{m-1}^{\left(\lambda^{k+1}-1\right)} & Y_{55} &= -\beta^{k+1} r_k^{\left(\lambda^{k+1}-1\right)}\\
Y_{26} &= \delta^{k+1} r_{m-1}^{\left(-\lambda^{k+1}-1\right)} & Y_{56} &= -\delta^{k+1} r_k^{\left(-\lambda^{k+1}-1\right)}\\
Y_{31} &= \zeta^k\left(r_k^{\left(\lambda^k+1\right)} - r_m^{\left(\lambda^k+1\right)}\right) & Y_{61} &= r_k^{\lambda^k}\\
Y_{32} &= \xi^k\left(r_k^{\left(-\lambda^k+1\right)} - r_m^{\left(-\lambda^k+1\right)}\right) & Y_{62} &= r_k^{-\lambda^k}\\
Y_{33} &= \psi^k\left(\tfrac{r_k^2-r_m^2}{2}\right) + \psi^{k+1}\left(\tfrac{r_{m-1}^2-r_k^2}{2}\right) & Y_{63} &= (\Gamma^k - \Gamma^{k+1}) r_k\\
Y_{34} &= \chi^k\left(\tfrac{r_k^3-r_m^3}{3}\right) + \chi^{k+1}\left(\tfrac{r_{m-1}^3-r_k^3}{3}\right) & Y_{64} &= (\Omega^k - \Omega^{k+1}) r_k^2\\
Y_{35} &= \zeta^{k+1}\left(r_{m-1}^{\left(\lambda^{k+1}+1\right)} - r_k^{\left(\lambda^{k+1}+1\right)}\right) & Y_{65} &= -r_k^{\lambda^{k+1}}\\
Y_{36} &= \xi^{k+1}\left(r_{m-1}^{\left(-\lambda^{k+1}+1\right)} - r_k^{\left(-\lambda^{k+1}+1\right)}\right) & Y_{66} &= -r_k^{-\lambda^{k+1}}
\end{aligned}
\tag{D.47}
$$

The vector $\boldsymbol{X}$ now includes the additional A_1^{k+1} and A_2^{k+1} constants:

$$
\begin{aligned}
X_1 &= A_1^k\\
X_2 &= A_2^k\\
X_3 &= \epsilon_x^0\\
X_4 &= \gamma^0\\
X_5 &= A_1^{k+1}\\
X_6 &= A_2^{k+1}
\end{aligned}
\tag{D.48}
$$

The terms of the vector $\boldsymbol{Z}$ for this case are presented in Eq. (D.49). The first four terms are exactly those presented in Eq. (D.40), and are associated with the loading applied to layer m. The last two terms, Z_5 and Z_6, are related to the boundary conditions of Eqs. (4.20) and (4.21) that exist at the interface between the k and $k+1$ plies. These terms enforce that the difference between the radial stresses of each ply, and the difference

in the radial displacements of each ply, at the ply interface, are zero.

$$\begin{aligned} Z_1 &= P_m \\ Z_2 &= P_{m-1} \\ Z_3 &= \frac{F_x^{\overline{m}}}{2\pi} \\ Z_4 &= \frac{T_x^{\overline{m}}}{2\pi} \\ Z_5 &= 0 \\ Z_6 &= 0 \end{aligned} \tag{D.49}$$

APPENDIX E Self-correcting mechanism of current method

The residual stress distributions determined using the current method will always adhere to the self-equilibrium requirement. The reason for this is rooted in the characteristics of the residual stresses themselves, and the method of calculating the residual loads released by each layer, described in Section 5. Consider the case when the wall thickness of the remaining pipe is infinitesimally thin, after the removal of M layers. The residual loads associated with this case are F_x^M and T_x^M, respectively. Using Eq. (5.12), for the case when $m = M$:

$$\begin{aligned} F_x^{\overline{M}} &= F_x^M - F_x^{M-1} \\ &= F_x^M - \left(F_x^{\overline{M-1}} + F_x^{M-2}\right) \\ &= F_x^M - \sum_{m=1}^{M-1} F_x^{\overline{m}} \end{aligned} \tag{E.1}$$

Eq. (E.1) can be rearranged to Eq. (E.2):

$$\begin{aligned} F_x^M &= F_x^{\overline{M}} + \sum_{m=1}^{M-1} F_x^{\overline{m}} \\ &= \sum_{m=1}^{M} F_x^{\overline{m}} \end{aligned} \tag{E.2}$$

Similarly, the overall residual torque load, T_x^M, can be described by Eq. (E.3):

$$T_x^M = \sum_{m=1}^{M} T_x^{\overline{m}} \tag{E.3}$$

The residual F_x^M and T_x^M loads must tend to zero as the wall thickness of the remaining

pipe tends to zero. This is because the area over which these loads can act, producing the final measured strain response, approaches zero. Since the final measured strains do not become infinite, but rather tend to the opposite of the residual strains that existed at the inner surface, the residual F_x^M and T_x^M loads must also tend to zero. Hence, by Eqs. (E.2) and (E.3), the summation of the layer residual loads, $F_x^{\overline{m}}$ and $T_x^{\overline{m}}$, for all removed layers, must approach zero. The calculated residual stress distributions will therefore always adhere to the self-equilibrating requirement. Consequently, there exists an inherent self-correcting mechanism in the current method of residual stress measurement, where errors in individual layer loads are compensated for by proceeding removed layers. Only the layers in the region of error will be affected. This is because the residual axial loads of each layer, $F_x^{\overline{m}}$, by Eq. (5.12), depend only on the loads F_x^m and F_x^{m-1}. So, if there were some inherent error in the calculated F_x^{m-2} value, it would not introduce any error in the axial load obtained for layer m, but only introduce error in the load determined for the $m-1$ layer. The same can be said for the layer torque loads, $T_x^{\overline{m}}$.

The self-correcting mechanism of the current method is now demonstrated. Consider the simulated linear strain variations of Fig. E.1, for strain gauges aligned in the axial, x, circumferential, θ, and 45° directions. Included in this figure are skewed fits for each strain variation. These fits are skewed for the first 30% of the removed thickness, simulating erroneous data over this region. Beyond this region, the skewed fits follow the linear variations exactly. It should be noted that there exists a discontinuous slope in strains where the skewed and linear variations meet. As a consequence, discontinuities in the resulting stress variations of these fits are expected. This is discussed in Section 5.

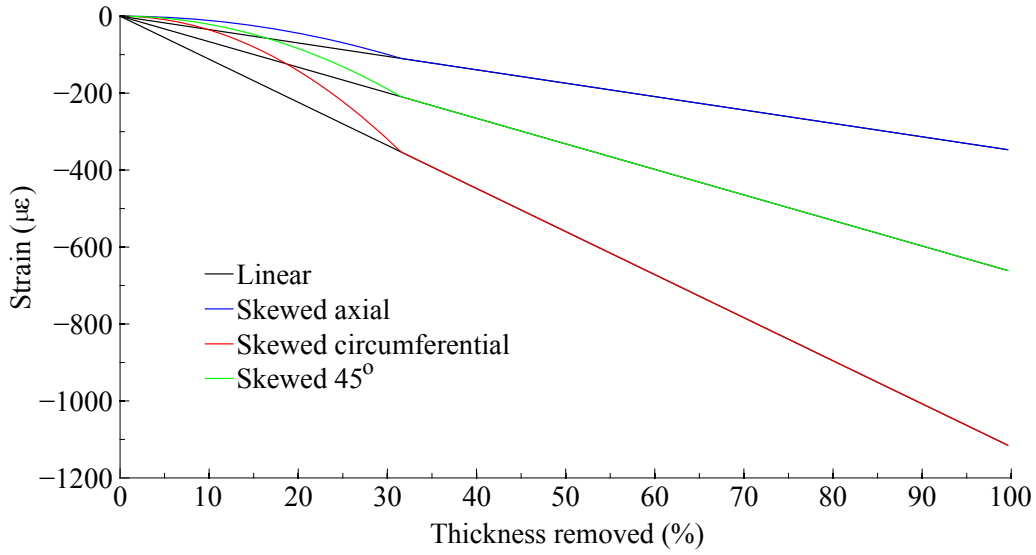

Figure E.1: Simulated strain variations

The pipe is assumed to be moderately thick-walled ($t/d_i = 0.1875$), with orthotropic material properties, corresponding to those of a filament-wound pipe. The wind angle was assumed to be $\pm 55°$, with the same material properties as those presented in Appendix F. Although this investigation does not consider a layered anisotropic pipe, to which the capabilities of the current method extend, the same behaviour can be expected. This is due to the fact that all pipes, whether orthotropic or anisotropic, are governed by the elastic relations presented in Section 4. The only difference between these configurations is that the normal axial and hoop stresses will be affected by the simulated shear strain variation, and visa versa. The axial and hoop stress distributions obtained using the current method, corresponding to the linear and skewed strain variations of Fig. E.1, are illustrated in Fig. E.2. Although not plotted as discontinuous, since a single layered pipe is simulated, it is evident that a discontinuity in both stress distributions exists in the region corresponding to the mismatch in slopes between the skewed and linear strain variations. It is clear from this figure that the stresses evaluated for the skewed strain regions do not affect the remaining stress distribution where the fit is exactly linear. Also, It is evident that in the region between the normalised radial positions of 0.7 and 1, the skewed axial and hoop stresses are overly tensile, compared to the stress distributions associated with the linear strain variations. These regions of overly tensile stress are compensated for by overly compressive stresses at the normalised radial positions between 0.4 to 0.7. This ensures that the skewed axial and hoops stress distributions adhere, to the requirement of self-equilibrium. All stress variations were integrated over the wall thickness to check this, and it is most certainly the case. This behaviour is exactly the self-correcting mechanism inherent in the current method of residual stress measurement.

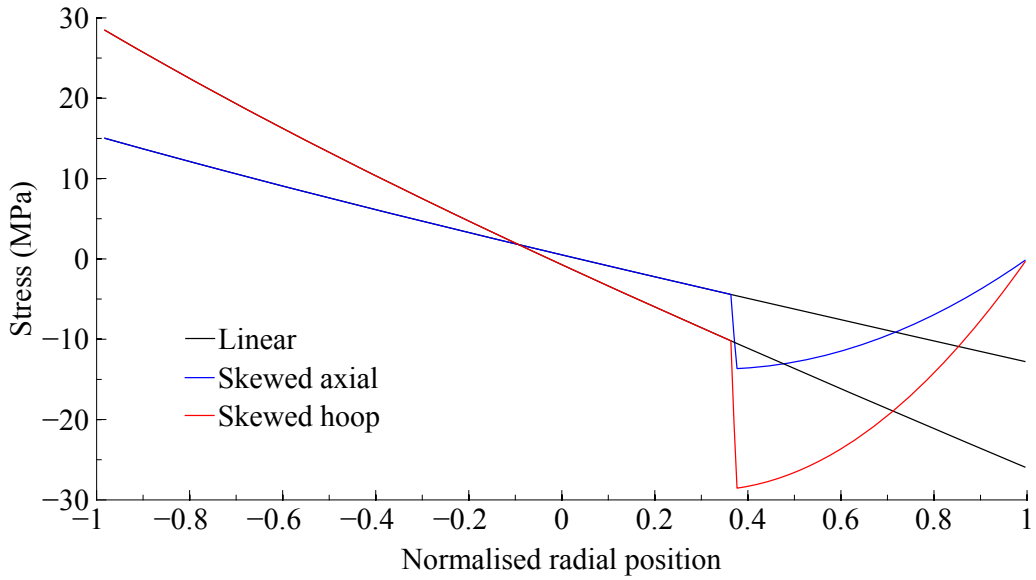

Figure E.2: Axial and hoop stress distributions

The corresponding radial and in-plane shear stress distributions are plotted in Fig. E.3. The skewed stress distributions, as with those of Fig. E.2, become exactly the distributions associated with the linear strain variations beyond the region of skewed fit. It is evident that there exists a discontinuity in the in-plane shear stress, due to the discontinuous slope between the skewed and linear shear strain responses. No discontinuity in radial stress in this region exists, however, since this stress is required to be continuous though the wall thickness. Also, it is clear that between the normalised radial positions of 0.7 and 1, the skewed shear stresses are overly compressive, compared to the shear stress distribution associated with the linear strain variations. These regions of overly compressive stress are compensated for by overly tensile stresses between the normalised radial positions of 0.4 to 0.7. As with the axial and hoop stresses, the self-correcting mechanism of the current method of residual stress measurement, ensures the self-equilibrating requirement is satisfied. The skewed radial stresses are overly compressive between the normalised radial positions of 0.4 and 1. Since these stresses are not required to have a zero-force resultant, no compensation of the overly compressive region is required.

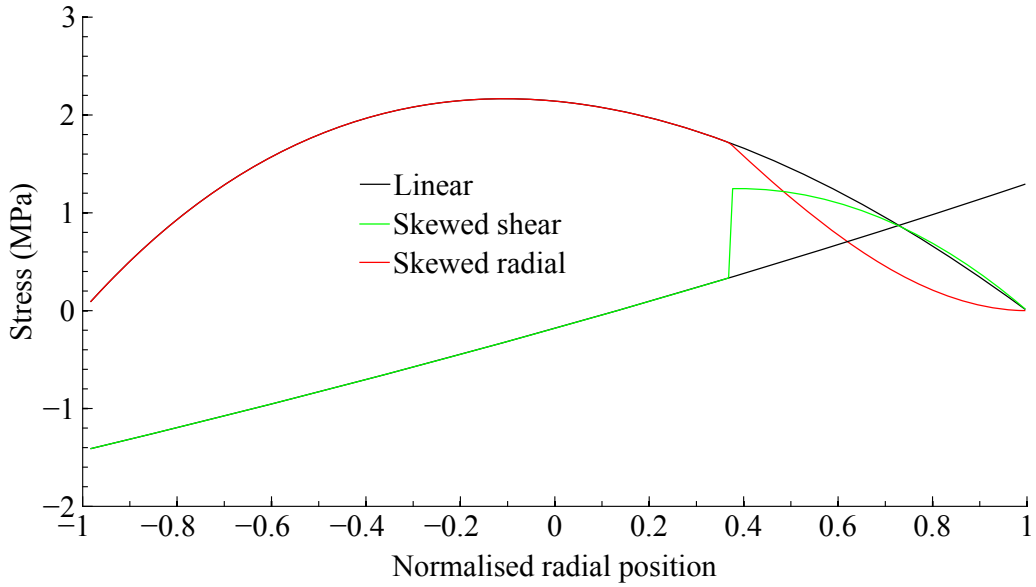

Figure E.3: Radial and shear stress distributions

APPENDIX F Material properties

F.1 E-Glass fibre

All of the filament-wound GFRP pipes considered within the context of this work were manufactured by GRP Tubing (Pty) Ltd of Somerset West, South Africa. The glass fibres used by this manufacturer were E-glass. The mechanical properties of E-glass fibres used throughout this work are presented in Table. F.1. The Young's modulus and Poisson's ratio values were obtained from the Engineering Materials Handbook [236], and the Shear modulus calculated using Eq. (A.15), which is applicable to any isotropic material.

Table F.1: E-Glass material properties

Young's modulus, E_f (MPa)	72000
Poissons ratio, ν_f	0.22
Shear modulus, G_f (MPa)	29508

F.2 Epoxy resin

The epoxy resin system used by the manufacturer of the filament-wound GFRP pipes is the Epikote L 1100 with the Epikure 294 curing agent. Unfortunately the material property data available [237] does not include the material Poisson's ratio, required for the estimation of the lamina properties using micromechanics, presented in Appendix A. For this reason material properties of the epoxy resin were measured in accordance with the requirements set out in the ASTM D 638 [238] testing standard. A flat plate of resin was prepared by following the mixing procedures of reference [237]. The resin was cured at room temperature for a period of 15 hours, and post-cured at 70°C for 10 hours [237]. After cure, 6 dogbone specimens were cut from the plate and ground down to constant

thickness of 5.35 mm, using a surface grinding machine. The geometry of these specimens is specified within ASTM D 638 [238]. Four sets of Kyowa KFG-1-120-C1-11 strain gauges, with a nominal resistance of 120 Ω and 1 mm gauge length were bonded to each specimen. Two gauges were aligned in the longitudinal direction, allowing for the determination of the Young's modulus, and two gauges were aligned in the transverse direction allowing for the Poisson's ratio of the epoxy to be determined. During testing the strain gauges were soldered to a National Instruments data acquisition system, equipped with SCXI-1520 and SCXI-1521/B strain cards. Tensile testing was performed using a MX 100 K tensile testing machine, manufactured by Lloyd Instruments. This machine was equipped with a 500 N load cell. For each specimen, two sets of tensile tests were performed, to ensure experimental repeatability. In each case, the tensile test speed of elongation was set to 2 mm/min, and the test was set to end at an applied load of 400 N. This corresponded to a strain response of roughly 2000 $\mu\epsilon$. From the measured data, the corresponding Young's modulus, Poisson's ratio and Shear modulus were determined. The average of these values obtained for each the specimen are presented in Table F.2. Included within this table are the material properties averaged across all specimens, which are the values that were used for the estimation of the lamina material properties.

Table F.2: Epoxy material properties

Specimen	Young's modulus, E_m (MPa)	Poissons ratio, ν_m	Shear modulus, G_m (MPa)
# 1	3248	0.373	1183
# 2	3198	0.388	1152
# 3	3237	0.368	1183
# 4	3174	0.414	1122
# 5	3217	0.409	1141
# 6	3226	0.402	1150
Average	3217	0.393	1155

The standard deviation in the measured Young's modulus values is 37 MPa, and 0.019 for the Poisson's ratio. These translate to deviations of 1.15% and 4.80%, respectively. The Young's modulus of the Epikote L 1100/Epikure 294 combination was provided [237] as 3160 MPa. This value is in excellent agreement with the average value of Young's modulus presented in Table F.2. More specifically the values are within 2% of one another. The minimal deviation in the results obtained for all specimens, as well as the agreement of these results with the data for this epoxy resin in reference [237] is evidence of the accuracy, and the reliability of the measured data.

F.3 Lamina properties

The fibre volume fraction, V_f, of the GFRP filament-wound pipes was specified by the manufacturer to be in the range of 0.529 to 0.567. For the purposes of this work, this was taken as 0.548, the mean value within this specified range. Knowledge of the fibre volume fraction, material properties of the E-glass, presented in Table F.1 and measured epoxy material properties, presented in Table F.2 allows for the estimation of unidirectional lamina material properties. These were calculated using micromechanics, the equations of which are presented in Appendix A. Table F.3 presents the results of these, in the material coordinate system $(1, 2, 3)$ of the lamina. The 1 direction is the orientation of the fibres, while the 2 direction is the in-plane direction, transverse to the fibre orientation, and the 3 direction is the through thickness direction, also aligned transversely to the fibre orientation.

Table F.3: Lamina material properties

Longitudinal modulus, E_1 (MPa)	40887
Transverse modulus, $E_2 = E_3$ (MPa)	7905
Shear modulus, $G_{12} = G_{13}$ (MPa)	2437
Shear modulus, G_{23} (MPa)	2855
Poissons ratio, $\nu_{12} = \nu_{13}$	0.298
Poissons ratio, ν_{23}	0.384

These material properties can be substituted directly into the equations presented in Appendix A to determine the transformed stiffness matrix, $\bar{\boldsymbol{C}}$, for a lamina rotated through any angle, ϕ.

APPENDIX G FE models for determining residual stresses

Finding the residual stress that existed at any radial location within the thick-walled orthotropic pipe by FE simulation requires three separate FE models. These were developed using the Patran/Nastran FE package. The purpose of the first two models is to determine the residual loads released by a particular layer m. These loads take the form of an axial force, $F_x^{\overline{m}}$, torque, $T_x^{\overline{m}}$, and internal and external pressure, P_m and P_{m-1}, respectively, and are calculated directly from the strain response of the remaining pipe to the material removal. The final model is utilised to find the residual stress that was present in layer m, prior to any material removal. This is done by applying the residual loads associated with the removal of this layer, to the layer itself. This is exactly the same process followed by the current method, presented in Section 5. To simulate regions far from edge effects, the geometry of all FE models were subject to the constraint of constant axial strain, ϵ_x^0, and twist per unit length, γ^0, through the wall thickness. This is the requirement of the exact elastic solution, as presented in Section 4, and was implemented through the use of multi-point constraints (MPC) [245]. The appropriate details of each FE model are discussed in the following Appendix.

G.1 Determining the residual loads of layer m

Two FE models were required to determine the residual loads released by an individual layer m. The first of these models is required to find the residual load released by the removal of all $m-1$ layers before layer m is removed. Although a two-dimensional axisymmetric model could be used for orthotropic material properties, no shear response, and hence residual T_x, can be obtained using this model type. For this reason, a three-dimensional model was used. The geometry simulated in each model was an annular ring, 2 mm thick, with an internal diameter of 80 mm and external diameter equal to the outer diameter of layer m. This diameter varied, depending on the through-thickness location

under consideration. The model geometry was meshed using CTETRA elements, which are tetrahedral elements [245]. These were specified to each comprise 10 nodes. A global edge length of 1 mm was set to define the element size. Fig. G.1 illustrates a typical CTETRA mesh used in the FE simulations. The material properties, were input as 3-D anisotropic material properties, where each component of the transformed stiffness matrix, $\bar{\boldsymbol{C}}$, were defined separately, and referenced to the cylindrical coordinate system (r, θ, x) of the ring. The terms of the transformed stiffness matrix were found using the equations presented in Appendix A, and the lamina properties presented in Appendix F.

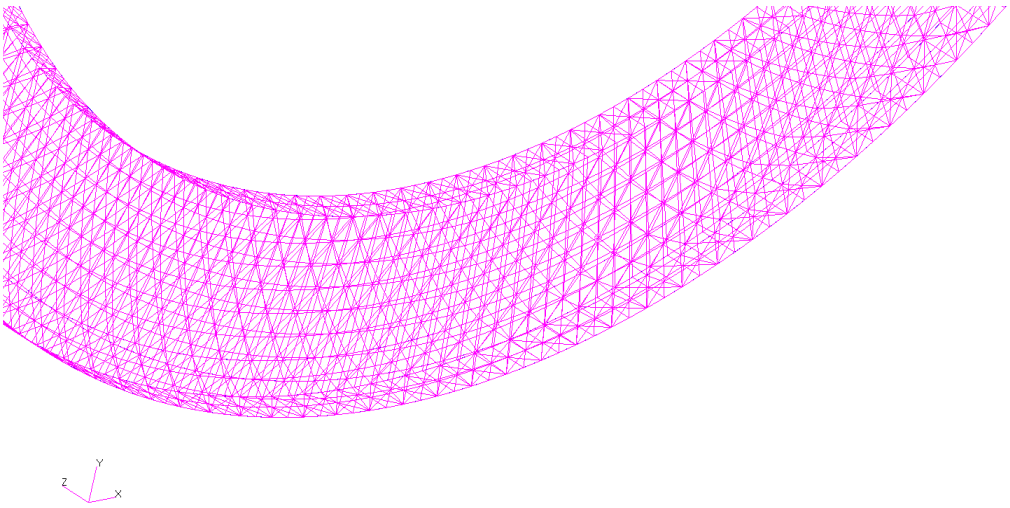

Figure G.1: CTETRA mesh used in FE models

A single face of the ring was constrained such that it could not move in either the axial direction (x) or rotate about the x axis. The opposite "free" face of the ring was constrained to move with constant axial displacement, and constant angle of twist about the x axis over the wall thickness, making the use of an MPC. This MPC was defined using rigid body elements (RBE's), more specifically RBE2 [245]. To define this MPC, an additional node needed to be created. The location of this node was defined to be at the centre of the ring, with the same axial location as the "free" face. This node was set as the independent node of the RBE2, while all the nodes associated with the "free" face were set as the dependant ones. The dependence of these nodes was set as the axial displacement, and rotation about the x axis. The first of these dependencies ensures all the nodes of the "free" face are constrained to move with the same axial displacement. The second dependence constraint of the MPC, ensures that each node of the "free" face rotates by the same angle about the x axis, and also displaces circumferentially through the same angle. The independent node of the MPC was then constrained to only move in the axial direction, and rotate about the x axis. Three load cases were created. In the first of these, a unit axial force, F_x, was applied to the independent node of the MPC. The MPC distributes the load among the

dependant nodes such that the constraint of constant axial displacement or strain, ϵ_x^0 is achieved. In the second load case a unit torque, T_x, orientated about the x axis of the ring, was applied to the independent node of the MPC. In the same fashion as the axial load, the torque load applied to the independent node is distributed among the dependant nodes of the "free" face, such that a constant angle of twist over this face is achieved. In this sense, a constant angle of twist per unit length, γ^0, over the thickness of the ring is maintained. The third load case was that of a unit pressure, P_O, applied to the outer surface of the ring. For each load case, the corresponding axial, ϵ_x, circumferential, ϵ_θ and shear strain, $\gamma_{x\theta}$, at the inner surface of the ring were extracted and written in the matrix form of Eq. (G.1).

$$\begin{bmatrix} \epsilon_x \\ \epsilon_\theta \\ \gamma_{x\theta} \end{bmatrix} = \begin{bmatrix} \epsilon_x^{F_x} & \epsilon_x^{T_x} & \epsilon_x^{P_O} \\ \epsilon_\theta^{F_x} & \epsilon_\theta^{T_x} & \epsilon_\theta^{P_O} \\ \gamma_{x\theta}^{F_x} & \gamma_{x\theta}^{T_x} & \gamma_{x\theta}^{P_O} \end{bmatrix} \begin{bmatrix} F_x = 1 \\ T_x = 1 \\ P_O = 1 \end{bmatrix} \tag{G.1}$$

Using Eq. (G.1), the residual loads released by the removal of $m-1$ layers were found. This was done by substituting the simulated strains after removal of the $m-1$ layers, ϵ_x^{m-1}, ϵ_θ^{m-1} and $\gamma_{x\theta}^{m-1}$ into Eq. (G.1), and solving for the residual loads, F_x^{m-1}, T_x^{m-1} and P_{m-1}:

$$\begin{bmatrix} F_x^{m-1} \\ T_x^{m-1} \\ P_{m-1} \end{bmatrix} = \begin{bmatrix} \epsilon_x^{F_x} & \epsilon_x^{T_x} & \epsilon_x^{P_O} \\ \epsilon_\theta^{F_x} & \epsilon_\theta^{T_x} & \epsilon_\theta^{P_O} \\ \gamma_{x\theta}^{F_x} & \gamma_{x\theta}^{T_x} & \gamma_{x\theta}^{P_O} \end{bmatrix}^{-1} \begin{bmatrix} \epsilon_x^{m-1} \\ \epsilon_\theta^{m-1} \\ \gamma_{x\theta}^{m-1} \end{bmatrix} \tag{G.2}$$

The second FE model was used to determine the residual loads released by the removal of m layers from the pipe. The model was identical to first FE model, apart from the outer diameter, which was set to the inner diameter of layer m. For the purposes of this investigation, the thickness of layer m was taken as 1% of the overall pipe thickness. So for a pipe of originally 150 mm wall thickness, the outer diameter simulated in the second FE model would be 3 mm smaller than that of the first FE model. All constraints and RBE2 definitions were the same as in the first FE models, with the same unit loads applied in each load case. As with the first FE model, the strain response at the inner surface to each load case were written in the matrix form of Eq. (G.1). The residual loads released by removal of all m layers were then found by solving Eq. (G.2), after substitution of the simulated strains, ϵ_x^m, ϵ_θ^m and $\gamma_{x\theta}^m$. Knowledge of these loads, along with the loads determined for the removal of all $m-1$ layers allowed for the residual axial, $F_x^{\overline{m}}$ and torque, $T_x^{\overline{m}}$, loads release by the individual layer m to be found. These were calculated using Eqs. (5.12) and (5.13), rewritten in Eqs. (G.3) and (G.4).

$$F_x^{\overline{m}} = F_x^m - F_x^{m-1} \tag{G.3}$$

$$T_x^{\overline{m}} = T_x^m - T_x^{m-1} \tag{G.4}$$

G.2 Determining the residual stresses in layer m

Determining the residual stress in the removed layer m required a third FE model. The geometry simulated in this model was, like the first and the second FE models, an annular ring of 2 mm thickness. The inner and outer diameters of this ring were exactly those of layer m. For the assumed thickness of each layer m, the difference between these diameters was exactly 3 mm. As with the other models, 10 noded CTETRA elements defined the mesh, but with a global edge length of 0.5 mm. The material properties were once again input as 3-D anisotropic, and referenced to the cylindrical coordinate system (r, θ, x). The constraints applied in this model were identical to those of the first and second models. This also made use of a RBE2 defined MPC, enforcing constant axial strain, ϵ_x^0, and twist per unit length, γ^0, while the opposite face was constrained from moving in the axial and circumferential directions. The axial and torque loads applied in the model were exactly those calculated using Eqs. (G.3) and (G.4) for this layer. These, as with the other FE models, were applied directly to the independent node of the MPC, but within a single load case. As discussed in Section 5, the residual radial stresses at the outer and inner surfaces of this layer must be P_{m-1} and P_m, respectively. To achieve these stresses, the pressure loads applied to the outer and inner surfaces of the ring in the FE model were $-P_{m-1}$ and $-P_m$, respectively. Finally, from the results of the FE model, the residual axial, σ_x, hoop, σ_θ, radial, σ_r, and in-plane shear, $\tau_{x\theta}$, stresses at the mid-radius of the this layer were extracted. The process of determining the residual loads and stresses in each layer was repeated 6 times; once for each of the different layer locations considered.

APPENDIX H Calibration of the LM35D temperature sensor

An LM35D temperature sensor was utilised to measure the ambient temperature within the room where experimental strain measurements were recorded. Before the layer removal experiment commenced, calibration of the temperature sensor was performed. The sensor requires a DC power supply of between 4 V and 30 V, and the output signal is directly proportional to temperature, 10 mV/°C with a typical accuracy of ±0.5°C [235]. In this sense the sensor does not require calibration if the typical accuracy is sufficient. To ensure that the more accurate temperature measurements could be taken, the particular sensor that was used throughout the experiment was calibrated.

The LM35D sensor was connected to the National Instruments DAQ system, equipped with an SCXI-1520 strain card. This card has the capability of supplying excitation voltage, while measuring the change in input signal. The voltage that was supplied to the sensor was 10.0 V. The calibration procedure was performed using a thermally insulated drum, which was filled with water. The temperature of the water was controlled by either adding ice, or boiling water. The sensor was submerged in the water, and the output signal measured by the DAQ system recorded. A T-type thermocouple connected to a Fluke 54 series II thermometer, with an accuracy of ±0.1°C, was also submerged in the water in close vicinity to the LM35 sensor. The calibration began with ice water, and the temperature of the water was increased by incrementally adding boiling water. The water was stirred after each addition of boiling water, and the LM35D output voltage recorded together with the stabilised temperature output of the thermometer. This procedure was repeated 12 times, until the water temperature was around 50°C. After the high temperature readings were taken, ice was added incrementally to the hot water. The measurement procedure was repeated until the water temperature was around 0°C. Fig. H.1 plots the measured temperature of the thermometer against the output voltage of the LM35 sensor. Included in this figure is the linear fit applied to the data, with $R^2 = 0.9999928$.

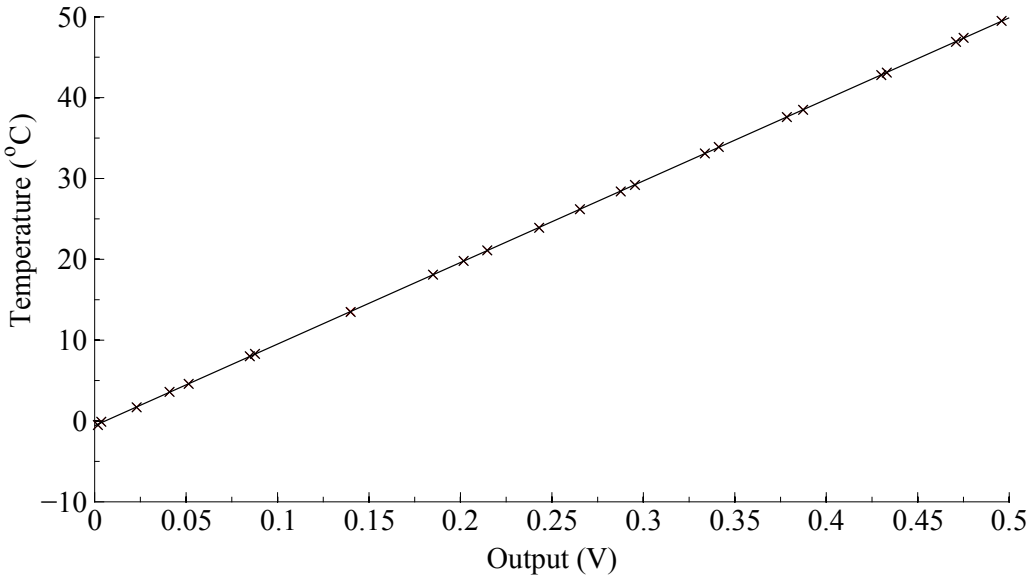

Figure H.1: LM35 calibration

The calibration equation associated with the linear fit is:

$$T = 100.911 \times U - 0.580 \tag{H.1}$$

where T is the temperature in degrees Celsius, and U is the output reading of the sensor in volts. Due to the linear relationship of the data, use of Eq. (H.1) applied to the output signal of the LM35D sensor produces results with an accuracy equal to that of the thermometer used, which is ± 0.1°C.

APPENDIX I Determination of required specimen length

The elastic approach of the current method assumes that the composite pipe is free from edge effects, where inter-laminar shear stresses, τ_{xr} and $\tau_{\theta r}$, cannot exist. For this reason the critical specimen length needed to be determined, where the behaviour of the mid-region of the specimens adhere to these requirements. A thermal FE model, simulating the orthotropic material properties corresponding to a $\pm 55^{\circ}$ filament-wound pipe, was used for this purpose. The assumed material properties were exactly those presented in Appendix F. This model also required knowledge of the coefficients of thermal expansion (CTE) of the assumed GFRP material.

I.1 Determining the coefficients of thermal expansion

The CTEs of the ply were estimated using micromechanics. For the purposes of this work, the CTE of the epoxy resin, $\alpha_m = 63\ \mu\epsilon/^{\circ}C$, and E-glass, $\alpha_f = 5.4\ \mu\epsilon/^{\circ}C$, were assumed [224]. Knowledge of these allowed the CTEs of a lamina, α_i, in the material coordinate system $(1, 2, 3)$, to be estimated. Eqs. (I.1) and (I.2) present the equations used to determine these values [240]:

$$\alpha_1 = \frac{1}{E_1}(\alpha_f E_f V_f + \alpha_m E_m V_m) = 7.45\ \mu\epsilon/^{\circ}C \tag{I.1}$$

$$\alpha_2 = \alpha_3 = (1+\nu_f)\alpha_f V_f + (1+\nu_m)\alpha_m V_m - \alpha_1 \nu_{12} = 41.08\ \mu\epsilon/^{\circ}C \tag{I.2}$$

The terms E_1 and ν_{12} of Eqs. (I.1) and (I.2) are the Young's modulus and major Poisson's ratios of the unidirectional lamina, respectively. These values were determined using the micromechanics relationships, presented in Appendix A. The terms E_f and E_m are the Young's modulus of the fibre and resin, respectively. The terms ν_f and ν_m are the fibre

and resin Poisson's ratios, and V_f and V_m are the fibre and resin volume fractions of the lamina, respectively. All of these properties are presented in Appendix F. The CTEs of the lamina rotated through the angle ϕ, in the pipe coordinate system (r, θ, x), can be found using Eq. (I.3) [224]. This equation is represented with the CTEs, estimated for an orthotropic filament-wound pipe, with a winding angle of $\pm 55°$. Since the material is considered orthotropic, the term $\alpha_{x\theta}$ is set to zero.

$$\begin{bmatrix} \alpha_x \\ \alpha_\theta \\ \alpha_r \\ 0 \\ 0 \\ \alpha_{x\theta} \end{bmatrix} = [\boldsymbol{T}_2]^{-1} \begin{bmatrix} \alpha_1 \\ \alpha_2 \\ \alpha_3 \\ 0 \\ 0 \\ 0 \end{bmatrix} = \begin{bmatrix} 30.02 \\ 18.51 \\ 41.08 \\ 0 \\ 0 \\ 0 \end{bmatrix} \mu\epsilon/°C \tag{I.3}$$

In Eq. (I.3), the term $\boldsymbol{T}_2$ is the transformation matrix, defined in Appendix A.

I.2 Thermal FE model

Since the filament-wound GFRP pipe can be considered orthotropic at the bulk scale, a two-dimensional axisymmetric FE model was used. The advantage of using a thermal model is that no external loads are required to generate the resulting stresses. The thermal expansion induces residual stresses much like during the curing process of the pipe, which is highly dependant of cure shrinkage of the resin system, and the thermal expansion due to the difference between curing temperature and operating temperature of the pipe. Thus the critical pipe length is dependant only on the geometry and the material properties of the pipe. The geometry modelled was that of the pipes considered in the experimental component of this work. These had an internal diameter of 80 mm and wall thickness of 15 mm. Only the $\pm 55°$ pipe was considered for this investigation, since simulating the laminated pipes, with a discontinuous residual strains at the ply interface, would be impractical. Finding the critical specimen length, where the region of the centre of the pipe is free from edge effects, required a number of models. A number of finite length models were generated, and the results of these compared to those of a infinite length model.

The Patran/Nastran FE package was utilised to generate the axisymmetric models. The geometry modelled in the finite length models was exactly half of the simulated specimen length, where the mid position of the specimen was treated as a symmetry boundary. These models began with a specimen length of 10 mm and increased in increments of 10 mm to a length of 250 mm. Fig. I.1 illustrates the geometry modelled in a typical

axisymmetric model for a pipe of inner radius R_I and outer radius R_O, and highlights the symmetry boundary which is constrained in the axial direction. The particular type of model used required a mesh comprising CTRIAX6 elements [245], which are 6-noded, triangular elements. Fig. I.2 illustrates a typical mesh used in these models. The typical edge length of the elements [245] were specified as 0.15 mm. As illustrated in Fig. I.1, all of the nodes associated with the symmetry boundary were constrained in the axial direction, while the "free" end of the specimen was free to move along this direction. The degrees of freedom not considered in the axisymmetric solution were then constrained over the entire geometry of the specimen, these were all the rotational components of the nodes [245], as well as out-of-plane motion being the circumferential displacement [245]. The orthotropic material properties were input as 3-D anisotropic material properties, where each term of the transformed stiffness matrix, $\bar{\boldsymbol{C}}$, were defined for the pipe coordinate system (r, θ, x). As discussed, the orthotropic material properties used correspond with those of a filament-wound $\pm 55^{\circ}$ pipe, with material properties as defined in Appendix F. The CTEs defined were those obtained in the previous section of this Appendix. These were defined in terms of the cylindrical coordinate system of the pipe. A constant temperature decrease of 325°C was simulated over the entire thickness of the pipe to generate the residual stress distributions. Although this temperature decrease may seem excessive, it must be noted that it accounts not only the thermal effect due to the difference between cure and operating temperature, but must also somewhat account for the component of cure shrinkage that too induces residual stresses.

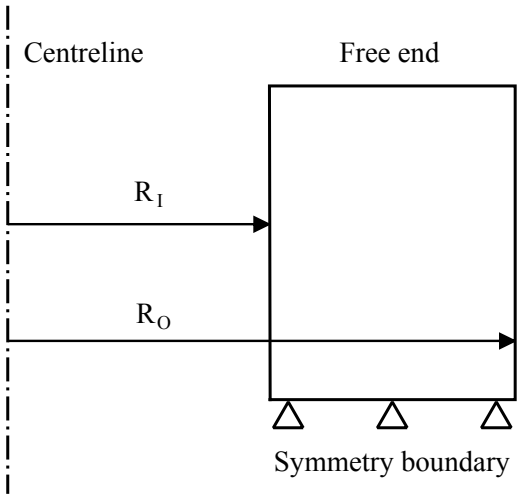

Figure I.1: Axisymmetric model

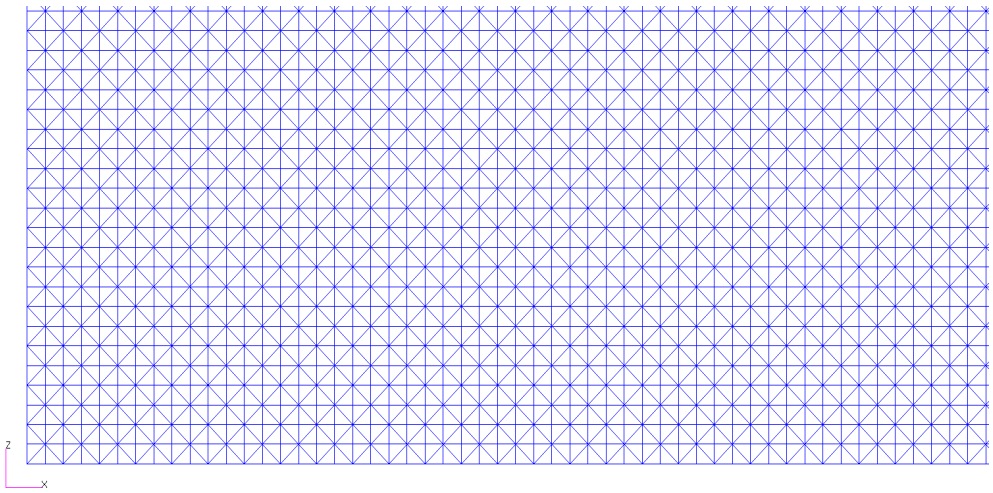

Figure I.2: CTRIAX6 mesh used in thermal FE models

The infinite length model was very similar to that of the finite length models. CTRIAX6 elements were also required for the mesh. These were specified to have a global edge length [245] of 0.15 mm. The length of pipe modelled was 5 mm. One end of the pipe was constrained in the axial direction, much like the edge of symmetry in the finite length models. The unused degrees of freedom were also constrained across all of the nodes within the model. To enforce constant axial strain, ϵ_x^0, over the thickness of the pipe, the requirement of an infinitely long pipe, an MPC was defined in the form of an RBE2. These types of constraints are discussed in Appendix G. An addition node was created, aligned with the centre line of the pipe, at the same axial location as the "free" end. This node was defined as the independent node of the RBE2, and all the nodes associated with the free end the dependant nodes. These were set to have a dependence of axial displacement. The dependant node of the RBE was then constrained to only move in the axial direction. The use of the RBE2 ensures that all of the nodes on the "free" end move with the same axial displacement, resulting in constant axial strain, ϵ_x^0, over the wall thickness of the pipe. The material properties were defined in the same way as those defined in the finite length models, with properties corresponding to those of a filament-wound $\pm 55^\circ$ pipe. The temperature decrease simulated over the pipe wall thickness was also 325°C.

To determine the critical specimen length, the resulting axial, σ_x, hoop stresses, σ_θ, at the inner surface of the finite length models, in the region of the symmetry boundary, were compared to those of the infinite length model. The inner surface results were chosen, since this is the region where the strain response of the specimens are measured in this work. Figs. I.3 and I.4 illustrate these results. In these figures, the stress results are all plotted against specimen length.

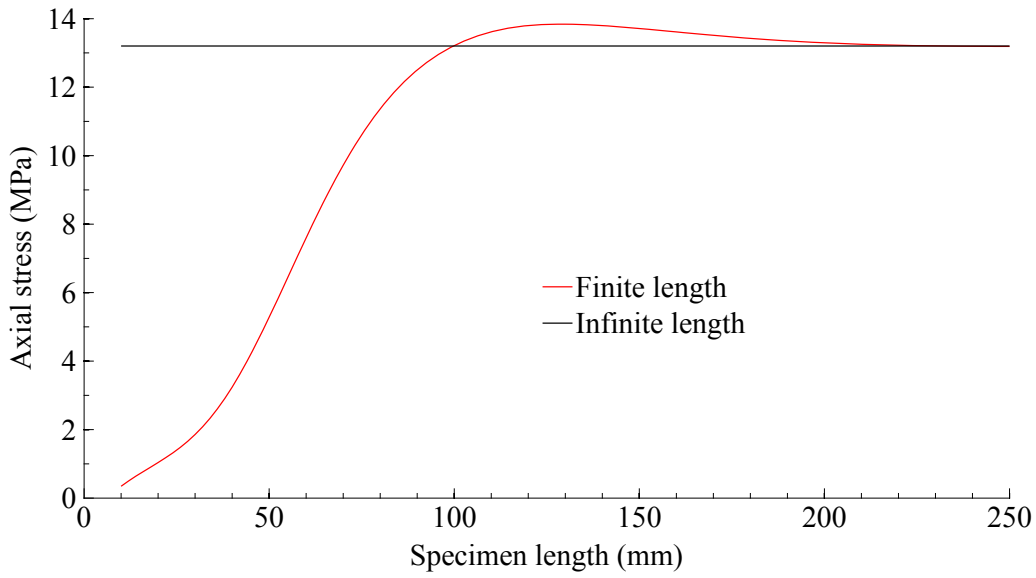

Figure I.3: Axial stress at inner surface, with increased specimen length

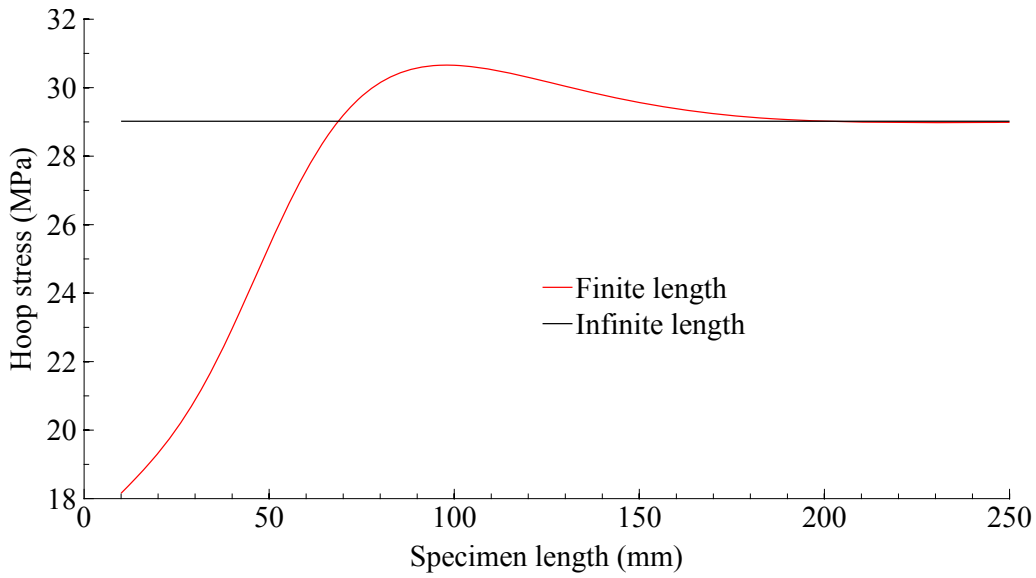

Figure I.4: Hoop stress at inner surface, with increased specimen length

It is clear from Figs. I.3 and I.4 that the minimum length required, such that the mid-region of the specimen is at far-field conditions, free from edge effects, is around 220 mm. This length, however, is impractical for the purposes of the residual stress measurement. Since the strain response of the specimens to layer removal was to be measured at the inner surface of the pipes, this length would make it very difficult to accurately align the strain gauges at the mid-region of the pipe, and almost impossible to access to solder the lead wires. For this reason the specimen length chosen needed to be shorter than

the required critical length. It was found that a specimen length of 120 mm was short enough such that the mid-region is easily accessible for strain gauge placement and lead wire soldering. Unfortunately, as seen in Figs. I.3 and I.4, a specimen of this length has not reached far field conditions within the mid-region of the pipe. The deviation between the axial, σ_x, and hoop stresses, σ_θ, of a specimen of this length is, however, within 5% of those of an infinitely long pipe. For the purposes of this investigation, this error was deemed acceptable, and differences in residual stress distributions as a result of this can be expected to fall within the error bounds of the experimental measurements.

To ensure that the largest error between the finite specimen length of 120 mm, and the infinite length pipe, fall within 5%, the resulting axial, σ_x, hoop, σ_θ, and radial stresses, σ_r, through the thickness of these pipes were compared to one another. Figs. I.5 to I.7 illustrates these stress distributions, plotted together against the normalised radial position. It is clear from Figs. I.5 and I.6 that the maximum deviation between the finite and infinite length results occurs at the inner surface of the pipes. Thus the maximum deviation between the axial and hoop stresses, over the entire wall thickness, between the 120 mm long specimen and infinite length model are within 5%. The maximum deviation in radial stress, as seen in Fig. I.7 occurs around the mid-radius of the specimen. This deviation is less than 4% of the infinite length value. All stress distributions at the mid-length of the 120 mm long specimen are therefore within 5% of far field conditions, and this pipe is therefore acceptable for the purposes of the experiment.

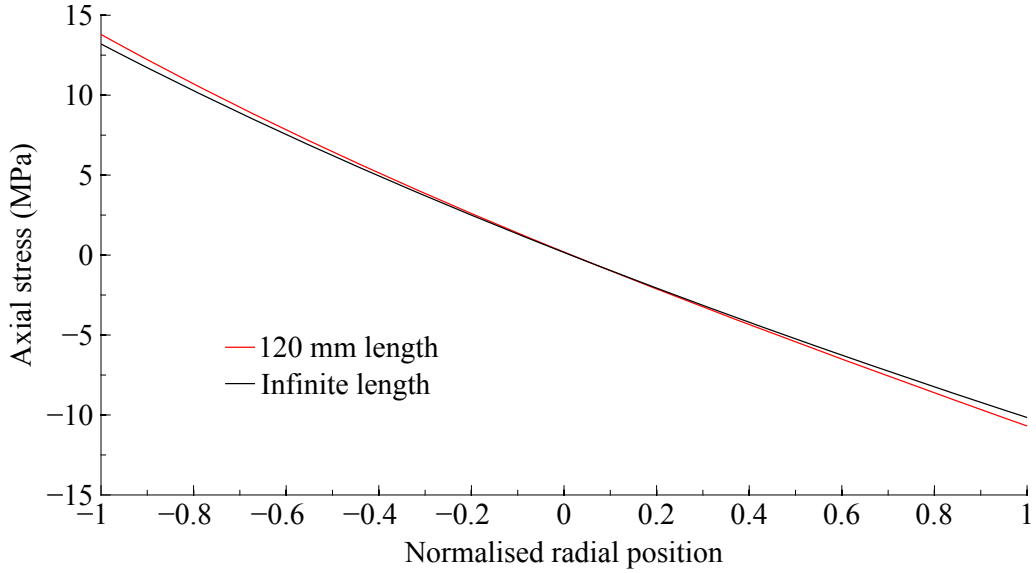

Figure I.5: Axial stress distribution for 120 mm long and infinite length pipes

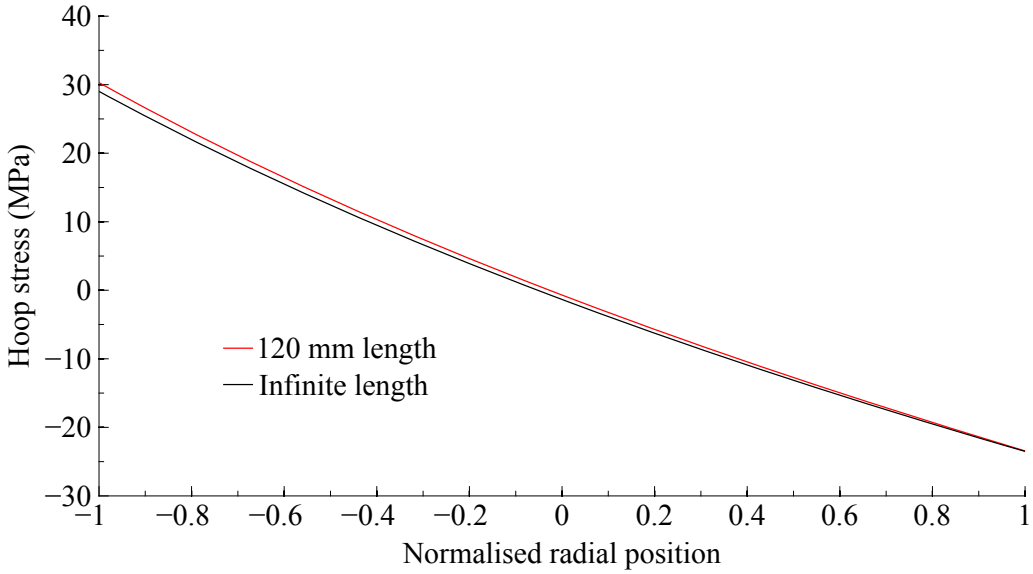

Figure I.6: Hoop stress distribution for 120 mm long and infinite length pipes

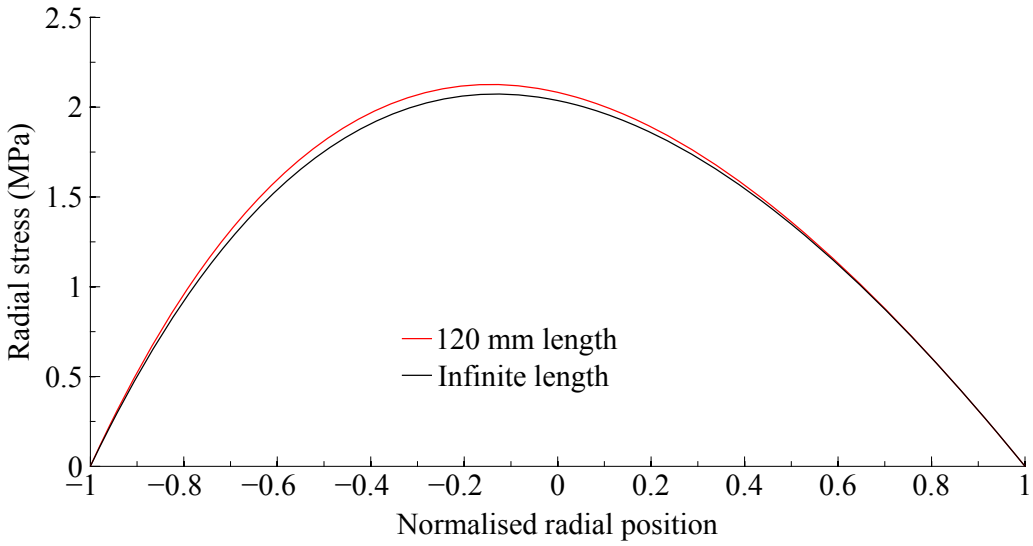

Figure I.7: Radial stress distribution for 120 mm long and infinite length pipes

APPENDIX J Temperature compensation of the measured strain data

Much care was taken to eliminate temperature effects within the recorded strains. To eliminate temperature effects associated with the grinding off of material from the outer surface of the specimens, and soldering of the strain gauges to the DAQ system, the output strains of each strain gauge were recorded only once they had stabilised with the ambient room temperature. As a result, there were long waiting periods between the grinding procedure, and measurement of the resulting strain response. This made it possible to only remove two layers from the specimens each day. Consequently, the experiment took a number of weeks to perform. Over this period, the stable temperature within the room, where the strain responses were recorded, drifted due to changes in ambient conditions. This temperature drift somewhat affected the strain readings, due to the thermo-mechanical response of the specimens, minor shifts in gauge factor, as well as changes in resistance of the strain gauges. For this reason, temperature compensation of the measured data was required, so that only the mechanical response to the removal of material could be determined. The temperature compensation required the room to be heated a number of times over the course of the experiment. This was done using fan heaters, which allowed a stable room temperature of roughly 23°C to be achieved. For each heating and cooling cycle, the strain response of the specimens was measured. From these results, distributions of fictitious CTEs, with the amount of material removed, were determined. These CTEs changed over the course of the experiment, since the geometry of the specimens, and thus the thermo-mechanical response to temperature also changed. The CTEs of each strain gauge were estimated by simply calculating the change in measured strain response with the change in temperature:

$$\begin{aligned} CTE(m) &= \frac{\Delta\epsilon}{\Delta T} \\ &= \frac{\epsilon^m_{T_2} - \epsilon^m_{T_1}}{T_2 - T_1} \end{aligned} \tag{J.1}$$

where ϵ_{T_2} and ϵ_{T_1} are the recorded strains at the elevated temperature, T_2, and ambient

room temperature, T_1, for the removal of m layers, respectively.

The experiment began with this procedure, so that the initial fictitious CTE for the removal of no layers could be found. It was then repeated at the end of each week during the course of the experiment, until the grinding procedure was terminated at a wall thickness of roughly 0.6 mm. The final temperature response was measured once the strain gauges had been cut out from the remaining geometry, and assigned to 100% material removed. Fig. J.1 illustrates the calculated CTEs for the strain gauge aligned in the axial direction, of the strain gauge rosette denoted "Gauge set C" of the ±75°/±36° pipe. It is clear from this figure that a total of 8 CTEs were measured over the duration of the experiment. Included in this figure is the 5th order least-squares polynomial fitted to this data, which allowed for estimation of the CTE values for any number of removed layers.

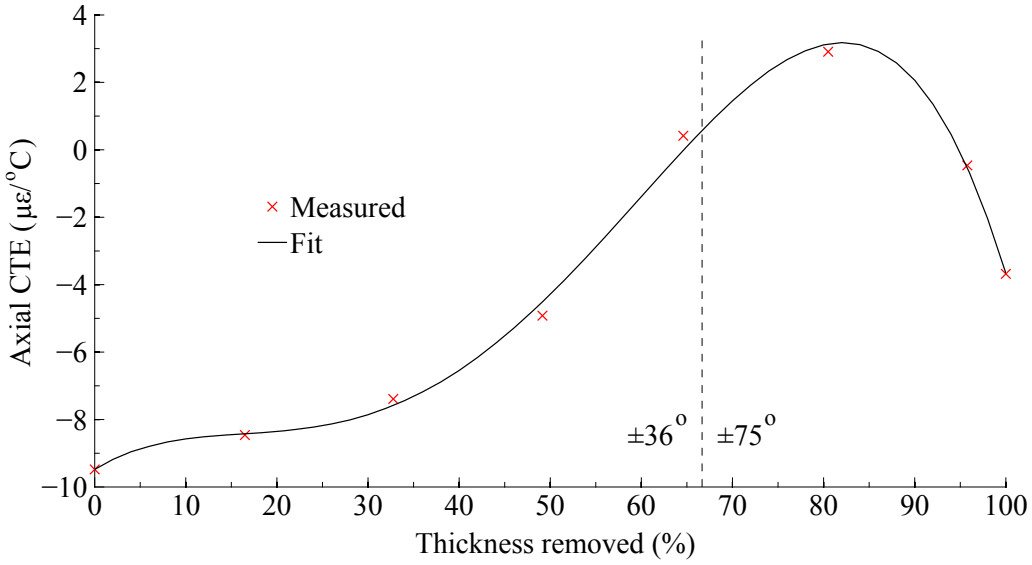

Figure J.1: Axial CTE distribution for ±75°/±36° pipe

Temperature compensation was performed by referencing the measured strain for the removal of each layer m, to a temperature of 20°C. Additionally, the strain data was zeroed with respect to the compensated strain for no removal of material. Eq. (J.2) illustrates the equation utilised to compensate for the drift in the stable room temperature:

$$\epsilon_{20}^{m} = \epsilon_{T_m}^{m} + CTE(m)\,[20 - T_m] - \epsilon_{20}^{0} \tag{J.2}$$

In Eq. (J.2), T_m is the stable temperature of the room, when strain $\epsilon_{T_m}^{m}$ was recorded. ϵ_{20}^{0} is the strain before the removal of any layers, referenced to 20°C. Fig. J.2 illustrates the temperature compensated measurements, plotted together with the uncompensated strain data measured by the axial strain gauge of "Gauge set C" of the ±75°/±36° specimen.

Included in this figure is the ambient temperature of the room, T_m, measured using the LM35D sensor.

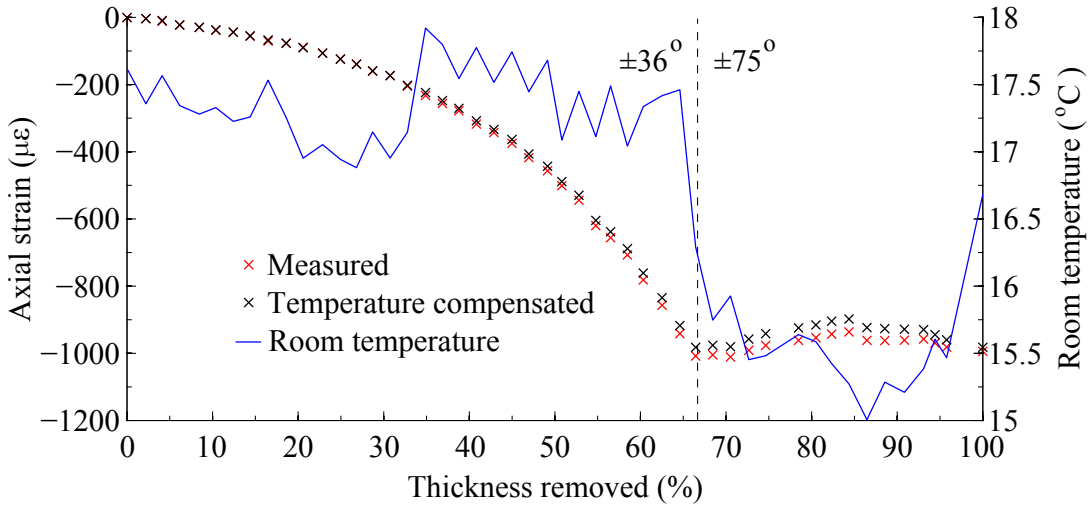

Figure J.2: Measured and thermally compensated axial strain variation of "Gauge set C" of the ±75°/±36° pipe

The process of CTE measurement and temperature compensation, as described in this Appendix, was performed for the strain response of each strain gauge of every test specimen, and these are the "measured" strain distributions presented in Section 8. It is clear from Fig. J.2 that the temperature compensation had only slightly altered the axial strain response of "Gauge set C" of the ±75°/±36° specimen. Although not shown, this was the case with all of the strain data of all of the test specimens, since the CTEs of every strain gauge were relatively small, and the temperature of the room varied only by a maximum of 3°C over the duration of the experiment.

APPENDIX K Measuring the temperature due to grinding

Any mechanical machining process applied to a component could potentially induce additional stresses. In the case of grinding, these could be introduced into the filament-wound GFRP specimens by grinding forces and the heat generated during the grinding process. To avoid this, the grinding forces and surface heat needed to be minimised. A FLIR T640 thermal imaging camera was used to measure the temperature reached during grinding of the test specimens. Before temperature measurements could be taken, the thermal camera needed to be calibrated. Calibrating the camera in this sense, is determining the correct emissivity to be used. Finding the correct emissivity required the use of a T-type thermocouple, connected to a Fluke 54 series II thermometer, and an oven. A test pipe was heated in the oven to a temperature of around 40°C. The outer surface temperature was measured with the thermocouple, which was bonded to the surface. The emissivity for the particular test section was found to be 0.93, at this temperature range, where the spot temperature of the camera matched the output reading of the thermocouple. Fig. K.1 is a picture taken during the calibration procedure.

To obtain the best possible temperature data, the thermal camera was set directly above the grinding machine, focussed on the region of contact between the grinding wheel and the test specimen. In this case, the maximum temperature reached by the pipe is directly measured, and the data does not require further interpretation. One of the images taken during this grinding test, for a grind depth of 0.025 mm, is illustrated in Fig. K.2. In this image it is clear that the temperature across the width of the grinding wheel is not uniform and localised heating occurs close to the leading edge of the grinding wheel. Further evidence is provided in Fig. K.3, which presents a plot of the surface temperature at every pixel in the enclosed area, Ar1, of Fig. K.2. The maximum measured temperature is in the region of 42°C. Since the FLIR camera measures the surface temperature and the temperature variation through the thickness reaches a peak at the surface, the maximum measured temperature using this procedure is the maximum temperature seen by any part of the pipe during grinding. Since the maximum temperature is well below the

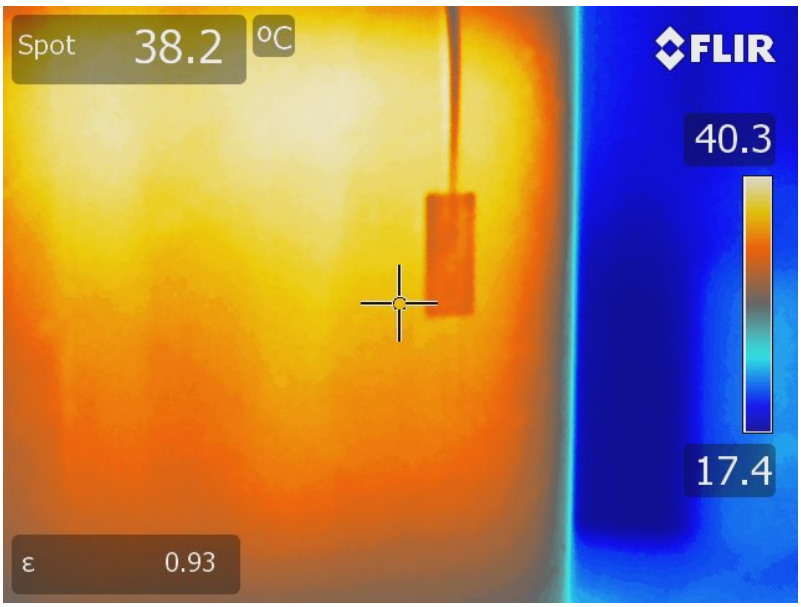

Figure K.1: Thermal camera calibration

peak post-cure temperature of 80°C, it is reasonable to assume that machining stresses introduced by grinding 0.025 mm off the thickness of a pipe are negligible.

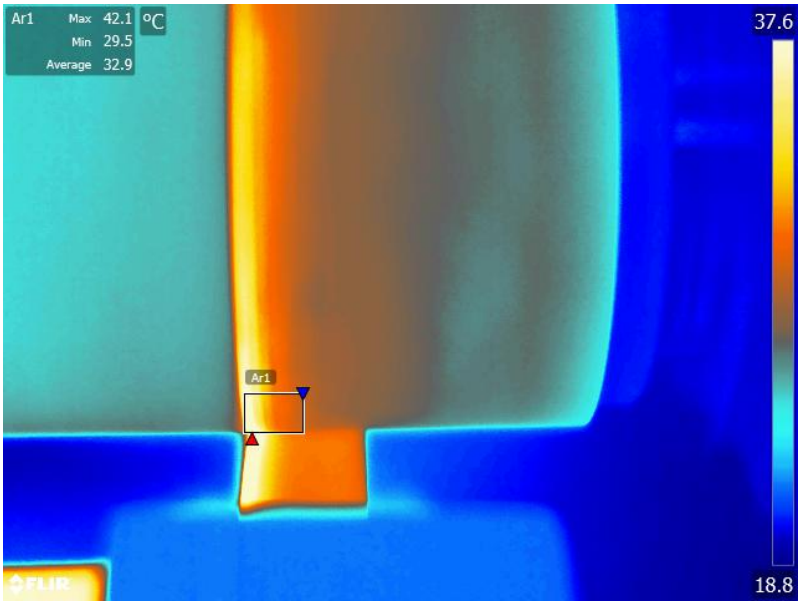

Figure K.2: Thermal image of grinding procedure

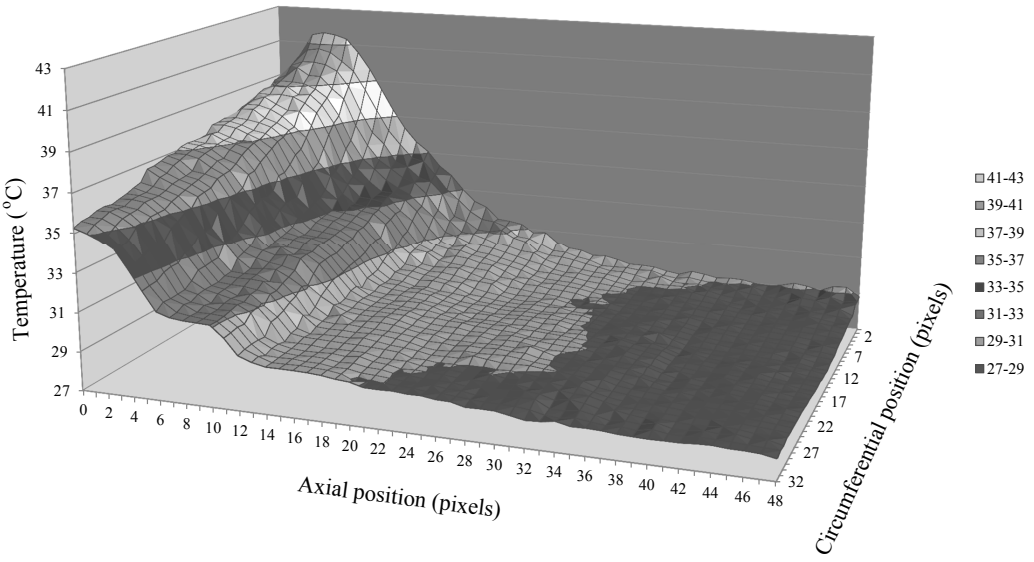

Figure K.3: Temperature profile of region Ar1

APPENDIX L Determining SD variations in measurement scatter

Considering the strain variations of Figs. 8.1 to 8.3, Figs. 8.9 to 8.11, and Figs. 8.17 to 8.19, it is clear that scatter in measured strain data generally increases with increased removal of material. As discussed, this error is not only a consequence of the quarter-bridge configuration used in obtaining the strain measurements, but also of the meso-scale non-homogeneous nature of the material from which the pipes were made. The local-scale anisotropy evidently played a more significant role in introducing scatter into the measured data as each specimen thickness decreased, most likely due to the relative increase in the ratio of local lamina thickness, oriented at a specific wind angle ϕ or $-\phi$, to the remaining wall thickness. To simulate this behaviour in the sensitivity analysis of Section 10, the variations of scatter in the measured strain data needed to be determined for each strain gauge orientation of each pipe configuration. This was done by calculating a running average SD in scatter, based upon the measured data of all three gauge sets. The definition for the SD of a finite population of size N [233] is

$$SD = \sqrt{\frac{1}{N}\sum_{j=1}^{N}(x_j - \bar{x})^2} \tag{L.1}$$

where x_j is the value of the jth datum point, and $\bar{x}$ is the mean value of all N data points.

For each strain gauge orientation of each of the pipe configurations, the SD value for the removal of the layer m was estimated by considering the measured values for the removal of the $m-2$ to $m+2$ layers, across all three gauge sets. In this sense, the SD value for each strain gauge orientation determined for the removal of each layer comprised a population of $N = 15$, 5 from each gauge set. Since the measured strain values varied with increased material removal, the mean value, $\bar{x}$, could not be taken as the mean value of all the measured data points, but was rather taken as the values of the least-squares polynomial fit for each of the layers removed in each gauge set. Under these conditions, Eq. (L.1) can written as Eq. (L.2).

$$SD_m = \sqrt{\frac{1}{15}\sum_{Y=A}^{C}\left[\sum_{j=m-2}^{m+2}(x_j - \bar{x}_j)^2\right]_Y} \tag{L.2}$$

The terms x_j and $\bar{x}_j$ in Eq. (L.2) are the measured strain and value of the polynomial fit for the removal of the layer j, respectively. These values are associated with the measured variation of "Gauge set Y" for the gauge orientation under consideration.

The SD values were found for the removal of the 3rd to the 3rd last layer of each pipe, for each strain gauge orientation. These were then plotted against the percentage (%) thickness removed, and least-squares polynomials fitted to the resulting SD variations. Each of these are presented in this Appendix. The polynomials fitted to each of the SD variations were utilised to estimate the corresponding SD values constraining the random scatter added to the "exact" data points for the sensitivity simulations of Section 10.

L.1 ±55° Filament-wound pipe

The SD variation determined of the axial strain responses of the ±55° pipe is illustrated in Fig. L.1. This is plotted together with the 2nd order least-squares polynomial fitted to the data. It is clear from this figure that the trend in SD is to increase with increased material removal and the range of the calculated SD values varies between roughly 4 $\mu\epsilon$ and about 24 $\mu\epsilon$. The polynomial fitted to the data is near linear across the entire range of material removal. There is a distinct waviness in the calculated SD values about the polynomial fit. These values, however, are only based upon the measured data of the three gauge sets and would likely become less wavy if more data were available.

The SD variation and corresponding 2nd order polynomial fit for the measured circumferential strain response of the ±55° pipe are presented in Fig. L.2. As with SD variation in axial strain, illustrated in Fig. L.1, the circumferential SD increases with increased material removal. The range of SD values determined for this strain response varies between roughly 6 $\mu\epsilon$ to about 35 $\mu\epsilon$, significantly larger than the maximum value of 24 $\mu\epsilon$ determined for the axial strain response. The waviness of the SD values of Fig. L.2 about the polynomial fit, is less severe than that of the axial strain response, seemingly approaching the smooth trend. Unlike the polynomial fitted to the data of Fig. L.1, the trend is quite non-linear, with the SD rapidly increasing from roughly 12 $\mu\epsilon$ to about 35 $\mu\epsilon$ between 50% and 100% thickness removed.

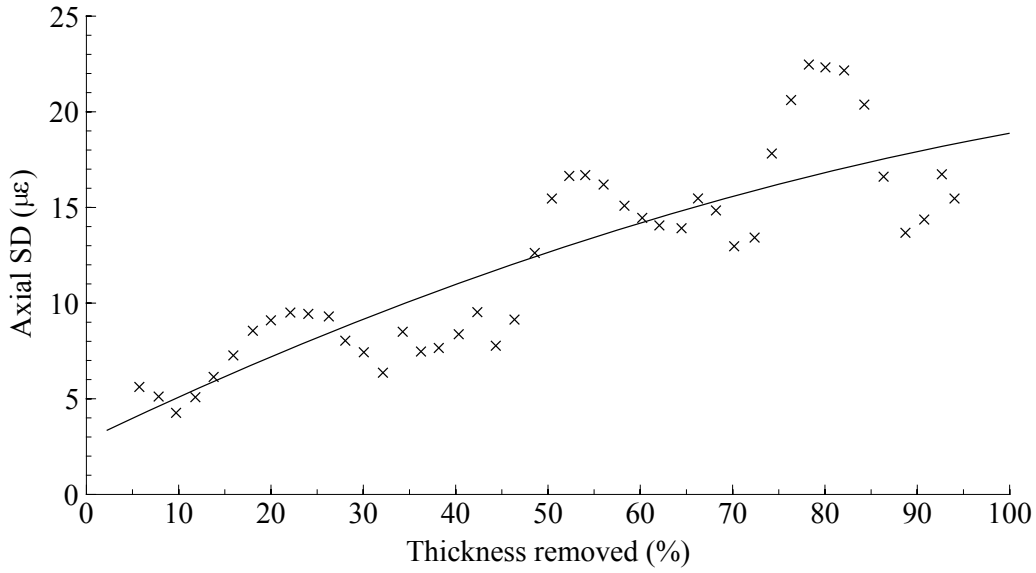

Figure L.1: Axial SD variation of the ±55° specimen

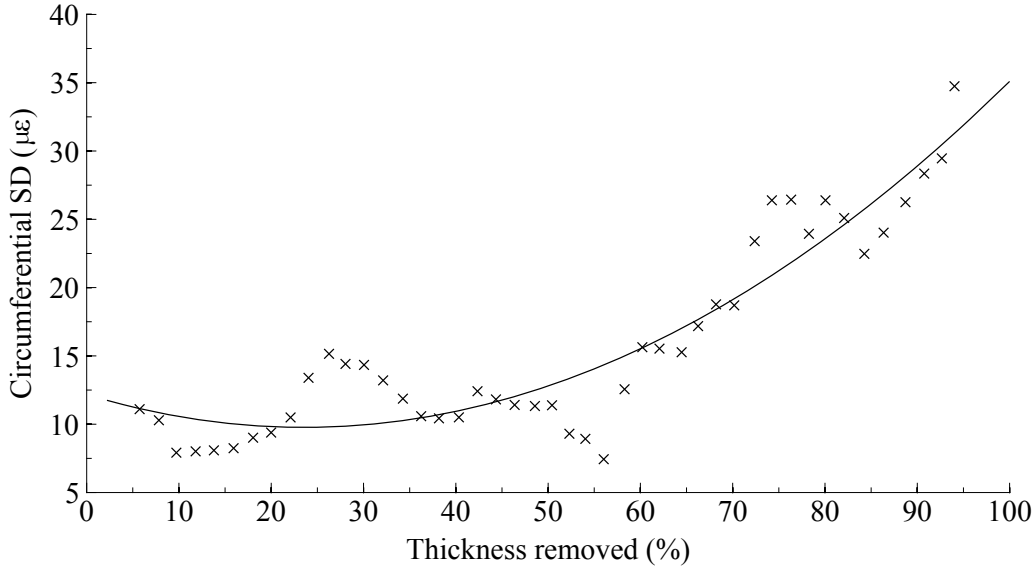

Figure L.2: Circumferential SD variation of the ±55° specimen

The SD variation and corresponding 2nd order polynomial fit for the measured 45° strain response of the ±55° pipe are illustrated in Fig. L.3. The trend in this polynomial is very similar to that of the polynomial fitted to the circumferential SD variation of Fig. L.2, with the SD rapidly increasing between 50% and 100% thickness removed. For this region the SD value increases from roughly 15 $\mu\epsilon$ to a maximum of about 50 $\mu\epsilon$. This is significantly larger than the maximum SD value of about 35 $\mu\epsilon$ obtained for the circumferential strain response. The waviness of the SD values about the polynomial fit, is the least severe of the three strain gauge orientations, and the range of calculated SD values varies between about 8 $\mu\epsilon$ and 46 $\mu\epsilon$.

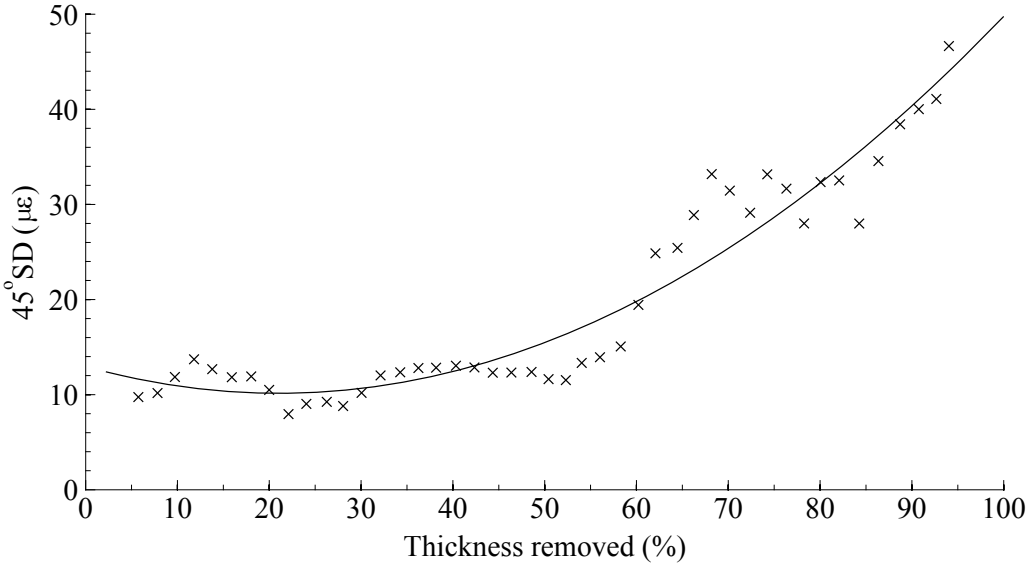

Figure L.3: 45° SD variation of the ±55° specimen

L.2 ±65°/±47° Filament-wound pipe

The SD variation and corresponding 2nd order polynomial fit for the measured axial strain response of the ±65°/±47° pipe are illustrated in Fig. L.4. Like the axial SD variation of the ±55° pipe, seen in Fig. L.1, the trend in the polynomial fit of Fig. L.4 is near linear, and increases with the removal of material. Additionally, both polynomial fits of these variations lie within the range of roughly 4 $\mu\epsilon$ to just less than 20 $\mu\epsilon$. The waviness of the calculated SD values about the polynomial fit of Fig. L.4 is, however, less pronounced than that of Fig. L.1.

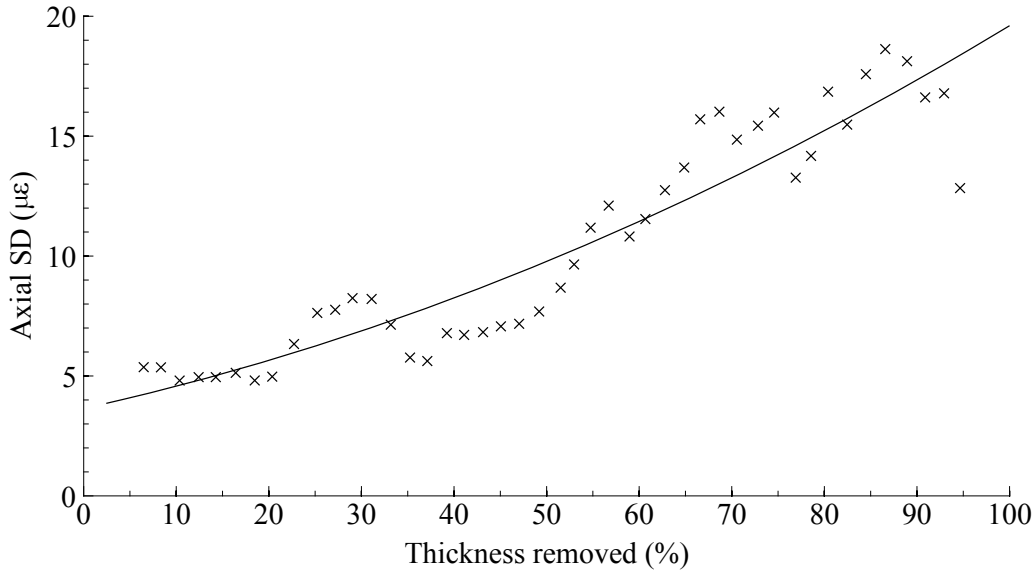

Figure L.4: Axial SD variation of the ±65°/±47° specimen

The variation in SD of the measured circumferential strain responses of the ±65°/±47° pipe, together with the 2nd order polynomial fitted to the data, are illustrated in Fig. L.5. The calculated SD values lie roughly between 5 $\mu\epsilon$ and 21 $\mu\epsilon$, and demonstrates significant waviness about the polynomial fit. As had been discussed, the SD values are only based upon the available results of three strain gauge sets. Should more data have been available, the scatter about the polynomial fit would have likely been significantly smaller. The polynomial fitted to the data of Fig. L.5 demonstrates a gradual increase in SD from just more than 5 $\mu\epsilon$ for about 2% thickness removed, to just above 22 $\mu\epsilon$ for 100% material removed. This range of values is significantly smaller than those obtained for the polynomial fitted to the circumferential strain data of the ±55° pipe, illustrated in Fig. L.2, which varied between about 10 $\mu\epsilon$ and 35 $\mu\epsilon$.

The SD variation and corresponding 2nd order polynomial fit for the measured 45° strain response of the ±65°/±47° pipe is presented in Fig. L.6. The polynomial fitted to the data is non-linear, with a rapid increase in SD between about 50% and 100% material removal. The range of SD values of this polynomial fit are the greatest of the three measured strain responses of the ±65°/±47° pipe, and like the polynomial fitted to the SD variation of the 45° strain responses of the ±55° pipe, seen in Fig. L.3, lie roughly between 10 $\mu\epsilon$ and 50 $\mu\epsilon$.

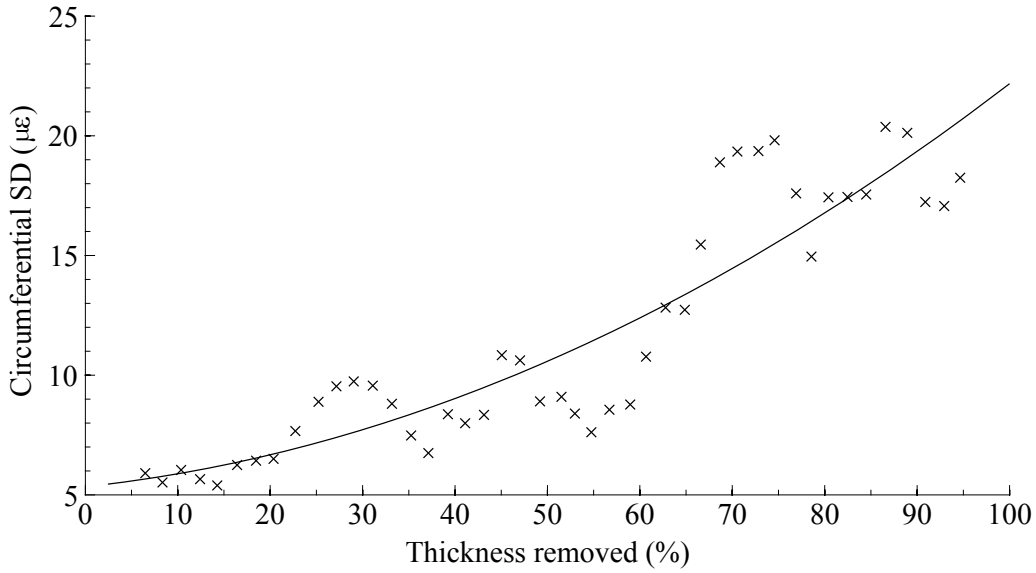

Figure L.5: Circumferential SD variation of the ±65°/±47° specimen

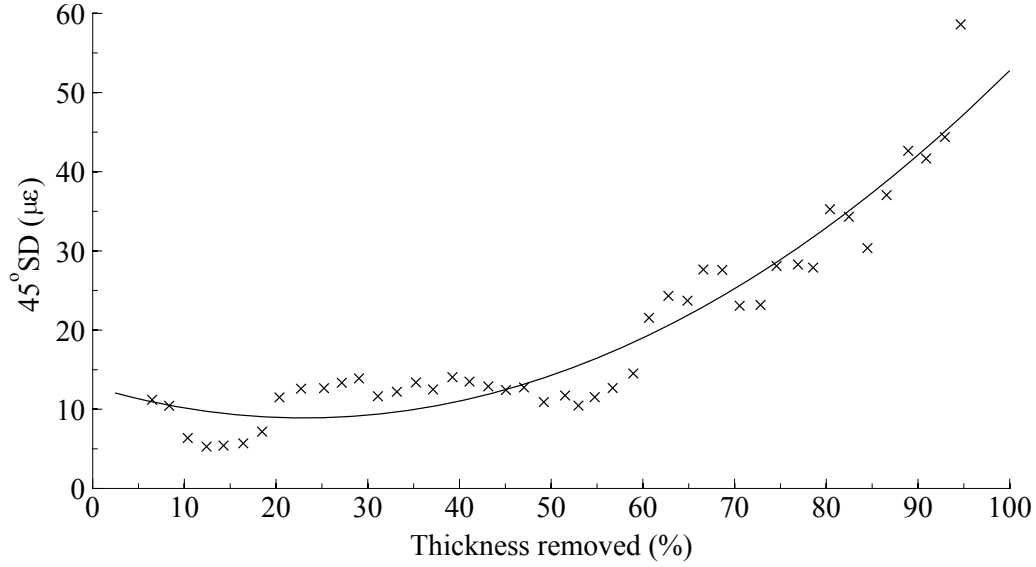

Figure L.6: 45° SD variation of the ±65°/±47° specimen

L.3 ±75°/±36° Filament-wound pipe

The variation in the calculated SD values of the axial strain responses of the ±75°/±36° pipe is illustrated in Fig. L.7. This is plotted together with the 2nd order polynomial fitted to the data. As with polynomials fitted to the the axial SD variations of the ±55° and ±65°/±47° pipes, seen in Figs. L.1 and L.4, the polynomial fitted to the SD variation of the ±75°/±36° pipe is largely linear over the range of material removal from the outer surface of the specimen. There also exists a large amount of scatter in the SD values over this range in comparison to the polynomial fitted to the data. This scatter, as discussed, would be expected to decrease if more data from which the SD values were calculated was available. The trend clearly shows an increase in SD with the amount of material removed, and the range of calculated SD values varies between roughly 3 $\mu\epsilon$ to 24 $\mu\epsilon$, resulting in the polynomial ranging between 1 $\mu\epsilon$ and about 18 $\mu\epsilon$. In addition, the maximum value within this range is very similar to those obtained for the both ±55° and ±65°/±47° pipes.

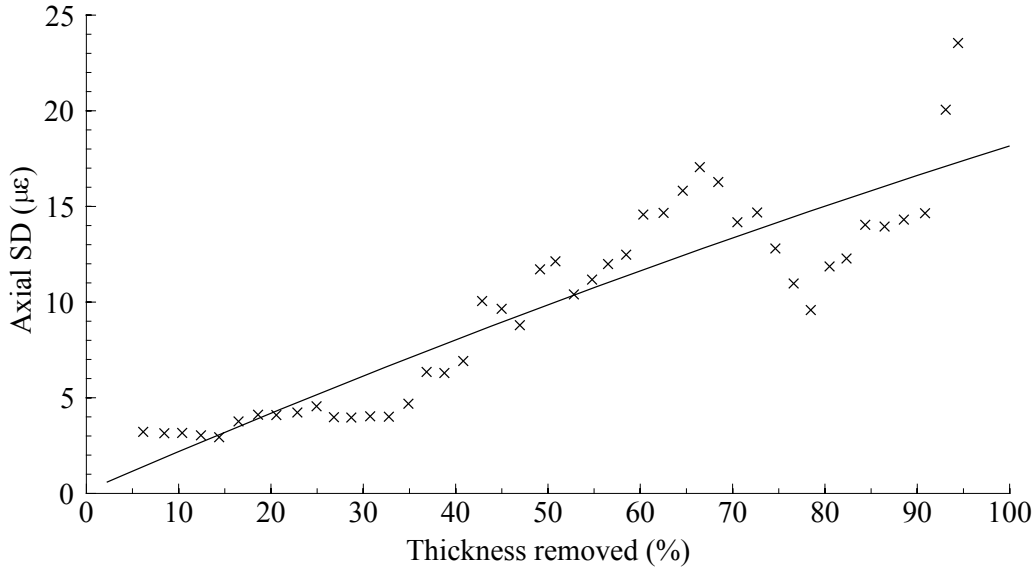

Figure L.7: Axial SD variation of the ±75°/±36° specimen

The SD variation and corresponding 2nd order least-squares polynomial fit for the measured circumferential strain responses of the ±75°/±36° is presented in Fig. L.8. The calculated SD values range between roughly 4 $\mu\epsilon$ to 17 $\mu\epsilon$. These minimum and maximum values occur at roughly 25% and 60% thickness removed, respectively. The maximum SD value seen by the polynomial fit occurs at 100% material removal, with a magnitude of roughly 13 $\mu\epsilon$. This is lower than the 22 $\mu\epsilon$ seen by the polynomial fitted to the circumferential SD variation of the ±65°/±47° pipe, shown in Fig. L.5. Additionally, these values are both significantly lower than the roughly 35 $\mu\epsilon$ obtained for the polynomial fitted to

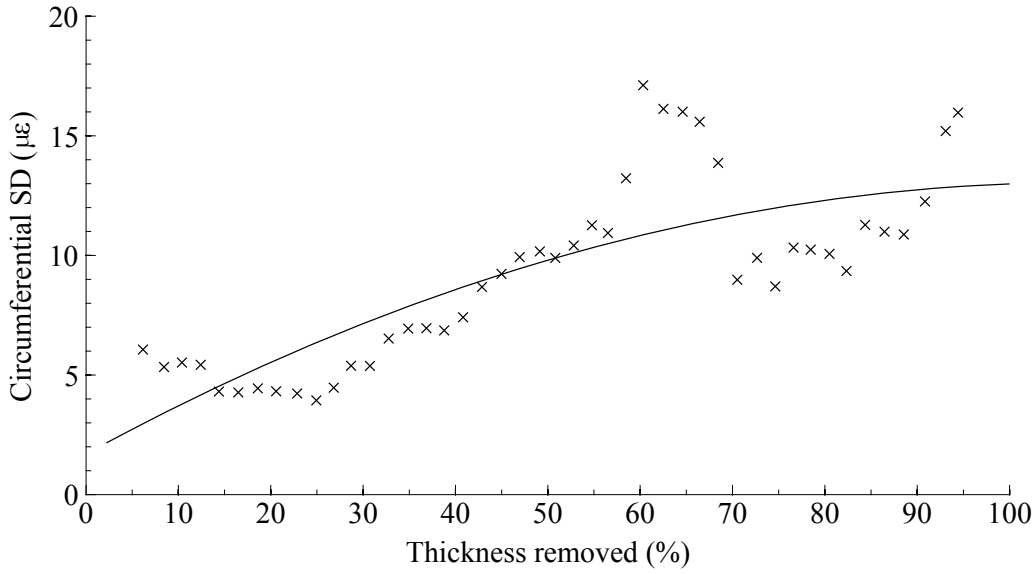

Figure L.8: Circumferential SD variation of the ±75°/±36° specimen

the circumferential SD variation of the ±55° pipe, seen in Fig. L.2. The scatter of the calculated SD values about the polynomial fit is quite large, with the maximum deviation of about 7 $\mu\epsilon$ between the calculate SD and polynomial fit for the region of 60% material removal.

The SD variation calculated for the 45° strain responses of the ±75°/±36° pipe, together with the 3rd order least-squares polynomial fit are illustrated in Fig. L.9. The trend in the polynomial fitted to the data is to gradually increase from just less than 5 $\mu\epsilon$ to just above 10 $\mu\epsilon$ from about 2% to 60% thickness removed. The SD values then rapidly increase to a value of roughly 50 $\mu\epsilon$ for 100% material removal. The waviness of the calculated SD values appears less than those of the axial and circumferential strain responses of Fig. L.7 and L.8. Additionally, the range of SD values of this strain response is very similar to those obtained for the 45° strain responses of the ±55° and ±65°/±47° pipes, illustrated in Figs. L.3 and L.6. This range is significantly larger than that obtained for the SD variations of the axial and circumferential orientations of the ±75°/±36° pipe shown in Figs. L.7 and L.8.

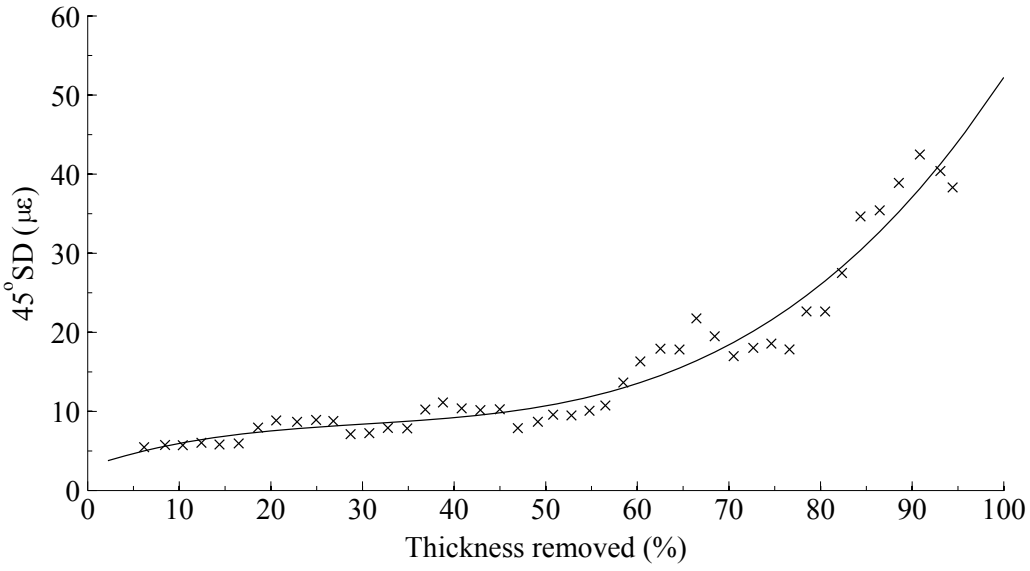

Figure L.9: 45° SD variation of the ±75°/±36° specimen

APPENDIX M Sensitivity analysis for the ±65°/±47° and ±75°/±36° filament-wound pipes

M.1 ±65°/±47° Filament-wound pipe

M.1.1 Full data set

Strain simulations

The 100 simulated axial strain variations of the full data set of the ±65°/±47° pipe, along with the 2nd to 4th order polynomial pair fitted to each variation, are illustrated in Fig. M.1. This figure has already been presented as Fig. 10.19 in the main body of the work, but is further discussed in this section. Included in this figure is the "exact" 4th and 2nd order polynomial pair fitted to the measured strain data, for removal of material from the outer and inner plies, respectively. These were originally presented in Fig. 8.9. This "exact" strain variation formed the basis upon which the scatter was added to generate each simulated strain variation. It is clear from Fig. M.1 that the simulated scatter about the "exact" variation increases with increased removal of material, as governed by the experimental SD variation of this gauge orientation, presented in Appendix L. For removal of material from the outer ±47° ply, there is a definite distinction between the majority of the 3rd and 4th order polynomial fits. The only region where the 2nd order fits are clearly distinguishable from these is between 0% and roughly 23% material removed, where they lie in the region of the upper bounds of the fits. The magnitude of the difference between the upper and lower bounds of the fits increases fairly rapidly from zero at 0% material removed, to roughly 20 $\mu\epsilon$ for about 8% thickness removed. This range then decreases to around 14 $\mu\epsilon$ at 22% thickness removed. From this point the difference between the upper and lower bounds then increases to close to 20 $\mu\epsilon$ for about 30% thickness removed, and is roughly maintained until around 45% thickness removed. Thereafter, this range increases

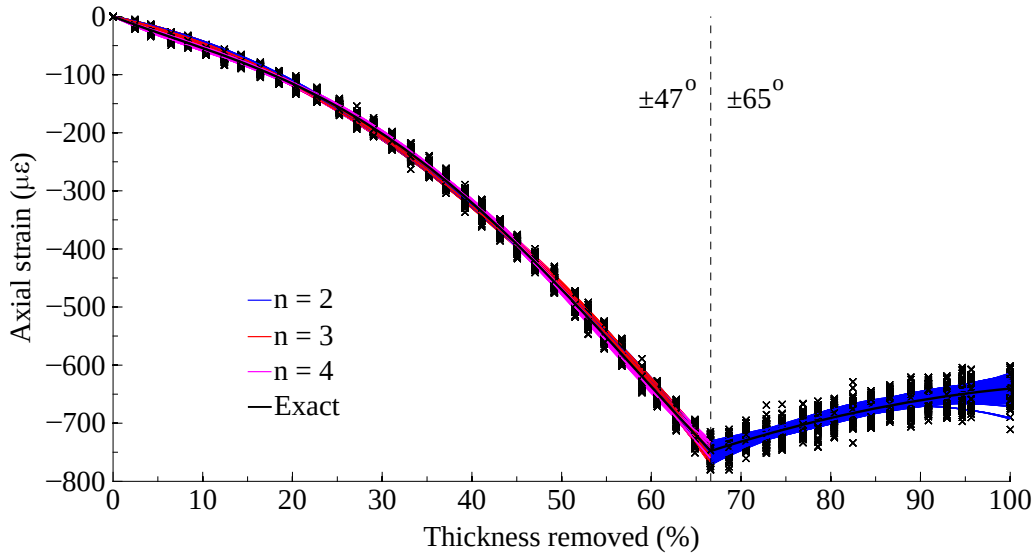

Figure M.1: Simulated axial strain variations and polynomial fits for the full data set of the ±65°/±47° pipe

gradually until a value of marginally less than 50 $\mu\epsilon$ is reached, at the region corresponding to removal of material at the ply interface. For removal of material from the inner ply, the magnitude of the difference between the bounds of the fits decreases to a value of around 25 $\mu\epsilon$, as 73% thickness removed is approached, and then increases to approximately 30 $\mu\epsilon$ at 82% thickness removed. This range is roughly maintained until about 90% thickness removed. Thereafter the range formed by the majority of the polynomial fits increases to about 70 $\mu\epsilon$, as 100% material removed is reached. There are, however, two outlying polynomial fits which define the lower bounds over this region. The difference between these and the upper bounds, in the region of 100% material removed, is around 100 $\mu\epsilon$. Over the full range of material removal, the bounds of the simulated data points generally lie well beyond the bounds of the polynomial fits. As has been discussed, this behaviour is directly associated with the number of data points describing each simulated strain variation. The large number of points of this data set constrains the polynomial fits to lie relatively close to the "exact" strain response.

The simulated circumferential strain variations and corresponding 2nd to 4th order polynomial pairs fitted to each distribution are illustrated in Fig. M.2. Included in this figure is the "exact" 4th and 2nd order polynomial pair fitted to the measured circumferential strain response of "Gauge set C", illustrated in Fig. 8.10. As with all simulations, the "exact" strain response formed the basis upon which scatter was added to generate the simulated strain variations. The simulated scatter of Fig. M.1 increases with increased material removal, as governed by the experimental SD variation determined for this gauge orientation. This is presented in Appendix L. The magnitude of the difference between

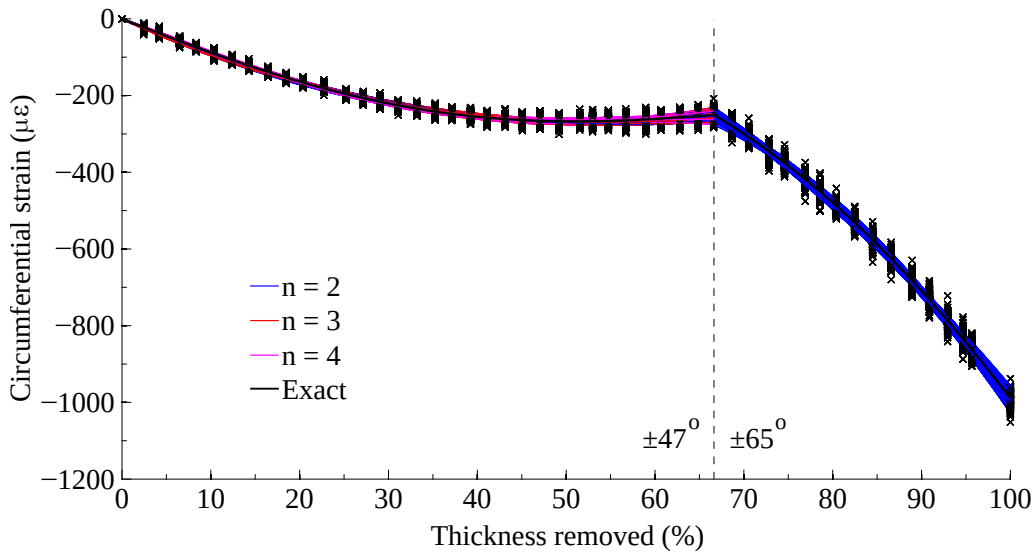

Figure M.2: Simulated circumferential strain variations and polynomial fits for the full data set of the ±65°/±47° pipe

the upper and lower bounds of the polynomial fits, over the region of material removal from the outer ±47° ply, increases gradually from zero, at 0% material removed, to about 50 $\mu\epsilon$ at the region corresponding to removal of material at the ply interface. For the removal of material from the inner ply, this range decreases to less than 30 $\mu\epsilon$ towards the region of about 72% thickness removed, and is roughly maintained through to about 90% thickness removed. From this point, the difference between the upper and lower bounds increases to a value of around 80 $\mu\epsilon$, as 100% material removed is reached. Due to the high number of data points describing each simulated strain variation, the bounds formed by the polynomial fits lie significantly closer to the "exact" strain response than those of the simulated data points.

The 100 simulated 45° strain variations of the full data set of the ±65°/±47° pipe are illustrated in Fig. M.3. Included in this figure are the 2nd to 4th order polynomial pairs fitted to each simulated variation, as well as the "exact" 4th and 2nd order polynomial pair fitted to the measured data, from which the simulated data was generated. The increase in scatter, with increased removal of material, is significantly larger than obtained for the simulated axial and circumferential strain responses of Figs. M.1 and M.2. The reason for this lies in the experimentally measured strain distributions, where the measurement scatter of the 45° strain gauges was significantly larger than that of the axially and circumferentially aligned strain gauges. The magnitude of the difference between the upper and lower bounds of the polynomial fits increases from zero, at 0% material removed, to about 25 $\mu\epsilon$ at about 8% thickness removed. For this region the upper and lower bounds are both defined by 4th order polynomials. This range then gradually decreases to approximately

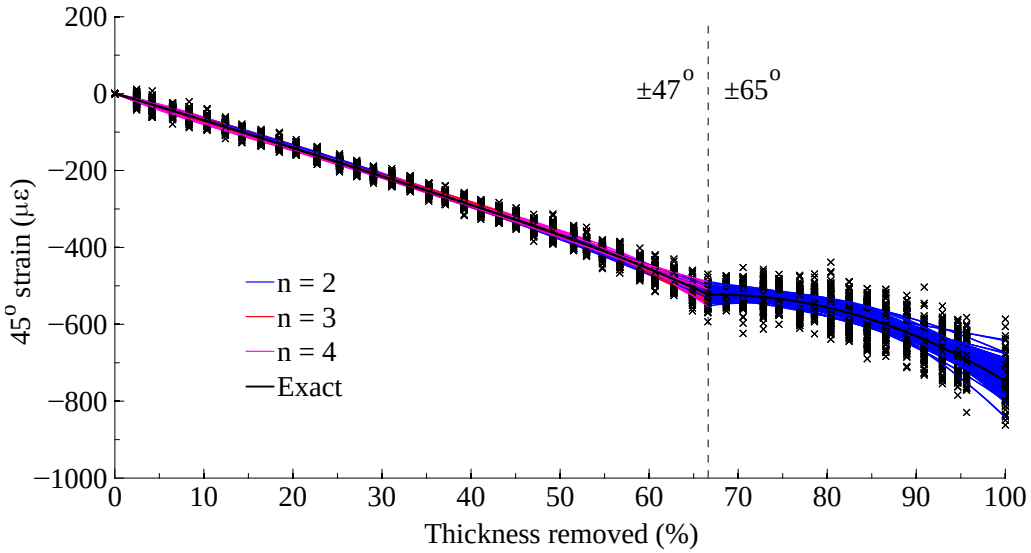

Figure M.3: Simulated 45° strain variations and polynomial fits for the full data set of the ±65°/±47° pipe

18 $\mu\epsilon$, as 35% thickness removed is approached, and then increases from this point to around 70 $\mu\epsilon$ at the region corresponding to removal of material at the ply interface. For the entire range of material removal from the outer ply, there are distinct regions where the trends in the different polynomial solutions are different. For instance, between 10% and 30% thickness removed the 2nd order polynomial fits seem to all lie above the "exact" strain response, while the region below comprises 4th order polynomials. Between 30% and 45% thickness removed, the region above the "exact" response is made up almost entirely of 3rd order polynomials, with 4th order solutions lying below. Additionally, between 45% and roughly 60% thickness removed, the lower bounds of the fits comprise 2nd order polynomials. For material removal from the inner ply, the bounds of possible strain distributions lie almost completely symmetrically about the "exact" strain response. As mentioned, all polynomials fitted to this data were of 2nd order. The magnitude of the difference between the bounds of the polynomial fits decreases from around 70 $\mu\epsilon$, at the region corresponding to removal of the ply interface, to roughly 50 $\mu\epsilon$ for about 73% thickness removed. The bounds formed by the majority of the polynomial fits then increases to more or less 150 $\mu\epsilon$ for 100% material removed. For this region, however, there are two separate polynomial fits which lie outside of this range. The difference between the upper and lower bounds for this region therefore increases to approximately 200 $\mu\epsilon$. Over the entire range of material removal, the bounds of the simulated data points lie well beyond those of the polynomial fits. As has been discussed, the large number of data points describing each simulated strain variation ensures that the corresponding polynomial fits lie relatively close to the "exact" strain response.

Residual stress distributions

The 900 axial stress distributions, associated with the possible combinations of the least-squares polynomial pairs fitted to the simulated axial and circumferential strain variations of Figs. M.1 and M.2, are illustrated in Fig. M.4. For illustrative purposes this figure has already been presented in the form of Fig. 10.20, but is further discussed in this Appendix. These comprise splines fitted to the residual stresses evaluated at the mid-radius of each layer, and are colour coded according to the order of polynomial fitted to the simulated axial strain variations of Fig. M.1 to which they correspond. Included in this figure is the "exact" stress distribution associated with the "exact" strain responses. The bounds of the stress distributions over the outer ply do not lie symmetrically about the "exact" solution. Additionally, the trends in the majority of the 4th order solutions are quite different from the solutions corresponding to 2nd and 3rd order polynomial fits, and demonstrate a large degree of waviness. The 2nd and 3rd order solutions, on the other hand, seem to bunch together, with a lower level of waviness. At the outer surface, the magnitude of the difference between the upper and lower bounds in stress is roughly 8 MPa, significantly larger than the 4 MPa obtained for the full data set of the $\pm 55^{\circ}$ pipe for the same region, seen in Fig. 10.4. This behaviour is a direct result of the fairly rapid increase in the range formed by the polynomials fitted to the simulated axial strain variations of Fig. M.1, for the first 10% of the thickness removed. Referring back to Fig. M.4, the difference between the upper and lower bounds in stress rapidly decreases away from the outer surface, to roughly 1.5 MPa, at the normalised radial position of about 0.86 and then increases again to around 2.5 MPa towards the normalised radial position of roughly 0.68. Over the remainder of the outer ply this range varies with the waviness of the stress solutions. At the ply interface, there is a significant level of sensitivity to measurement scatter, and the magnitude of the difference between the upper and lower bounds of stress in this region is roughly 3.5 MPa. This range, however, is significantly lower than the difference between the bounds in stress at the outer surface of the pipe. Over the inner ply, the magnitude of the difference between the bounds at the ply interface is also about 3.5 MPa, but this quickly decreases away from this point, to less than 1 MPa at the normalised radial position of about -0.6. Over the remainder of this ply, this range varies slightly but never exceeds 1 MPa.

The residual hoop stress distributions of the $\pm 65^{\circ}/\pm 47^{\circ}$ pipe, associated with all possible combinations of the polynomial pairs fitted to the simulated strain variations of Figs. M.1 and M.2, are presented in Fig. M.5. These are colour coded according to the order in polynomial fitted to the circumferential strain variations to which they correspond. As with the axial stress distributions of Fig. M.4, the majority of stress solutions within the outer ply, resulting from 4th order polynomial fits, are significantly more wavy than the 2nd

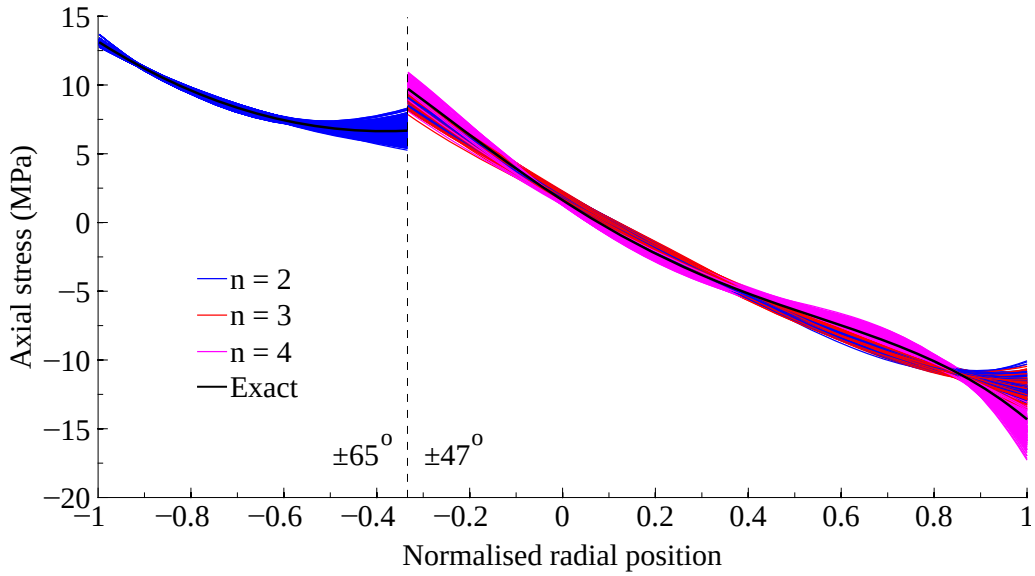

Figure M.4: Axial stress variations for the full data set of the ±65°/±47° pipe

and 3rd order solutions, which share similar trends. Over this ply, the bounds of the hoop stress solutions lie almost symmetrically about the "exact" stress distribution, which lies within the region common to the 2nd, 3rd, and 4th order solutions. At the outer surface, the magnitude of the difference between the upper and lower bounds in stress is roughly 10 MPa. Away from the outer surface, the magnitude of this range decreases quickly to around 2 MPa, at the normalised radial position of approximately 0.83, followed by an increase to around 4 MPa at the normalised radial position of 0.65. Thereafter, the difference between the bounds in stress varies with the waviness of the solutions until it reaches a magnitude of about 8 MPa at the region of the ply interface. The difference between the bounds of the 2nd order solutions of the inner ply for this region is slightly larger, with a magnitude of close to 10 MPa. As with the axial stress distributions of Fig. M.4, this range decreases rapidly away from this point, to a value of roughly 2 MPa at normalised radial position of -0.6. Over the remainder of this ply, the difference between the upper and lower bounds varies slightly, until it reaches a magnitude of approximately 2.5 MPa at the inner surface.

The 900 radial stress distributions of the ±65°/±47° pipe, associated with the combinations of the polynomial pairs fitted to the simulated strain variations of Figs. M.1 and M.2, are plotted in Fig. M.6. Each distribution is colour coded according to the order of polynomial fitted to the circumferential strain data of Fig. M.2 to which they correspond. Included in this figure is the "exact" radial stress distribution, associated with the "exact" strain variations of this gauge set. As required, each distribution is continuous over the ply interface, and tends to zero at the outer and inner surfaces of the pipe. Unlike the axial

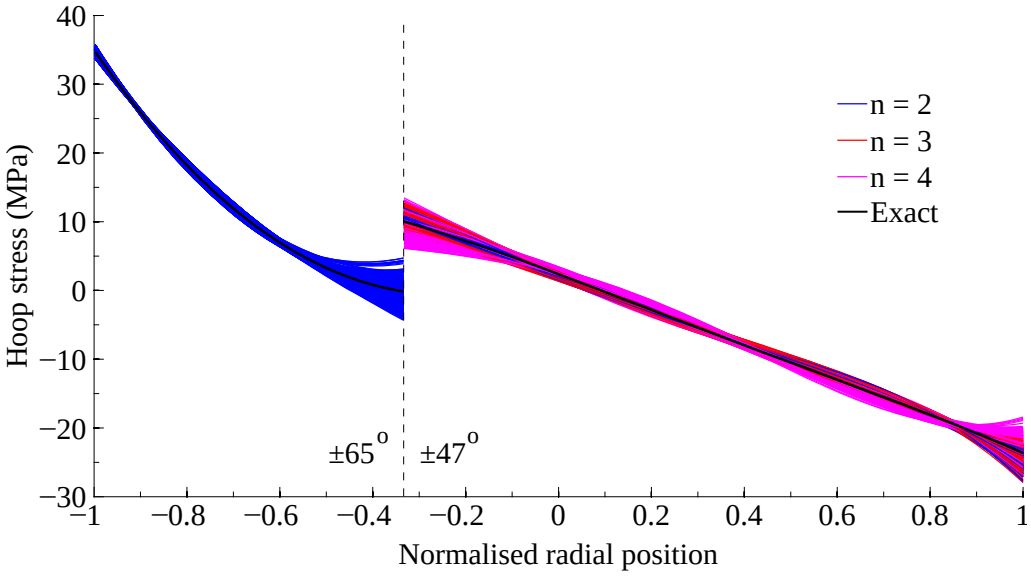

Figure M.5: Hoop stress variations for the full data set of the ±65°/±47° pipe

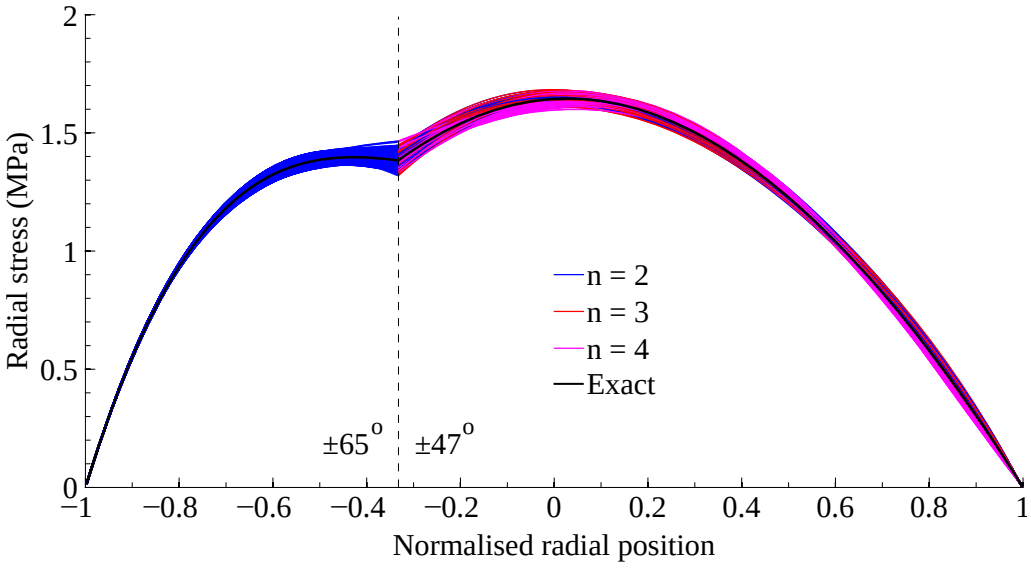

Figure M.6: Radial stress variations for the full data set of the ±65°/±47° pipe

and hoop stress distributions of Figs. M.4 and M.5, the different order solutions do not demonstrate any distinct waviness. Rather, the difference between the upper and lower bounds in stress increases gradually from zero at the outer surface to a maximum value of about 0.2 MPa at the ply interface. This maximum difference is slightly larger than that obtained for radial stress distributions of the full data set of the ±55° pipe, illustrated in Fig. 10.6. Within the inner ply, the difference between the bounds in stress gradually decreases from the value of around 0.2 MPa at the ply interface down to zero at the inner surface of the pipe.

The 2700 in-plane residual shear stress distributions of the ±65°/±47° pipe, associated with all the combinations of the polynomial pairs fitted to the simulated axial, circumferential and 45° strain variations of Figs. M.1 to M.3, are illustrated in Fig. M.7. Included in this figure is the "exact" shear stress distribution of this gauge set. Each solution in stress is color coded according to the order of polynomial fitted to the simulated 45° strain data to which they correspond. For the outer ply wound at ±47°, the bounds of the shear stress distributions do not lie symmetrically about the "exact" stress distribution, and these are defined by 4th order stresses over most of the thickness of this ply. Each stress distribution of this ply oscillates about the zero-stress state, expected to exist through the thickness of this pipe. At the region of the outer surface, the difference between the upper and lower bounds is quite large, with a magnitude of close to 14 MPa. This range rapidly decreases away from this surface, to a value of about 2.5 MPa at the normalised radial position of 0.87, and then increases to more or less 5 MPa toward the normalised radial position of 0.7. Over the remainder of the outer ply, the magnitude of the difference between the upper and lower bounds in stress varies with the waviness of the distributions, until a value of about 6 MPa is reached the at the region of the ply interface. Over the inner ply, the shear stress distributions are much less wavy than those obtained for the outer ply. The reason for this is simply because the polynomials fitted to the simulated strain data of Figs. M.1 to M.3 for removal of material from this ply were all limited to 2nd order. All solutions, however, approach the expected zero-stress state toward the inner surface of the pipe. The magnitude of the difference between the bounds in these stress solutions is slightly less than 8 MPa at the ply interface. This range then rapidly decreases to a value of less than 2 MPa, towards the normalised radial position of about -0.52, and is roughly maintained through to the normalised radial position of -0.8. From this point, the difference between the bounds decreases to around 1 MPa as the normalised radial position of -0.9 is reached, and then somewhat rapidly increases to a magnitude of roughly 2.5 MPa at the inner surface of the pipe.

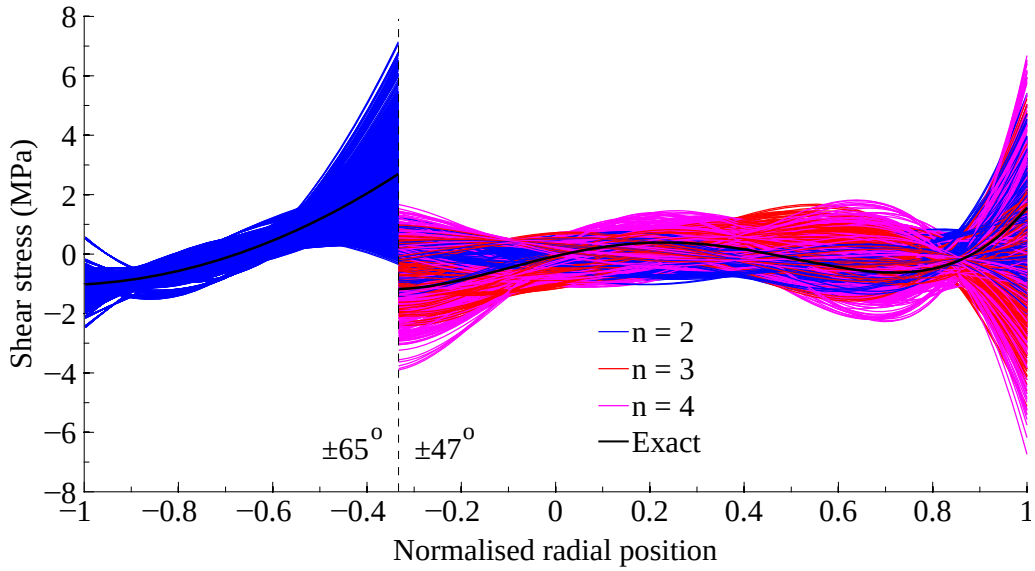

Figure M.7: Shear stress variations for the full data set of the ±65°/±47° pipe

M.1.2 Reduced data set

Strain simulations

The 100 simulated axial strain variations of the reduced data set of the ±65°/±47° pipe, together with the 2nd to 4th order polynomial pairs fitted to each variation, are illustrated in Fig. M.8. This figure has also been presented as Fig. 10.21 in the main body of this thesis, but for the purposes of clarity is further discussed in this Appendix. Included in this figure are the "exact" 2nd order polynomials fitted to the measured axial response of this data set, seen in Fig. 9.7. It is clear from Fig. M.8 that the level of scatter of the simulated data points increases with increased removal of material, as governed by the SD variation of the experimental scatter for this gauge orientation. This variation is presented in Appendix L, and is the same variation which constrained the scatter of the simulated axial strain variations of the full data set of Fig. M.1. Compared to the polynomial pairs fitted to these strain variations, the bounds of the polynomials fitted to the simulated data of Fig. M.8 lie significantly further apart, and almost entirely engulf the range of simulated data points. This behaviour, as has been discussed, is a direct result of the reduced number of data points describing each strain variation. Reducing the number of data points increases the probability that all the data, for a particular simulation, lie either above or below the "exact" strain response. The corresponding polynomial fits of the reduced data set are thus less constrained, than those of the full data set, to lie close to the "exact" strain response. This is behaviour which can be expected in any real experiment. The magnitude of the difference between the upper and lower bounds of the

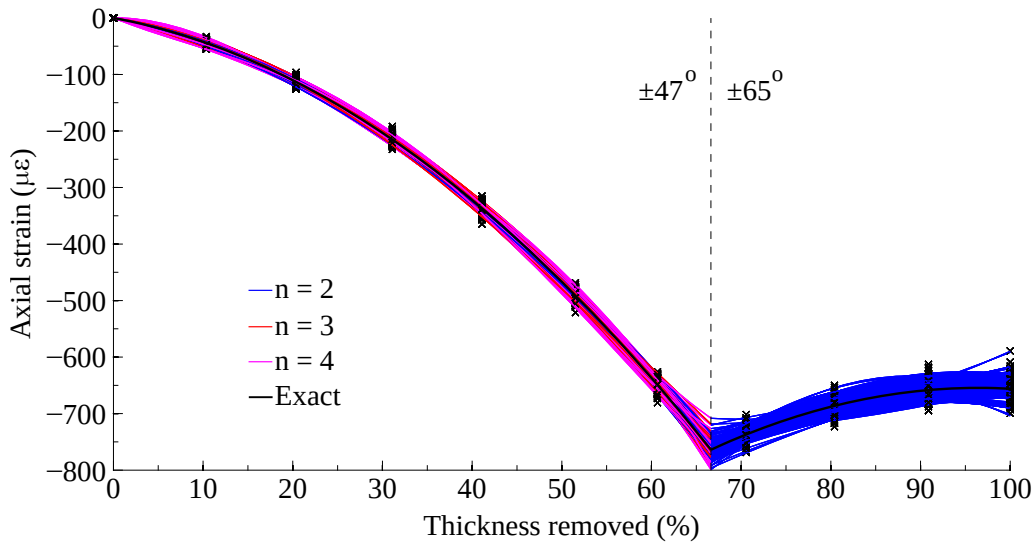

Figure M.8: Simulated axial strain variations and polynomial fits for the reduced data set of the ±65°/±47° pipe

polynomial fits of Fig. M.8 increases rapidly from zero, at 0% material removed, to about 25 $\mu\epsilon$ for around 8% thickness removed. This range then gradually decreases to roughly 20 $\mu\epsilon$ towards 20% thickness removed. From this point, the difference between the upper and lower bounds of the polynomial fits increases gradually to a magnitude of about 45 $\mu\epsilon$ for roughly 60% thickness removed. Thereafter, this range increases fairly rapidly to a magnitude of approximately 100 $\mu\epsilon$ at the region corresponding to material removal at the ply interface. Over the region corresponding to removal of material from the inner ply, this range decreases to a magnitude of roughly 60 $\mu\epsilon$ for about 73% thickness removed, and then increases to approximately 70 $\mu\epsilon$ for 85% thickness removed. Between this point and 100% material removed, this range is more or less maintained for the majority of the polynomial fits. For the region between about 95% and 100% thickness removed, however, there are a handful of fits that lie outside of this range, and the difference between the bounds of these fits at 100% material removed is roughly 115 $\mu\epsilon$.

The 100 simulated circumferential strain variations of the reduced data set of the ±65°/±47° pipe, and corresponding 2nd to 4th order polynomial pairs fitted to these data, are illustrated in Fig. M.9. Included in this figure is the "exact" 2nd order polynomial pair originally fitted the measured circumferential response of Fig. 9.7. The scatter of the simulated data of Fig. M.9 about the "exact" strain response increases with increased material removal, constrained by the same SD variation governing the magnitude of the scatter of the simulated circumferential strain variations of the full data set, illustrated in Fig. M.2. Due to the reduced number of data points describing each strain variation of Fig. M.9, the bounds of the fits lie much closer to those of the simulated data points than the bounds

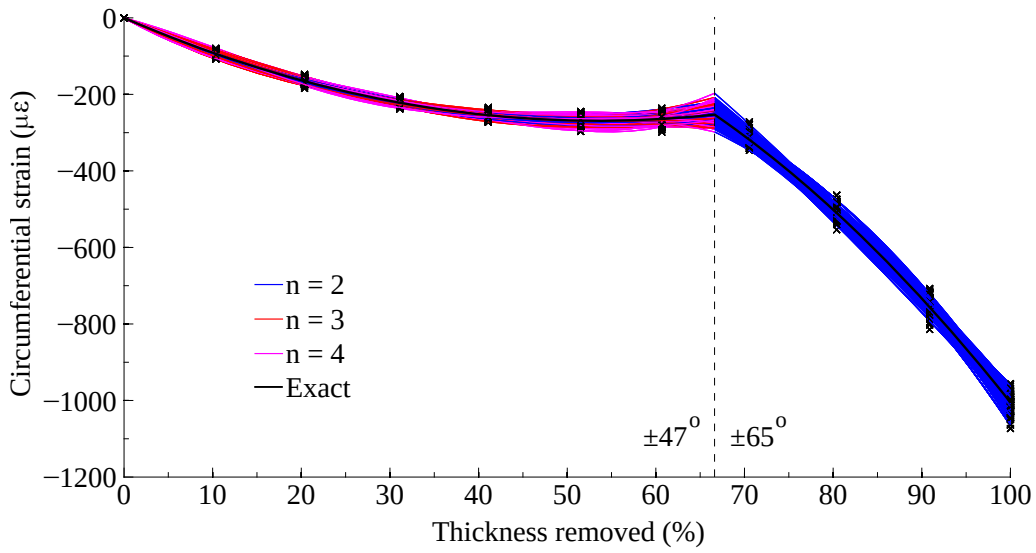

Figure M.9: Simulated circumferential strain variations and polynomial fits for the reduced data set of the ±65°/±47° pipe

of the polynomials fitted to the simulated circumferential strain variations of Fig. M.2. For removal of material from the outer ±47° ply, there is no real distinction between the trends of the different order polynomials. The magnitude of the difference between the upper and lower bounds of these polynomials increases from zero, at 0% material removed, to about 35 $\mu\epsilon$ at 10% thickness removed. This range then gradually deceases to around 25 $\mu\epsilon$ towards 34% thickness removed, followed by an increase in magnitude to in the region of 50 $\mu\epsilon$ for 50% thickness removed. From this point to around 60% thickness removed, the difference between the upper and lower bounds of the polynomial fits is more or less maintained. This range then increases fairly rapidly to about 100 $\mu\epsilon$ at the region corresponding to removal of material at the ply interface. For removal of material from the inner ±65° ply, the magnitude of the difference between the upper and lower bounds decreases to about 55 $\mu\epsilon$ at around 70% thickness removed, followed by an increase to about 80 $\mu\epsilon$ for 85% thickness removed. Thereafter, the difference between the upper and lower bounds decreases to less than 65 $\mu\epsilon$ for 93% thickness removed, followed by an increase to a magnitude of close to 110 $\mu\epsilon$ for the region corresponding to removal of material at the inner surface of the pipe.

The simulated 45° strain variations and corresponding polynomial fits of the reduced data set of the ±65°/±47° pipe are illustrated in Fig. M.10. Included in this figure are the "exact" 2nd order polynomials fitted to the measured 45° strain response of this data set, illustrated in Fig. 9.7. It is upon this response that scatter was added to generate the strain variations of Fig. M.10. The SD variation governing the magnitude of the scatter was the same as that used for the 45° strain simulations of the full data set, shown in

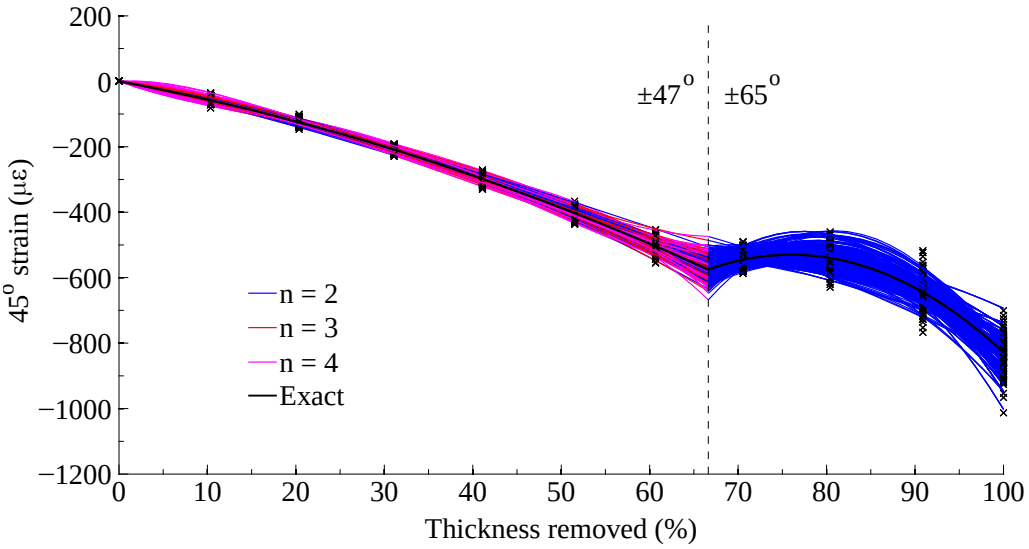

Figure M.10: Simulated 45° strain variations and polynomial fits for the reduced data set of the ±65°/±47° pipe

Fig. M.3. Despite the same level of scatter, the bounds of the polynomial fits of Fig. M.10 lie significantly further apart than those of Fig. M.3. This behaviour is associated with the reduction of the number of data points describing each strain variation. The difference between the upper and lower bounds of the polynomial fits of Fig. M.10 increases rapidly from zero, for 0% material removed, to roughly 50 $\mu\epsilon$ for 5% thickness removed. This range decreases to a value of about 33 $\mu\epsilon$, for 20% thickness removed, and then steadily increases to approximately 200 $\mu\epsilon$ at the region corresponding to removal of material at the ply interface. For removal of material from the inner ply, the difference between the upper and lower bounds of the 2nd order polynomial fits decreases to about 100 $\mu\epsilon$ at around 70% thickness removed. This range then increases to about 180 $\mu\epsilon$ for 85% thickness removed. For the majority of the polynomial fits, this range decreases to more or less 125 $\mu\epsilon$ for 95% thickness removed, followed by in increase to a magnitude of 220 $\mu\epsilon$ at 100% material removed. Between 90% and 100% thickness removed, however, there are a handful of polynomial fits that lie outside of these bounds, which form a range of roughly 300 $\mu\epsilon$ at the region of material removal at the inner surface of the pipe. This is almost identical to the range of simulated scatter for this region.

Residual stress distributions

The 900 axial residual stress distributions of the reduced data set of the ±65°/±47° pipe, associated with the different possible combinations of the polynomial pairs fitted to the simulated axial and circumferential strain variations of Figs. M.8 and M.9, are illustrated

in Fig. M.11. This figure has been already presented as Fig. 10.22, but is discussed further in this Appendix. Included in this figure is the "exact" stress distribution, associated with the "exact" strain variations of this data set. The stress distributions are colour coded according to the order of polynomial fitted to the simulated axial strain variations to which they correspond, and comprise splines fitted to the values in stress determined at the mid-radius of 50 layers numerically simulated to be removed. As has been discussed, increasing the amount of calculation points across the wall thickness addresses the issue of the loss of resolution in the radial stress distributions of the reduced data sets of the laminated pipes. Fitting splines to more data points also provides a better estimate of the other residual stress components, especially if they vary significantly in regions through the wall thickness. Over the entire wall thickness of the pipe, the bounds of the stress solutions lie significantly further apart than those of the axial stress distributions of the full data set, illustrated in Fig. M.4. Over the outer ply of $\pm 47^{\circ}$, the different order stress solutions of Fig. M.11 do not form trends distinctly different from one another, but the majority of the upper and lower bounds are defined by 4th order solutions. The difference between these bounds is largest at the outer surface of the pipe, with magnitude of about 11 MPa. This range rapidly decreases to slightly more 2 MPa, at the normalised radial position of about 0.85. From this point, the difference between bounds in stress increases until it reaches a magnitude of more than 3 MPa at the normalised radial position of 0.7. Over the remaining thickness of this ply, this range varies with the waviness of the stress solutions, until it reaches a magnitude of about 6 MPa at the ply interface. At this position, the difference between the upper and lower bounds of the stress solutions of the inner ply is slightly larger, with a magnitude of roughly 7 MPa. This range rapidly decreases away from the ply interface, to a value of around 1 MPa, at the normalised radial position of -0.62, and is thereafter somewhat maintained through to the inner surface of the pipe.

The corresponding hoop stress distributions of the reduced data set, associated with the 900 possible combinations of the polynomial pairs fitted to the simulated strain variations of Figs. M.8 and M.9, are presented in Fig. M.12. These stress distributions are colour coded according to the order of polynomial fitted to the circumferential strain variations to which they correspond, and comprise splines fitted to the stresses evaluated at the mid-radius of 50 layers numerically simulated to be removed. As has been discussed, this was done to better resolve the residual radial stress distributions of the laminated pipes, but also allows a better estimate of the other stress components to be obtained, especially in regions where they may vary quite rapidly. Due to the decreased amount of data points describing each of the simulated strain responses of this data set, the bounds of the stress distributions of Fig. M.12 lie significantly further apart than those of the hoop stress distributions of the full data set, illustrated in Fig. M.5. Over the region of the outer ply, the upper and lower bounds in the stress distributions of Fig. M.12 are defined by 3rd

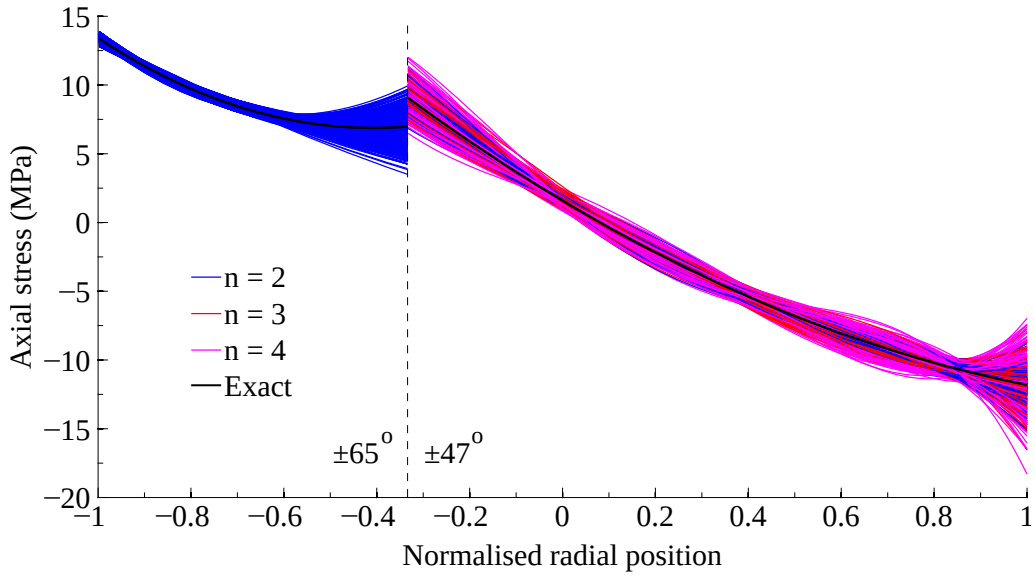

Figure M.11: Axial stress variations for the reduced data set of the ±65°/±47° pipe

and 4th order solutions. At the outer surface, the magnitude of the difference between these bounds is roughly 18 MPa. This range rapidly decreases away from this surface to a magnitude of about 3 MPa at the normalised radial position of about 0.85. Between this point, and the normalised radial position of 0.1, the difference between the upper and lower bounds varies with the waviness of the stress solutions, but never exceeds 7 MPa. Towards the ply interface, there is a significant increase in the sensitivity of this stress component to the simulated scatter, and the difference between the bounds in stress increases to a maximum of roughly 20 MPa. Over the inner ply, the difference between the bounds in stress at the ply interface is around 18 MPa. Away from this region, this range rapidly decreases, and reaches a value of around 3 MPa at the normalised radial position of -0.6. Between this point and the inner surface of the pipe, the difference between the upper and lower bounds in stress varies slightly, but never exceeds about 3.5 MPa.

The 900 radial stress distributions of the reduced data set of the ±65°/±47° pipe, associated with the possible combinations of the polynomial pairs fitted to the simulated strain variations of Figs. M.8 and M.9, are illustrated in Fig. M.13. These are plotted together with the "exact" stress distribution, associated with the "exact" strain response of this data set. Each solution in stress is colour coded according to the order of polynomial fitted to the circumferential strain variation to which it corresponds. As required, the each stress distribution is continuous over the ply interface, and tends to zero at the inner and outer surfaces of the pipe. For reasons already discussed, the upper and lower bounds of the stress solutions lie significantly further apart than those of the radial stress distributions obtained for the simulated strain variations of the full data set, shown in

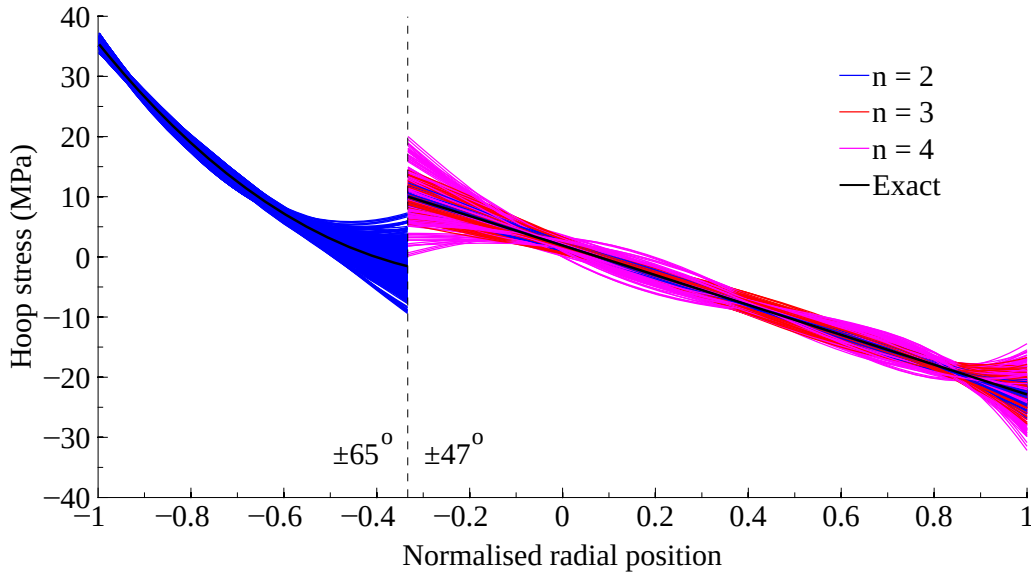

Figure M.12: Hoop stress variations for the reduced data set of the ±65°/±47° pipe

Fig. M.6. Over the region corresponding to the outer ply, the difference between the upper and lower bounds in stress increases rapidly from zero at the outer surface of the pipe, to approximately 0.2 MPa at the normalised radial position of 0.8. This range is maintained through to the normalised radial position of about 0.2, and then increases to a maximum of 0.4 MPa at the ply interface. Over the inner ply, the difference between the upper and lower bounds in stress decreases rapidly from the ply interface, to a value of close to 0.2 MPa at the normalised radial position of about -0.5. Thereafter, this range gradually decreases down to zero at the inner surface of the pipe.

The 2700 shear stress distributions, associated with the possible combinations of the 2nd to 4th order polynomial pairs fitted to the simulated axial, circumferential and 45° strain variations of Figs. M.8 to M.10, are illustrated in Fig. M.14. These are colour coded according to the order of polynomial fitted to the 45° strain data of Fig. M.10 to which they correspond. As with the axial, hoop and radial stress results, the upper and lower bounds of the stress distributions of Fig. M.14 lie significantly further apart than those obtained for the shear stress distributions of the full data set, shown in Fig. M.7. Additionally, these bounds do not lie symmetrically about the "exact" solution. Over the outer ±47° ply, the bounds of the 2nd order solutions lie closest to the "exact" stress distribution. The bounds of the 3rd order solutions lie further apart, and demonstrate a higher level of waviness. Over the majority of the thickness of this ply, the bounds of the 4th order solutions lie furthest from the "exact" distribution, and are significantly more wavy than the 2nd and 3rd order solutions. All solutions, however, oscillate about the expected zero-stress state, associated with the filament-wound nature of the pipe. The difference between the

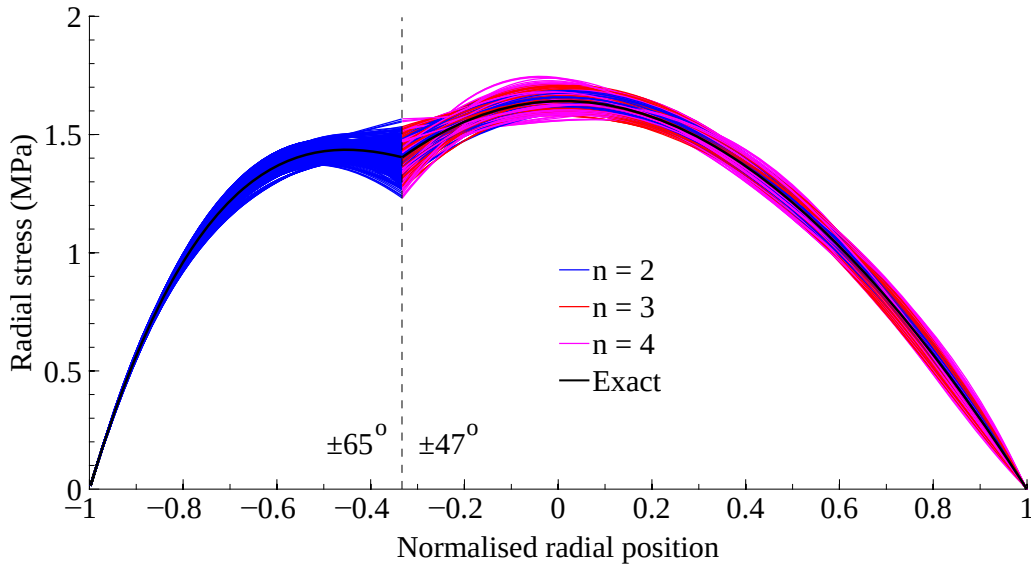

Figure M.13: Radial stress variations for the reduced data set of the ±65°/±47° pipe

upper and lower bounds at the outer surface is in the region of 24 MPa. Away from outer surface, this range rapidly decreases to less than 4 MPa at the normalised radial position of about 0.83. Over the remainder of the pipe this range varies with the waviness of the stress solutions, until it reaches a final value of roughly 14 MPa at the ply interface. For the inner ply, the magnitude of the difference between the upper and lower bounds in stress at the ply interface is about 23 MPa, which is similar sensitivity to that seen at the outer surface of the pipe. This range then decreases rapidly to a value close to 3 MPa at the normalised radial position of -0.58. For the remainder of the thickness of the inner ply, the difference between the upper and lower bounds in stress never exceeds 5 MPa. Between the ply interface and the normalised radial position of -0.6, the majority of the solutions in stress do not oscillate about the expected zero-stress state, but these do approach this value closer to the inner surface. All solutions, however, adhere to the zero-torque equilibrium requirement, a consequence of the self-correcting nature of the current method of residual stress measurement.

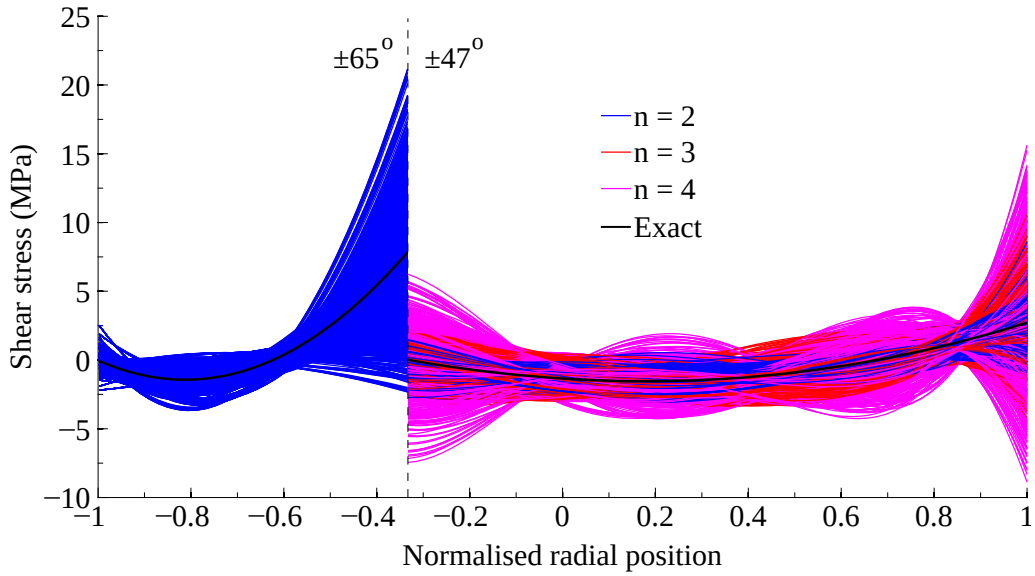

Figure M.14: Shear stress variations for the reduced data set of the ±65°/±47° pipe

M.2 ±75°/±36° Filament-wound pipe

M.2.1 Full data set

Strain simulations

The 100 simulated axial strain variations of the full data set of the ±75°/±36° pipe are illustrated in Fig. M.15. Included in this figure are the different polynomial pairs fitted to each variation. These comprise 3rd and 4th order polynomials fitted to the data corresponding to removal of material from the outer ply, along with 3rd order polynomials fitted to the data corresponding to removal of material from the inner ply. Polynomials of 2nd order were not considered for the region of material removal from the outer ply, since these did not adequately fit the simulated data. Also included in Fig. M.15 is the "exact" 4th and 3rd order polynomial pair, fitted to the measured data of this gauge set, seen in Fig. 8.17. For the first 15% of the thickness removed, the vast majority of 3rd order polynomial fits lie below the "exact" strain variation. Additionally, many of these fits lie beyond the lower bounds of the simulated data points for this region. A large variation between the resulting axial stress distributions in the region of the outer surface of the pipe can thus be expected. The magnitude of the difference between the upper and lower bounds of the polynomial fits increases rapidly from zero, at 0% material removed to roughly 18 $\mu\epsilon$ for about 7% thickness removed. This range then decreases to around 12 $\mu\epsilon$ at 20% thickness removed. From this point the difference between the bounds of the fits gradually increases to approximately 50 $\mu\epsilon$, at the region of the ply interface.

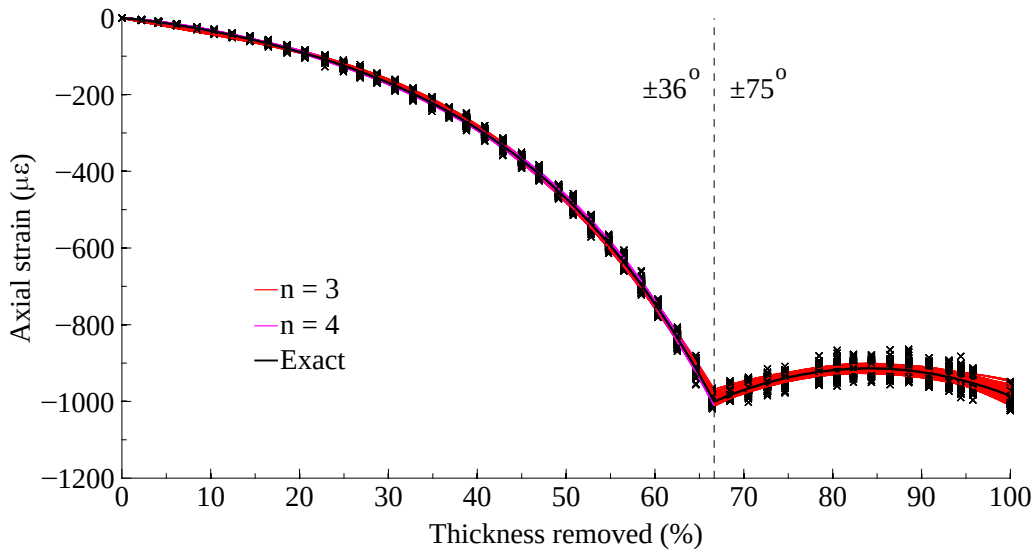

Figure M.15: Simulated axial strain variations and polynomial fits for the full data set of the ±75°/±36° pipe

Between about 16% and 65% thickness removed, all the polynomial fits lie relatively close to the "exact" strain variation, well within the bounds of the simulated data points. The same can be said for the region corresponding to removal of material from the inner ply. The difference between the upper and lower bounds of the polynomial fits decreases from 50 $\mu\epsilon$ at the region corresponding to the ply interface, to about 28 $\mu\epsilon$ at 80% thickness removed. This is significantly smaller than the 100 $\mu\epsilon$ range formed by the simulated data points for this region. As more material is removed, the difference between the bounds of the polynomial fits increases gradually to marginally less than 40 $\mu\epsilon$, for 95% thickness removed, and thereafter increases fairly rapidly to around 75 $\mu\epsilon$ for the region of material removal at the inner surface.

The 100 simulated circumferential strain variations of the full data set of the ±75°/±36° pipe are presented in Fig. M.16. The scatter in the simulated data increases with increased material removal from the outer ply, but is almost constant for removal of material from the inner ply. This behaviour is governed by the SD variation for the circumferential strain gauge of this pipe, presented in Appendix L, which tends to asymptote toward a constant SD value. Included in Fig.M.16 are the different polynomial pairs fitted to the simulated strain variations. For each simulation, 2nd to 5th order polynomials were fitted to the data corresponding to the removal of material from the outer ±36° ply. The 5th order polynomials were included since the "exact" strain variation was of the same order. The corresponding polynomials fitted to the data for removal of material from the inner ±75° ply were all constrained to 2nd order, the same as that of the "exact" strain variation. Over the region corresponding to the outer ply, there is a notable distinction

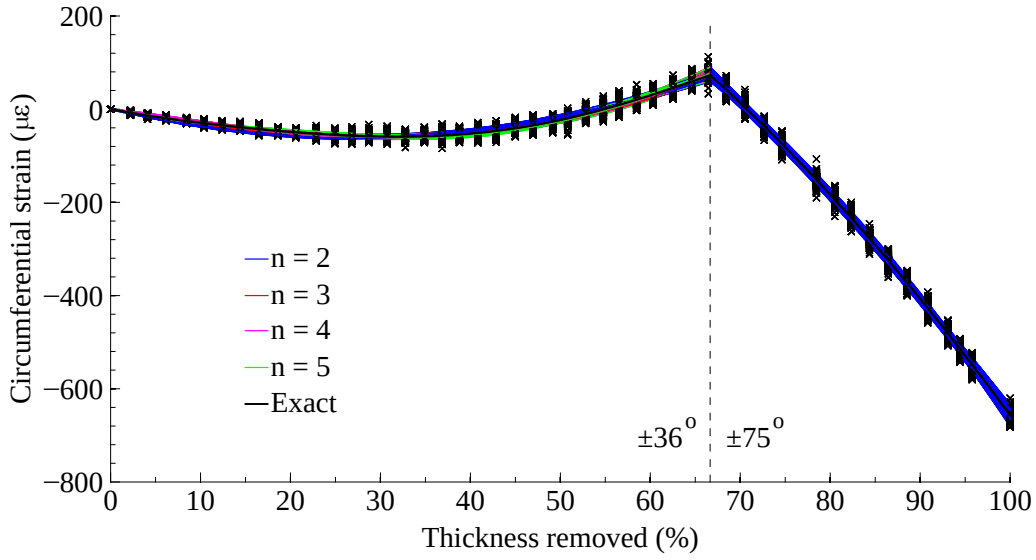

Figure M.16: Simulated circumferential strain variations and polynomial fits for the full data set of the ±75°/±36° pipe

between the trends of the different order polynomials. The magnitude of the difference between the upper and lower bounds of these fits increases from zero, at 0% material removed, to close to 20 $\mu\epsilon$ for 20% thickness removed, followed by a slight decrease down to 15 $\mu\epsilon$ at 30% thickness removed. Thereafter, this range increases to slightly less than 20 $\mu\epsilon$ at about 43% thickness removed, and is roughly maintained through to around 60% thickness removed. From this point onwards, the magnitude of the difference between the bounds of the fits increases fairly rapidly to about 38 $\mu\epsilon$ in the region corresponding to material removal at the ply interface. For the removal of material from the inner ±75° ply, the magnitude of the difference between the upper and lower bounds of the 2nd order polynomial fits decreases to less than 30 $\mu\epsilon$, at around 70% thickness removed, and this range is somewhat maintained through to 95% thickness removed. Between this point and 100% material removed, the difference between the upper and lower bounds of the polynomial fits increases to about 50 $\mu\epsilon$.

The 100 simulated 45° strain variations of the full data set of the ±75°/±36° pipe are illustrated in Fig. M.17. Included in this figure are the polynomials fitted to each of these variations. These polynomials were constrained between 3rd and 4th order for the region of material removal from the outer ±36° ply, and limited to only 2nd order for the region of removal of material from the inner ±75° ply. As with the axial strain variations of this pipe, 2nd order polynomials were not considered for the region corresponding to removal of material from the outer ply since these did not adequately fit the data for this region. Also included in Fig. M.17 is the "exact" 4th and 2nd order polynomial pair fitted to the measured data of this data set, originally presented Fig. 8.19. As previously discussed,

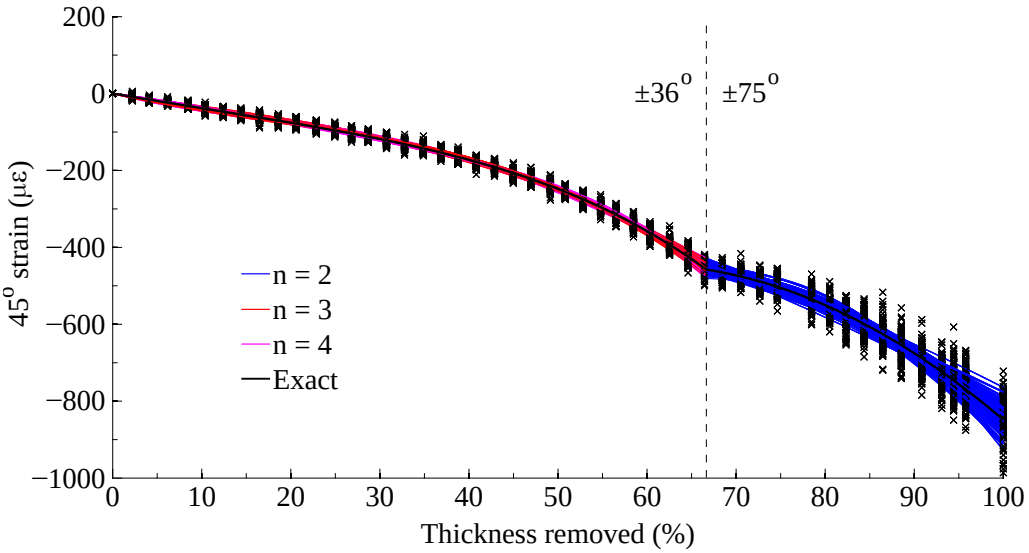

Figure M.17: Simulated 45° strain variations and polynomial fits for the full data set of the ±75°/±36° pipe

this is the strain variation to which scatter was added to generate each of the simulated strain distributions. Over the entire range of material removal, the upper and lower bounds of the simulated data points lie well beyond the bounds of the polynomial fits. This behaviour is directly associated with the large number of data points describing each simulated strain variation, which constrains the polynomial fits to lie close to the "exact" distribution. The difference between the upper and lower bounds of the simulated data points increases gradually from about 30 $\mu\epsilon$ at about 2% thickness removed, to slightly less than 100 $\mu\epsilon$ in region of material removal from the ply interface. Thereafter, the magnitude of the scatter rapidly increases to close to 300 $\mu\epsilon$ for 100% material removed. This behaviour is a direct result of the large increase of the SD of the experimental scatter for the 45° strain gauge orientation of this pipe. This SD variation which constrains the magnitude of the simulated scatter, is illustrated in Appendix L. Referring to Fig. M.17, for the region corresponding to removal of the outer ply, the trends in the 3rd and 4th order polynomial fits are very similar. The magnitude of the difference between the upper and lower bounds of these fits increases gradually from zero, at 0% material removed, to roughly 20 $\mu\epsilon$ at 15% thickness removed. This range is more or less maintained through to around 45% thickness removed. From this point the difference between the bounds of the fits increases until a magnitude of about 25 $\mu\epsilon$ is reached for 52% thickness removed, and this value is somewhat maintained through to 60% thickness removed. Thereafter, this range increases fairly rapidly to a magnitude of 60 $\mu\epsilon$ at the region corresponding to removal of material from the ply interface. For removal of material from the inner ply, the difference between the upper and lower bounds of the polynomials fits decreases slightly to about 50 $\mu\epsilon$, at 70% thickness removed, and then increases again to more than 65 $\mu\epsilon$ at

80% thickness removed. Thereafter, this range decreases to around 50 $\mu\epsilon$ at roughly 87% thickness removed, followed by a final rapid increase to a value of approximately 200 $\mu\epsilon$ at 100% material removed.

Residual stress distributions

The 800 residual axial stress distributions of the full data set of the $\pm75^\circ/\pm36^\circ$ pipe, consequence of the possible combinations of the polynomial pairs fitted to the simulated axial and circumferential strain variations of Figs. M.15 and M.16, are illustrated in Fig. M.18. For illustrative purposes, this figure has already been presented in the form of Fig. 10.27 in the main body of this thesis, but is further discussed in this Appendix. As previously discussed, due to the bulk-scale orthotropic material properties, these stresses depend only on the axial and circumferential strain responses. Each stress distribution is colour coded according to the order of polynomial fitted to the simulated axial strain response of Fig. M.15 to which it corresponds, and comprises splines fitted to the stresses evaluated at the mid-radius of each removed layer. Due to the self-correcting nature of the current method of residual stress measurement, all solutions adhere to the requirement of self-equilibrium. Over the outer $\pm36^\circ$ ply, there is a clear distinction between the trends of the 3rd and 4th order solutions. At the outer surface, the majority of the 3rd order stress solutions are more compressive than the 4th order solutions, which lie almost symmetrically about the "exact" stress distribution. The difference between the upper and lower bounds of the stresses is greatest for this region, with a value of roughly 7.5 MPa. The magnitude of this range rapidly decreases to approximately 1.5 MPa, at the normalised radial position of 0.87, and then increases with the waviness of the stress solutions, to about 2.5 MPa at the normalised radial position of 0.65. Toward the normalised radial position of about 0.38, the difference between the upper and lower bounds of the stress solutions decreases to more or less 1.3 MPa, and then increases to approximately 2.5 MPa at the region of the ply interface. Within the inner ply of this pipe, the magnitude of the difference between the upper and lower bounds of the stress solutions at the ply interface is slightly larger than 2.5 MPa. This value, however, rapidly decreases to less than 1 MPa at the normalised radial position of around -0.56, and is roughly maintained through to the inner surface of the pipe.

The residual hoop stress distributions of the full data set of the $\pm75^\circ/\pm36^\circ$ pipe, associated with the 800 possible combinations of the polynomial pairs fitted to the simulated strain variations of Figs. M.15 and M.16, are plotted in Fig. M.19. Included in this figure is the "exact" hoop stress distribution, associated with the "exact" strain variations of this

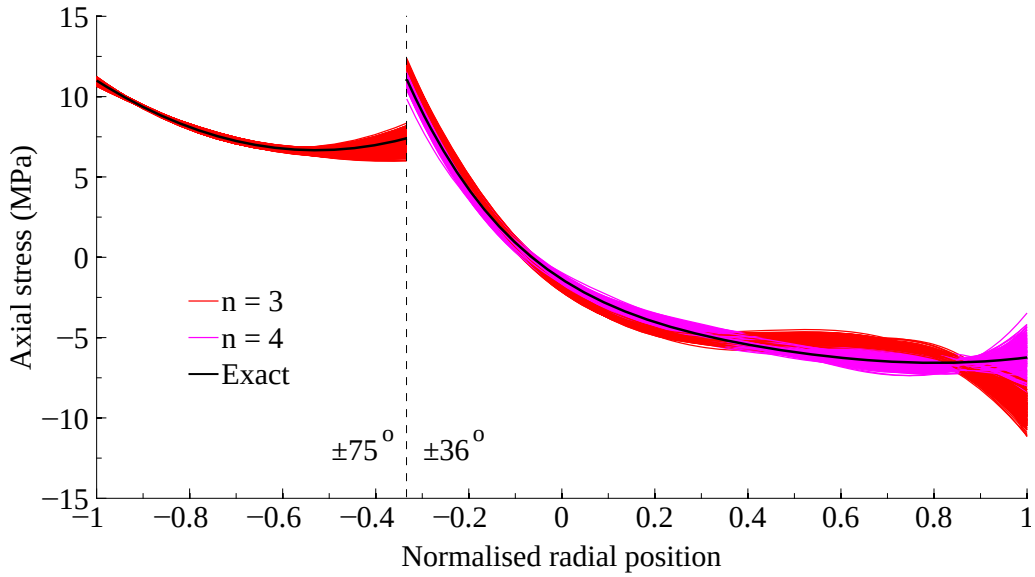

Figure M.18: Axial stress variations for the full data set of the ±75°/±36° pipe

data set. All stress solutions adhere to the requirement of self-equilibrium, and are colour coded according to the order of polynomial fitted to the circumferential strain data to which they correspond. Over much of the thickness of the outer ±36° ply, the trends of the 3rd and 4th order solutions are very similar. These are, however, clearly distinguishable from the trends of the 2nd and 5th order solutions. Although "exact" stress distribution is a 5th order solution, the trend of this is very similar to those of the 3rd and 4th order solutions. At the outer surface of the pipe, the 5th order solutions fan out and lie over the full range of stresses. The more compressive stresses are dominated by 2nd order solutions, while the least compressive stresses comprise mostly 4th order solutions. The difference between the upper and lower bounds for this region is roughly 10 MPa, which is very similar to the sensitivity seen by the hoop stress distributions of the full data set of the ±65°/±47° pipe, shown in Fig. M.5. This range rapidly decreases away from the outer surface, and fluctuates with the waviness of the stress solutions. Between the normalised radial positions of 0.85 and -0.15, however, the magnitude of the difference between the upper and lower bounds in stress never exceeds 5 MPa. As the ply interface is approached, the sensitivity of the stress solutions to scatter increases, and the magnitude of the difference between the upper and lower bounds in stress increases to approximately 12 MPa in this region. This value is larger than that obtained at the outer surface of the pipe, and can be attributed to the presence of the 5th order solutions. In this region, the majority of the 5th order solutions become more compressive than the lower order solutions and form a range of about 3 MPa. The absence of these solutions would reduce the difference between the upper and lower bounds in this region less than 10 MPa. This behaviour emphasises the care that must be taken when considering high order polynomial

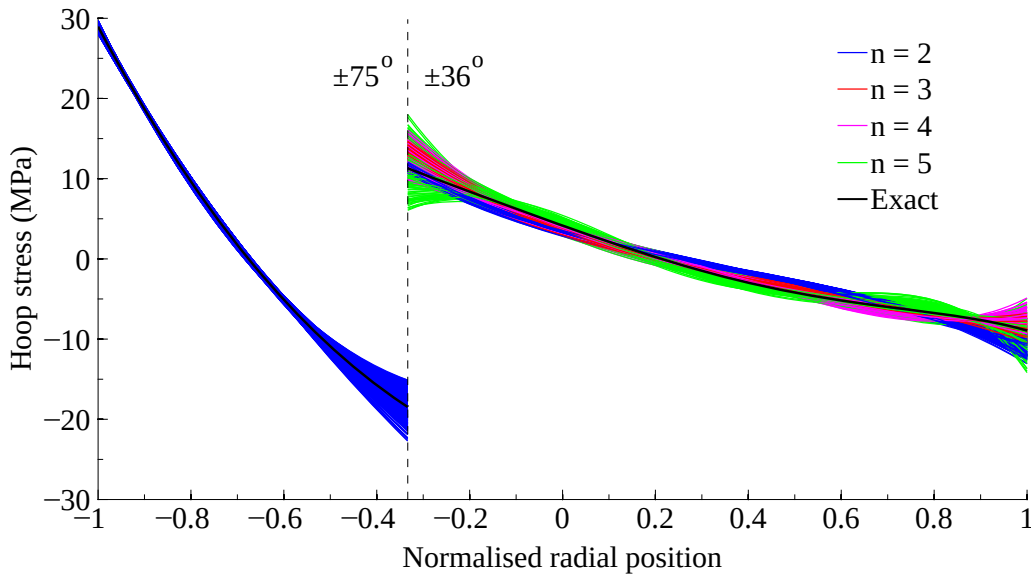

Figure M.19: Hoop stress variations for the full data set of the ±75°/±36° pipe

fits. These not only introduce unwanted waviness in the stress solutions, but also increase the level of uncertainty. For the inner ±75° ply, the difference between the upper and lower bounds of the 2nd order solutions at the ply interface is around 7 MPa, and this discrepancy rapidly decreases to about 2 MPa at the normalised radial position of roughly -0.58. Over the remainder of this ply, this range is roughly maintained, with minimal fluctuation.

The corresponding 800 residual radial stress distributions are illustrated in Fig. M.20. Each solution is colour coded according to the order of polynomial fitted to the simulated circumferential strain data of Fig. M.16 to which it corresponds. As required, these stresses all tend to zero at the inner and outer surfaces of the pipe, and are continuous over the ply interface. Over much of the thickness of the outer ply, the 2nd order solutions form notably distinguishable trends from the other solutions, and define the upper bound between the normalised radial positions of 1 to about 0.4. Further toward the ply interface, these solutions cross over the "exact" stress distribution to define the lower bounds in stress between the normalised radial positions of about 0.3 and -0.15. The 3rd to 5th order solutions all display very similar trends over much of the thickness of the outer ply, but between the normalised radial positions of 1 and 0.75, the 4th order solutions clearly define the lower bounds of the stress distributions. The magnitude of the difference between the upper and lower bounds in stress increases from zero, at the outer surface of the pipe, to about 0.1 MPa at the normalised radial position of 0.2, where the peak radial stress of the outer ply occurs. This range decreases slightly to a value of about 0.08 MPa at the normalised radial position of about -0.2, and then increases to a maximum of slightly less than 0.12 MPa at the ply interface. Over the inner ply, the difference between the

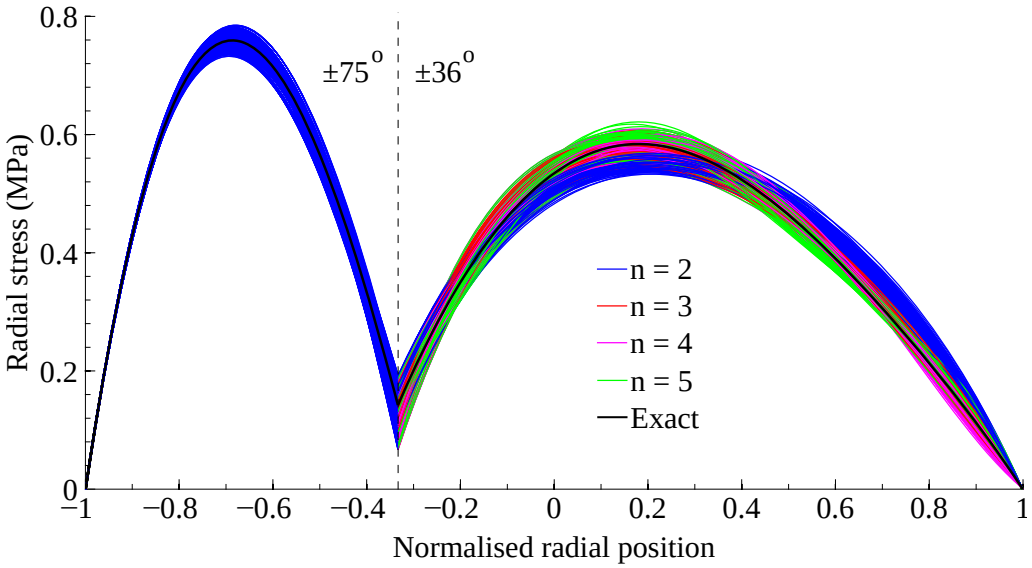

Figure M.20: Radial stress variations for the full data set of the ±75°/±36° pipe

upper and lower bounds decreases to roughly 0.05 MPa, at the normalised radial position of about -0.7, where the peak stress of this ply occurs, and thereafter rapidly decreases to zero at the inner surface of the pipe.

The in-plane shear stress distributions of the ±75°/±36° pipe, associated with the 1600 possible combinations of polynomial pairs fitted to the simulated strain data of Figs. M.15 to M.17, are presented in Fig. M.21. Each stress distribution is colour coded according to the order of polynomial fitted to the simulated 45° strain data to which it corresponds. Included in Fig. M.21 is the "exact" stress distribution, plotted as the thick black lines. The upper and lower bounds of the stress solutions do not lie symmetrically about the "exact" stress distribution, but all solutions oscillate about the zero-stress line, which is expected to exist because of the filament-wound nature of this pipe. Over much of the outer ply, there is no clear distinction between the trends of the 3rd and 4th order solutions. The difference between the upper and lower bounds of these distributions is maximum at the outer surface, with a value of close to 9 MPa. This value is smaller than the difference of about 14 MPa between the upper and lower bounds in shear stress obtained at the outer surface of the ±65°/±47°, illustrated in Fig. M.7. This range rapidly decreases to approximately 1.5 MPa at the normalised radial position of 0.85, and thereafter fluctuates with the waviness of the solutions toward the ply interface. Over this region the magnitude of this range rarely exceeds 3 MPa. For the inner ±75° ply, the difference between the upper and lower bounds at the ply interface is marginally larger than 5 MPa, but this magnitude rapidly decreases to close to 1 MPa, towards the normalised radial position of -0.58. Over the remaining thickness of this ply, the difference between the upper and lower bounds in stress fluctuates slightly, until it reaches a final value of about 2 MPa at

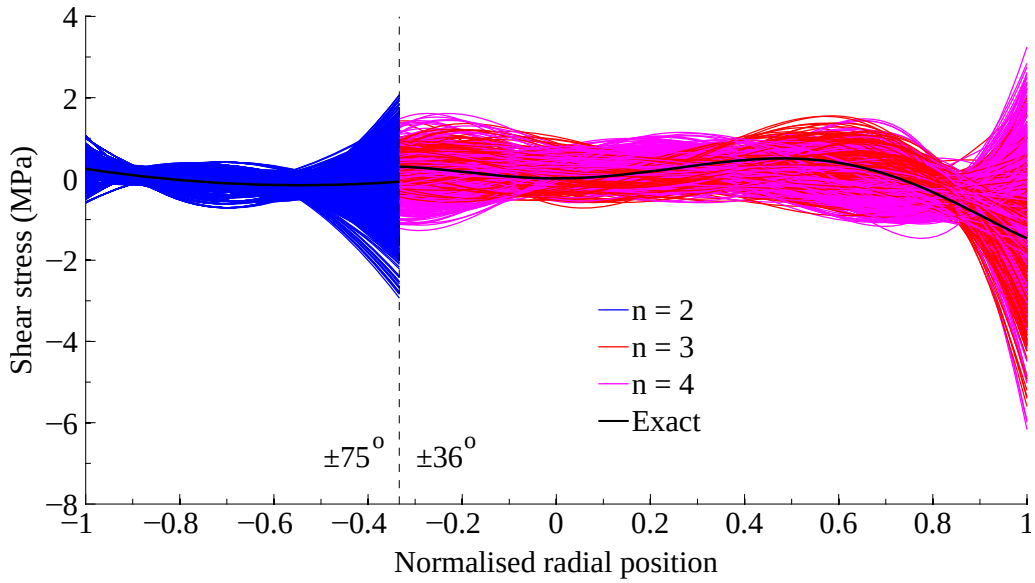

Figure M.21: Shear stress variations for the full data set of the ±75°/±36° pipe

the inner surface of the pipe.

M.2.2 Reduced data set

Strain simulations

The 100 simulated axial strain variations of the reduced data set of the ±75°/±36° pipe are presented in Fig. M.22. These distributions were simulated by addition of scatter to the "exact" strain response, taken as the polynomial pair fitted to the measured data of this data set, illustrated in Fig. 9.12. The scatter added to this distribution was constrained by the same SD variation utilised for the axial strain simulations of the full data set, seen in Fig. M.15. Included in Fig. M.22 are the polynomial pairs fitted to the each of the simulated strain responses. The fits corresponding to removal of material from the outer ±36° ply were limited to 3rd and 4th order, the latter being the same as that of the "exact" strain variation, while the polynomials fitted to the data corresponding to removal of material from the inner ±75° ply were constrained to only 2nd order. Over the entire range of material removal, the bounds of the polynomial fits lie significantly further apart than those of Fig. M.15, and almost entirely engulf the simulated data points. As previously discussed, this behaviour is a direct result of the reduced number of data points describing each simulated strain variation of this data set, and the polynomial fits are therefore less constrained to lie close to the "exact" strain response. Between 0% and 7% thickness removed, the difference between the upper and lower bounds of the fits increases

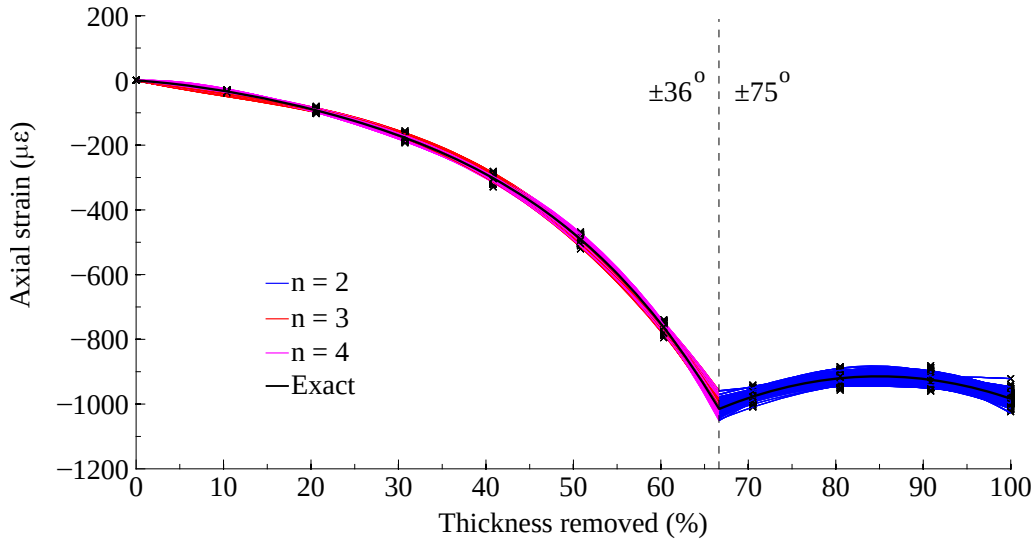

Figure M.22: Simulated axial strain variations and polynomial fits for the reduced data set of the ±75°/±36° pipe

rapidly from zero to greater than 30 $\mu\epsilon$. This range then decreases slightly to around 20 $\mu\epsilon$, at 20% thickness thickness removed, followed by an increase to close to 100 $\mu\epsilon$ at the region corresponding to material removal at the ply interface. The upper and lower bounds of the polynomial fits, for removal of material from the majority inner ±75° ply, lie almost symmetrically about the "exact" strain response. The difference between these bounds decreases to approximately 60 $\mu\epsilon$ at roughly 72% thickness removed. This range increases gradually to about 70 $\mu\epsilon$ at 85% thickness removed, followed by a decrease down to 60 $\mu\epsilon$ at 95% thickness removed. Between this point and 100% material removed, the range formed by the majority of the polynomial fits increases to about 80 $\mu\epsilon$. There is, however, a single polynomial fit defining the upper bound, which increases this range to more than 110 $\mu\epsilon$.

The simulated circumferential strain responses of the reduced data set of the ±75°/±36° pipe are illustrated in Fig. M.23. This figure includes the polynomial pairs fitted to each of the simulated variations. The polynomials fitted to the data corresponding to removal of material from the outer ply were varied between 2nd and 4th order, while the polynomials fitted to the data corresponding to the inner ply were limited to 2nd order. Also included in Fig. M.23 is the "exact" strain response, comprised of the 2nd order polynomials fitted to the measured data of this data set, initially presented in Fig. 9.12. This variation formed the basis upon which the scatter was added to produce each simulated strain distribution of Fig. M.23. The majority of the simulated data points lie within the bounds of the polynomial fits, and these bounds lie significantly further apart than those of the polynomials fitted to the simulated circumferential strain variations of the full data set

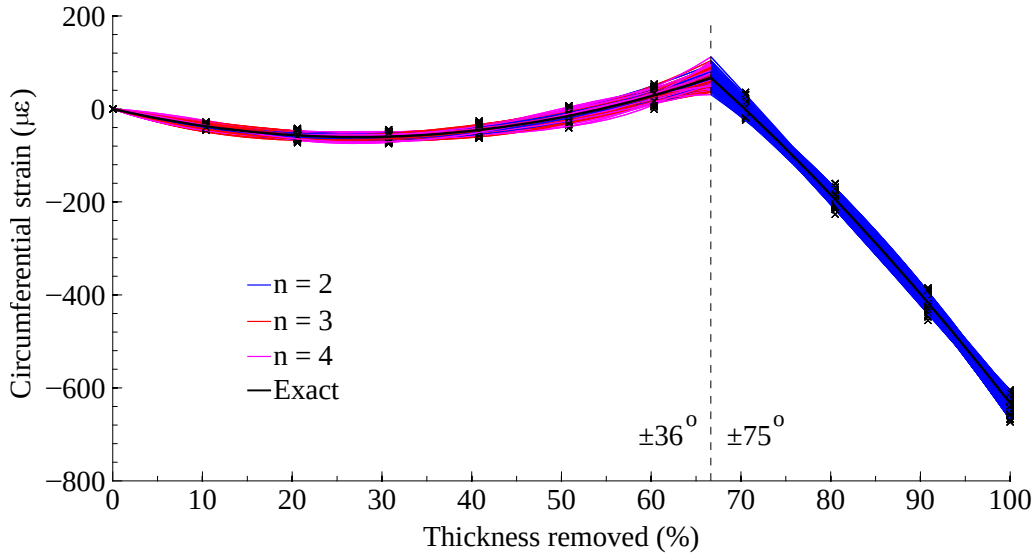

Figure M.23: Simulated circumferential strain variations and polynomial fits for the reduced data set of the ±75°/±36° pipe

shown in Fig. M.16. For removal of material from the outer ply, the magnitude of the difference between the upper and lower bounds of the fits increases fairly rapidly from zero, at 0% material removal, to more than 30 $\mu\epsilon$ at 10% of the thickness removed. From this point, this difference increases gradually to more than 80 $\mu\epsilon$ for removal of material at the ply interface. For removal of material from the inner ply, the magnitude of the difference between the bounds of the polynomial fits decreases to about 40 $\mu\epsilon$ at 75% thickness removed. This range then increases to close to 50 $\mu\epsilon$ for 85% thickness removed, followed by a decrease to 40 $\mu\epsilon$ at close to 95% thickness removed. Over the final 5% of the thickness removal, the difference between the upper and lower bounds of the polynomial fits increases to more than 70 $\mu\epsilon$.

The 100 simulated 45° strain variations of the reduced data set are illustrated in Fig. M.24. These were generated by addition of scatter to the "exact" 3rd and 2nd order polynomial pair fitted to the measured variation of this data set, illustrated in Fig. 9.12. Included in Fig. M.24 are the polynomial pairs fitted to the simulated data. As with the 45° simulations of the full data set, illustrated in Fig. M.17, the polynomials fitted to the data corresponding to removal of material from the outer ±36° ply were constrained to 3rd and 4th order, while those fitted to the data associated with removal of material from the inner ±75° ply were limited to only 2nd order. For reasons already discussed, the bounds of these polynomial fits, over the full range of material removal, lie considerably further apart than those fitted to the simulated 45° data of the full data set, and nearly encompass all of the simulated data points. The magnitude of the difference between the upper and lower bounds of these fits increases rapidly from zero, at 0% material removed, to about 40 $\mu\epsilon$

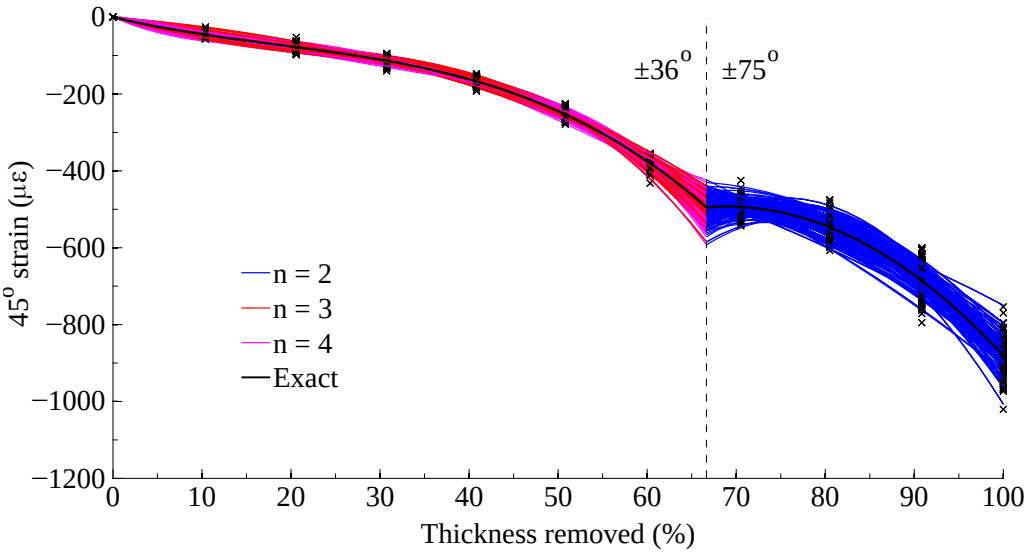

Figure M.24: Simulated 45° strain variations and polynomial fits for the reduced data set of the ±75°/±36° pipe

at close to 8% thickness removed. This value decreases slightly to approximately 30 $\mu\epsilon$ towards 25% of the thickness removed, followed by a gradual increase to around 50 $\mu\epsilon$ at 50% thickness removed. Between 55% thickness removed and the region corresponding to removal of material at the ply interface, the difference between the upper and lower bounds of the polynomial fits increases rapidly to about 170 $\mu\epsilon$. Over the region of material removal from the inner ply, the magnitude of the difference between the bounds of the fits rapidly decreases to around 90 $\mu\epsilon$ at roughly 73% thickness removed. This range then increases to a magnitude of more than 110 $\mu\epsilon$ for 80% of the wall thickness removed. For the majority of the strain fits, this range decreases slightly to around 100 $\mu\epsilon$ at 95% thickness removed, followed by an increase to the value of just less than 180 $\mu\epsilon$ for removal of material at the inner surface. There are, however, a handful of polynomial fits that lie beyond these bounds. The magnitude of the difference between these fits for 100% material removed is about 260 $\mu\epsilon$.

Residual stress distributions

The residual axial stress distributions of the reduced data set of the ±75°/±36° pipe are illustrated in Fig. M.25. This figure comprises 600 stress distributions, associated with the possible combinations of the polynomials fitted to the simulated axial and circumferential strain variations of Figs. M.22 and M.23, respectively. Each stress distribution is colour coded according to the order of polynomial fitted to the axial strain data to which it corresponds. Included in Fig. M.25 is the "exact" residual stress distribution, associated

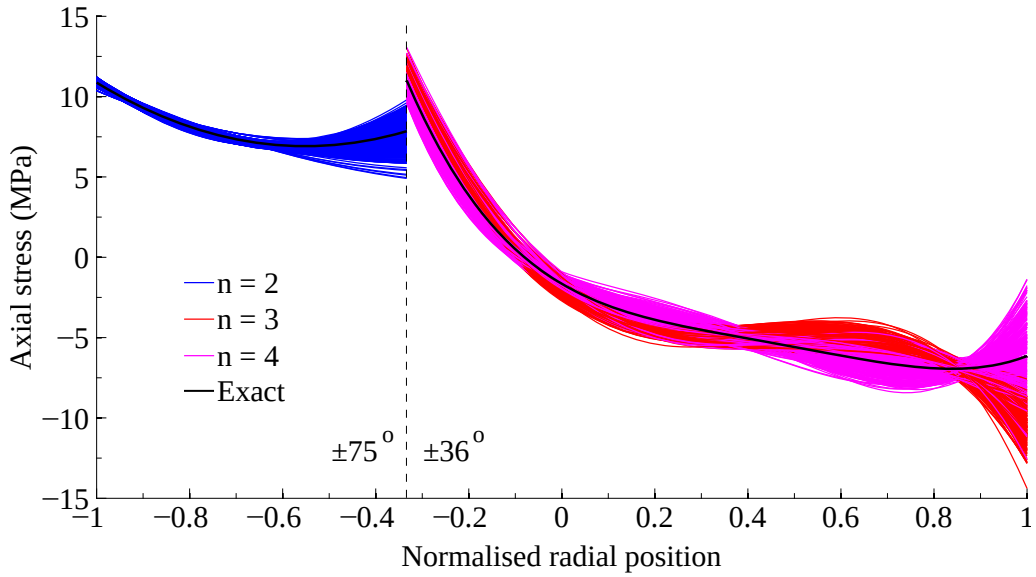

Figure M.25: Axial stress variations for the reduced data set of the ±75°/±36° pipe

with the "exact" strain variations of this data set. As with the axial stress results of the full data set, seen in Fig. M.18, the majority of the 3rd and 4th order solutions over the outer ±36° ply form trends that are clearly distinguishable from one another. The magnitude of the difference between the upper and lower bounds of these solutions is largest at the outer surface, with a value of roughly 13 MPa. This is nearly double the magnitude of the difference between the bounds of stress distributions of the full data set, shown in Fig. M.18, for this region. As previously discussed, this behaviour is a direct result of the increased range of the polynomials fitted to the simulated strain variations of the reduced data set, associated with the reduction in the number of data points describing each of these variations. The difference between the bounds of the stress distributions of Fig. M.25 rapidly decreases away from the outer surface, to less than 2 MPa at the normalised radial position of about 0.87. This range then increases to around 8 MPa at the normalised radial position of 0.67, and continues to vary with the waviness of the stress solutions until it reaches a value of slightly less than 4 MPa at the normalised radial position of -0.2. As more material is removed the magnitude of this range is more or less maintained through to the ply interface. In this region, the magnitude of the difference between the bounds of the stress solutions over the inner ply is roughly 5 MPa. This range rapidly decreases to approximately 1.2 MPa toward the normalised radial position of -0.63, and thereafter, is somewhat maintained through to the inner surface of the pipe.

The corresponding residual hoop stress distributions of the reduced data set of the ±75°/±36° pipe are illustrated in Fig. M.26. These are colour coded according to the order of polynomial fitted to the circumferential strain data of Fig. M.23 to which they correspond, and are plotted together with the "exact" stress distribution, associated with the "exact"

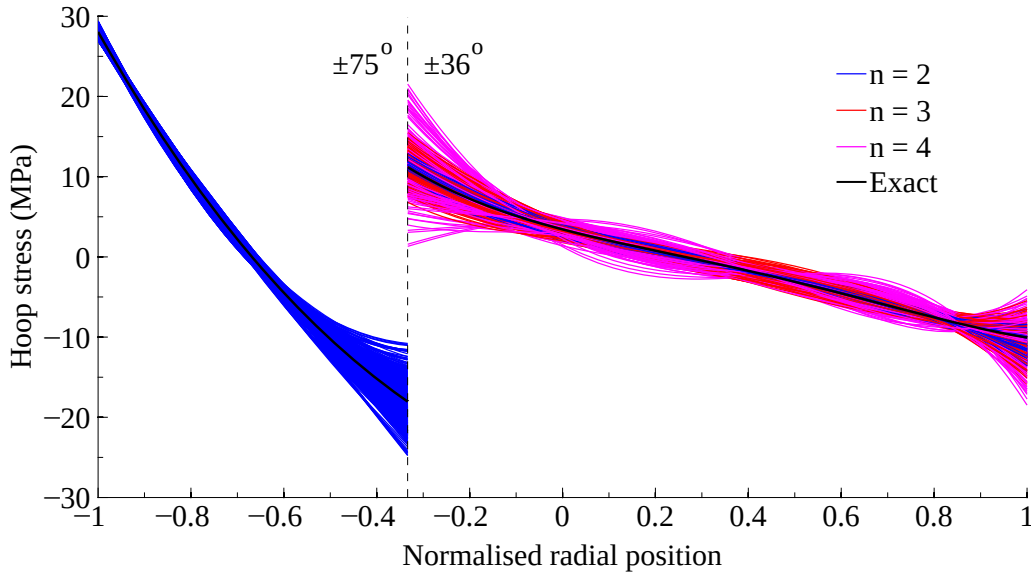

Figure M.26: Hoop stress variations for the reduced data set of the ±75°/±36° pipe

strain variation of this data set. Over the entire wall thickness of the pipe, the bounds of the stress solutions lie significantly further from the "exact" distribution, as compared to those of the the hoop stress results of the full data set, illustrated in Fig. M.19. This behaviour is a direct result of the reduction in the number of data points describing the strain variations of the reduced data set, which adversely affects the uncertainty in the resulting stress distributions. Although there is no clear distinction between the trends of the different order solutions over the outer ±36° ply, it is clear that the waviness of these increases with increased polynomial order. Over most of this ply thickness, the upper and lower bounds are defined almost entirely by 4th order solutions. At the outer surface, the magnitude of the difference between these bounds is close to 15 MPa, about 5 MPa greater than that obtained at the same region for the full data set. This range rapidly decreases to around 3 MPa, at the normalised radial position of 0.82, and then fluctuates with the waviness of the stress solutions between this point and the normalised radial position of -0.1. Within this region, the difference between the bounds never exceeds 6 MPa. There is a significant increase in the sensitivity of the solutions to the simulated scatter toward the ply interface, where the difference between the upper and lower bounds of these solutions increases rapidly to roughly 20 MPa. For the stress solutions over the inner ply, the difference between the upper and lower bounds is a maximum at the ply interface, with a magnitude of just less than 15 MPa. This range quickly decreases to approximately 3 MPa at the normalised radial position of -0.6, and is approximately maintained, with minimal fluctuation, over the remainder of this ply.

The 600 residual radial stress distributions of the reduced data set of the ±75°/±36° pipe, associated with the possible combinations of the polynomial pairs fitted to the simulated axial and circumferential strain variations of Figs. M.22 and M.23, are illustrated in Fig. M.27. As with the radial stress distributions of the ±55° and ±65°/±47° pipes, each solution in stress is colour coded according to the order of polynomial fitted to the circumferential strain data to which it corresponds. Over the majority of the wall thickness of the pipe, the magnitude of the difference between the upper and lower bounds of these solutions is significantly greater than the difference between the bounds of the radial stress distributions of the full data set, illustrated in Fig. M.20. This is a direct result of the reduction in the number of data points describing each simulated strain variation of this data set. From the outer surface, to the normalised radial position of 0.8, the magnitude of the difference between the bounds in stress increases rapidly from zero to about 0.14 MPa. This range is roughly maintained through to the normalised radial position of about 0.1. From this point, a handful of outlying solutions cause this range to increase to approximately 0.2 MPa at the normalised radial position of -0.05. Thereafter the difference between the upper and lower bounds in stress decreases to around 0.14 MPa at the normalised radial position of -0.2. This is followed by an increase in sensitivity toward the ply interface, where the magnitude of this difference increases to a maximum of greater than 0.32 MPa. This is about 0.2 MPa greater than the difference between the upper and lower bounds of the radial stresses of the full data set for this region. Over the inner ±75° ply, the difference between the upper and lower bounds in stress decreases to a value of around 0.12 MPa, at the normalised radial position of -0.52, and this difference is maintained through to the region of highest stress over this ply, which occurs at the normalised radial position of -0.7. Thereafter, this range rapidly decreases down to zero at the inner surface of the pipe.

The in-plane residual shear stress distributions of the reduced data set of the ±75°/±36° pipe, associated with the 1200 possible combinations of the polynomial pairs fitted to the simulated axial, circumferential, and 45° strain data of Figs. M.22 to M.24, are illustrated in Fig. M.28. These are plotted together with the "exact" stress distribution, and are colour coded according to the order of polynomial fitted to the 45° strain data to which they correspond. Each stress distribution adheres to the requirement of self-equilibrium, resulting from the self-correcting nature of the current method. The upper and lower bounds of these stress variations lie significantly further from the "exact" solution, than those of the full data set, seen in Fig. M.21. Each solution, however, still oscillates about the zero-stress state expected to exist through the thickness of filament-wound pipes. The largest difference between the upper and lower bounds in stress occurs at the outer surface, with a magnitude of roughly 20 MPa. This is more than double the difference between the bounds of the shear stresses of the full data set for this region. This magnitude rapidly

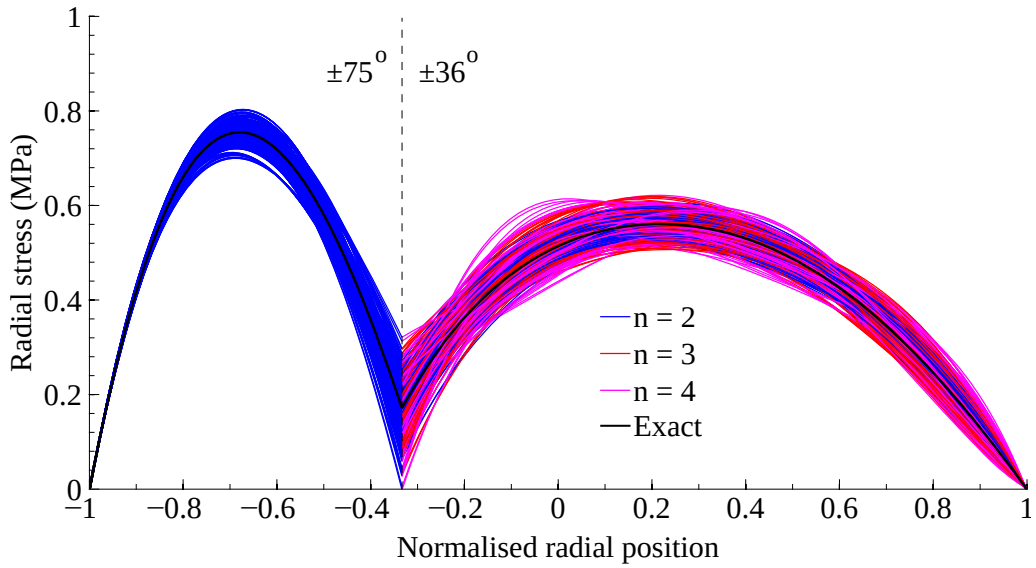

Figure M.27: Radial stress variations for the reduced data set of the ±75°/±36° pipe

decreases to slightly larger than 3 MPa, at the normalised radial position of about 0.83. Over the remainder of the outer ply the difference between the upper and lower bounds fluctuates, but never exceeds 7 MPa. At the ply interface, the magnitude of this range is approximately 6 MPa. In this region, the bounds of the stresses over the inner ply is close to 10 MPa, but this rapidly decreases away from the ply interface, to around 2 MPa at the normalised radial position of -0.6. Over the remainder of this ply thickness, this range varies slightly until it reaches a value of about 2.5 MPa at the inner surface of the pipe.

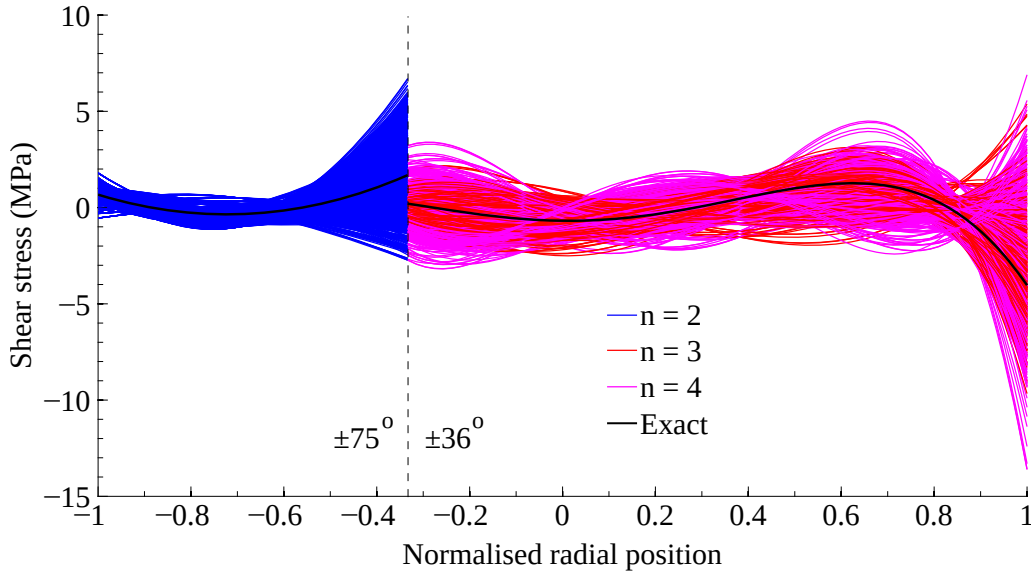

Figure M.28: Shear stress variations for the reduced data set of the ±75°/±36° pipe